# A novel machine learning-based satellite retrieval of volcanic ash for Meteosat covering the petrological variability

**Dennis Piontek**

München 2022

# A novel machine learning-based satellite retrieval of volcanic ash for Meteosat covering the petrological variability

**Dennis Piontek**

Dissertation
der Fakultät für Physik
der Ludwig-Maximilians-Universität
München

vorgelegt von
Dennis Piontek
aus Bonn-Duisdorf

München, den 20. Januar 2022

Erstgutachter: Prof. Dr. Bernhard Mayer
Zweitgutachter: Prof. Dr. Christiane Voigt
Tag der mündlichen Prüfung: 4. April 2022

# Contents

**Zusammenfassung** **v**

**Abstract** **vii**

**Publications** **ix**

**1 Introduction** **1**
1.1 Motivation: Why is remote sensing of volcanic ash necessary? . . . . . 1
1.2 Scientific topics . . . . . 4

**2 Fundamentals** **7**
2.1 Volcanic eruptions . . . . . 7
2.1.1 Volcanoes . . . . . 7
2.1.2 Volcanic clouds . . . . . 9
2.1.3 Volcanic ash . . . . . 10
2.2 Radiative transfer theory . . . . . 19
2.2.1 Electromagnetic radiation . . . . . 19
2.2.2 Blackbody radiation . . . . . 20
2.2.3 Absorption and scattering . . . . . 21
2.2.4 Radiative transfer equation . . . . . 25
2.3 Geostationary passive imagers . . . . . 26
2.3.1 MSG/SEVIRI . . . . . 26
2.3.2 Other imagers in the geostationary ring . . . . . 27
2.4 Artificial neural networks . . . . . 32
2.4.1 Multilayer perceptron . . . . . 32
2.4.2 Training . . . . . 35
2.4.3 Interpretation . . . . . 38
2.5 Current volcanic ash satellite retrievals using artificial neural networks . . . 39

**3 Papers** **41**
3.1 P1: Volcanic ash refractive indices and optical properties . . . . . 41
3.2 P2: Development of the new volcanic ash retrieval VACOS . . . . . 57
3.3 P3: Validation and application of VACOS . . . . . 87

**4 Conclusions and outlook** **125**

**A List of abbreviations** **141**

**Bibliography** **143**

**Acknowledgements** **163**

# Zusammenfassung

Vulkanaschepartikel sind eine Gefahr für die Luftfahrt, da sie in Triebwerken schmelzen und sich anschließend an kritischen Komponenten ablagern können. Dies kann zu einem totalen Leistungsverlust führen. Daher werden Satellitenmessungen zur kontinuierlichen, großräumigen Detektion von Vulkanasche eingesetzt, was durch die hohe Variabilität der atmosphärischen Bedingungen und der Ascheeigenschaften erschwert wird, etwa der bisher weitgehend vernachlässigten petrologischen Zusammensetzung.

Diese Arbeit befasst sich mit einem neuen, universell einsetzbaren Verfahren zur Bestimmung von Vulkanasche. Die volumengewichtete Mittelung bekannter Brechungsindizes der Vulkanaschekomponenten (Gläser, Minerale, Hohlräume) gemäß typischer Phasenverteilungen ermöglicht die Ableitung eines Effektivwertes. Es zeigt sich, dass Porosität, Siliziumdioxidgehalt und das Glas zu Kristall-Verhältnis den Brechungsindex in abnehmendem Maße beeinflussen. Zusammensetzung und Partikelgröße haben vergleichbare Auswirkungen auf die optischen Eigenschaften, insbesondere auf den Massenextinktionskoeffizienten. Strahlungstransferrechnungen zeigen, dass geostationäre Satellitenbildgeber gegenüber Variationen der Massensäule ($m_{\mathrm{col}}$), der Aschewolkenoberkante ($z_{\mathrm{top}}$) und des Effektivradius ($r_{\mathrm{eff}}$) am empfindlichsten sind. Das vertikale Massenprofil und der Siliziumdioxidgehalt haben kleinere, aber beobachtbare Auswirkungen.

Basierend auf diesen Erkenntnissen wird der neue Algorithmus VACOS (Volcanic Ash Cloud properties Obtained from SEVIRI) entwickelt, der sich auf Helligkeitstemperaturen im thermischen Infrarot des Radiometers SEVIRI an Bord der geostationären Meteosat Second Generation Satelliten und auf Daten eines numerischen Wettervorhersagemodells stützt. Es verwendet künstliche neuronale Netze, die mit synthetischen Beobachtungen trainiert werden, welche ein breites Spektrum an atmosphärischen Bedingungen, typischen makrophysikalischen Aschewolkeneigenschaften, und insbesondere die Variabilität der optischen Eigenschaften aufgrund verschiedener Aschearten abdecken. VACOS führt eine pixelweise Klassifizierung durch und ermittelt $z_{\mathrm{top}}$, $r_{\mathrm{eff}}$ und die optische Dicke der Asche bei 10.8 µm ($\tau_{10,8}$, konvertierbar in $m_{\mathrm{col}}$ mit einem fallspezifischen Faktor). Eine Leistungscharakterisierung anhand simulierter Daten zeigt einen mittleren absoluten prozentualen Fehler von $\lesssim 40\,\%$ für $m_{\mathrm{col}}$ für Ascheschichten mit einem wahren $\tau_{10,8}$ von $\geq$0,1, $\lesssim 10\,\%$ für $z_{\mathrm{top}}$ für Ascheschichten oberhalb von 5 km, und $\lesssim 35\,\%$ für $r_{\mathrm{eff}}$ für tatsächliche $r_{\mathrm{eff}}$ von 0,6–6 µm. Echte $m_{\mathrm{col}}$ von 0,2–1 $\mathrm{g\,m^{-2}}$ und eine Detektion unter Verwendung des abgeleiteten $\tau_{10,8}$ mit einem Schwellenwert von 0,04 führt zu einer Erkennungswahrscheinlichkeit von ~93 % bei einer Fehlalarmrate von ~1 %. Die allgemeine Anwendbarkeit von VACOS wird durch den Vergleich mit weltraumgestützten Lidar-Messungen sowie Flugzeugmessungen des Deutschen Zentrums für Luft- und Raumfahrt und der Facility for Airborne Atmospheric Measurements für die Ausbrüche des Puyehue-Cordón Caulle (2011) und des Eyjafjallajökull (2010) demonstriert. Eine Plausibilitätsprüfung mit einem Modellensemble des letzteren zeigt eine gute Übereinstimmung in der räumlich-zeitlichen Aschebedeckung, aber Abweichungen von $\gtrsim$ 100 km bei Entfernungen $\gtrsim$ 1000 km vom Vulkan auf Grund von Modellungenauigkeiten. Aufgrund seiner Anwendbarkeit unter einer Vielzahl von Szenarien ist VACOS bestens geeignet für Luftverkehrsanwendungen.

# Abstract

Volcanic ash particles are a threat to aviation as they can melt within jet engines and subsequently resolidify on critical components, potentially leading to a total loss of power. Thus, satellite measurements are used for the continuous large-scale detection of volcanic ash, which is complicated by the high variability in the atmospheric conditions and the ash properties, e.g., the yet mostly neglected petrological composition.

This thesis focuses on a new general-purpose volcanic ash satellite retrieval. Volume-weighted averaging of known refractive indices of the volcanic ash components (glasses, minerals, voids) according to generic phase distributions allows to derive an effective value. It is shown that porosity, silica content and glass-to-crystal ratio affect the refractive index to a decreasing extent. Composition and particle size have comparable impact on the optical properties, especially the mass extinction coefficient. Radiative transfer calculations show that geostationary satellite imagers are most sensitive to variations in the mass load ($m_{\mathrm{col}}$), the ash cloud top height ($z_{\mathrm{top}}$) and the effective radius ($r_{\mathrm{eff}}$); the vertical mass profile and the silica content have smaller, yet a noticeable impact.

Based on these insights, the new algorithm VACOS (Volcanic Ash Cloud properties Obtained from SEVIRI) is developed, relying on thermal infrared brightness temperatures from the radiometer SEVIRI aboard the geostationary Meteosat Second Generation satellites and auxiliary data from a numerical weather prediction model. It applies artificial neural networks trained with synthetic observations covering a wide range of atmospheric conditions, typical macrophysical ash cloud properties, and in particular the variability of optical properties due to different ash types. VACOS performs a pixelwise classification and retrieves $z_{\mathrm{top}}$, $r_{\mathrm{eff}}$ and the ash optical depth at 10.8 µm ($\tau_{10.8}$, convertible to $m_{\mathrm{col}}$ using a case-dependent factor). A performance characterization using simulated data indicates a mean absolute percentage error of $\lesssim 40\,\%$ for $m_{\mathrm{col}}$ for ash layers with a true $\tau_{10.8}$ of $\geq 0.1$, $\lesssim 10\,\%$ for $z_{\mathrm{top}}$ for layers above 5 km, and $\lesssim 35\,\%$ for $r_{\mathrm{eff}}$ for true $r_{\mathrm{eff}}$ of 0.6–6 µm. True $m_{\mathrm{col}}$ of 0.2–1 $\mathrm{g\,m^{-2}}$ and a detection scheme using the retrieved $\tau_{10.8}$ with a threshold of 0.04 leads to a probability of detection of ~93 % at a false alarm rate of ~1 %. The general applicability of VACOS is demonstrated by comparing it with spaceborne lidar retrievals as well as aircraft measurements by Deutsches Zentrum für Luft- und Raumfahrt and the Facility for Airborne Atmospheric Measurements for the eruptions of Puyehue-Cordón Caulle (2011) and Eyjafjallajökull (2010). A plausibility check with a model ensemble of the latter indicates a good agreement in the spatio-temporal ash coverage, but offsets $\gtrsim 100$ km at distances $\gtrsim 1000$ km from the volcano caused by model inaccuracies. Overall, VACOS is ideally suited for aviation applications due to its applicability in a wide range of scenarios.

# Publications

This dissertation builds upon three first-author papers included here. In addition, the work led to contributions to thee co-authored papers. They are abbreviated as **P1** to **P6** in the introduction, conclusions and outlook.

**P1**: Piontek, D., Hornby, A.J., Voigt, C., Bugliaro, L., and Gasteiger, J.: Determination of complex refractive indices and optical properties of volcanic ashes in the thermal infrared based on generic petrological compositions, *Journal of Volcanology and Geothermal Research*, 411, 107174, 2021. DOI: 10.1016/j.jvolgeores.2021.107174

**P2**: Piontek, D., Bugliaro, L., Schmidl, M., Zhou, D.K., and Voigt, C.: The New Volcanic Ash Satellite Retrieval VACOS Using MSG/SEVIRI and Artificial Neural Networks: 1. Development, *Remote Sensing*, 13, 3112, 2021. DOI: 10.3390/rs13163112

**P3**: Piontek, D., Bugliaro, L., Kar, J., Schumann, U., Marenco, F., Plu, M., and Voigt, C.: The New Volcanic Ash Satellite Retrieval VACOS Using MSG/SEVIRI and Artificial Neural Networks: 2. Validation, *Remote Sensing*, 13, 3128, 2021. DOI: 10.3390/rs13163128

**P4**: Bugliaro, L., Piontek, D., Kox, S., Schmidl, M., Mayer, B., Müller, R., Vázquez-Navarro, M., Peters, D.M., Grainger, R.G., Gasteiger, J., and Kar, J.: Combining radiative transfer calculations and a neural network for the remote sensing of volcanic ash using MSG/SEVIRI, *Natural Hazards and Earth System Sciences Discussions*, in review, 2021. DOI: 10.5194/nhess-2021-270

**P5**: Plu, M., Scherllin-Pirscher, B., Arnold Arias, D., Baro, R., Bigeard, G., Bugliaro, L., Carvalho, A., El Amraoui, L., Eschbacher, K., Hirtl, M., Maurer, C., Mulder, M.D., Piontek, D., Robertson, L., Rokitansky, C.-H., Zobl, F., and Zopp, R.: An ensemble of state-of-the-art ash dispersion models: towards probabilistic forecasts to increase the resilience of air traffic against volcanic eruptions, *Natural Hazards and Earth System Sciences*, 21, 2973–2992, 2021. DOI: 10.5194/nhess-21-2973-2021

**P6**: Plu, M., Bigeard, G., Sič, B., Emili, E., Bugliaro, L., El Amraoui, L., Guth, J., Josse, B., Mona, L., and Piontek, D.: Modelling the volcanic ash plume from Eyjafjallajökull eruption (May 2010) over Europe: evaluation of the benefit of source term improvements and of the assimilation of aerosol measurements, *Natural Hazards and Earth System Sciences*, 21, 3731–3747, 2021. DOI: 10.5194/nhess-21-3731-2021

# Chapter 1

# Introduction

## 1.1 Motivation: Why is remote sensing of volcanic ash necessary?

The 2010 eruption of the Icelandic volcano Eyjafjallajökull (pronounced as "A-ya-fyat-la-yœk-utl", Alexander, 2013) did not come unannounced, as indications for volcanic activity (e.g., earthquakes and surface deformations) had been observed since the beginning of the 1990s (Gudmundsson et al., 2010, 2012). They intensified in the first months of 2010, leading to a short effusive fissure at the flank of the volcano on 20 March and producing lava until 12 April (Sigmundsson et al., 2010). A short intermission followed; then on 14 April at around 01:30 UTC in the night, an explosive eruption started. Unusually high amounts of fine volcanic ash were produced as the magma had a rather high silica content (~60 wt.%) and was additionally powered by the glacier on top of the volcano (Gudmundsson et al., 2012, Watson, 2015). The ash plume (Figure 1.1) reached heights of up to ~10 km, and strong north-westerly winds drove the ash cloud towards Scandinavia, the United Kingdom and continental Europe in the following days (Petersen, 2010).

Volcanic ash clouds are a threat to air traffic security due to a reduction of visibility, ash and volcanic gases in the cockpit and cabin, damaging of instruments (e.g., the pitot tube), and abrasion of wings and windshields (Casadevall, 1994). Most important, volcanic ash might melt and resolidify within jet turbines, leading to at least temporary malfunctioning (Przedpelski and Casadevall, 1994). In December 1989 a KLM Boeing 747-400 aircraft unknowingly entered the ash cloud of Redoubt Volcano in Alaska and subsequently lost power on all four engines. Although the engines could be restarted, the damage to the aircraft was totaled to about US$80 million (Casadevall, 1994). Overall, 129 encounters of aircraft with volcanic ash have been reported between 1953 and 2009, some even at distances >1000 km from the volcano. In 9 cases, temporary loss of at least one engine occurred, with 2 encounters taking place even at daylight at distances of about 250 km and 930 km from the vent (Guffanti et al., 2010). This is also caused by the fact that potentially hazardous ash concentrations might not be visually distinguishable from harmless concentrations by flight crews (Weinzierl et al., 2012). Thus, nine *Volcanic*

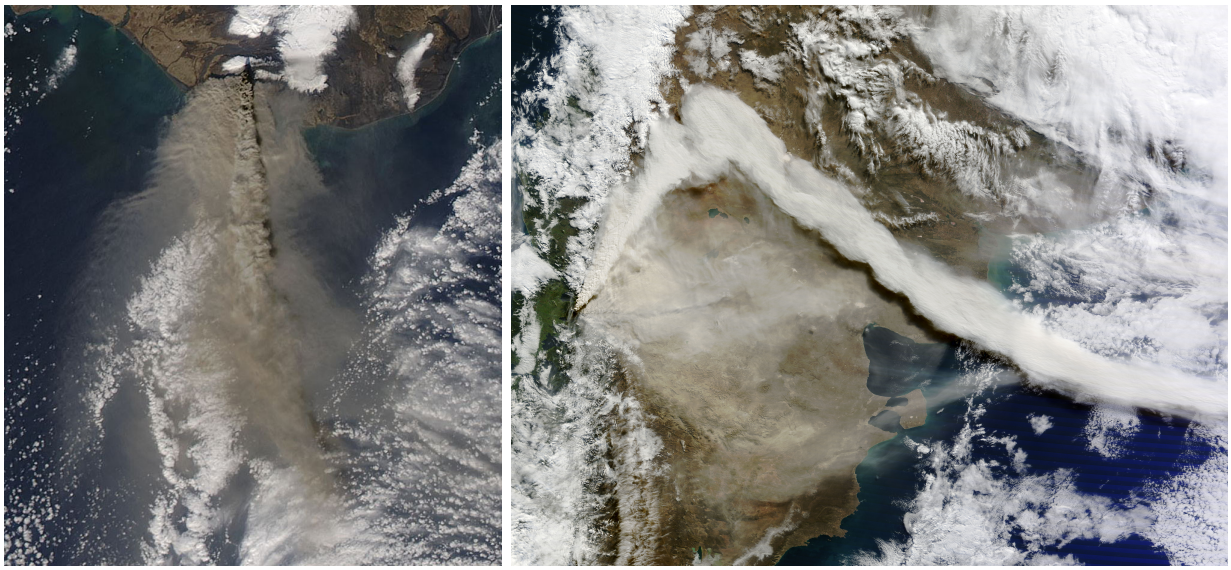

Figure 1.1: *Moderate Resolution Imaging Spectroradiometer* (MODIS) satellite images of volcanic ash plumes of Eyjafjallajökull on 17 April 2010 (left) and Puyehue-Cordón Caulle on 6 June 2011 (right); "Eruption of Eyjafjallajökull Volcano, Iceland April 17 [Detail]" (https://www.flickr.com/photos/24662369@N07/4530571303) and "Puyehue-Cordón Caulle Volcano" (https://www.flickr.com/photos/24662369@N07/5804670439) by NASA Goddard Space Flight Center, licensed under CC BY 2.0 (https://creativecommons.org/licenses/by/2.0/).

*Ash Advisory Centers* (VAACs) were founded in the 1990s, each covering a part of the globe, with the task to perform numerical volcanic ash transport and dispersion modeling in the event of an eruption to provide forecasts on the volcanic ash contamination to the responsible institutions (Bolić and Sivčev, 2011). At the time of the Eyjafjallajökull eruption, the *International Civil Aviation Organization* (ICAO) recommended "regardless of ash concentration—AVOID AVOID AVOID", such that during the first days in April 2010, extensive parts of the European airspace were closed, leading to the cancellation of $> 100\,000$ flights and lost revenues to the airlines in the order of US$1.7 billion (Bolić and Sivčev, 2011, Budd et al., 2011). Peaking at 18 April, nearly 80 % of all flights in Europe were postponed (Alexander, 2013).

The first eruptive phase of Eyjafjallajökull lasted from 14 to 18 April. It was followed by a calmer phase until 4 May. Then a second explosive phase began and lasted until 17 May, again producing large amounts of volcanic ash contaminating parts of the northern Atlantic and reaching mainland Europe (Gudmundsson et al., 2012). By then it was decided to change regulations to not only differentiate ash-contaminated from ash-free zones, but to establish multiple zones based on the ash volume concentration (Bolić and Sivčev, 2011, Langmann et al., 2012), although the corresponding threshold values (initially $0.2\,\mathrm{mg\,m^{-3}}$ and $2\,\mathrm{mg\,m^{-3}}$, later raised to $2\,\mathrm{mg\,m^{-3}}$ and $4\,\mathrm{mg\,m^{-3}}$, ICAO, Schumann et al., 2011) were decided rather arbitrarily (Alexander, 2013, Watson, 2015). Finally, from 18 to 22 May,

the volcanic activity decreased and—apart from minor activity in June—finally ceased (Gudmundsson et al., 2012).

The numerical ash transport and dispersion models as applied by the VAACS are initialized by a source term, including the vertical mass profile, particle size and compositional properties of the volcanic ash emitted from the vent. The distribution of the volcanic ash is then forced by the meteorology as given by numerical weather prediction models, and various atmospheric processes for removal and alteration of the ash particles (Langmann et al., 2012, Mackie et al., 2016). However, comparisons of model results with in situ measurements and satellite observations indicated weaknesses of the VAAC predictions, e.g., overestimation of the spatial extent of the ash contamination by one order of magnitude (Eliasson and Yoshitani, 2015, Eliasson et al., 2014), fine-structured ash clouds instead of large scale coverage for distal locations (Weber et al., 2012), and differences in the order of 100 km in the horizontal location with respect to the real ash clouds (Schumann et al., 2011). Numerical dispersion calculations can be improved by better constraining volcanic emissions. For instance, Stohl et al. (2011) applied a dispersion model-based inversion scheme to satellite retrievals of volcanic ash loads for the 2010 Eyjafjallajökull eruption to derive a time and height-dependent eruption source term, leading to improvements in the agreement of dispersion model results and satellite observations with respect to the spatial ash contamination. The authors found that ash concentrations over Europe (i.e., 10° W–30° E, 36° N–60° N) remained below the critical limit of $4\,\mathrm{mg\,m^{-3}}$ (which triggers airspace closure) in principle all the time in spring 2010.

Still, dispersion models might loose predictive power with increasing runtime as small inaccuracies (e.g., in the meteorological forcing fields) might lead to enormous errors (Dacre et al., 2016), such that satellite retrievals might be preferred to model results. In addition, numerous volcanoes are situated at remote locations such that they are mainly observable from space. Depending on the instrument, satellite measurements can provide extensive spatial coverage in real time and at high temporal resolutions (e.g., the full disc of Earth every 15 min and less, Schmetz et al., 2002a) , or low/infrequent spatial coverage but with a high spatial resolution (e.g., horizontal resolutions below 1 km and vertical resolutions down to 0.03 km, Watson et al., 2004, Winker et al., 2009) or spectral resolution (e.g., down to $0.25\,\mathrm{cm^{-1}}$, Hilton et al., 2012). Many volcanic ash detection algorithms rely on its spectral signature in the thermal infrared spectrum which can produce a negative difference in the brightness temperatures at 11 µm and 12 µm (Prata, 1989), allowing to discriminate it from cirrus clouds (Inoue, 1985). However, the volcanic ash detection is complicated, for example, by the presence of volcanic ash under a very diverse set of geographic and atmospheric conditions; a large variation in volcanic ash types from different eruptions (Mackie et al., 2016, Reed et al., 2018); complex vertical ash mass profiles (Marenco et al., 2011); sulfur dioxide emitted by some volcanoes and influencing the infrared spectrum (Gray and Bennartz, 2015); mineral dust clouds and arid Earth surfaces which produce a spectral signal similar to the one of ash (Ackerman, 1997, Watkin, 2003); and water vapor, liquid and ice water clouds hiding the ash-specific spectral signature (Watkin, 2003). At the same time, only a very limited number of spectral bands is provided by the satellite imagers used for real-time monitoring of volcanic ash. Thus, its detection and the retrieval

of its properties becomes a non-trivial inversion problem.

Apart from the direct impact to aircraft in operation, volcanic ash can also affect the infrastructure in relative proximity to the volcanic source: airports might be affected if the corresponding airspace is ash contaminated or ash deposits reduce the traction of runways (Guffanti et al., 2009); power outages, e.g., caused by flashovers due to moist volcanic ash covering insulators or collapse of transmission poles/lines due to the weight of the deposited ash (Wilson et al., 2012); disruption of water supply and disposal, e.g., by interfering the water sources/pumps/distribution systems, changing physical and chemical water properties or unusually high water demands (Wilson et al., 2012); components relying on constant air exchange might be damaged, e.g., computers, ventilation and air conditions (Wilson et al., 2012); tephra deposition can damage buildings, e.g., due to roof collapse (Spence et al., 2005). In addition, volcanic ash might pose a threat to health, especially if inhaled (Horwell and Baxter, 2006).

Volcanic eruptions can also influence the global climate on time scales of years. The main impact comes from the emitted sulfur dioxide and the resulting sulfate in the stratosphere. The latter has a cooling effect to the surface as it scatters incoming solar light but at the same time heats the stratosphere by absorbing thermal and near-infrared radiation. If this heating takes place at low latitudes, the increased temperature gradient with respect to high latitudes can lead to warmer continental winters on the northern hemisphere via strengthening of the polar vortex (Langmann, 2014, Robock, 2000, Timmreck, 2012). With respect to volcanic ash, its direct radiative effect (i.e., the direct interaction with incoming solar and outgoing thermal radiation), as well as the indirect radiative effect (i.e., influencing cloud formation, cloud coverage, droplet sizes and precipitation when ash particles act as cloud condensation or ice nuclei) have in most cases only a spatially and temporally limited impact (Langmann, 2013), due to the comparably short atmospheric lifetime on the order of days to weeks (Grainger et al., 2013). However, sedimented ash might modify the planetary albedo (Langmann, 2013). For instance, Flanner et al. (2014) indicated that in the case of the 2010 Eyjafjallajökull eruption warming due to volcanic ash deposited on snow and ice surfaces (especially in Greenland) notably counteracted the cooling by atmospheric sulfates.

## 1.2 Scientific topics

As described above, there is a clear need for volcanic ash retrievals via satellite in the context of aviation safety. Usually, those methods rely on radiative transfer calculations based on the optical properties of volcanic ash, which in turn are related to its complex refractive index. Due to a lack of alternatives, the majority of algorithms developed in the past decades utilized only two laboratory measurements of this quantity in the thermal infrared by Pollack et al. (1973), Volz (1973) (additional volcanic ash samples were investigated by Deguine et al. (2020), Grainger et al. (2013), Ishimoto et al. (2016), Reed et al. (2018) only recently, see Section 2.1.3 for details). However, an accurate assumption of the complex refractive index is necessary as some studies indicated that it has a non-negligible

impact on the performance of volcanic ash retrievals in the thermal infrared (Prata et al., 2019, Western et al., 2015). Thus, the first hypothesis is:

**1.** *For volcanic ash, the petrological composition and the effective particle radius have a similarly strong impact on its optical properties in the thermal infrared spectrum, such that both need to be accounted for in radiative transfer.*

This contrasts earlier assumptions, e.g., by Wen and Rose (1994), who concluded that the particle size is of greater importance than the volcanic ash composition with respect to mass load retrievals. To test the hypothesis, a novel method is developed to derive complex refractive indices based on typical petrological compositions of volcanic ash (a comparable approach was used for mineral dust by Lee and Park, 2014, Sokolik and Toon, 1999). With this technique, a set of complex refractive indices is composed for different bulk silica contents, glass-to-crystal ratios and porosities. Calculating the optical properties for these refractive indices in combination with different particle sizes and shapes allows to compare the individual importance.

The retrieval of multiple quantities of volcanic ash clouds is of interest: the mass load and especially the mass volume concentration; the cloud top height and geometrical thickness, or more general, the vertical mass profile; the effective particle radius and shape; and the composition, e.g., the silica content and the glass-to-crystal ratio. The mass load can be used to quantify the total mass emission of a volcanic eruption (Corradini et al., 2016, Gudmundsson et al., 2012, Prata and Prata, 2012). Ash mass concentration and height are needed for the aviation safety evaluation (ICAO, Watson, 2015). Vertical mass profiles or mass loads are necessary for the comparison with numerical ash transport and dispersion models (Dacre et al., 2016, Muser et al., 2020). Particle size and shape influence sedimentation (Grainger et al., 2013, Mackie et al., 2016) and aggregation (Brown et al., 2012). Mass concentration and size (and, thus, the particle number concentration) can be used to quantify aerosol–cloud interaction (Langmann, 2013). Unfortunately, not all quantities are retrievable due to the limited spectral resolution of the used instrument (here the *Spinning Enhanced Visible and Infrared Imager* on the *Meteosat Second Generation* satellites, MSG/SEVIRI); physical limits in the sensitivity; or mutual cancellation of the effects of different properties. Hence, it is investigated:

**2.** *What is the information content of typical spaceborne geostationary infrared observations by passive imagers like MSG/SEVIRI with respect to volcanic ash cloud properties?*

The question is answered by calculating and analyzing corresponding optical properties of volcanic ash and performing radiative transfer calculations for different ash clouds.

Based on the results related to the first two topics, the new volcanic ash retrieval *Volcanic Ash Cloud properties Obtained from SEVIRI* (VACOS) is developed. It utilizes MSG/SEVIRI and artificial neural networks trained with synthetic observations, and is intended to be generally applicable to different volcanic eruptions. Thus, the training data

set builds upon atmospheric data covering its daily, annual and inter-annual variability; the full MSG/SEVIRI disc including different geographies and realistic scene-dependent sea and land surface emissivities; volcanic ash clouds with a wide range of typical micro- and macrophysical properties; and an extensive set of volcanic ash refractive indices representing different ash compositions. The last point together with the choice of a radiative transfer-based training data set constitutes the main novelty of this algorithm compared to existing artificial neural network-based volcanic ash retrievals, which are limited to only a few volcanic eruptions due to the choice of their training data (**P4**, Gray and Bennartz, 2015, Picchiani et al., 2011, 2014, Piscini et al., 2014, Zhu et al., 2020, see Section 2.5 for details). Thus, the question is:

**3.** *How accurate is the general-purpose volcanic ash satellite retrieval VACOS for MSG/SEVIRI using artificial neural networks with respect to the detection of volcanic ash clouds and the derivation of their mass column concentration, cloud top height and effective particle radius?*

The performance of VACOS is analyzed using simulated data, CALIPSO/CALIOP (*Cloud-Aerosol Lidar and Infrared Pathfinder Satellite Observation*, *Cloud Aerosol Lidar with Orthogonal Polarization*) retrievals of the Puyehue-Cordón Caulle ash cloud in 2011 as well as airborne measurements and transport and dispersion model results of the Eyjafjallajökull eruption in 2010.

The rest of this cumulative thesis is structured as follows: In Section 2, a literature overview on the most essential topics and tools of this work is given, namely volcanic ash as the object of interest; radiative transfer theory; geostationary passive imagers and in particular MSG/SEVIRI; artificial neural networks; and the currently existing volcanic ash satellite retrievals using artificial neural networks. Note that these summaries are intended to provide a general introduction, introducing basic facts and figures, concepts and technical terms; they are not complete reviews of the fields. Furthermore, additional information is given in the papers included in this work, e.g., the connection of the volcanic ash's microphysical properties to the optical properties is investigated in **P1** and a more extensive review of the existing volcanic ash passive satellite remote sensing techniques is presented in **P2**; it is not repeated here to avoid redundancy. Section 3 forms the main part, containing reprints of the papers. Note that they do not necessarily deal with the scientific topics individually. Thus, in Section 4, the work is summarized, each scientific topic is addressed again in detail and an outlook is given.

# Chapter 2

# Fundamentals

## 2.1 Volcanic eruptions

In the following subsections, the basics of volcanic eruptions, ash cloud formation and volcanic ash properties are introduced. Note that further information is provided in Section 3, e.g., the relation between volcanic ash composition, its microphysical properties and the resulting optical properties is described in **P1**, whereas ash cloud properties are reviewed in **P2**.

### 2.1.1 Volcanoes

The majority of the volcanoes currently present on the Earth's surface are located at the rims of *tectonic plates* (Figure 2.1), for instance, around the Pacific Ocean (the so-called *Ring of Fire*) with volcanoes at the western coast of the Americas, along the Aleutians, Kamchatka, Japan, the Philippines, Malaysia, Indonesia, Papua New Guinea and the surrounding islands; in the Caribbean at the boundary of the Caribbean plate; in and around the Mediterranean at the boundary of the African and the Eurasian plate. Other famous examples are the Hawaiian volcanoes in the Pacific or the Icelandic volcanoes in the Atlantic (Lockwood and Hazlett, 2010, Siebert et al., 2011).

The tectonic plates are able to move relative to each other, leading either to divergent or convergent behavior. The former happens within the oceanic basins. The weaker/thinner crust of the Earth allows the rise of material from the interior and subsequently the formation of new crust, which further drives the separation of the plates. The result is the globally-interconnected *Mid-Ocean Ridge*. For the most part, it resides underwater (with Iceland being one of the few exceptions). Convergent movement takes place mainly where oceans meet continents. As the continental plates generally consist of lower density rocks, the oceanic plates dive below them. At some depth, water carried by the subducting plate is released, which lowers the melting temperature of the surrounding rocks and as a consequence triggers their melting. Additionally, intraplate volcanism can take place if mantle plumes rise from deep below the Earth's surface (potentially from the boundary of Earth's core and its mantle). As the overlying plates move, these plumes form linear chains of

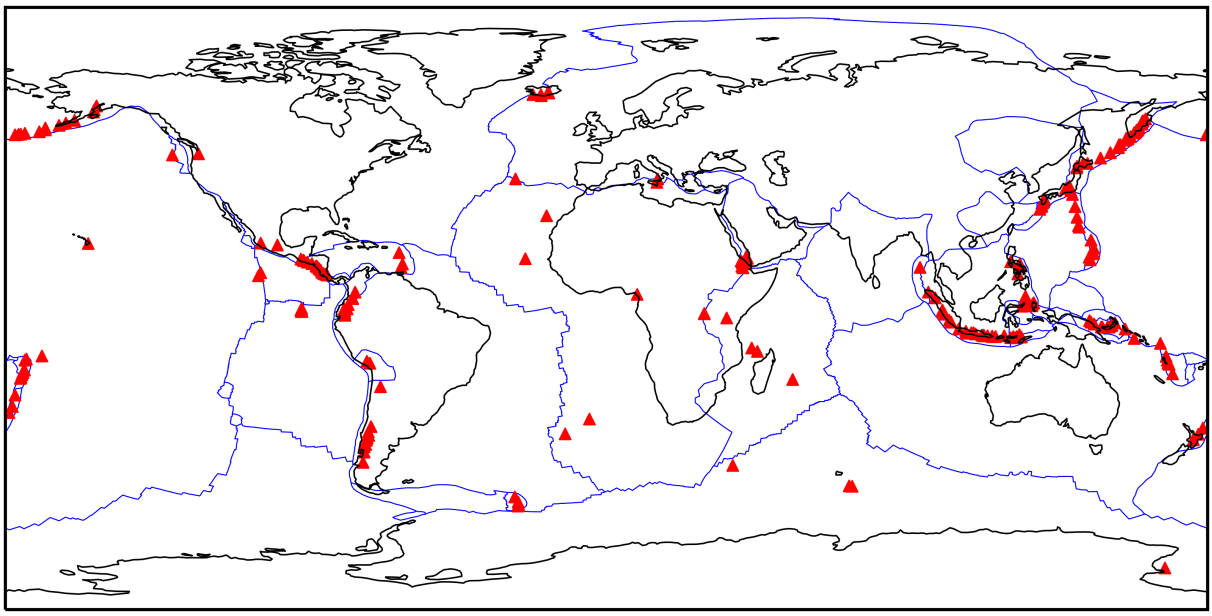

Figure 2.1: Locations of volcanic eruptions since 2000 as listed by the Smithsonian Global Volcanism Program (red, Venzke, 2021), with boundaries of continents (black) and tectonic plates (blue, Bird, 2003).

volcanoes, especially in the Pacific (e.g., the Hawaiian islands). In all cases, melted rock containing dissolved gases, called *magma*, can be created. Due to differences in the density of the crusts material and the melted magma, the latter rises until it reaches some neutral buoyancy level, where it might form a magma chamber or even a complex reservoir, potentially only a few kilometer beneath the surface (Lockwood and Hazlett, 2010).

Finally, the eruption of a volcano could be initiated by various events. The current theory is that some initial breaking of the magma chamber slightly reduces the pressure within the chamber, leading to exsolution of volatiles, which could expand in the cracks of the chamber walls and lead to further fracturing. This process might repeat and accelerate and—if the surface is reached—could lead to an eruption. Different events (or combinations thereof) are speculated to start this process. First, the introduction of magma from deeper levels might increase the chamber's pressure. Second, crystals might form in the magma and sediment to the chamber's bottom, such that in the chamber's uppermost part remains a melt of lower density, together with accumulated exsolved gases. This evolution of the melt might increase the pressure on the chamber's ceiling. Third, even minor changes in the crust due to weather or tides might be enough to bring the magma chamber out of its equilibrium (Lockwood and Hazlett, 2010).

Explosive eruptions are further driven by gases which exsolve from the magma as the pressure decreases, forming bubbles and turning the magma into a froth. They continue to grow and rapidly expand in volume, leading to the explosive behavior and the ejection of volcanic material. If the magma comes in contact with external water (e.g., sea water,

glaciers, crater lakes), the water turns into steam explosively, increasing the strength of the event and leading to a *hydromagmatic* eruption (Langmann, 2013, Lockwood and Hazlett, 2010).

### 2.1.2 Volcanic clouds

*Magma* denotes melted rock under the Earth's surface, potentially including gas bubbles and crystals. Above the surface, it is called *lava*, or *tephra* if fragmented (Lockwood and Hazlett, 2010, Mackie et al., 2016). The fragmentation is caused, for instance, by the fast expansion and the resulting stress of the gas bubbles; by abrupt changes in the overall pressure (e.g., when the volcanic dome collapses); or by water coming in contact with the melt which either turns into steam explosively or quickly quenches the melt, potentially bursting later on (Mackie et al., 2016). The part of the tephra with particle sizes <2 mm is called *volcanic ash* (Mackie et al., 2016). Further sub-classifications are relative and depend on the scientific field, as pointed out by Stevenson et al. (2015). E.g., particles with sizes $\gtrsim$ 1 µm are called *coarse* in atmospheric sciences (Wallace and Hobbs, 2006), whereas in volcanology sizes of the order 0.1–1 mm are considered coarse (Lockwood and Hazlett, 2010, Wilson et al., 2012). Here, particles with sizes $\lesssim$ 10 µm are in the focus, as these travel furthest in volcanic ash clouds (Grainger et al., 2013).

Based on observations and analog/numerical experiments, the following simple model has been established for common eruptions. Above the volcanic vent, the eruption column rises (Figure 2.2). In the lowermost part, volcanic emissions rise due to gas thrust. This region constitutes about 10 % of the column. Material is emitted with velocities up to ~700 m s$^{-1}$ and then slows down to <100 m s$^{-1}$ due to drag forces. As the column rises, surrounding air is entrained and heated, thereby reducing the effective density of the column. If the density is below that of the environment, convective lift starts. The convective region makes up 50–90 % of the column, with updraft velocities of most eruption styles varying between a few meters per second and ~80 m s$^{-1}$. If the effective density is not low enough, the eruption column collapses, potentially leading to a *pyroclastic density current* with the volcanic material rapidly moving downhill. Alternatively, pyroclastic density currents are also often caused by collapsing volcanic domes. Also in this case, ambient air might be entrained such that at some point parts of the pyroclastic density current start to rise convectively. After the convective lift and due to the vertical momentum, the ash might rise above the neutral buoyancy level, creating an overshooting top. It falls back and spreads laterally, forming an umbrella cloud. In the presence of wind, ash transport begins and an *ash plume* forms (Lockwood and Hazlett, 2010, Mackie et al., 2016, Self and Walker, 1991).

In general, umbrella clouds and ash plumes form in the upper half of the troposphere (Self and Walker, 1991), e.g., at altitudes of 3–10 km for Eyjafjallajökull in 2010 (Gudmundsson et al., 2012) and up to 15 km for Puyehue-Cordón Caulle in 2011 (Klüser et al., 2013). Extreme events might reach heights >25 km (Mackie et al., 2016, Siebert et al., 2011, Sparks et al., 1986, Sparks, 1986) and up to about 50 km (Self and Walker, 1991). An ash cloud itself can have a geometrical thickness of up to few kilometers, consisting

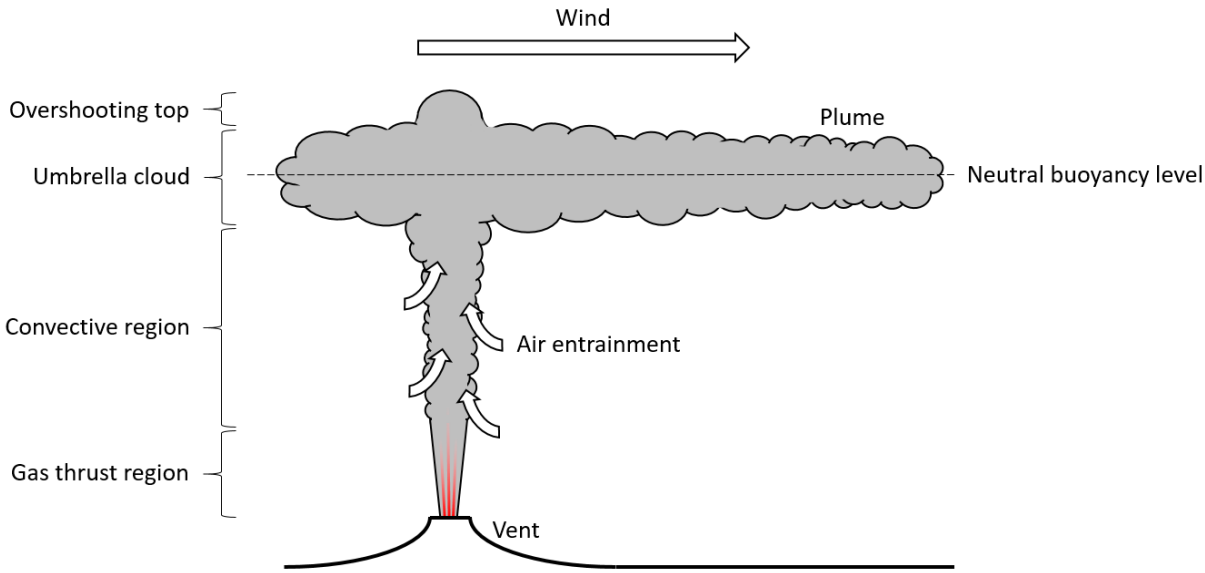


Figure 2.2: Sketch of an volcanic eruption column and the consequent ash plume.

of one or more layers (Marenco et al., 2011, Schumann et al., 2011). Typical ash mass concentrations depend strongly on the lifetime, with concentrations of a few 100 µg m$^{-3}$ at distances of 1000–2000 km from the source (Marenco et al., 2011, Schumann et al., 2011) but concentrations of the order of 1 mg m$^{-3}$ (Weber et al., 2012) to 1 g m$^{-3}$ (Przedpelski and Casadevall, 1994) at distances of a few kilometers from the volcano.

### 2.1.3 Volcanic ash

#### Composition and microphysical properties

Chemically, magma contains mainly silica ($SiO_2$) with 40–75 wt.% (Langmann, 2013, Lockwood and Hazlett, 2010). Further common oxides are titanium dioxide ($TiO_2$), aluminium oxide ($Al_2O_3$), ferric oxide ($Fe_2O_3$), ferrous oxide (FeO), manganese oxide (MnO), magnesium oxide (MgO), calcium oxide (CaO), sodium oxide ($Na_2O$), potassium oxide ($K_2O$) and phosphorus pentoxide ($P_2O_5$) (Best, 2003, Nakagawa and Ohba, 2002, Prata et al., 2019). Compositions with a high silica content (roughly >65 wt.%) are called *felsic*, whereas low silica contents (<50 wt.%) are called *mafic*; otherwise one speaks of *intermediate* compositions (Lockwood and Hazlett, 2010). A typical classification scheme utilizes the silica content versus the summed weight percentage of $Na_2O$ and $K_2O$. Based on this classification, various volcanic products are named, e.g., *basalt*, *andesite* or *rhyolite* (Lockwood and Hazlett, 2010, Siebert et al., 2011). As silica forms polymer chains in magmatic melts, an increasing silica content results in an increasing viscosity of the magma. In addition, higher silica contents partly correlate with higher amounts of volatiles (i.e., gases dissolved in magma; typically 0.5–7 wt.%), primarily water vapor ($H_2O$) but also sulfur dioxide ($SO_2$) and carbon dioxide ($CO_2$) due to a tendency of felsic melts to have a higher volatile sol-

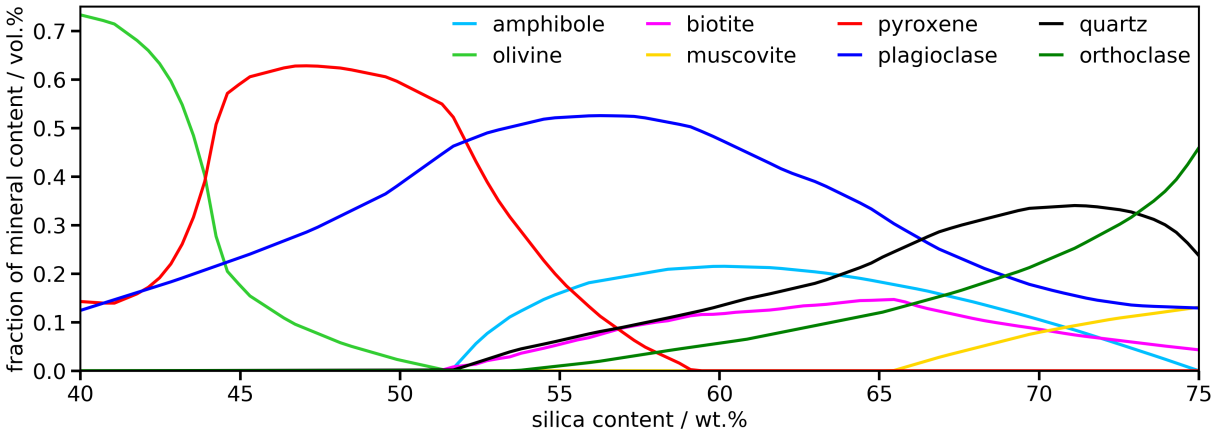


Figure 2.3: Contribution of typical minerals to the crystalline content of volcanic ash depending on the silica content; numbers are extracted from Jerram and Petford (2011).

ubility than more mafic ones. Clearly, the viscosity also determines the mobility of the exsolved volatiles, i.e., the gas bubbles. And as the volatiles drive the eruption, an increased amount of gases trapped in the magma (either in bubbles or dissolved) leads to an increased explosiveness (Langmann, 2013, Lockwood and Hazlett, 2010, Sigurdsson et al., 1999).

Within the melt, crystalline minerals are formed both during storage (usually larger crystals called *phenocrysts*) and ascent (usually smaller crystals called *microlites*). Those have different chemical compositions, melting temperatures and densities, and as a consequence different minerals predominate in magma of different silica contents (Figure 2.3). For example, quartz, alkali feldspar and sodium-rich plagioclase dominate for felsic magma, whereas calcium-rich plagioclase, olivine and pyroxene is present in mafic rocks (Jerram and Petford, 2011, Nakagawa and Ohba, 2002, Rogers, 2015). As not all melt crystallizes before and during the eruption, the ejected volcanic ash consists of a mixture of crystals and volcanic glass (Wilson et al., 2012). They are either internally mixed with one or more crystals embedded in a glassy groundmass, or externally with each particle consisting either of a mineral or of glass, see Figure 2.4 (Hornby et al., 2019, Shipley and Sarna-Wojcicki, 1982). Note that the minerals (except for quartz) have a lower silica content than the bulk magma, and consequently the remaining glass has a higher silica content than the bulk magma (Mackie et al., 2016). The petrological composition itself is not fixed, but changes with the distance from the the volcanic source, as the (denser) crystals sediment faster (e.g., at distances of the order of 100 km from the vent) than the glass shards. Thus, distal ash contains mostly glassy particles and has a higher silica content than the original magma (Mackie et al., 2016, Shipley and Sarna-Wojcicki, 1982).

Due to the exsolved gases, the volcanic glass might be porous and contains bubbles (vesicles) and overall porosity can be quite high, e.g., >80 % (Sparks, 1978). However, when considering fine ash, the actual sizes of the bubbles needs to be considered. Using backscattered electron images or stereo-scanning electron microscopy, and considering the

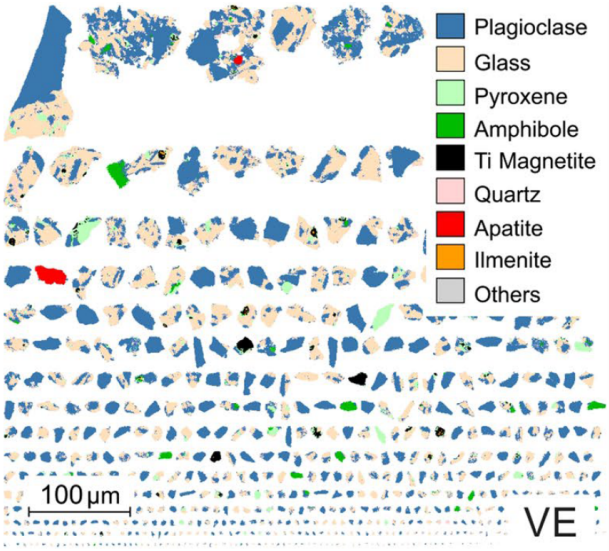


Figure 2.4: Minerals and volcanic glass present in a volcanic ash sample originating from a vulcanian explosion at the Santiaguito dome complex, Guatemala; the phases were determined using *Quantitative Evaluation of Minerals by Scanning Electron Microscopy / Particle Mineralogical Analysis* (QEMSCAN/PMA) with a resolution of 1 µm; extracted from a figure of Hornby et al. (2019), licensed under CC BY 4.0 (http://creativecommons.org/licenses/by/4.0/).

number density, size distributions with peaks at diameters of the order of 10–20 µm were measured (Genareau et al., 2012, 2013), but also peak diameters of ~0.5 µm (Colucci et al., 2013). With respect to the volume, bubbles with diameters of 10–600 µm contribute the major part (Cioni et al., 2014, Genareau et al., 2013, Klug and Cashman, 1994). Still, even for particles with effective diameters of 1.5–2.8 µm in the plume of a degassing volcano, Shcherbakov et al. (2016) deduced porosities of 18–35 % from the aerosol refractive index. Ash densities are $<1\,\mathrm{g\,cm^{-3}}$ in the case of high vesicularity; with decreasing particle size/decreasing porosity, the density increases (Mackie et al., 2016). Volcanic glasses have densities of $\sim 2.4\,\mathrm{g\,cm^{-3}}$, whereas minerals often have $\sim 3\,\mathrm{g\,cm^{-3}}$ and larger (Shipley and Sarna-Wojcicki, 1982, Wilson et al., 2012).

The typical volcanic ash particle size decreases with the ash cloud's lifetime and distance from the source; a log-normal distribution (see Equation 7 in **P1** and Limpert et al., 2001) is often used to describe size measurements (Farlow et al., 1981, Grainger et al., 2013, Stevenson et al., 2015). However, definite figures depend heavily on the type of eruption as well as the measurement technique. For instance, based on deposits, median grain sizes in the order of 1–10 mm at distances of 25 km from the source have been reported for magmatic eruptions, whereas sizes of the order of 0.1 mm have been found at the same distance for hydromagmatic eruptions (Mackie et al., 2016). Airborne in situ measurements indicated mainly particle diameters of 10–30 µm at distances of around 100 km (Mackie et al., 2016). For the effective particle radius (i.e., the area-weighted radius) of Eyjafjallajökull ash in

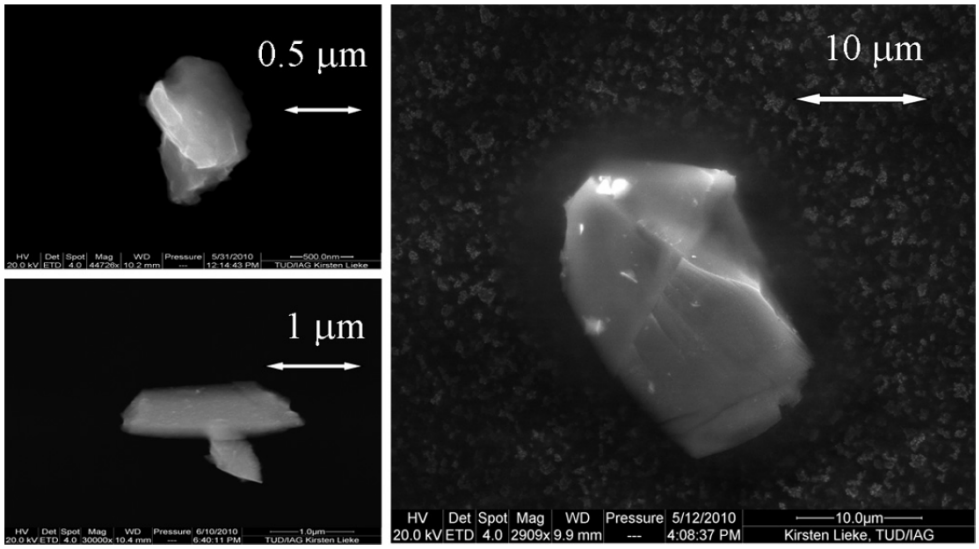


Figure 2.5: Images of volcanic ash particles created using *Scanning Electron Microscopy* (SEM); the samples were collected in situ in the Eyjafjallajökull ash plume above the North Sea at 2 May 2010; taken without changes from Schumann et al. (2011), licensed under CC BY 3.0 (https://creativecommons.org/licenses/by/3.0/).

2010, Johnson et al. (2012) found 0.5–2 µm at distances of ~1400 km and Schumann et al. (2011) 0.65–1.4 µm at ~1760 km; Weber et al. (2012) measured particle radii of roughly 0.2–3 µm about 1950 km from the source (and even smaller particles might have been present in significant amounts). Satellite-based remote sensing retrievals of volcanic ash of different volcanoes and under different conditions led to effective radii of 0.5–9 µm (Grainger et al., 2013), 1.1–2.7 µm (Ishimoto et al., 2016) and 0.16–3.09 µm (Ishimoto et al., 2021). In the discipline of *cryptotephra*, median shard diameters of 5–100 µm have been found even at distances >1000 km (Mackie et al., 2016, Stevenson et al., 2015). The log-normal distribution's form is parameterized by two quantities: besides a radius (e.g., the effective or the median radius), one uses the geometric standard deviation. Typical values for it are of the order 1.38–1.74 (Farlow et al., 1981, Stevenson et al., 2015).

The shape of the ash particles (e.g., Figures 2.5 and 2.6) is highly variable (Vogel et al., 2017), including blocky particles, glass shards originating from the hulls of fragmented gas bubbles and foam like, vesicular ash flakes (Mackie et al., 2016). However, glassy shards tend to dominate at large distances, i.e., beyond 50–250 km (Genareau et al., 2013, Shipley and Sarna-Wojcicki, 1982), and smaller particles (i.e., particle diameter $\lesssim$ 5 µm) tend to be more spherical than larger ash particles (Vogel et al., 2017).

Further changes of the volcanic ash with traveled distance are related to atmospheric processes. Gravitational settling is determined by the terminal velocity which exhibits a non-negligible dependence on the particle shape, with a factor of ~2 difference between spherical and highly non-spherical particles. Model calculations for particles of diameters of 1–10 µm and different shapes resulted in terminal velocities of about 0.05–5 mm $s^{-1}$,

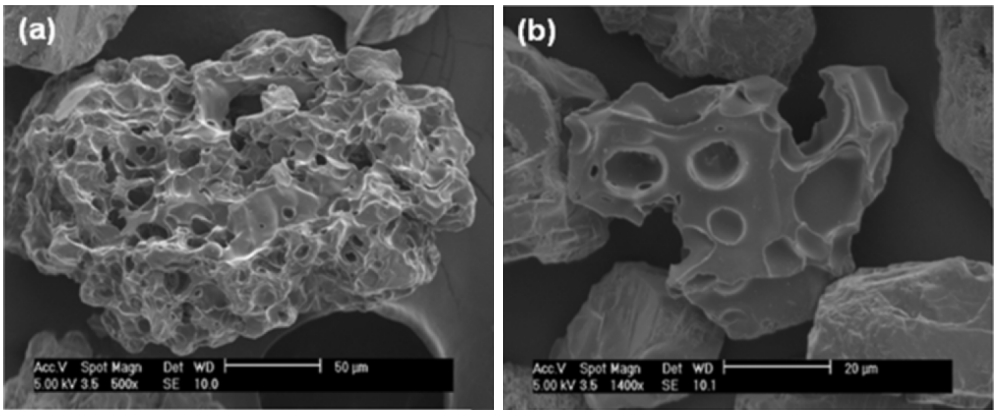


Figure 2.6: Images of volcanic ash particles created using SEM; the samples are from the eruption of Mount St. Helens at 18 May 1980; extracted from a figure of Genareau et al. (2013), licensed under CC BY 2.0 (https://creativecommons.org/licenses/by/2.0/).

respectively (Mackie et al., 2016). Reduction of small ash particles is further increased due to *aggregation* (also *coagulation*), i.e., fine ash particles may collide and form aggregates with sizes in the order of 10 µm–10 mm, which again have higher fall-out velocities. In the presence of water (from the magma, external water bodies or the atmospheric water vapor), their creation is caused by hydrometeor formation or surface tensions when covered/mixed with liquids. In the absence of liquid water, ash particles might cling together due to electrostatic charges (e.g., caused by particle collisions) or their entwined irregular surfaces. Scavenging from volcanic-emitted gases can lead to the creation of crystals on the surfaces of ash particles, holding multiple particles together (Brown et al., 2012, Langmann, 2014, Mackie et al., 2016). The surface of volcanic ash particles might be further altered due to emitted gases, e.g., sulfuric acid might condensate on the surface and sulfates might be adsorbed (Langmann, 2013, Rose, 1977, Wilson et al., 2012).

### Complex refractive index

The chemical and petrological composition influence the complex *refractive index* of volcanic ash (Kolokolova and Gustafson, 2001). Back in 1973, Pollack et al. (1973) and Volz (1973) measured the refractive index in the thermal infrared of a handful volcanic ash samples in the laboratory, which were then heavily used in the following decades (e.g., Gangale et al., 2010, Ishimoto et al., 2016, Prata, 1989, Prata and Grant, 2001, Pugnaghi et al., 2013, Wen and Rose, 1994, Yu et al., 2002). Only in recent years, additional refractive indices in the thermal infrared were derived from various ash samples to cover a wider range of possible ash types. Deguine et al. (2020), Grainger et al. (2013), Reed et al. (2018) measured the spectral extinction and the size distribution and assumed specific shapes to derive the refractive index from the optical properties. Using spaceborne hyperspectral brightness temperature measurements, Ishimoto et al. (2016) applied a two-step retrieval to derive micro- and macrophysical ash cloud properties in a first step under the

assumption of refractive indices from Pollack et al. (1973), and the actual imaginary part of the refractive index in a second step by keeping all other previously retrieved quantities constant. Prata et al. (2019) fitted linear wavelength-dependent functions to both parts of the ash refractive index (from Reed et al., 2018), using either the silica content or the ratio of non-bridging oxygens to tetrahedrally coordinated cations as an argument (thus, both arguments reflect the chemical composition of the volcanic ash). The coefficient of determination $R^2$ was used to quantify how good the fits reproduce the original measurements; although values >0.5 were found for some parts of the spectrum, it was <0.5 around wavelengths of 9–10 µm, i.e., around the peak of the imaginary part of the refractive index of volcanic ash.

The variability of the refractive indices is large: results from Reed et al. (2018) and Deguine et al. (2020) show large deviations between different ash samples (a factor of 2–3) and also significant differences between the results of the two studies for the same samples (up to a factor of 2), potentially due to the different shape assumptions (Deguine et al., 2020). This variability also influences, for instance, volcanic ash satellite retrievals in a non-negligible fashion (Prata et al., 2019, Wen and Rose, 1994, Western et al., 2015).

### Role as cloud condensation and ice nuclei

Volcanic ash (just as other aerosols) might impact liquid and ice water clouds. Depending on the temperature, the relative humidity $RH$ and the aerosol properties, ash particles might act as *cloud condensation nuclei* (CCN) to produce liquid water clouds or as *ice nuclei* (IN) to form cirrus clouds (Wallace and Hobbs, 2006). A common conception (which is by no means sufficiently tested in all aspects, Boucher et al., 2013, Fan et al., 2016, Langmann, 2013) assumes that CCNs together with water vapor under supersaturated conditions lead to the formation of droplets, and consequently to increases in the cloud cover, liquid water path, droplet number concentration and finally to precipitation, which reduces the cloudiness again. However, if the CCN number concentration is sufficiently high, the available water vapor may be used up to form only small droplets. In this case, cloud cover, liquid water path and droplet number concentration are again increased, but average droplet size is decreased with respect to the previous case and, thus, precipitation is inhibited (e.g., Rosenfeld et al., 2001). As a result, the lifetime of the clouds increases. As discussed by Durant et al. (2008), there might be a similar situation for INs: a small number of INs in a supercooled cloud might trigger ice particle growth (by the *Wegener-Bergeron-Findeisen process*, Storelvmo and Tan, 2015) leading to precipitation, whereas a large number of INs (e.g., as might be present after a volcanic eruption) might form many small ice particles, each of which unable to further grow to become large enough to precipitate. Note that these simple pictures are most probably complicated by further micro- and macrophysical feedbacks dependent on the atmospheric conditions and geographical location, which might weaken or modify the straight-forward relationships (Rosenfeld et al., 2008, Stevens and Feingold, 2009). The aerosol-cloud interaction also varies with different cloud types (Fan et al., 2016). Apart from modifying the water cycle, these aerosol–cloud interactions can also have radiative impacts, e.g., the increased cloud cover increases the

planetary albedo (Albrecht, 1989), especially for clouds over dark surfaces such as oceans, whereas the increased droplet number concentration at reduced droplet sizes increases the reflectivity of the clouds even more (Twomey, 1977). Further, water also influences volcanic ash: the formation of hydrometeors is an important process in the wet aggregation of volcanic ash particles (Brown et al., 2012, Mackie et al., 2016). Due to their larger size, ash aggregates sediment faster than their constituents. Thus, aggregation has to be properly incorporated in transport and dispersion models which otherwise overestimate the amount of fine distal ash.

For INs, different freezing modes exist which are active at different temperatures, which again depend also on the aerosol properties. In the case of volcanic ash, laboratory experiments show that *contact freezing* (i.e., an aerosol particle touches the surface of a liquid water droplet from the inside or from the outside, Durant and Shaw, 2005) takes place at $-11.2 \pm 1°$ C (Fornea et al., 2009) or about $-17.5°$ C (Shaw et al., 2005). *Immersion freezing* (i.e., the particle is completely inside the droplet) begins at $-12$ to $-25°$ C (Jahn et al., 2019) and $-26$ to $-30°$ C (Schill et al., 2015), at $-18.3 \pm 2°$ C (Fornea et al., 2009) or approximately $-22°$ C (Shaw et al., 2005). Without differentiation between contact and immersion mode, Durant et al. (2008) found a mean freezing temperature of $-19.9 \pm 2.1°$ C. Note that Schill et al. (2015) found two of their three ash samples to initiate immersion freezing only at temperatures just above the onset of homogeneous freezing. *Deposition freezing* (i.e., water vapor directly forms ice on the IN's surface) was observed between $-30$ and $-38°$ C, with the effectiveness depending on the temperature and the relative humidity with respect to ice $RH_{\mathrm{ice}}$ (Kulkarni et al., 2015), and starting between $-38$ and $-48°$ C at $RH_{\mathrm{ice}} = 105\,\%$ (Schill et al., 2015). Finally, in the absence of any INs, *homogeneous freezing* begins—depending on the droplet size—between $-35$ and $-41°$ C (Wallace and Hobbs, 2006). Besides the temperature dependence also the particle properties have an impact. For example, freezing temperature slightly decreases with increasing silica content (Durant et al., 2008) and particle size (Durant et al., 2008, Jahn et al., 2019). Maters et al. (2019) compared different ash samples and their remelted and quenched analogs in the laboratory and found increased immersion mode freezing temperatures for the ash compared to the glass samples; for samples containing certain minerals such as alkali feldspar; and for lower amounts of certain oxides such as $Fe_2O_3$, MgO and CaO. Genareau et al. (2018) found increased ice nucleation activity in the immersion mode for increasing amounts of $K_2O$ and decreasing amounts of MnO and $TiO_2$. Volcanic gases are capable of increasing or decreasing the ability of ash to form ice at high temperatures (400–800° C); for example, an enhancing effect was observed with a mixture of $H_2O$ and $SO_2$ (Maters et al., 2020). With respect to possible surface coatings, Kulkarni et al. (2015) found reduced deposition freezing activity if Arizona test dust is covered with $H_2SO_4$ which decreased the crystallinity.

In nature, ice within volcanic clouds has been observed at various occasions (Rose et al., 2004). Also in the case of the Eyjafjallajökull eruption in 2010, various studies found signs for IN activity. For example, Steinke et al. (2011) investigated immersion (starting at $-21°$ C) and deposition freezing (starting at $-31°$ C and $RH_{\mathrm{ice}} = 126\,\%$) due to Eyjafjallajökull ash experimentally using a cloud chamber and found that frozen fractions

of the volcanic ash particles of 0.1 % were reached at −24° C for the immersion mode and at −40° C and $RH_{\mathrm{ice}} = 116\,\%$ for the deposition mode. A similar study was executed by Hoyle et al. (2011); they found the onset of immersion freezing at −10 to −23° C for a small number of particles. But comparing bulk freezing experiments (sensitive to the most IN-active particles) with the behavior of the average ash particle showed that the latter lowered the freezing temperatures only by 3–4° C compared to the homogeneous freezing mode. In addition, the IN activity was in parts significantly lower than for Arizona test dust and certain minerals. Note that differences in the measured freezing temperatures in the studies might also be caused by different ash particle sizes (Jahn et al., 2019, Steinke et al., 2011), e.g., Kulkarni et al. (2015) considered particles with diameters <1 µm; Hoyle et al. (2011) had ash particles with mostly diameters of ∼1 µm, but very few particles had even sizes >100 µm; Steinke et al. (2011) used particles with diameters generally <10 µm; Jahn et al. (2019) focussed on sizes <37 µm; and Schill et al. (2015) had effective particle diameters <60 µm. However, Shaw et al. (2005), Fornea et al. (2009) and Durant et al. (2008) investigated particles with diameters of 100–300 µm, 250–300 µm and 1–1000 µm, respectively. Still, by analyzing ground-based air samples in northern Italy, Belosi et al. (2011) found increased concentrations of aerosols in the accumulation and and coarse mode compared to a presumably ash-free situation, as well as increased ratios of IN to aerosol number concentrations. Evaluating ground-based lidar measurements in Germany, volcanic ash-induced cirrus clouds were observed (e.g., Rolf et al., 2012, Seifert et al., 2011). Rolf et al. (2012) deduced increases of the IN number concentration by one order of magnitude (i.e., $0.1\,\mathrm{cm}^{-3}$) from lidar data, and decreases in the ice particle radius (to around 10 µm) from accompanying model calculations. Seifert et al. (2011) found ice in aged ash clouds at higher-than-normal temperatures (i.e., at temperatures below −15° C all ash clouds formed ice, instead of −25° C for normal clouds) and partly at significantly lower-than-normal altitudes. Flight campaigns found hints for ice/ice coated ash visually due to the whitish color of the plume top (Weber et al., 2012); during in situ measurements in form of collocated high relative humidities, mass concentrations, ice water contents and particle diameters (Johnson et al., 2012, Marenco et al., 2011); and in lidar results (Schumann et al., 2011). Using polar-orbiting satellites, Kahn and Limbacher (2012) retrieved ice within the ash plume close to the vent using the *Multi-angle Imaging SpectroRadiometer* (MISR) with four channels at 446–866 nm and nine viewing angles in forward and backward direction. Waquet et al. (2014) considered the same scene using total and polarized radiances in the visible and near-infrared spectrum from the instrument *Polarization and Directionality of Earth Reflectance* (POLDER); although their method worked in principle, it struggled at the center of the plume close to vent. The authors assumed that this was caused by ice which was not incorporated in their retrieval.

There are also satellite-based investigations (all using MODIS products alongside other retrievals or models) on the impact of volcanic emissions on the meteorological cloud properties: Gassó (2008) presented mostly qualitative case studies of degassing volcanoes (i.e., at the Aleutian Islands and the South Sandwich Islands) and weakly explosive eruptions and their impact on meteorological clouds in the lower troposphere, finding increases in the cloudiness and decreased cloud droplet effective radii. Analyzing multiyear data for

effects on trade cumuli by the degassing of $SO_2$ by the Hawaiian Kīlauea volcano, Yuan et al. (2011) found additionally on average a reduction in precipitation, an increase in cloud top height, and—as a consequence of the microphysical changes and increased cloud coverage—an increase in the atmospheric shortwave albedo. Findings of reduced average effective droplet radius and an increased shortwave upward flux were confirmed by Ebmeier et al. (2014) by investigating data of multiple years and multiple island volcanoes (Kīlauea, Yasur, Piton de la Fournaise) with satellite images rotated according to the horizontal wind direction. In contrast, Malavelle et al. (2017) also observed particle size reduction but no significant changes in cloud cover and liquid water path when comparing satellite retrievals with results of general circulation models for the Holuhraun eruption 2014–2015. Prata et al. (2020) reported indications for an ash-poor deep convective eruption cloud in the upper troposphere created by the phreatomagmatic eruption of the Anak Krakatau in 2018; they found significant ice loads and reduced ice particle radii compared to the surrounding meteorological ice clouds, and assumed—based on extremal updraft velocities and cloud top temperatures—that mainly homogeneous freezing took place.

## 2.2 Radiative transfer theory

In the following, the foundations of the radiative transfer theory are summarized, based mainly on Liou (2002), Mayer et al. (2019), Thomas and Stamnes (1999), Wallace and Hobbs (2006), unless otherwise noted. It descibes the propagation of electromagnetic radiation (e.g., within the atmosphere) and its interaction with matter due to *emission*, *absorption* and *scattering*.

### 2.2.1 Electromagnetic radiation

Electromagnetic radiation is an energy form which has wave as well as particle properties. Due to the wave properties, one considers the *wavelength* $\lambda$ (in the context of atmospheric radiation usually in nm or µm) and the *frequency* $\widetilde{\nu}$ (in $\mathrm{s}^{-1}$ or Hz), which are related by

$$c = \lambda \cdot \widetilde{\nu} \tag{2.1}$$

where $c = 2.998 \times 10^8\,\mathrm{m\,s^{-1}}$ is the constant propagation velocity of the electromagnetic radiation in vacuum, the *speed of light*. In the thermal range, the *wavenumber* $\nu$ (often in $\mathrm{cm}^{-1}$) is also regularly used, with

$$\nu = \frac{1}{\lambda}. \tag{2.2}$$

Due to its particle properties, electromagnetic radiation is quantized in form of *photons* which carry an energy $\Delta E$ (in J) with

$$\Delta E = h\widetilde{\nu} \tag{2.3}$$

with *Planck's constant* $h = 6.626 \times 10^{-34}\,\mathrm{J\,s}$. The descriptions in form of wavelength, wavenumber, frequency or energy are equivalent; mainly the wavelength is used in this work.

Depending on the wavelength, electromagnetic radiation is qualitatively categorized in major spectral ranges (Figure 2.7). The human eye is sensitive to the wavelengths of circa 400–700 nm, called the *visible* spectrum. Towards smaller values, *ultraviolet* denotes wavelengths of 10–400 nm and *X-ray* the spectrum of 0.01–10 nm. Photons of even shorter wavelength are called *gamma rays*. Longer wavelengths of 0.7–1000 µm define the *infrared* spectrum, which which includes the subranges of the *near infrared* at 0.7–3.5 µm and the *thermal infrared* at 3.5–100 µm. For wavelengths $> 1000$ µm follows the *microwave* spectrum. This work focuses on measurements in the thermal infrared spectral range.

A central quantity of the radiative transfer is the *radiance* $I_\lambda(\mathbf{r}, \theta, \phi, t)$ (also *monochromatic intensity*), defined as energy per time per area per solid angle per wavelength (in $\mathrm{W\,m^{-2}\,sr^{-1}\,\mu m^{-1}}$). $\mathbf{r}$ denotes the positional vector, $\theta$ and $\phi$ the zenith and azimuth angles, respectively, of the direction into which the radiation propagates in a polar coordinate system, and $t$ the time. Consider the situation that radiation within the wavelength range $\mathrm{d}\lambda$ and the time $\mathrm{d}t$ is emitted from an area $\mathrm{d}A$ into a solid angle $\mathrm{d}\Omega = \sin\theta\,\mathrm{d}\theta\,\mathrm{d}\phi$. Let $\mathrm{d}A$

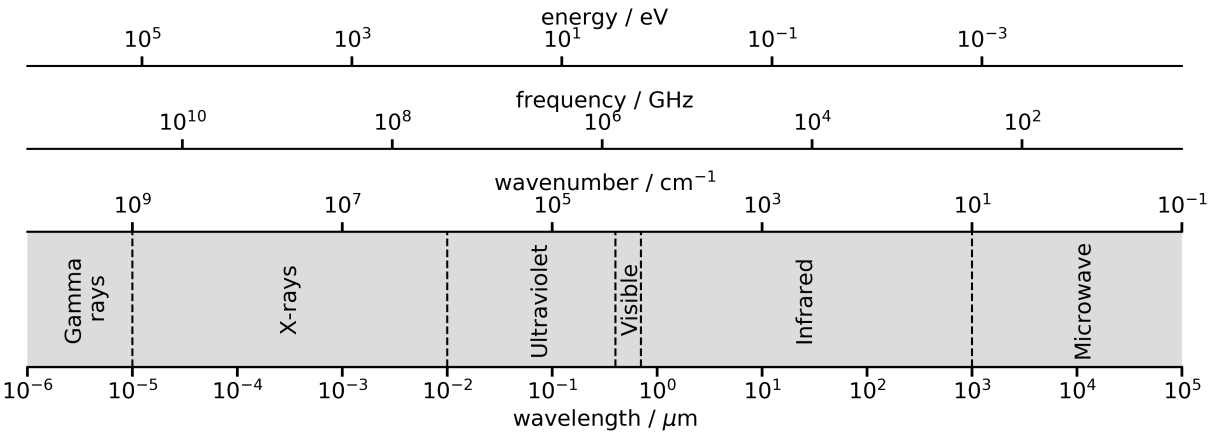


Figure 2.7: Overview of the electromagnetic spectrum.

define the polar coordinate system such that the zenith angle $\theta$ is the angle between the normal of $\mathrm{d}A$ and the direction towards $\mathrm{d}\Omega$. In this case, the radiance is corrected by a factor $\cos\theta$ to project $\mathrm{d}A$ on a plane whose normal vector points in the direction given by $\theta$ and $\phi$. Thus, for the radiance holds

$$I_\lambda(\mathbf{r}, \theta, \phi, t) = \frac{\mathrm{d}E}{\cos\theta\,\mathrm{d}\Omega\,\mathrm{d}A\,\mathrm{d}\lambda\,\mathrm{d}t}. \tag{2.4}$$

Integrating the radiance with respect to $\cos\theta\,\mathrm{d}\Omega$ gives the *monochromatic irradiance* (or *monochromatic flux density*). Further integrating with respect to the wavelength leads to the *irradiance* (or *total flux density of radiant energy*). Finally, also integrating over the area results in the *total flux*.

### 2.2.2 Blackbody radiation

All matter absorbs and emits radiation. A *blackbody* is an idealized body that absorbs all radiation falling on it, i.e., it has the maximum possible absorption capacity. A cavity with a small entrance is an approximation of a blackbody: radiation entering the cavity will be reflected in the inside again and again until it is finally absorbed; thus, from the outside, the hole appears to be a blackbody. The emission of a blackbody is described by *Planck's law*, with the radiance being

$$B_\lambda(T) = \frac{2hc^2}{\lambda^5\left(e^{hc/\lambda k_B T} - 1\right)} \tag{2.5}$$

with *Boltzmann's constant* $k_B = 1.3806 \times 10^{-23}\,\mathrm{J\,K^{-1}}$. The Sun's surface has a temperature of ~5800 K, whereas temperatures of 200–300 K prevail at the Earth's surface and within the troposphere. The corresponding blackbody radiation (Figure 2.8) has only minor overlap around 3.5 µm. Thus, solar and thermal radiation can be treated as independent considering passive remote sensing problems.

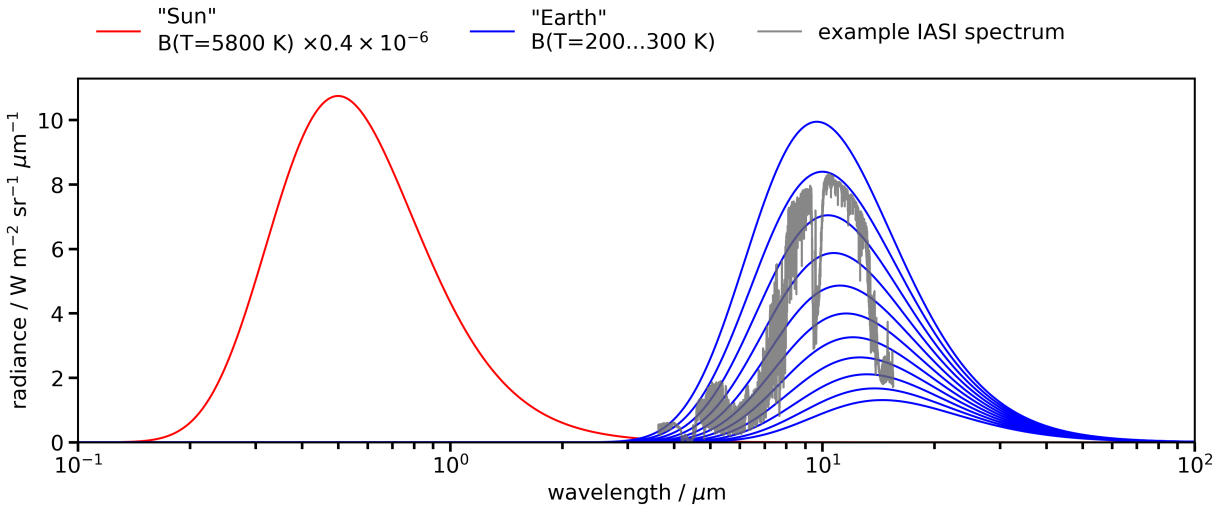


Figure 2.8: Blackbody radiance for temperatures of 200–300 K (blue, in 10 K steps with the lowermost and uppermost graph corresponding to 200 K and 300 K, respectively) and 5800 K (red, scaled for comparability to the blue graphs), and an example spectrum measured by the *Infrared Atmospheric Sounding Interferometer* (IASI, gray) showing that the top-of-atmosphere radiance emitted from the Earth corresponds to Planck's function of different temperatures depending on the wavelength.

To quantify the difference between the theoretical blackbody and real objects (so-called *gray bodies*), Planck's law is used to introduce the *emissivity* $\epsilon_\lambda$ as

$$\epsilon_\lambda = \frac{I_\lambda(\text{emitted})}{B_\lambda(T)} \tag{2.6}$$

with $\epsilon_\lambda = 1$ for a blackbody but $\epsilon_\lambda < 1$ a gray body. Furthermore, the *absorptivity* $\alpha_\lambda$, *reflectivity* $R_\lambda$ and *transmissvity* $T_\lambda$ are defined as the ratios between the absorbed, reflected or transmitted radiance, respectively, and the incoming radiance. Under the condition of a *thermodynamic equilibrium* (i.e., a system is simultaneously in a thermal, radiative, mechanical and chemical equilibrium), one can derive *Kirchhoff's law*

$$\epsilon_\lambda = \alpha_\lambda. \tag{2.7}$$

In the atmosphere, this condition is not generally satisfied, but a *local thermodynamic equilibrium* is given at altitudes up to 60–70 km.

### 2.2.3 Absorption and scattering

Atmospheric molecular gases can interact with radiation under certain conditions (e.g., to first order, changes in the electric dipole vector of the molecule must be possible, such that the electromagnetic field can couple to it). The absorption of a photon by a molecule

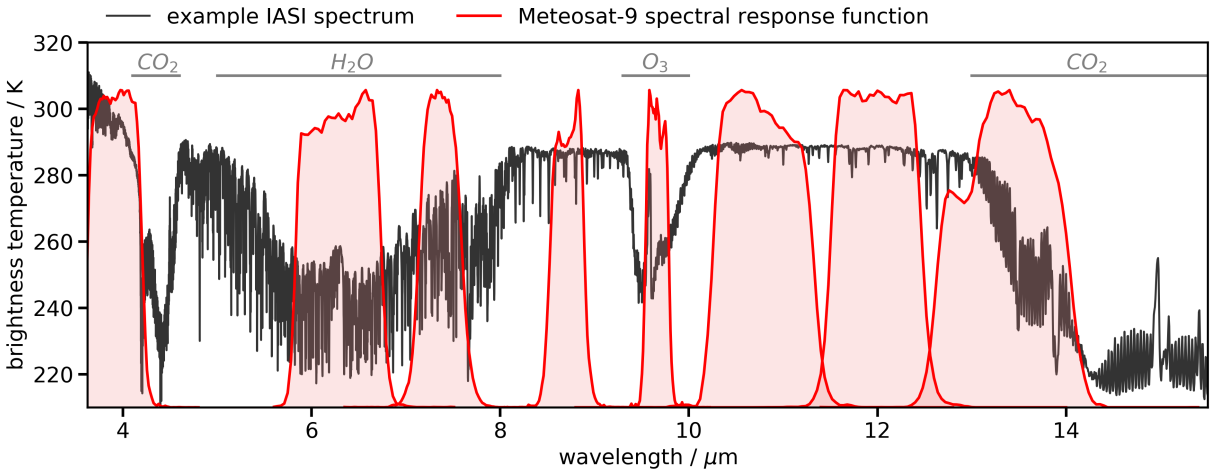


Figure 2.9: Brightness temperature spectrum measured by the *Infrared Atmospheric Sounding Interferometer* (black), indications of main gas features (grey) and the peak-normalized spectral response functions of Meteosat-9 (red, see Section 2.3.1).

increases its energy, whereas the emission decreases the energy. Molecules can carry energy in form of *translational energy*, *rotational energy*, *vibrational energy* and *electronic energy*. The last three forms are quantum-mechanically quantized, such that interactions can take place only with photons of a specific energy which equals the difference in the discrete energy levels. Changing the rotational energy is connected to energies in the microwave and far-infrared spectrum; vibrational and combinations of vibrational and rotational energy transitions lead to interactions in the infrared spectrum; electronic energies are related to the visible and ultraviolet spectrum.

Focusing on the thermal infrared (Figure 2.9), most important atmospheric gases are water vapor, carbon dioxide and ozone, with water vapor producing a band around 6.25 µm, carbon dioxide around 4.3 µm and especially 15 µm, and ozone around 9.6 µm. Furthermore, the spectrum is influenced by carbon monoxide, methane, nitrous oxide, nitric oxide and chlorofluorocarbons, but their impact is comparably small such that they can be neglected when considering a broad-band radiometer as is done in this work. The spectral region 8.3–12.5 µm is called *atmospheric window*, as it is mostly transparent except for the ozone.

Absorption by solids (e.g., aerosol particles) can happen due to electronic excitation, i.e., an electron is lifted to a higher-energy state. Thus, conductors tend to be highly absorbing in the visible and infrared, whereas insulators are rather transparent. Energies in the thermal infrared can cause vibrations in the solid (i.e., vibrations of single molecules or even of the complete lattice). In the case of liquids, absorption is connected to interactions between the liquid's molecules. The bulk properties of solids and liquids relevant to absorption and scattering are given by the complex *refractive index* $m$ with

$$m = n + \mathrm{i}k. \tag{2.8}$$

Liquid and ice water clouds influence radiation in the atmospheric window. Liquid water clouds and cirrus clouds composed of large ice crystals are similar to blackbodies in the atmospheric window, whereas thin cirrus clouds of small particles (i.e., effective radii $\lesssim$ 30 µm) have a size-dependent absorption peak around 12 µm which results in a spectral signature that can be used for its discrimination and detection (Ackerman et al., 1990, Smith et al., 1998).

In addition, molecules, droplets, ice crystals and aerosols lead to scattering of radiation. Light can be scattered out of the viewing direction, such that scattering increases extinction, but can also be scattered into it, thereby increasing the amount of radiation. The mathematical description of the scattering process is generally complicated and depends on the object size, shape and wavelength. The *size parameter* $x$ is defined as

$$x = \frac{2\pi a}{\lambda} \tag{2.9}$$

with $a$ being the particle radius. For spherical objects and $x \gtrsim 1$, the *Lorenz-Mie scattering* takes place; the corresponding theory can be derived directly from Maxwell's equations. It exhibits strong scattering in forward direction and is roughly wavelength-independent. Cloud droplets and spherical aerosol particles (with sizes of roughly 1–10 µm) can be treated with Lorenz-Mie theory. For $x \ll 1$, Lorenz-Mie scattering simplifies to *Rayleigh scattering*, corresponding to the situation of a single electromagnetically-induced dipole moment creating the scattered field. Rayleigh scattering leads to a radiance being proportional to $\lambda^{-4}$ and equal scattering in forward and backward direction. This approximation is applied to gas molecules ($a \approx 1 \times 10^{-4}$ µm). For $x \gg 1$, scattering can be described by *geometric optics*, i.e., light can be modeled by parallel rays being refracted according to *Snell's law*. This simplification can be used for raindrops ($a \approx 1$ cm).

The situation becomes more complicated for spheroids, non-spherical objects (e.g., ice crystals) or irregular-shaped particles (e.g., dust particles or volcanic ash). Spheroidal particles can be treated with the *T-matrix* method: incoming and scattered electromagnetic waves are expanded with respect to vector spherical wave functions, with the relation of the corresponding coefficients (the T-matrix) being derived using boundary conditions at the scatterer's surface. For non-spherical particles such as ice crystals, the geometric optics approach can be utilized as well. The theory might be extended by applying a *Monte Carlo* approach, i.e., a large number of light rays is calculated with random initialization, scattering and absorption. Comparing the initial with the resulting light rays allows to approximate the object's scattering properties. Another numerical approach is the *finite-difference time domain method*. In this case, space and time are discretized and electric and magnetic fields for each grid cell are alternately calculated based on the surrounding fields in the preceding time step, thereby effectively simulating the propagation of an initial electromagnetic wave. Numerous modifications and variations of all aforementioned approximations as well as other approaches exist (Kahnert, 2003, Wriedt, 2009, Yang et al., 2015).

Independent of the method, a set of *optical properties* parameterizes the scattering and absorption properties. The absorption and scattering *cross sections* $\sigma_{\text{abs}}$ and $\sigma_{\text{sca}}$

are defined as the ratio between the radiance absorbed or scattered (in all directions), respectively, by the molecule/particle and the incident radiance. They have the unit of a geometrical area which represents the effective area of the object presented to the incident beam with respect to scattering and absorption. The extinction cross section $\sigma_{\text{ext}}$ is the sum of both, i.e.,

$$\sigma_{\text{ext}} = \sigma_{\text{abs}} + \sigma_{\text{sca}}. \tag{2.10}$$

The *mass extinction coefficient* $k_{\text{ext}}$ is given by

$$k_{\text{ext}} = \frac{\sigma_{\text{ext}}}{M} \tag{2.11}$$

with unit mass $M$. The *extinction coefficient* $\beta_{\text{ext}}$ is defined as

$$\beta_{\text{ext}} = \sigma_{\text{ext}} n = k_{\text{ext}} \rho \tag{2.12}$$

with $n$ denoting the particle number density and $\rho$ the mass concentration. Similar relations hold for the *absorption* and *scattering coefficients* $\beta_{\text{abs}}$ and $\beta_{\text{sca}}$, respectively, with

$$\beta_{\text{ext}} = \beta_{\text{abs}} + \beta_{\text{sca}}. \tag{2.13}$$

The *single scattering albedo* $\omega$ is given by

$$\omega = \frac{\beta_{\text{sca}}}{\beta_{\text{ext}}} = \frac{\beta_{\text{sca}}}{\beta_{\text{abs}} + \beta_{\text{sca}}}. \tag{2.14}$$

The *optical depth* $\tau$ is defined as

$$\tau = \int \beta_{\text{ext}} \, \mathrm{d}s = \int k_{\text{ext}} \rho \, \mathrm{d}s \tag{2.15}$$

with the integral along the optical path $s$. For scattering processes, the *scattering phase function* $P(\theta, \phi; \theta', \phi')$ is a normalized distribution describing the relative intensity of radiation scattered the from incoming angles $\theta'$, $\phi'$ to the outgoing direction $\theta$, $\phi$. From the given angles, the scattering angle $\Theta$ describing the deflection of the radiation can be derived as

$$\cos\Theta = \cos\theta' \cos\theta + \sin\theta' \sin\theta \cos(\phi' - \phi) \tag{2.16}$$

such that the phase function can be given by this argument as $P(\cos\Theta)$. Furthermore, to investigate the dominance of forward or backward scattering, the *asymmetry parameter* $g$ can be calculated as

$$g = \frac{1}{2} \int_{-1}^{1} P(\cos\Theta) \cos\Theta \, \mathrm{d}\cos\Theta \tag{2.17}$$

with $g = 1$ for forward scattering, $g = 0$ for isotropic scattering and $g = -1$ for backward scattering.

### 2.2.4 Radiative transfer equation

The general, time-independent, monochromatic radiative transfer equation for a plane-parallel atmosphere is given by

$$\begin{aligned}\cos\theta\frac{\mathrm{d}I_\lambda(z,\theta,\phi)}{\mathrm{d}z} = & - \beta_{\mathrm{ext},\lambda}(z)I_\lambda(z,\theta,\phi) \\ & + \beta_{\mathrm{emis},\lambda}(z)B_\lambda\left(T(z)\right) \\ & + \frac{1}{4\pi}\beta_{\mathrm{sca},\lambda}(z)\int_0^{2\pi}\int_0^{\pi}P(z;\theta,\phi;\theta',\phi')I(z,\theta',\phi')\sin\theta'\,\mathrm{d}\theta'\,\mathrm{d}\phi'\end{aligned} \tag{2.18}$$

with $z$ describing the vertical dimension and $T(z)$ the vertical temperature profile. The three terms on the right hand side describe the different sources/sinks of the radiance.

The first term in Equation 2.18 describes the extinction of radiation due to absorption and deflection of photons into another direction. Neglecting the other two terms, the differential equation is solved by

$$I_\lambda(z,\theta,\phi) = I_\lambda(z=0,\theta,\phi)\exp\left(-\int_0^z\frac{\beta_{\mathrm{ext},\lambda}(z)}{\cos\theta}\,\mathrm{d}z\right) \tag{2.19}$$

which is the *Beer–Bouguer–Lambert law.* Thus, the radiance decreases exponentially with increasing optical depth.

The second term in Equation 2.18 describes the emission of radiation according to Planck's law. Due to Kirchhoff's law (Equation 2.7), the emission coefficient $\beta_{\mathrm{emis},\lambda}$ can be substituted by $\beta_{\mathrm{abs},\lambda}$. Neglecting scattering in Equation 2.18, i.e., setting $\beta_{\mathrm{sca},\lambda} = 0$, one obtains *Schwarzschild's equation.* Substituting $\mathrm{d}s = \mathrm{d}z/\cos\theta$, its solution is

$$I_\lambda(s_1) = I_\lambda(0)\exp\left(-\tau_\lambda(s_1,0)\right) + \int_0^{s_1}B_\lambda\left(T(s)\right)\exp\left(-\tau_\lambda(s_1,s)\right)\beta_{\mathrm{abs},\lambda}(s)\,\mathrm{d}s \tag{2.20}$$

$$\tau_\lambda(s_1,s) = \int_s^{s_1}\beta_{\mathrm{abs},\lambda}(s')\,\mathrm{d}s' \tag{2.21}$$

with $s \in [0, s_1]$.

The third term in Equation 2.18 describes the scattering of photons from another direction $\theta'$, $\phi'$ into the considered direction $\theta$, $\phi$. To solve the radiative transfer equation, temperature profile, densities, cross sections for absorption and scattering, phase functions and boundary conditions are necessary. The atmospheric profiles can be obtained, e.g., from standard atmospheres, vertical measurements or model calculations. Optical properties can be calculated according to the approaches mentioned above and under the assumption of certain microphysical properties. For the calculation of the radiative transfer, the libRadtran framework is used in this work (Emde et al., 2016, Mayer and Kylling, 2005).

## 2.3 Geostationary passive imagers

### 2.3.1 MSG/SEVIRI

The main satellite instrument utilized in this work is the *Spinning Enhanced Visible and InfraRed Imager* (SEVIRI), which is a passive imager aboard the geostationary *Meteosat Second Generation* (MSG) satellites operated by the *European Organisation for the Exploitation of Meteorological Satellites* (EUMETSAT). The MSG spacecraft are spinning around an axis in north-south direction, thereby measuring radiation coming from the Earth along lines in the east-west direction. The temporal resolution for full disc coverage is 15 min. SEVIRI has 12 channels. Three bands are in the visible and near-infrared spectrum and are centered at 0.6 µm, 0.8 µm and 1.6 µm. Eight bands are in the thermal infrared at 3.9 µm, 6.2 µm, 7.3 µm, 8.7 µm, 9.7 µm, 10.8 µm, 12 µm and 13.4 µm. Finally, one channel is a high resolution visible (HRV) broadband, covering roughly 0.4 to 1.1 µm and half of the SEVIRI disc at each revolution. The spectral sensitivity of the channels is characterized by the *spectral response functions*, shown in Figure 2.10 for Meteosat-9. Some of the channels cover specific components of the atmosphere, i.e., the channels at 6.2 µm and 7.3 µm are influenced by water vapor, whereas the bands at 9.7 µm and 13.4 µm are affected by ozone and carbon dioxide, respectively. Other channels, e.g., at 8.7 µm, 10.8 µm and 12 µm are located within the atmospheric window and, thus, are used to observe meteorological clouds, aerosols or the Earth's surface. The spatial resolution at the sub-satellite point is 1 km for the HRV band and 3 km for the other channels (Schmetz et al., 2002a).

Radiances in the visible channels are converted to reflectances, whereas an equivalent brightness temperature is derived for the measurements in the thermal channels. The latter corresponds to a temperature $T$ such that the convolution of Planck's function $B(\lambda, T)$ and the normalized spectral response function equals the measured radiance (EUMETSAT/2). Typical measurement noise of the thermal channels is on the order of 0.04 to 0.24 K (EUMETSAT/3). Examples for a scene on 6 June 2011, 12:00 UTC are given in Figure 2.11. The observations were made shortly after the eruption of the volcano Puyehue-Cordón Caulle on 4 June 2011 (Debling et al., 2011), with its ash plume visible in the south-west of the SEVIRI disc (red rectangle).

As of 16 November 2021, four MSG satellites have been launched, named Meteosat-8 to -11 or alternatively MSG1 to 4. They are deployed at different longitudes (Table 2.1), with the current main operational satellite (MSG4) located at 0°E with a backup (MSG2) at 3.5°E. MSG3 operates at 9.5°E in rapid-scan mode, covering only the upper third of the SEVIRI disc (including Northern Africa and Europe) but at an increased temporal resolution of 5 min. MSG1 was moved to 41.5°E to cover the Indian Ocean (*Indian Ocean Data Coverage*, WMO/MSG1).

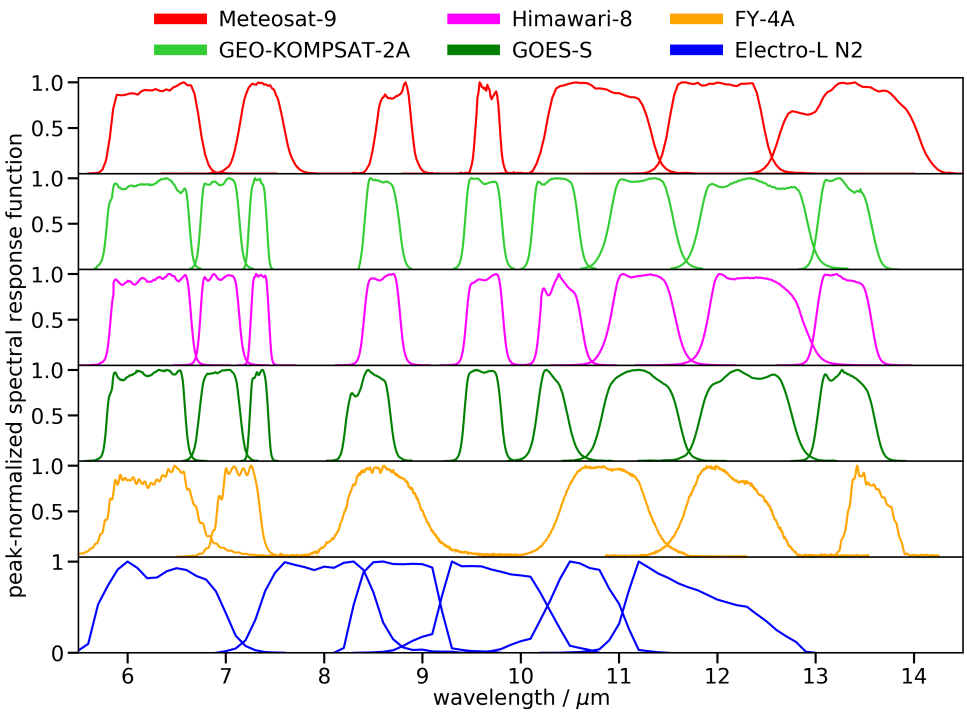


Figure 2.10: Peak-normalized spectral response functions of the currently active, advanced imagers aboard geostationary satellites; only channels between 5 $\mu$m and 15 $\mu$m are shown (data from EUMETSAT/1).

### 2.3.2 Other imagers in the geostationary ring

Note that there are other geostationary satellites with imagers comparable to the MSG series, such that methods developed for MSG/SEVIRI are potentially transferable to those as well. As of 16 November 2021, there are at least 20 satellites in the geostationary orbit carrying a passive moderate resolution optical imager with channels in the thermal infrared, operated by the United States, Europe, Japan, South Korea, China, Russia and India (see Table 2.1 and references therein). They are located at different longitudes and, thus, their field of views cover most parts of the Earth. Another 18 satellites are currently planned to be launched within the next two decades. 13 different imagers are carried by the spacecraft (see Table 2.2 and references therein) of which 10 are already in orbit and 3 are still under development or need to be launched. The imagers can roughly be divided into two classes. The older instruments (which are about to fade out) generally have three channels in the thermal infrared in the range 5–15 µm: one in the water vapor regime around 7 µm, one or two in the atmospheric window around 11 µm and and one to cover $CO_2$ around 13 µm. The newer instruments have 6–9 channels in the thermal infrared with smaller bandwidths, and increased spatial and temporal resolution of around 2 km and 10 to 15 min, respectively. Besides SEVIRI, this new generation of imagers includes the *Advanced Baseline Imager* (ABI, Schmit et al., 2005, 2017), the *Advanced Himawari Imager* (AHI, Bessho et al., 2016),

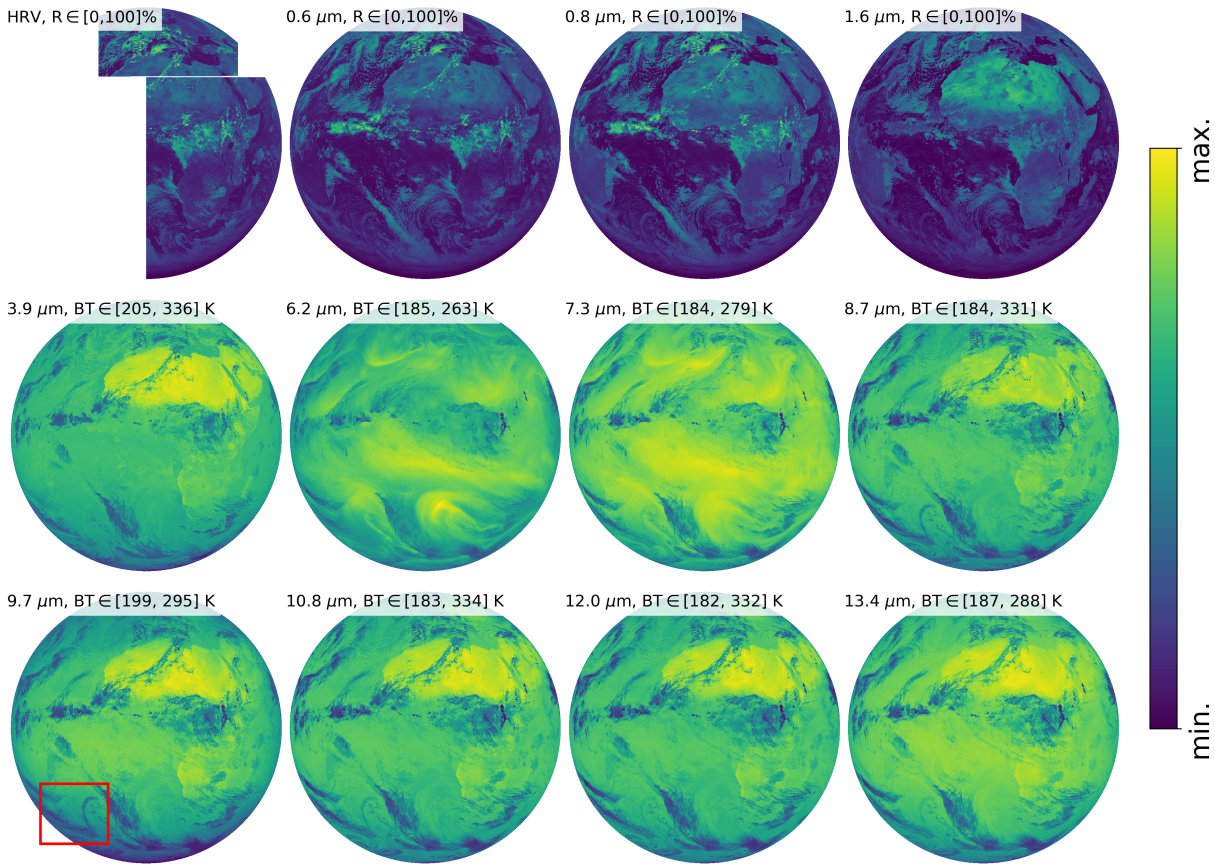


Figure 2.11: Reflectances (R) and brightness temperatures (BT) for the 12 MSG/SEVIRI channels for a scene at 6 June 2011, 12:00 UTC; the colorbar applies to all channels, with the extrema given in brackets for each plot; the red rectangle points to the volcanic ash plume emitted by Puyehue-Cordón Caulle.

the *Advanced Meteorological Imager* (AMI, KMA), the *Advanced Geostationary Radiation Imager* (AGRI, Yang et al., 2017) and the Electro-L imager (MSU-GS, Rublev et al., 2018). These instruments alone already cover the largest part of the globe (Figure 2.12). Also they have spectral channels with similar spectral response functions (Figure 2.10). ABI, AHI and AMI have roughly the same spectral properties as they carry the same instrument (L3Harris). In comparison to SEVIRI, they have additional bands (3 instead of 2 channels in the water vapor regime as well as in the atmospheric window) and the bands tend to be narrower (e.g., the band centered at 13.3 µm). AGRI has similar bandwidths as SEVIRI, but misses the ozone channel around 9.7 µm, whereas MSU-GS has broader channels and misses the carbon dioxide channel around 13.4 µm.

Starting from 2022/2023, the new satellite series *Meteosat Third Generation* (MTG) should be launched to successively replace MSG (WMO/OSCAR). Those carry the *Flexible Combined Imager* (FCI), which has similar thermal channels as SEVIRI but with narrower

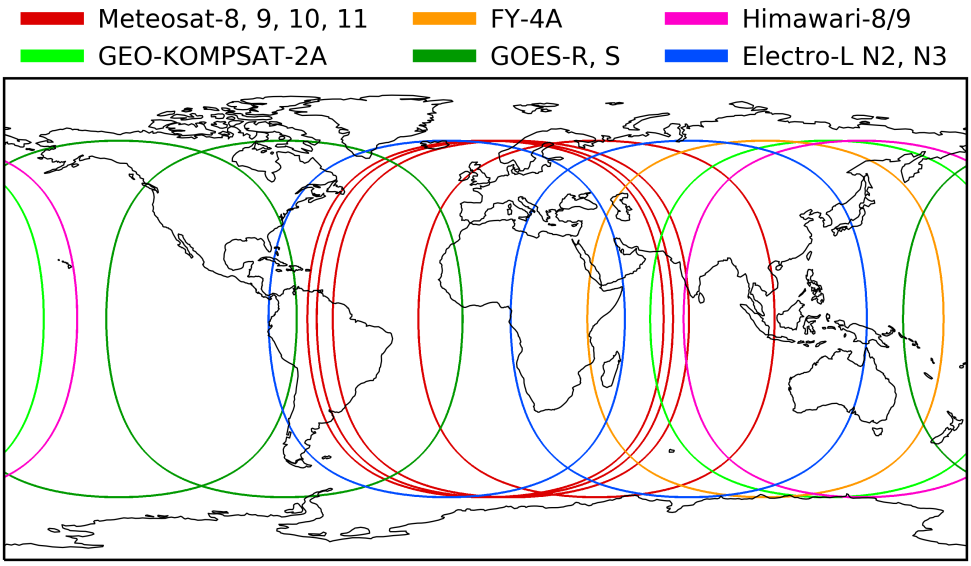


Figure 2.12: Field of view of all currently active advanced moderate resolution optical imagers aboard geostationary satellites; the colored borders correspond to viewing zenith angles of 75°.

spectral response functions and a higher temporal and spatial resolution of 10 min and $\leq$ 2 km, respectively (Durand et al., 2015).

Table 2.1: Current and future geostationary satellites carrying a moderate resolution optical imager with channels in the thermal infrared; information are taken from WMO's OSCAR database (Observing Systems Capability Analysis and Review Tool, WMO/OSCAR); longitudes correspond to the current or planned positions and might differ from earlier locations; launch dates are given as YYYY-MM-DD; data effective 16 November 2021.

| Acronym | Launch | End of life | Program | Agencies | Longitude | Imager | Status |
|---|---|---|---|---|---|---|---|
| Electro-L N2 | 2015-12-11 | ≥ 2025 | Electro | RosHydroMet, Roscosmos | 14.5° W | MSU-GS | Operational |
| Electro-L N3 | 2019-12-24 | ≥ 2029 | Electro | RosHydroMet, Roscosmos | 76° E | MSU-GS | Operational |
| Electro-L N4 | ≥ 2022 | ≥ 2032 | Electro | RosHydroMet, Roscosmos | 14.5° W / 76° E / 166° E | MSU-GS | Planned |
| Electro-L N5 | ≥ 2023 | ≥ 2033 | Electro | RosHydroMet, Roscosmos | 14.5° W / 76° E / 166° E | MSU-GS | Planned |
| Electro-M N1 | ≥ 2025 | ≥ 2035 | Electro | RosHydroMet, Roscosmos | 14.5° W | MSU-GSM | Planned |
| Electro-M N2 | ≥ 2026 | ≥ 2036 | Electro | RosHydroMet, Roscosmos | 76° E | MSU-GSM | Planned |
| Electro-M N3 | ≥ 2029 | ≥ 2039 | Electro | RosHydroMet, Roscosmos | 165.8° E | MSU-GSM | Planned |
| FY-2F | 2012-01-13 | ≥ 2021 | Feng-Yun 2 | CMA, NRSCC | 112° E | S-VISSR | Stand-by |
| FY-2G | 2014-12-31 | ≥ 2021 | Feng-Yun 2 | CMA, NRSCC | 105° E | S-VISSR | Operational |
| FY-2H | 2018-06-05 | ≥ 2022 | Feng-Yun 2 | CMA, NRSCC | 79° E | S-VISSR | Operational |
| FY-4A | 2016-12-10 | ≥ 2021 | Feng-Yun 4 | CMA, NRSCC | 104.7° E | AGRI | Operational |
| FY-4B | 2021-06-02 | ≥ 2028 | Feng-Yun 4 | CMA, NRSCC | 123.5° E | AGRI, GHI | Commissioning |
| FY-4C | ≥ 2025 | ≥ 2032 | Feng-Yun 4 | CMA, NRSCC | | AGRI | Planned |
| FY-4D | ≥ 2026 | ≥ 2033 | Feng-Yun 4 | CMA, NRSCC | | AGRI | Planned |
| FY-4E | ≥ 2027 | ≥ 2034 | Feng-Yun 4 | CMA, NRSCC | | AGRI | Planned |
| FY-4F | ≥ 2030 | ≥ 2037 | Feng-Yun 4 | CMA, NRSCC | | AGRI | Planned |
| FY-4G | ≥ 2033 | ≥ 2040 | Feng-Yun 4 | CMA, NRSCC | | AGRI | Planned |
| GEO-KOMPSAT-2A | 2018-12-04 | ≥ 2029 | Commun., Oceanogr. & Meteorol. Satell. | KMA, KARI, ME, MLTM | 128.2° E | AMI | Operational |
| GISAT-2 | ≥ 2022 | ≥ 2029 | Geostation. High Resolut. Imager | ISRO | 83° E | MX-LWIR | Planned |
| GOES-14 (O) | 2009-06-27 | ≥ 2021 | Geostation. Oper. Environ. Satell. 2nd Gen. | NOAA, NASA | 105° W | IMAGER (GOES) | Stand-by |
| GOES-15 (P) | 2010-03-04 | ≥ 2021 | Geostation. Oper. Environ. Satell. 2nd Gen. | NOAA, NASA | 128 W | IMAGER (GOES) | Stand-by |
| GOES-16 (R) | 2016-11-19 | ≥ 2027 | Geostation. Oper. Environ. Satell. 3rd Gen. | NOAA, NASA | 75.2° W | ABI | Operational |
| GOES-17 (S) | 2018-03-01 | ≥ 2029 | Geostation. Oper. Environ. Satell. 3rd Gen. | NOAA, NASA | 137.2° W | ABI | Operational |
| GOES-18 (T) | 2022 | ≥ 2033 | Geostation. Oper. Environ. Satell. 3rd Gen. | NOAA, NASA | 137° E | ABI | Planned |
| GOES-19 (U) | ≥ 2024 | ≥ 2035 | Geostation. Oper. Environ. Satell. 3rd Gen. | NOAA, NASA | 75° W / 137° W | ABI | Planned |
| Himawari-8 | 2014-10-07 | ≥ 2030 | Himawari 3rd Gen. | JMA | 140.7° E | AHI | Operational |
| Himawari-9 | 2016-11-02 | ≥ 2030 | Himawari 3rd Gen. | JMA | 140.7° E | AHI | Stand-by |
| INSAT-3D | 2013-07-25 | ≥ 2022 | Indian National Satell. 3 | ISRO | 82° E | IMAGER (INSAT) | Operational |
| INSAT-3DR | 2016-09-08 | ≥ 2025 | Indian National Satell. 3 | ISRO | 74° E | IMAGER (INSAT) | Operational |
| INSAT-3DS | ≥ 2022 | ≥ 2029 | Indian National Satell. 3 | ISRO | | IMAGER (INSAT) | Planned |
| Meteosat-8 | 2002-08-28 | ≥ 2022 | Meteosat Second Generation | EUMETSAT, ESA | 41.5° E | SEVIRI | Operational |
| Meteosat-9 | 2005-12-21 | ≥ 2025 | Meteosat Second Generation | EUMETSAT, ESA | 3.5° E | SEVIRI | Stand-by |
| Meteosat-10 | 2012-07-05 | ≥ 2030 | Meteosat Second Generation | EUMETSAT, ESA | 9.5° E | SEVIRI | Operational |
| Meteosat-11 | 2015-07-15 | ≥ 2033 | Meteosat Second Generation | EUMETSAT, ESA | 0° E | SEVIRI | Operational |
| MTG-I1 | ≥ 2023 | ≥ 2031 | Meteosat Third Generation | EUMETSAT, ESA, EC | 0° E | FCI | Planned |
| MTG-I2 | ≥ 2025 | ≥ 2033 | Meteosat Third Generation | EUMETSAT, ESA, EC | 0° E | FCI | Planned |
| MTG-I3 | ≥ 2032 | ≥ 2040 | Meteosat Third Generation | EUMETSAT, ESA, EC | 0° E | FCI | Planned |
| MTG-I4 | ≥ 2036 | ≥ 2044 | Meteosat Third Generation | EUMETSAT, ESA, EC | 0° E | FCI | Planned |

Table 2.2: Properties of the moderate resolution optical imagers *Advanced Baseline Imager* (ABI), *Advanced Himawari Imager* (AHI), *Advanced Meteorological Imager* (AMI), *Spinning Enhanced Visible Infra-Red Imager* (SEVIRI), *Flexible Combined Imager* (FCI), *Advanced Geostationary Radiation Imager* (AGRI), the Electro-L imager (MSU-GS), *Multispectral Long Wave Infrared* (MX-LWIR), the GOES and INSAT imagers (IMAGER), *Stretched Visible and Infrared Spin Scan Radiometer* (S-VISSR) and *Geostationary High-speed Imager* (GHI); full disc coverage is given for the operational settings, which might include limited area coverage at a higher temporal resolution; design specifications are given for the channel properties, except for ABI, AHI and AMI for which measured channel properties are given for the instruments aboard GOES-R, Himawari-8 and GEO-KOMPSAT-2A, respectively; only channels between 5 $\mu$m and 15 $\mu$m are shown, with $\lambda$ and $\Delta\lambda$ denoting the central wavelength and the bandwidth, respectively.

| Acronym | ABI | | AHI | | AMI | | SEVIRI | | FCI | | AGRI | | MSU-GS | | MX-LWIR | |
|---|---|---|---|---|---|---|---|---|---|---|---|---|---|---|---|---|
| Full disc cov. | 15 min | | 10 min | | 10 min | | 15 min | | 10 min | | 15 min | | 30 min | | 30 min [c] | |
| Resolution | 2 km | | 2 km | | 2 km | | 3 km | | 2 km [a] | | 4 km [b] | | 4 km | | 1.5 km | |
| in $\mu$m | $\lambda$ | $\Delta\lambda$ | $\lambda$ | $\Delta\lambda$ | $\lambda$ | $\Delta\lambda$ | $\lambda$ | $\Delta\lambda$ | $\lambda$ | $\Delta\lambda$ | $\lambda$ | $\Delta\lambda$ | $\lambda$ | $\Delta\lambda$ | $\lambda$ | $\Delta\lambda$ |
| | 6.19 | 0.80 | 6.24 | 0.82 | 6.21 | 0.84 | 6.25 | 0.8 | 6.30 | 1.00 | 6.25 | 0.90 | 6.35 | 1.30 | | |
| | 6.93 | 0.42 | 6.94 | 0.40 | 6.94 | 0.40 | | | | | | | | | | |
| | 7.34 | 0.19 | 7.35 | 0.19 | 7.33 | 0.18 | 7.35 | 1.00 | 7.35 | 0.50 | 7.10 | 0.40 | 8.00 | 1.00 | 7.35 | 0.50 |
| | 8.44 | 0.43 | 8.59 | 0.37 | 8.59 | 0.36 | 8.70 | 0.80 | 8.70 | 0.40 | 8.50 | 1.00 | 8.70 | 1.00 | 8.50 | 0.40 |
| | 9.61 | 0.38 | 9.63 | 0.38 | 9.62 | 0.38 | 9.66 | 0.56 | 9.66 | 0.30 | | | 9.70 | 1.00 | 9.60 | 0.40 |
| | 10.33 | 0.30 | 10.40 | 0.42 | 10.35 | 0.47 | 10.80 | 2.00 | 10.50 | 0.70 | 10.70 | 0.80 | 10.70 | 1.00 | 10.80 | 1.00 |
| | 11.21 | 0.78 | 11.24 | 0.67 | 11.23 | 0.66 | | | | | | | | | | |
| | 12.29 | 0.92 | 12.38 | 0.97 | 12.37 | 1.11 | 12.00 | 2.00 | 12.30 | 0.50 | 12.00 | 1.00 | 11.70 | 1.30 | 12.00 | 1.00 |
| | 13.28 | 0.57 | 13.28 | 0.56 | 13.29 | 0.56 | 13.40 | 2.00 | 13.30 | 0.60 | 13.50 | 0.60 | | | 13.25 | 0.50 |
| Sources | 1, 2 | | 3, 4 | | 5 | | 6 | | 7 | | 8 | | 9, 10, 11 | | 12 | |

| Acronym | IMAGER (GOES) | | IMAGER (INSAT) | | S-VISSR | | GHI | |
|---|---|---|---|---|---|---|---|---|
| Full disc cov. | 25 min | | 30 min | | 30 min | | 1 min [e] | |
| Resolution | 4 km | | 4 km [d] | | 5 km | | 2 km | |
| in $\mu$m | $\lambda$ | $\Delta\lambda$ | $\lambda$ | $\Delta\lambda$ | $\lambda$ | $\Delta\lambda$ | $\lambda$ | $\Delta\lambda$ |
| | 6.50 | 1.50 | 6.80 | 0.60 | 6.95 | 1.30 | | |
| | 10.70 | 1.00 | 10.80 | 1.00 | 10.80 | 1.00 | 11.40 | 2.20 |
| | | | 12.00 | 1.00 | 12.00 | 1.00 | | |
| | 13.30 | 0.80 | | | | | | |
| Sources | 1 | | 13 | | 8, 14 | | 15 | |

[a]: the channel at 10.8 µm of FCI can also operate in a high resolution mode of 1 km
[b]: later version of AGRI are planned to have an increased resolution of 2 km and 4 additional channels
[c]: MX-LWIR needs 30 min to scan India
[d]: the water vapor channel at 6.8 µm of the INSAT imager has only a resolution of 8 km
[e]: GHI covers an area of 2000 km × 2000 km within 1 min
1: Schmit et al. (2005), 2: Schmit et al. (2017), 3: Bessho et al. (2016), 4: JMA, 5: KMA, 6: Schmetz et al. (2002a), 7: Durand et al. (2015), 8: Yang et al. (2017), 9: Rublev et al. (2018) 10: CGMS, 11: WMO/MSU-GS, 12: WMO/MX-LWIR, 13: WMO/IMAGER-INSAT, 14: WMO/S-VISSR, 15: WMO/GHI

## 2.4 Artificial neural networks

*Artificial neural networks* (ANNs) are a part of the machine learning toolbox. After original, biologically-inspired research in the 1940s, the field experienced significant boosts in the 1980s with the establishment of a training algorithm for neural networks of multiple layers, and again around 2006, when methods for the training of deep neural networks were found (Goodfellow et al., 2018). ANNs are quite versatile as they can be used for classification as well as function approximation (Gardner and Dorling, 1998). Thus, ANNs are applied in a variety of fields nowadays, e.g., for computer vision, speech recognition or natural language processing, using specialized structures such as *convolutional neural networks*, *recurrent neural networks* or *auto-encoders* (Bengio, 2012, Goodfellow et al., 2018, Rumelhart et al., 1986a). It has also been applied frequently in the context of atmospheric sciences (Gardner and Dorling, 1998, Hsieh and Tang, 1998), Earth system sciences (Liu et al., 2010, Reichstein et al., 2019) and remote sensing (Mas and Flores, 2008). In the following we focus exclusively on the basic structure, the *feedforward multilayer perceptron*.

### 2.4.1 Multilayer perceptron

In principle, multilayer perceptrons can be imagined as advanced fitting methods. In their basic form they consist of at least three types of *layers*: one input layer, one or more intermediate (so-called *hidden*) layers and one output layer. The input layer consists of the input data, whereas the output layer contains one or more output quantities that should be derived from the input features. Each layer is made up of so-called *neurons*: they receive the weighted sum of the results of the previous layer's neurons and use it as the argument of an *activation function*; the result is forwarded to the following layer (see Figure 2.13). More quantitatively: Let us assume a structure with multiple layers, with the $m$th layer consisting of $N_m$ neurons. The numerical value forwarded to the subsequent layer by $n$th neuron in the $m$th layer is denoted as $x_{m,n}$. $x_{m,n}$ itself is calculated from the previous layers neurons by

$$x_{m,n} = f\left(\sum_{i=0}^{N_{m-1}} w_{m,n;i}\; x_{m-1,i} + b_{m,n}\right) \tag{2.22}$$

where $w_{m,n;i}$ and $b_{m,n}$ are tunable parameters of the structure, called *weight* and *bias*, respectively, and $f$ being the chosen activation function (Gardner and Dorling, 1998).

Different functions can and have been used as activation functions (Figure 2.14). Generally, the perceptron is defined to have a threshold function as activation (Bishop, 1995)

$$f_{\text{thrs}}(x) = \begin{cases} 0, & x < 0 \\ 1, & x \geq 0 \end{cases}. \tag{2.23}$$

Usually, continuous and differentiable functions are chosen (Bishop, 1995, LeCun et al., 2012), e.g., the *logistic function*

$$f_{\text{logistic}}(x) = \frac{1}{1 + e^{-x}} \tag{2.24}$$

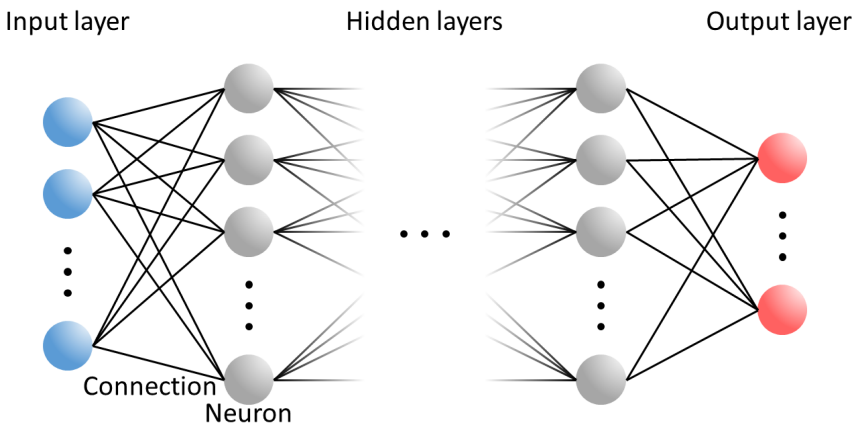


Figure 2.13: Sketch of a multilayer perceptron; black dots indicate that generally an arbitrary amount of hidden layers and neurons per layer can be chosen.

or the related *hyperbolic tangent*

$$f_{\tanh}(x) = \frac{e^x - e^{-x}}{e^x + e^{-x}} = 2f_{\text{logistic}}(2x) - 1. \tag{2.25}$$

Linear functions might be applied by single neurons (e.g., in the output layer for the approximation of a continuous function, Goodfellow et al., 2018), but not generally. If linear activation functions are used for all neurons, the outputs would be linear in the input features; only the use of simple, non-linear activation functions enables the modeling of complex, non-linear functions by the multilayer perceptron (Gardner and Dorling, 1998). For classification tasks with $N$ categories of which only one should be activated for each case (i.e., the output layer consists of $N$ neurons of which one should be 1 and the others 0) , the *softmax function* can be utilized in the output layer, defined for the $i$th neuron as

$$f_{\text{softmax}}(\mathbf{x}; i) = \frac{e^{x_i}}{\sum_{j=1}^{N} e^{x_j}} \tag{2.26}$$

with $\mathbf{x} = (x_1, ..., x_N) \in \mathbb{R}^n$ describing the weighted sums at all neurons in the output layer before applying any activation function. Then the outputs are normalized and can be *interpreted* as the posterior probabilities of the individual categories (Bishop, 1995, Goodfellow et al., 2018).

As the sigmoid functions have significant slopes only around $x = 0$ but behave asymptotically for large $|x|$, such that the result of the neuron changes only insignificantly when changing $x$ (e.g., due to a modification in the weights), one usually normalizes the input features to be within $[0, 1]$ or standardizes them by

$$x \mapsto \bar{x} = \frac{x - \mu_x}{\sigma_x} \tag{2.27}$$

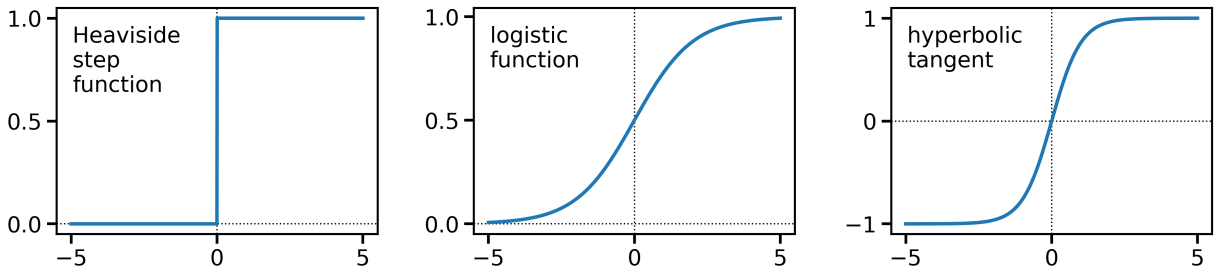


Figure 2.14: Common activation functions used for multilayer perceptrons.

with $\mu_x$ and $\sigma_x$ being the mean and the standard deviation of the input feature, respectively (Bishop, 1995). Similarly, target values need to be adjusted if a bounded activation function is used in the output layer. In particular, the majority of the target values should not be located at the asymptotes of the sigmoid. The use of normalized/standardized inputs and outputs also allows them to be treated numerically the same, even if they correspond to physically very different quantities (e.g., a temperature around 273 K versus the cosine of an angle between $\pm 1$). It is also recommendable to use uncorrelated input features (LeCun et al., 2012).

Using this setup, a function can be approximated by the multilayer perceptron by choosing appropriate values for the weights and the biases. For instance, assuming only an input and an output layer with one neuron each and a linear activation function, applying the multilayer perceptron would correspond to performing a linear fit. Increasing the complexity (i.e., number of hidden layers and neurons) of the multilayer perceptron and applying non-linear activation functions allows also the approximation of a wide range of non-linear relations (Hecht-Nielsen, 1989, Hornik, 1991, Hornik et al., 1989).

The potential of a multilayer perceptron can be visualized with a simple example (adapted from Bishop, 1995). Assume a continuous function $H(x, y) : \mathbb{R}^2 \to \mathbb{R}$ should be modeled. Discretize the two-dimensional input space. Consider a first grid cell described by the borders $x_0$, $x_1$, $y_0$, $y_1$. Constructing a multilayer perceptron $h$ such that

$$h(x_0 < x < x_1, y_0 < y < y_1) = H\left(\frac{x_0 + x_1}{2}, \frac{y_0 + y_1}{2}\right) \tag{2.28}$$

allows to approximate the function $H$ for this grid cell. Decreasing the grid size will reduce the deviation of $h$ with respect to $H$. To find $h$, a structure with two input neurons (i.e., $x$ and $y$), two hidden layers and one output neuron is considered. The first hidden layer contains four neurons describing the limits of the grid cell, i.e.,

$$z_1 = f_{\text{thrs}}(x - x_0) \tag{2.29}$$
$$z_2 = f_{\text{thrs}}(x_1 - x) \tag{2.30}$$
$$z_3 = f_{\text{thrs}}(y - y_0) \tag{2.31}$$
$$z_4 = f_{\text{thrs}}(y_1 - y) \tag{2.32}$$

and in the second hidden layer, insert a neuron functioning as a logical AND, i.e., it forwards 1 when the grid cell is active. It is descibed by

$$z_5 = f_{\text{thrs}}(z_1 + z_2 + z_3 + z_4 - 3.5). \tag{2.33}$$

Finally, assume a linear activation function in the output neuron following

$$h(x, y) = z_5 \cdot H\left(\frac{x_0 + x_1}{2}, \frac{y_0 + y_1}{2}\right). \tag{2.34}$$

Additional grid cells can be modeled by adding corresponding neurons in the hidden layers and summands to the output neuron. More input dimensions can be introduced by using more neurons in the first hidden layer analog to the ones shown.

### 2.4.2 Training

The central step in the creation of an ANN is the iterative *training*. After setting up the ANN's architecture, the weights and biases are randomly initialized. Then one uses a training data set consisting of samples of input data and the corresponding true output values for *supervised learning*; the targets can originate, for instance, from manual labeling, a simulation or another data set. The ANN is applied to the input data and the resulting outputs are compared to the target output to calculate the difference in form of a *loss function*. All weights and biases are now modified in order to reduce the loss function. The resulting ANN is again applied to the training input data and this procedure is repeated until the loss function is sufficiently small, i.e, a point close to the global minimum is reached (Bishop, 1995, Gardner and Dorling, 1998). In practice, this is complicated, e.g., by being trapped in local minima, at saddle points, on plateaus, or being distracted by exploding gradients (Goodfellow et al., 2018). The loss function $E$ between the $N$ retrieved values $r_i$ and the truth $t_i$ can be an arbitrary error function, e.g., the *mean squared error*

$$E_{\text{MSE}} = \frac{1}{N} \sum_{i=1}^{N} (r_i - t_i)^2 . \tag{2.35}$$

In the case of a classification task, one might also calculate the *cross-entropy*

$$E_{\text{CE}} = -\sum_{i_i}^{N} t_i \log(r_i). \tag{2.36}$$

If there is only one correct result, i.e., $t_i = 1$ and $t_{j \neq i} = 0$, this simplifies to $E_{\text{CE}} = -\log(r_i)$, such that $r_i$ is trained to become 1. The total loss of the training data set is the sum of the loss for individual samples (Bishop, 1995).

For simplicity, we suppress the indices of $w_{m,n;i}$ from now on, and instead introduce the incrementing counter $t$ to label different learning steps. All weights $w_t$ are combined

in a vector $\mathbf{w}_t$. A *gradient descent* algorithm is applied to adjust the $w_t$ such that the loss function is reduced. In a simplest form one applies

$$w_t = w_{t-1} - \eta \left.\frac{\partial E}{\partial w}\right|_{\mathbf{w}_{t-1}} \tag{2.37}$$

where $\eta$ denotes the *learning rate*. The derivatives $\left.\frac{\partial E}{\partial w}\right|_{\mathbf{w}_{t-1}}$ for the connections to the output layer are easily calculated. Applying the chain rule, one can move stepwise to the previous layers to calculate the corresponding derivatives; hence the name *backpropagation* (LeCun et al., 2012, Rumelhart et al., 1986a,b). The training speed can be increased by using more elaborate updating rules. *Momentum* denotes using an average of the previous gradients such that

$$m_t = \mu m_{t-1} + \eta \left.\frac{\partial E}{\partial w}\right|_{\mathbf{w}_{t-1}} \tag{2.38}$$

$$w_t = w_{t-1} - m_t, \tag{2.39}$$

which allows to accelerate the movement through loss space similar to a ball physically accelerating when rolling downhill; $\mu < 1$ parameterizes the momentum. Applying the momentum already to calculate the gradient leads to *Nesterov's accelerated gradient*, i.e., using $\left.\frac{\partial E}{\partial w}\right|_{\mathbf{w}_{t-1}-\mu\mathbf{m}_{t-1}}$ in Eq. 2.38 with $\mathbf{m}_t$ being the vector of all $m_t$ (Dozat, 2016, Ruder, 2016). The choice of $\eta$ is crucial: a value that is too low leads to a slow training, whereas a value that is too high might prohibit convergence of the loss function altogether, as the algorithm constantly oscillates around or jumps out of the minima (Bishop, 1995, LeCun et al., 2012). Instead of a constant value, $\eta$ can be related to the gradients as done by the *RMSProp* algorithm

$$n_t = \kappa n_{t-1} + (1-\kappa) \left( \left.\frac{\partial E}{\partial w}\right|_{\mathbf{w}_{t-1}} \right)^2 \tag{2.40}$$

$$w_t = w_{t-1} - \frac{\eta}{\sqrt{n_t} + \epsilon} \left.\frac{\partial E}{\partial w}\right|_{\mathbf{w}_{t-1}} \tag{2.41}$$

with $\epsilon \ll 1$ and $\kappa < 1$. It allows to effectively reduce the learning rate for weights that have already experienced large changes, to find the minimum of the loss function with a smaller step size. Combining all these elements leads to the *Nesterov-accelerated adaptive moment estimation* algorithm (Dozat, 2016, Ruder, 2016).

Instead of evaluating the ANN for the full training data set before updating the parameters (called *batch* gradient descent), one can also do so after subsets (*mini-batches*) or individual samples (*stochastic learning*), especially if differences in the samples are not too large. This speeds up the the training, as the weights are changed more often. It

might also lead to better training performances, as the use of small numbers of samples introduces a noise which can allow to explore larger parts of the parameter space (LeCun et al., 2012, Ruder, 2016).

The initial weights are usually drawn randomly as it is important to initialize the neurons differently to "break" the internal symmetry of the ANN (Goodfellow et al., 2018). However, an arbitrary choice of the initial weights potentially leads to large absolute inputs to the activation functions, letting them operate in the nearly constant regime. Thus, for the initialization, one might use a distribution which depends on the ANN's architecture, i.e., with a standard deviation $\sigma_w = \frac{1}{\sqrt{N}}$ for $N$ neurons in the preceding layer (*LeCun normal distribution*, Bishop, 1995, LeCun et al., 2012). Also it is not clear a priori that a given initialization leads to a (global) minimum; thus, one might repeat training with different initializations and compare the resulting configurations (Bishop, 1995, Goodfellow et al., 2018).

A common phenomenon during training is the occurrence of *overfitting*, i.e., the ANN starts to learn the inherent noise of the training data set and, as a result, performs worse for new unseen samples. Thus, the available data is usually split into a training, a validation and a test data set. The training data is used for the adjustment of the ANN, whereas the validation data set is regularly evaluated during the training. After an initial phase of decreasing loss functions for both training and validation data, overfitting might lead to a further decay of training loss with a simultaneous increase in validation loss; *early stopping* describes a strategy to stop training as soon as this point is reached. However, as the loss function is usually not monotonically decreasing but might exhibit numerous local minima, the definition of a stopping criterion is not straightforward. Alternatively, the process might be terminated manually. Since the validation data set is now part of this extended training algorithm, the final performance of the ANN is evaluated on the independent test data set (Prechelt, 2012).

Further *regularization* strategies to avoid overfitting include the reduction of ANN complexity, either by design or automatically by adding a penalty term to the loss function to force unimportant weights to become zero/small. Examples are $\lambda \sum |w|$ for L1 or $\lambda \sum w^2$ for L2 regularization, parameterized by $\lambda$ (Bengio, 2012, Goodfellow et al., 2018). The number of training samples can be artificially increased by adding altered versions of the given samples, for instance, translations or rotations can be applied to images if the final ANN should internalize the corresponding invariances. A small random noise can be added to the inputs or weights during training to increase robustness (Goodfellow et al., 2018). *Dropout* denotes a technique of randomly deactivating different input and hidden neurons for parts of the training. This resembles the training of multiple ANNs with subsequent averaging of their outputs (as explicitly done for the *bootstrap aggregating* method), but does so using a single model. Turning off arbitrary neurons also increases the robustness of the ANN, as each unit must be redundant (Goodfellow et al., 2018).

An overall difficulty in the context of ANN training is the choice of all *hyperparameters*, including parameters describing the ANN architecture (e.g., number of hidden layers, number of neurons) and the training algorithm (e.g., learning rate, momentum, minibatch size,

regularization) as a rigorous theory for their determination is missing but parameters are to some degree interdependent as well as problem-dependent. Thus, one needs to search for efficient settings either manually, or automatically via a random or systematic search in hyperparameter space. Alternatively, frequently applied default values can be chosen or at least used as a starting point (Bengio, 2012, Goodfellow et al., 2018).

### 2.4.3 Interpretation

Interpetation of the trained ANNs, i.e., of their weights, is—except for small and simple examples—hardly feasible. A common practice is to try to quantify the importance of single weights. First, one can assume that the absolute value of a weight is related to its relevance for the model. Second, the impact on the loss function can be considered when setting a weight to zero, which corresponds to its removal. Third, the change of the loss function can be investigated when slightly varying the weight, i.e., the analysis of the derivative of the loss function with respect to the weight. These methods have been applied for *pruning*, i.e., the significance of the weights of a large, trained ANN is calculated and the least important connections are removed to obtain a smaller structure with similar performance. Alternatively, complete neurons can be removed based on the impact of their presence on the loss function (Bishop, 1995). In principle, these methods can also be used to investigate the importance of individual input features of an ANN. For example, Strandgren et al. (2017b) evaluated the weights connected to an input neuron to deduce its relevance, whereas Piscini et al. (2014) applied the pruning method to find the important input quantities.

## 2.5 Current volcanic ash satellite retrievals using artificial neural networks

Satellite retrievals based on ANNs can have various advantages, e.g., they can be quite robust with respect to signal perturbations (Corradini et al., 2014) or complicated meteorological conditions (Zhu et al., 2020) and—after the training and compared to, for instance, approaches based on optimal estimation (Rodgers, 2000)—they are rather fast (Picchiani et al., 2011, Strandgren et al., 2017a), such that the operational application is possible. Thus, multiple volcanic ash retrievals utilize them. Picchiani et al. (2011) used them for the detection and the retrieval of the mass load of volcanic ash clouds from MODIS images, and Picchiani et al. (2014) for the classification of MODIS pixels using six different classes (representing ash above sea, ash above liquid/ice water clouds, liquid/ice water clouds, sea surface, ice surface, land surface). Piscini et al. (2014) retrieved the optical depth at 11 µm, the volcanic ash and $SO_2$ column concentrations and the effective radius from MODIS data using ANNs. Gray and Bennartz (2015) applied them for the detection of volcanic ash and $SO_2$-rich ash, respectively, from MODIS observations. Zhu et al. (2020) made use of ANNs to derive the ash cloud top height from MSG/SEVIRI measurements. Noteworthy is the nature of the used training data sets: In all cases, real satellite observations were used as training data, from one (Picchiani et al., 2011, Piscini et al., 2014), two (Picchiani et al., 2014, Zhu et al., 2020) or at most seven (Gray and Bennartz, 2015) different volcanoes. Thus, those retrievals are mostly tailored for specific volcanoes, e.g., for Etna (Picchiani et al., 2011) or for Icelandic volcanoes (Picchiani et al., 2014). In addition, the true values of the ash cloud properties are not known when using real satellite images as training data. Instead, they are inferred from other retrieval methods (Picchiani et al., 2011, 2014, Piscini et al., 2014), model calculations (Gray and Bennartz, 2015) or collocated data from other satellite instruments (Zhu et al., 2020).

A different approach was applied for VADUGS (*Volcanic Ash Detection Using Geostationary Satellites*, Kox et al., 2013), which runs operationally at the German weather service since 2015 (DWD). It uses MSG/SEVIRI brightness temperatures in the thermal infrared spectrum and applies a simple ANN with a single hidden layer of 600 neurons to derive simultaneously the ash mass load and the ash cloud top height. The ANN was trained with synthetic observations, simulated with the radiative transfer model libRadtran (**P4**). In contrast to the previously mentioned algorithms, the target values for the training of VADUGS were exactly known as they were part of the input data for the radiative transfer calculations. Qualitative checks proved that the resulting algorithm is able to provide convincing results: realistic volcanic ash clouds were detected for the eruptions of Eyjafjallajökull in 2010 and Puyehue-Cordón Caulle in 2011 with reasonable ash mass loads and ash cloud top heights (Graf et al., 2015, Kox et al., 2013). This demonstrates that the approach of VADUGS—combining synthetic observations with ANNs—is in principle promising. However, VADUGS showed deficits in its generalizability: it produced unsatisfying results when applied to a simulated test data set covering a wide range of possible scenes (**P4**), and an intercomparison exhibited quite low correlations ($\lesssim 0.2$) between the

mass load retrieval of VADUGS and other satellite-based volcanic ash retrievals. Validation of cloud top height retrievals against CALIPSO results showed even poorer performances of VADUGS, with an overestimation of heights around 5 km by a factor of ~2 (WMO, 2015). In addition, VADUGS was again tailored to one specific volcanic eruption (i.e., the eruption of Eyjafjallajökull in 2010), as only a single refractive index of the corresponding ash was used and only atmospheric data from the year of the incident.

# Chapter 3

# Papers

## 3.1 P1: Volcanic ash refractive indices and optical properties

Determination of complex refractive indices and optical properties of volcanic ashes in the thermal infrared based on generic petrological compositions

**Dennis Piontek**, Adrian J. Hornby, Christiane Voigt, Luca Bugliaro, Josef Gasteiger
Journal of Volcanology and Geothermal Research 2021, 411, 107174.

**Overview** Refractive indices and corresponding optical properties are important aerosol properties for radiative transfer calculations. For volcanic ash, the amount of available data has been very sparse until recently. In this paper, volcanic ash properties are reviewed—especially particle size, shape, petrological composition and porositiy—and a novel method is developed for the calculation of realistic refractive indices in the thermal infrared between 5 µm and 15 µm. It is applied to create a comprehensive set of refractive indices for different ash types; those are mainly influenced by the silica content and the porosity, and only to a smaller degree by the glass fraction. In addition, the resulting optical properties exhibit a significant variability, with a similarly large influence by composition and size distribution. A simple model is utilized to approximate brightness temperatures for different ash types and indicates that the ash composition is retrievable to some degree by passive remote sensing instruments such as MSG/SEVIRI.

**Author contribution** I reviewed the literature for volcanic ash properties and developed the method with help from AH. JG provided the program to calculate the optical properties. I developed additional software to calculate refractive indices, conducted the calculations and the analyses, prepared all figures and wrote the manuscript. LB and CV supervised the research. All authors discussed results and reviewed manuscript drafts.

Journal of Volcanology and Geothermal Research 411 (2021) 107174

Contents lists available at ScienceDirect

Journal of Volcanology and Geothermal Research

journal homepage: www.elsevier.com/locate/jvolgeores

# Determination of complex refractive indices and optical properties of volcanic ashes in the thermal infrared based on generic petrological compositions

D. Piontek [a,*], A.J. Hornby [b,c], C. Voigt [a,d], L. Bugliaro [a], J. Gasteiger [e]

[a] Deutsches Zentrum für Luft- und Raumfahrt, Institut für Physik der Atmosphäre, Oberpfaffenhofen, Germany
[b] Ludwig-Maximilians-Universität München, Department of Earth and Environmental Sciences, Munich, Germany
[c] Cornell University, Department of Earth and Atmospheric Sciences, Ithaca, NY, USA
[d] Johannes Gutenberg-Universität Mainz, Institut für Physik der Atmosphäre, Mainz, Germany
[e] Universität Wien, Aerosol Physics and Environmental Physics, Vienna, Austria

ARTICLE INFO

*Article history:*
Received 8 September 2020
Received in revised form 4 January 2021
Accepted 6 January 2021
Available online 9 January 2021

*Keywords:*
Volcanic ash
Refractive index
Optical properties
Remote sensing
Thermal infrared

ABSTRACT

The spaceborne detection of volcanic ash clouds at infrared wavelengths helps to avoid regions with enhanced volcanic ash concentrations that pose a threat to aviation. Current volcanic ash data retrievals require detailed information on microphysical properties and the refractive index of volcanic ash, which are highly variable. Uncertainties in the latter currently limit the quality of volcanic ash nowcasts. Here, we introduce a novel method to calculate the complex refractive indices of volcanic ashes at wavelengths from 5 to 15 μm from measurements of their individual components based on generic petrological ash compositions. Thereby the refractive indices for volcanic glasses and bulk volcanic ashes of different chemical compositions are derived. The variability of the latter is mainly influenced by the silica content and the porosity and to a minor degree by the glass-to-crystals ratio. Calculating optical properties exhibits an equally large impact of bulk composition and grain size distribution, whereas particle shape is considered less important for particle sizes of the order 1 μm. Using these optical properties to determine brightness temperature differences between the 11 μm and 12 μm channels we show that the effect of ash composition is non-negligible for modern satellite instruments. Particularly, the dependence of the volcanic ash on the silica content (and to a much smaller extent on the glass-to-crystals ratio) is observable in its refractive index, its optical properties and the brightness temperature difference, indicating that composition might be retrievable to some degree by remote sensing methods.

© 2021 The Authors. Published by Elsevier B.V. This is an open access article under the CC BY license (http://creativecommons.org/licenses/by/4.0/).

## 1. Introduction

Volcanic ash emitted during eruptive activity poses a serious threat to critical infrastructure on the ground (Wilson et al., 2012) and to aircraft in operation, where contact with a volcanic ash plume or cloud can lead to damage and engine failure (Casadevall, 1994); here the term *plume* is used for volcanic emissions that are still attached to the vent, and *cloud* once they are detached. Incidents at distances of 1000 km and more have been reported (Guffanti et al., 2010). Therefore, the eruption of Eyjafjallajökull in 2010 led to the prolonged closure of large parts of the European air space (Schumann et al., 2011) with estimated economic losses in the aviation industry of $1.7 billion (Budd et al., 2011).

In order to reduce the impact of future eruptions, satellite remote sensing methods have been developed and applied to monitor volcanic ash plumes and clouds, and thereby calibrate/validate volcanic ash transport and dispersion models (Stohl et al., 2011; Dacre et al., 2016). For that polar orbiting as well as geostationary passive optical imagers are used (e.g. Pavolonis et al., 2015), often equipped with channels in the atmospheric window at 11 to 12 μm (Schmetz et al., 2002a; Watkin, 2003; Watson et al., 2004; Schmit et al., 2005; Bessho et al., 2016). Volcanic ash has been commonly detected using the difference in satellite-measured brightness temperatures at 11 μm and 12 μm ($BTD_{11-12}$), which is negative for volcanic ash clouds under certain conditions (e.g. small ash particles, low amounts of water or ice present, see Prata, 1989; Guéhenneux et al., 2015), but positive for ice clouds (Inoue, 1985) – the latter is another typical application of those channels. More recent volcanic ash retrieval algorithms (e.g. for mass concentrations or cloud top heights) make use also of other channels in the thermal infrared and visible spectrum (Prata and Grant, 2001; Pavolonis et al., 2006; Francis et al., 2012), hyperspectral data (Gangale et al., 2010; Clarisse et al., 2010) or more advanced concepts (Pavolonis et al., 2013; Pugnaghi et al., 2013; Piscini et al., 2014). Many of those are based on

* Corresponding author.
*E-mail address:* dennis.piontek@dlr.de (D. Piontek).

https://doi.org/10.1016/j.jvolgeores.2021.107174
0377-0273/© 2021 The Authors. Published by Elsevier B.V. This is an open access article under the CC BY license (http://creativecommons.org/licenses/by/4.0/).

radiative transfer calculations, which in turn require the microphysical properties and the complex refractive index of the volcanic ash, Eq. (1), for the accurate simulation of brightness temperatures as a function of optical, micro- and macrophysical properties (e.g. Prata and Grant, 2001; Yu et al., 2002; Gangale et al., 2010; Pugnaghi et al., 2013; Ishimoto et al., 2016).

$$m = n + ik \tag{1}$$

Unfortunately, the volcanic ash properties are quite variable (Langmann, 2013), depending e.g. on the geographic location (Rogers, 2015) and the eruption style of the volcano (Polacci et al., 2019). Atmospheric processes further change the properties of the volcanic ash plumes and clouds (Langmann, 2013). In this study we focus on fine, distal ash, i.e. particles of a few micrometers in size which can travel within volcanic ash clouds thousands of kilometers. The corresponding typical properties are reviewed in the methods section of this paper.

The microphysical properties of volcanic ashes, in particular the particle size distribution and the particle shape, can have a large impact on their optical properties. Wen and Rose (1994) compared radiative transfer calculations for volcanic ash clouds using different refractive indices (from Pollack et al., 1973; Volz, 1973) and different size distributions (uniform, gamma and log-normal) and found that the size distribution is more important for a mass retrieval than the refractive index, and that $BTD_{11-12}$ is negative for effective radii less than 5 μm but can be positive for larger particles. Also the form of the brightness temperature spectrum is sensitive to the particle size (Gangale et al., 2010). Assuming a log-normal distribution with an uncertainty in the spread (i.e. geometric standard deviations of 1.8 to 2.5) can lead to uncertainties of > 20% in the retrieval of mass column loadings (Western et al., 2015). Newman et al. (2012) compared equal volume spheres (Mie calculation) with randomly oriented hexagonal columns of aspect ratio unity (T-matrix calculation) as volcanic ash particles, and found differences of up to 10% for extinction cross sections in the infrared. Non-spherical rugged vesicular volcanic ash particles were compared with mass-equivalent spheres as well as volume-equivalent spheres with an effective refractive index corrected for the vesicles by Kylling et al. (2014). Although similar for small sizes, significant differences in the optical properties were found for larger particles (e.g. for mass-equivalent radii > 4 μm at the wavelength 12 μm when comparing non-spherical small vesicle particles with volume-equivalent spherical small vesicle particles). The volume-equivalent approach generally modeled reality better.

A limited number of measurements of the refractive indices of volcanic ash exist in the ultraviolet, visible and near-infrared part of the spectrum (Vogel et al., 2017). In the infrared Pollack et al. (1973) presented laboratory measurements of obsidian, basaltic glass and andesite, and Volz (1973) of pumice (all in form of polished rock slabs, KBr or pure pellets). These data sets have been used for decades in volcanic ash retrievals (e.g. Prata, 1989; Wen and Rose, 1994; Prata and Grant, 2001; Yu et al., 2002; Gangale et al., 2010; Pugnaghi et al., 2013; Ishimoto et al., 2016). However, it is known that these retrievals are very sensitive to the refractive index (Wen and Rose, 1994; Western et al., 2015; Prata et al., 2019), and thus an accurate assumption of the refractive index could significantly improve them.

Recent studies have attempted to address this shortcoming: Grainger et al. (2013), Reed et al. (2018) and Deguine et al. (2020) performed laboratory measurements to determine the refractive indices for various volcanic ash samples of different geographical origin, composition and in suspension. Ishimoto et al. (2016) used hyperspectral data collected by satellite and established refractive indices (from Pollack et al., 1973) to constrain the parameters (effective radius, optical depth, cloud pressure height and the volume fraction for a mixture of known refractive indices of volcanic ashes) of multiple volcanic ash clouds. In a second step, those parameters were fixed and the imaginary part of the refractive index was retrieved. Wavelength-dependent variations up to factors of two or three were found for the refractive index in the infrared, indicating that the accurate knowledge of the refractive index is important.

In case of a future volcanic eruption a consolidated refractive index model together with the necessary, early, rapid chemical or mineralogical analysis of a sample would be sufficient to predict the refractive index of the volcanic ash and increase the performance of the satellite retrievals. To this end, Prata et al. (2019) performed wavelength-dependent linear regressions for both parts of the complex refractive index of volcanic ash with respect to either the silica content $x_s$ or the ratio of non-bridging oxygens to tetrahedrally coordinated cations, using the refractive indices from Reed et al. (2018).

A different approach is to estimate the refractive index for a specific volcanic ash by calculating the corresponding weighted average of the known refractive indices of minerals, glasses and gas bubbles based on their typical abundance in volcanic ashes. It allows the refractive index to be calculated for different compositions and to consider aging processes, e.g. the increase of glass to mineral ratio or the decrease of porosity (Shipley and Sarna-Wojcicki, 1982; Mackie et al., 2016). Thus, a more accurate estimate of the refractive index for an application can be made, and its variability can be investigated by changing the composition within realistic ranges. The impact on the optical properties of the composition in comparison to the microphysics can be analyzed, as has been done for mineral dust (e.g. Hansell Jr. et al., 2011). The uncertainty of retrievals relying on one specific refractive index can be investigated, and it enables to consider the possibility to retrieve the volcanic ash composition remotely. Therefore we use this approach, which was previously implemented for mineral dust in a similar fashion (Sokolik and Toon, 1999; Lee and Park, 2014). For volcanic ash Klüser et al. (2013) achieved good results using a limited set of refractive indices of minerals in remote sensing applications.

The paper is organized as follows: In the methods section (Sec. 2) we describe an approach to determine the refractive indices of volanic ashes based on their composition, discuss the influence of porosity, the mineral content and a technique to determine the refractive indices of volcanic glasses. We also compile the microphysical properties (size, shape) of volcanic ash particles from literature and outline a simple model to determine $BTD_{11-12}$. In the results section (Sec. 3) we determine the refractive indices of volcanic glasses and the bulk refractive indices of generic volcanic ashes. Then we quantify the impact of composition and microphysical properties on the optical properties. In the discussions section (Sec. 4) the results are analyzed and the different parameters are ranked regarding their importance for the determination of volcanic ash optical properties. The influence of the composition on the $BTD_{11-12}$ is quantified as an example. Finally, we give a conclusion.

## 2. Methods

In the following we first describe a procedure to calculate the complex refractive index and the bulk density of different volcanic ashes (Sec. 2.1). Second, we review microphysical properties (size, shape) of volcanic ash particles (Sec. 2.2). Using all these properties we are then able to calculate the optical properties and the brightness temperature difference $BTD_{11-12}$ of volcanic ashes (Sec. 2.3).

### 2.1. Model for the refractive index and the bulk density of volcanic ash

Generally, volcanic ash particles are created by the fragmentation of volcanic rocks (e.g. due to explosion of small bubbles of exsolved volatiles within a magmatic froth, reaction of hot magma with water in phreatomagmatic eruptions or milling during pyroclastic flows). Therefore they are highly irregular. Magma typically consists of a suspension of silicate melt, large minerals grown slowly in deep magma reservoirs (phenocrysts), small minerals grown during magma ascent (microlites) and exsolved bubbles. After fragmentation, volcanic ash particles

represent fragments containing these components in different proportions, with the silicate melt quenched to a volcanic glass, as well as lithic material collected during the eruption (Langmann, 2013; Jerram and Petford, 2011; Sen, 2014). The latter category is negligible for many eruptions, and is neglected for the purposes of this study. In the following we parameterize the remaining components and combine the individual refractive indices to a single effective refractive index.

### 2.1.1. Parameterization of the effective refractive index

There are different possible indices available to parameterize the composition of volcanic rocks. In the following we use the silica content $x_s$ (in weight percent, wt.%) of volcanic ashes, which is often determined and regularly used for their classification (Rogers, 2015). It depends on the tectonic location of the individual volcano and the magma genesis conditions, as well as storage, segregation and mixing within a subvolcanic plumbing system prior to eruption (Rogers, 2015; Freundt and Schmincke, 1992). Variations have been determined even within a single eruption event (Gudmundsson et al., 2012).

Other indices have been proposed as well: Prata et al. (2019) investigated the correlation between the refractive index of volcanic ash and the silica content as well as the polymerisation of the melt, defined by the ratio between nonbridging oxygens and tetrahedrally coordinated cations; the latter was favored due to a wider spectral range with coefficients of determination $R^2 > 0.5$. Cooper et al. (2002) showed that the ratio of silica and the amount of oxides of Si, Ca, Fe and Mg was superior to the silica content with respect to the correlation between their index and the position of specific spectral features (Christiansen and transparency feature). As these indices reflect not only the silica present in a rock, but also the abundance of specific elements, they might be able to better represent the chemical and therefore also mineralogical composition.

Aerosols can be mixed internally (each particle consists of multiple components) or externally (each particle consists of a single component which can differ between particles, Lesins et al., 2002). Except for the most silicic compositions consisting only of glass shards, volcanic ash contains both types of mixtures: Crystals surrounded by volcanic glass (Shipley and Sarna-Wojcicki, 1982; Casadevall, 1994) as well as single crystals fragments or glass sherds (Hornby et al., 2019). Following ash emissions, surface brines and salts formed from ash-gas reactions involving sulfur dioxide and other volatiles emitted at the eruption might be possible (Rose, 1977; Langmann, 2013; Casas et al., 2019), but are neglected for simplicity in this work. The volume weighted averaging has been used for external mixtures (Ebert et al., 2002; Ball et al., 2015) as well as internal mixtures (Sokolik and Toon, 1999; Lesins et al., 2002; Lee and Park, 2014) and is therefore used here. Note that other approximations (Bruggeman, Maxwell-Garnet) exist for the calculation of internal mixtures. Although these might lead to different results, there are indications that the impact of the mixing formula is mostly rather small in the infrared (Sokolik and Toon, 1999; Lesins et al., 2002; Lee and Park, 2014).

The complex refractive index of the different components/mixtures is denoted $m_x$, with $n_x$ the real and $k_x$ the imaginary part. Volume weighted averaging of the components gives the effective refractive indices of the mineral part $m_{min}$, of the solid volcanic material $m_{volc}$ including volcanic glass and minerals, and of the volcanic ash mixture $m_{eff}$ including volcanic glass, minerals and voids, Eqs. (2) to (4).

$$m_{eff} = f_{void} m_{void} + (1 - f_{void}) m_{volc} \tag{2}$$

$$m_{volc} = f_{glass} m_{glass} + \left(1 - f_{glass}\right) m_{min} \tag{3}$$

$$m_{min} = \sum_i f^i_{min} m^i_{min} \tag{4}$$

$f_{void}$ denotes the volume fraction that is occupied by gas pockets with respect to the volume of a convex hull covering the complete porous particle, $f_{glass}$ the volume fraction occupied by volcanic glass with respect to the solid volume, and $f^i_{min}$ the volume fraction of the $i^{th}$ mineral with respect to the crystalline volume. The bulk rock density is calculated similarly.

### 2.1.2. Porosity

One central driver of volcanic eruptions is the nucleation of gas bubbles due to supersaturation of the magma by volatile elements. These might grow with time and finally burst explosively. For ash particles the volume fraction filled by bubbles can be higher than 80% (Sparks, 1978). However, the actual porosity of the ash particles is size dependent: if the bubble size distribution peaks at sizes smaller than the particle size distribution, a significant amount of gas pockets might be present. But when the original bubbles are larger than the particles, porosity should be negligible, and the particles will contain bubble wall fragments.

Theoretical considerations suggest that the majority of bubbles in volcanic ash should have a size of a few micrometers or larger (Sparks, 1978). Measured bubble sizes in volcanic ash show multiple peaks, indicating multiple bubble nucleation processes (Klug and Cashman, 1994; Genareau et al., 2012, 2013; Colucci et al., 2013). Using backscattered electron images (Klug and Cashman, 1994) and stereo-scanning electron microscopy (Genareau et al., 2012, 2013) bubble size distributions have been shown to typically peak at diameters of 10 to 20 μm, but also at radii of 0.3 μm (Colucci et al., 2013). Using nitrogen gas adsorption Delmelle et al. (2005) concluded that the contribution from bubbles of diameters < 0.05 μm to the porosity is rather negligible; their pore size distributions showed small peaks for 0.005 μm. Mills and Rose (2010) found differences in the surface area estimates of a factor 8 for volcanic ash of size < 130 μm between nitrogen gas adsorption and three-dimensional scanning electron microscope stereo-pair analyses (resolution of 0.01 μm), which they contribute at least partially to the occurrence of microporosity. From in-situ measurements of plumes of degassing volcanoes Shcherbakov et al. (2016) derived for particles with effective diameter of 1.5 to 2.8 μm a porosity of 18 to 35% based on the measured aerosol refractive index. Further work to constrain the effect of microporosity on the refractive index is encouraged, but note that with respect to the total volume occupied by the gas pockets the main contribution comes from bubbles with diameters larger than 10 μm (Genareau et al., 2013; Cioni et al., 2014).

Other factors have an influence on the presence of bubbles as well. For instance a higher silica content connected to a higher viscosity might lead to smaller bubbles and a higher porosity (Genareau et al., 2013). Also the distance from the volcano is an important parameter, as larger and denser particles will sediment faster. Shipley and Sarna-Wojcicki (1982) reported that at distances of 50 km and farther the finest ash consists mainly of glass shards of fragmented porous particles. Also Genareau et al. (2013) showed that for distances farther than 250 km from the eruptive vent/location simple particles (glassy shards without vesicles, diameter < 30 μm) contribute the major part to the ash with respect to the mass, whereas more complex particles (larger with multiple imprints of bubbles and probably internal vesicles) contribute less and less. However, in-plume measurements by Rose et al. (1980) showed that in crystal-bearing volcanic ash the smallest fractions consist of crystal fragments.

In this work, we consider mainly particles with radii of a few micrometers. As many measurements indicate that bubbles are of a similar size or larger, we assume no internal bubbles in most parts of this work, i.e. $f_{void} = 0$. For particles larger than roughly 10 μm, this assumption does not hold. In this case we follow Kylling et al. (2014) and assume $m_{void} = 1$. Alternatively, pumice (a volcanic glass with a porous texture) as a component (using Volz, 1973) can be considered. The density of vesicles filled with air is significantly lower than typical volcanic ash densities, such that we assume $\rho_{void} = 0$ g cm$^{-3}$.

*2.1.3. Crystals*

The presence of typical minerals as well as their relative volume abundance can be related to the silica content according to the distribution in Fig. 3.10 (a classification scheme for igneous rocks) in Jerram and Petford (2011) (see also Rogers, 2015; Sen, 2014; Nakagawa and Ohba, 2002) for typical silica contents $x_s$, Eq. (5).

$$x_s \in \{45, 50, 55, 60, 65, 70, 75\}\ \text{wt.\%} \tag{5}$$

The corresponding volume fractions with respect to the bulk silica content are given in Table 1. In reality the composition might slightly deviate from the distribution in Table 1. Therefore, instead of directly applying Eq. (4), we use these fractions $f^i_{\text{min}}$ as mean values, assuming a certain variability in the composition. We add a random normally distributed value (mean of 0, width of 0.2) to each fraction $f^i_{\text{min}}$, set resulting negative values to zero and normalize the distribution. Using Eq. (4) with this new phase distribution gives us $m'_{\text{min}}$. The mean of $m'_{\text{min}}$, $\overline{m}_{\text{min}}$, is determined by repeating the calculation $N$ times and averaging the results. $N = 10\,000$ was found to be sufficient to get the maximum of the wavelength-dependent standard deviation of the real and imaginary part of $\overline{m}_{\text{min}}$ being $< 0.03$. $\overline{m}_{\text{min}}$ and a similarly calculated density are used from now on; for simplicity we drop the bar. Note that for the refractive index a slightly different composition is used than for the density, as corresponding data for amphibole are lacking. Thus, the relative composition for the refractive index is calculated by dropping amphibole prior to normalization.

The mineral phase distribution of Jerram and Petford (2011) included potassium feldspar, plagioclase and pyroxene. The first is here represented by orthoclase. The type of plagioclase changes depending on the silica content, being sodium-rich for felsic and calcium-rich for mafic ashes (Jerram and Petford, 2011). Therefore we use albite, labradorite and anorthite to represent this behavior. For $x_s = 75$ wt.% the plagioclase is assumed to consist only of albite, for $x_s = 54$ wt.% of labradorite and for $x_s = 40$ wt.% of anorthite. In between we apply a linear interpolation and use a mixture of two minerals. The composition of labradorite equals on average 40% (30 to 50%) albite and 60% (50 to 70%) anorthite (Ralph, 2020a). The pyroxene is assumed to contain orthopyroxenes (here enstatite) and clinopyroxenes (here diopside) in equal parts. Furthermore, quartz, muscovite, biotite, amphibole and olivine are used.

Note that we assume that the minerals with the largest contribution with respect to the crystalline volume also lead to the major contributions to the refractive index and the density. However, there are minor components with respect to the volume, that might still be able to have non-negligible influence (Best, 2003). Magnetite for instance, an iron-oxide, has a much higher density than most other components as well as a different refractive index, see Table 2 and Fig. 1. Therefore, we assume that 1 vol.% of the ash consists of magnetite as a representative of all iron- and titanium oxides (already included in Table 1).

The wavelength dependence of the real and imaginary part of the minerals in Table 1 (taken from different sources, see Table 2) is shown in Fig. 1. Various refractive indices are calculated using dispersion analysis as described in the corresponding papers (anorthite, clinopyroxene, muscovite, labradorite, obsidian, olivine, orthoclase, orthopyroxene). Cases where multiple indices were given for the different orientations of the crystal with respect to the electromagnetic field or measurement techniques are averaged assuming equal weighting (biotite, muscovite, labradorite, obsidian, orthoclase). For quartz the ordinary and the extraordinary ray are mixed 2:1 (Peterson and Weinman, 1969). This corresponds to the assumption of random orientation of the particles. Also note that some materials were glassy (albite). For small wavelengths ($< 7$ μm) we assume a constant refractive index $m = 1.4 + 0 \cdot \mathrm{i}$ if missing.

The wavelength dependence of the component refractive indices already shows some noteworthy features. Fig. 1 (g, h) shows the minerals typical for felsic rocks, while Fig. 1(c, d) shows minerals of mafic rocks. The peaks of the imaginary part of the felsic minerals are slightly shifted towards smaller wavelengths with respect to the mafic minerals, Fig. 1 (h, d). Similarly, the steep rise of the real part is shifted to smaller wavelengths for felsic minerals compared to the mafic minerals, Fig. 1 (g, c). Crystalline quartz has a significantly higher peak in the imaginary part than all other minerals, Fig. 1 (g). Note that diopside shows besides its own characteristic features also peaks at the same wavelengths as quartz, Fig. 1 (c, d). Fig. 1 (a, b) shows volcanic glasses for comparison: they exhibit the same tendencies and features as the crystals (except for magnetite) but with peaks at different wavelengths and they appear smoother. Magnetite has a completely different refractive index than all other components for 5 to 15 μm without prominent features, Fig. 1 (e, f); they appear for larger wavelengths (16 to 50 μm) instead (Glotch and Rossman, 2009).

The densities are taken from other sources than the refractive indices, see Table 2, and therefore might correspond to slightly different samples. For instance the refractive index used for albite is taken from Mutschke et al. (1998). However, their sample was in the glass state and had a density of only 2.36 g cm$^{-3}$. As we want to approximate crystals, we assume a higher density of $2.625 \pm 0.025$ g cm$^{-3}$ corresponding to crystalline albite (Ralph, 2020b). In many cases an interval of possible densities was given. Then we use the mean and half of the width as the uncertainty.

**Table 1**
Rounded volume fractions $f^i_{\text{min}}$ of mineral phases in volcanic ash with respect to the crystalline part according to Fig. 3.10 in Jerram and Petford (2011) for different bulk silica contents. The minerals are orthoclase (OC), quartz (Q), albite (AL), labradorite (L), anorthite (AN), enstatite (E), diopside (D), olivine (OL), muscovite (MU), biotite (B), amphibole (AM) and magnetite (MA). See text for further explanation.

| Mineral | Silica content $x_s$ / wt.% | | | | | | |
|---|---|---|---|---|---|---|---|
| | 45 | 50 | 55 | 60 | 65 | 70 | 75 |
| OC | 0.00 | 0.00 | 0.01 | 0.06 | 0.12 | 0.22 | 0.45 |
| Q | 0.00 | 0.00 | 0.06 | 0.13 | 0.23 | 0.33 | 0.23 |
| AL | 0.00 | 0.00 | 0.02 | 0.13 | 0.17 | 0.13 | 0.13 |
| L | 0.08 | 0.27 | 0.49 | 0.34 | 0.15 | 0.04 | 0.00 |
| AN | 0.15 | 0.11 | 0.00 | 0.00 | 0.00 | 0.00 | 0.00 |
| E | 0.29 | 0.29 | 0.09 | 0.00 | 0.00 | 0.00 | 0.00 |
| D | 0.29 | 0.29 | 0.09 | 0.00 | 0.00 | 0.00 | 0.00 |
| OL | 0.17 | 0.02 | 0.00 | 0.00 | 0.00 | 0.00 | 0.00 |
| MU | 0.00 | 0.00 | 0.00 | 0.00 | 0.00 | 0.08 | 0.13 |
| B | 0.00 | 0.00 | 0.05 | 0.12 | 0.14 | 0.08 | 0.04 |
| AM | 0.00 | 0.00 | 0.16 | 0.21 | 0.18 | 0.10 | 0.00 |
| MA | 0.01 | 0.01 | 0.01 | 0.01 | 0.01 | 0.01 | 0.01 |

*2.1.4. Glasses*

For felsic compositions volcanic ash often consists mostly of glassy particles and only to a minor fraction of minerals. Thus, the glass volume fraction $f_{\text{glass}}$ is often rather high. Vogel et al. (2017) showed that the glass fraction (analyzed from the areas of glass and minerals in two-dimensional images of ash particles) is proportional to the silica content $x_s$. During its lifetime $f_{\text{glass}}$ might increase even more due to sedimentation of the crystals, which have a higher density and a less rugged surface than the glass shards (Shipley and Sarna-Wojcicki, 1982; Mackie et al., 2016). This can lead to glass fractions of up to 1 (Heiken, 1974; Rose et al., 2003).

Measurements of the refractive index and the silica content of various volcanic glasses have been performed by Pollack et al. (1973). However, the silica content of the glass might be considerably higher than the silica content of the bulk magma as a result of the crystals (except quartz) being less silicic than the bulk material. Therefore, an increase in crystalization increases the difference in silica content between glass and bulk, up to 10 wt.% (Mackie et al., 2016). In addition, Reubi and Blundy (2009) showed that melt inclusions (i.e. melt trapped in phenocrysts) have a bimodal compositional distribution with a significant absence of intermediate compositions (i.e. 59 to 66 wt.%), although

**Table 2**
Literature sources for the refractive indices at the given wavelengths λ and their densities ρ.

| Component | Refractive Index Source | λ / μm | Remark to sample/meas. | Density Source | $\rho$ / g cm$^{-3}$ |
|---|---|---|---|---|---|
| Quartz glass ($SiO_2$ 100 wt.%) | Kitamura et al. (2007) | 0.21 to 50 | combination of different measurements | Wakaki et al. (2007) | 2.202 ± 0.001 |
| Obsidian ($SiO_2$ 75 wt.%) | Koike et al. (1989) | 2.5 to 400 | KBr pellet (transmission), slab of bulk (reflection) | Clark (1966) | 2.37 ± 0.04 |
| Basaltic glass ($SiO_2$ 53.45 wt.%) | Pollack et al. (1973) | 0.2 to 50 | slab of bulk (reflection) | Clark (1966) | 2.78 ± 0.07 |
| Orthoclase | Arnold et al. (2014) | 2.5 to 40 | slab of crystalline material (reflection) | Best (2003) | 2.59 ± 0.04 |
| Quartz | Spitzer and Kleinman (1961), Peterson and Weinman (1969) | 0.768 to 37 | slabs of crystalline material (reflection, transmission) | (Best, 2003) | 2.65 ± 0.01 |
| Albite (Plagioclase) | Mutschke et al. (1998) | 6.7 to 500 | slabs of glassy material (reflection) | Ralph (2020b) | 2.625 ± 0.025 |
| Labradorite (Plagioclase) | Ye et al. (2019) | 5 to 44.4 | slab of crystalline material (reflection) | $0.6\rho_{anorthite} + 0.4\rho_{albite}$ (Ralph, 2020a) | 2.70 ± 0.05 |
| Anorthite (Plagioclase) | Aronson and Strong (1975) | 6.25 to 40 | slab of crystalline material (reflection) | Ralph (2020c) | 2.75 ± 0.01 |
| Enstsatite (Orthopyroxene) | Roush et al. (1991) | 5 to 25 | KBr pellet (reflection) | Best (2003) | 3.55 ± 0.35 |
| Diopside (Clinopyroxene) | Aronson and Strong (1975), | 5.88 to 43.48 | slab of crystalline material (reflection) | Best (2003) | 3.35 ± 0.15 |
| Olivine | Mukai and Koike (1990) | 72 to 200 | KBr pellet (transmission) | Best (2003) | 3.8 ± 0.6 |
| Muscovite | Aronson and Strong (1975), Vedder (1964) | 6.67 to 31.25 | slab of crystalline material (reflection) | Ralph (2020d) | 2.825 ± 0.055 |
| Biotite | Querry (1983) | 0.25 to 55.56 | slab of crystalline material (reflection) | Haldar and Tišljar (2014) | 3.05 ± 0.35 |
| Amphibole (Hornblende) | NA | NA | NA | Best (2003) | 3.275 ± 0.225 |
| Magnetite | Glotch and Rossman (2009) | 5 to 100 | slab of crystalline material (reflection) | Ralph (2020e) | 5.175 ± 0.001 |

they are widespread. They proposed that intermediate compositions might be created by magma mixing, and therefore contain volcanic glasses with a silica content up to about 15 wt.% higher.

To circumvent this problem the refractive indices of volcanic glasses are derived from bulk ash samples, for which the bulk silica content is known. We invert Eqs. (2) to (4) to obtain $m_{glass}$ from $m_{eff}$, i.e. the bulk refractive index, by making assumptions on the remaining quantities ($f_{void}$, $m_{void}$, $f_{glass}$ and $m_{min}$, see details below). The refractive indices of bulk volcanic ash samples are taken from Reed et al. (2018) and Deguine et al. (2020), who investigated samples of seven (Grímsvötn 2011, Aso 1993, Eyjafjallajökull 2010, Tongariro 2012, Spurr 1992, Nisyros, Askja 1875) and six (Etna 2017, Grímsvötn 2011, Calbuco 2015, Eyjafjallajökull 2010, Puyehue-Cordón Caulle 2011, Chaitén 2008) different volcanic eruptions, respectively. The samples cover silica contents $x_s$ from 49.1 to 70.7 wt.% and 46.5 to 74.1 wt.%, respectively; $x_s$ of the Spurr sample was not given, and therefore is taken from Vogel et al. (2017). The particle diameter are mostly < 3 μm. The silica contents were determined by X-ray fluorescence analysis and the refractive indices from the extinction spectra of volcanic ash suspended in nitrogen in the infrared to ultraviolet spectrum. The densities were given neither by Reed et al. (2018) nor by Deguine et al. (2020); thus, we use the linear relation by Vogel et al. (2017) to calculate the bulk dense rock equivalent density of volcanic ash from the silica content; an uncertainty of 0.1 g cm$^{-3}$ is assumed. As the particles are small we assume that porosity is negligible, i.e. $f_{void} = 0$ (therefore, $m_{void}$ is not needed). For the glass $f_{glass} = x_s/100$ wt.% ± 0.05 is chosen (Vogel et al., 2017). The mineral composition is based on the rounded $x_s$ (to 45, 50, 55 wt.% etc., see Table 1); the uncertainty is set to 2.5 wt.%. The potential impact of the adjusted parameters is demonstrated with an example, then $m_{glass}$ is calculated using the assumptions. Negative values are set to zero.

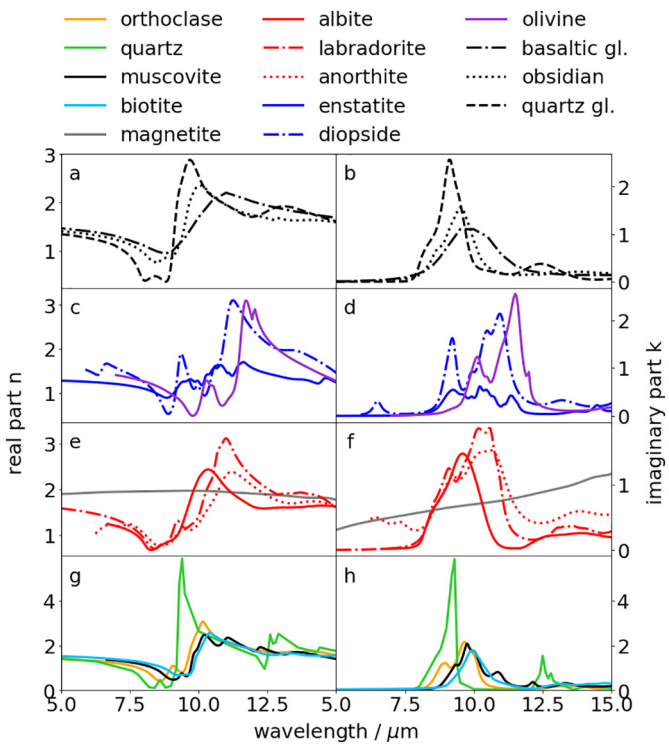


**Fig. 1.** Wavelength dependence of the real and imaginary part of the refractive index of the minerals and glasses in use.

We combine our volcanic glass calculations with the laboratory measurements of basaltic glass, obsidian and quartz, see Table 2. For basaltic glass the silica content ($x_s$ = 53.45 wt.%) was given by Pollack et al. (1973). For obsidian the silica content was not given, but the refractive index is similar to the obsidian refractive index in Pollack et al. (1973), with values around $x_s$ = 75 wt.%. Quartz glass as a pure silicate glass (i.e. $x_s$ = 100 wt.%) does not appear as a volcanic glass in nature. However, as the volcanic glasses from mafic to felsic have an increasing silica content, quartz glass can be considered as an extrapolation of this regime. Note that for basaltic glass and obsidian we ignore the possible difference between bulk and glass silica content. The refractive indices of the glasses, Fig. 1, show a similar behavior as the minerals with respect to the silica content, but the peaks are generally smaller and overall smoother.

In the next step we follow Prata et al. (2019) and perform separately a wavelength-dependent linear regression for the real ($n$) and

imaginary part ($k$) of the refractive index of volcanic glass, using $x_s$ as the independent variable. For instance the peak of $k$ shifts towards smaller wavelength with increasing $x_s$ for volcanic glasses (see Sec. 2.1.3). Therefore, it is possible that for a specific wavelength $k$ first increases, reaches a maximum, and then decreases again. Thus, we assume for the fit a quadratic function, Eq. (6).

$$g_i = a_i + b_i x_s + c_i x_s^2 \tag{6}$$

$g_i$ is $n$ or $k$ of volcanic glass at a wavelength $i$, and $a_i$, $b_i$, $c_i$ are the corresponding fit coefficients. Finally, we use these functions to calculate the real and the imaginary part of the refractive index of volcanic glasses from 45 to 100 wt.% with the corresponding $1\sigma$ prediction band. Again, occasional negative values are set to zero. Similarly, we calculate the density, only using a linear instead of a quadratic function.

### 2.2. Microphysical properties of volcanic ash

Next we compile typical sizes and shapes of volcanic ash in order to quantify the impact of these microphysical properties on the optical properties of volcanic ash. Then we compare these impacts with the effects of the composition in order to select parameters for the determination of a representative set of optical properties.

#### 2.2.1. Size distribution of volcanic ash particles

First, we select the type of size distribution for volcanic ash particles. The Weibull distribution has been reported from measurements (Stevenson et al., 2015), in addition the modified gamma distribution (Prata, 1989; Prata and Grant, 2001; Gangale et al., 2010) or more often the log-normal distribution (Farlow et al., 1981; Prata, 1989; Prata and Grant, 2001; Yu et al., 2002; Gangale et al., 2010; Grainger et al., 2013; Lee et al., 2014; Stevenson et al., 2015) has been used to characterize volcanic ash particles. Also multi-modal distributions have been reported (e.g. Wohletz et al., 1989; Riley et al., 2003). As the size of volcanic tephra variees over a large regime, we use log-normal distributions (Limpert et al., 2001) described by Eq. (7).

$$n(r) = \frac{N_0 \ \exp\left[-\frac{1}{2}\left(\frac{\ln(r)-\ln(r_m)}{\ln(s)}\right)^2\right]}{\sqrt{2\pi}\ \ln(s)\ r} \tag{7}$$

$N_0$ denotes the total particle number density, $r$ the radius (see also Sec. 2.2.2 for non-spherical particles), $r_m$ the median and $s$ the geometric standard deviation parameterizing the width of the distribution. The effective radius $r_{\mathrm{eff}}$, defined as the quotient of the third to the second moment of $n(r)$, becomes Eq. (8).

$$r_{\mathrm{eff}} = r_m \exp\left(\frac{5}{2}\ln(s)^2\right) \tag{8}$$

With respect to remote sensing applications, we are interested in fine ash particles and consider $r_{\mathrm{eff}} \in \{0.6, 1.8, 3, 4.5, 6\}$µm. This regime has been investigated in the laboratory (Reed et al., 2018; Deguine et al., 2020), in-situ (Rose et al., 1980; Schumann et al., 2011) and in many remote sensing applications (Pugnaghi et al., 2013; Grainger et al., 2013; Ishimoto et al., 2016). However, there is some unsolved discrepancy between the typical sizes in air- and spaceborne investigations and those found for cryptotephra. The latter shows systematically higher values, e.g. median number diameters (i.e. long axis length as used in the field of cryptotephra) of 20 to 70 µm at distances of about 1000 km (Stevenson et al., 2015) or mode diameters (average of 64 diameters) for mass density distributions of 90 µm at 1400 km (Rose et al., 2003). These variations might arise from differences in the measuring techniques and their sensitivities (Stevenson et al., 2015). Theoretically, considering only sedimentation for spherical ash particles, those larger particles are expected to fall out of the atmosphere fast, e.g. particles with radii around 20 µm should stay in the troposphere less than one day, whereas particles with radii of 1 µm might remain up to months (Grainger et al., 2013). However, as volcanic ash particles are not spherical but sometimes highly irregular, their terminal velocity might be significantly lower, and therefore their atmospheric residence time could be longer (Rose et al., 2003; Riley et al., 2003).

Typical values for the spread $s$ in Eq. (7) are 1.53 to 1.74 (for ash from Mt. St. Helens, Farlow et al., 1981), 2.1 (for ash from Mt. Redoubt, Wen and Rose, 1994), 1.38 to 1.66 (from cryptotephra, Stevenson et al., 2015) or 1.5 to 1.77 (applied in Grainger et al., 2013). Thus, we consider $s \in \{1.5, 2.0\}$ in the following analysis.

#### 2.2.2. Shape of volcanic ash particles

Second, we consider the shape of volcanic ash particles. These usually have a very rugged surface. However, for simplicity we confine our analysis to spheres and pro- and oblate spheroids. Kylling et al. (2014) showed that the differences in optical properties between non-spherical rugged vesicular volcanic ash particles and volume-equivalent spheres with an effective refractive index corrected for the vesicles is small for the sizes considered here. For larger particles these differences as well as the variability between different realistic particle shapes increases.

Typical aspect ratios of volcanic ash are 1.4 (Vogel et al., 2017), 1.38 to 1.81 (Ball et al., 2015), 1.8 to 2.2 (Schumann et al., 2011), 1.4 to 2.5 (Riley et al., 2003). Vogel et al. (2017) suggest that the aspect ratio decreases to 1.25 to 1.3 for radii smaller than 5 µm. The density distribution with respect to the aspect ratio can be parameterized by a modified log-normal distribution, Eq. (9) (Gasteiger and Wiegner, 2018).

$$n(\varepsilon) = \frac{\exp\left[-\frac{1}{2}\left(\frac{\ln(\varepsilon-1)-\ln(\varepsilon_0-1)}{\sigma_{\mathrm{ar}}}\right)^2\right]}{\sqrt{2\pi}\ \sigma_{\mathrm{ar}}\ (\varepsilon-1)} \tag{9}$$

$\varepsilon$ denotes the aspect ratio, $\varepsilon_0$ its median and $\sigma_{\mathrm{ar}}$ the spread. Kandler et al. (2007) described Saharan dust by Eq. (9) with $\varepsilon_0 = 1.64$ and $\sigma_{\mathrm{ar}} = 0.66$. To show that the same distribution can be used for volcanic ash we apply it to the aspect ratio distribution of two Sakurajima samples from Miwa et al. (2015), Fig. 2. Fitting yields $\varepsilon_0 = 1.7$ and $\sigma_{\mathrm{ar}} = 0.45$. Thus, we consider $\varepsilon_0 \in \{1.5, 2.0\}$ and $\sigma_{\mathrm{ar}} \in \{0.45, 0.66\}$ in the following analysis.

The definition of a radius is ambiguous for non-spherical particles. We consider the cross-section-equivalent radius in our study (except when stated otherwise), Eq. (10).

$$r_c = \sqrt{\frac{C_{\mathrm{geo}}}{\pi}} \tag{10}$$

$C_{\mathrm{geo}}$ denotes the orientation-averaged cross section of the particles (Gasteiger and Wiegner, 2018). Other definitions of the radius, e.g. via the volume ($r_{\mathrm{v}}$) or the volume to cross-section ratio ($r_{\mathrm{vcr}}$), are given in Gasteiger and Wiegner (2018). As these different definitions result in different values for the radius for the same particle, and as the size

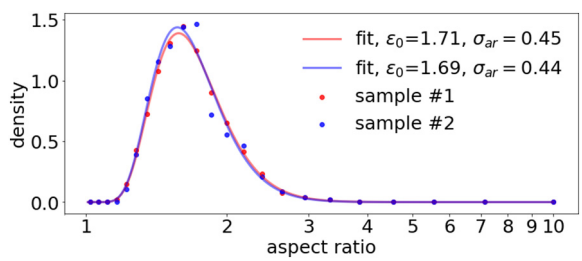


**Fig. 2.** Fit of the modified log-normal distribution to the aspect ratio distribution given by Miwa et al. (2015).

distribution has a large impact on the optical properties (as will be shown in Sec. 3.2), the radius definition may introduce a significant uncertainty in the optical properties. Gasteiger and Wiegner (2018) pointed out that the appropriate choice depends on the measurement technique applied to determine the size distribution. However, we combine literature values from different measurement techniques. Thus, the influence of the radius definition on the optical properties is investigated in a sensitivity study.

### 2.3. Optical properties of volcanic ash and a simplified model for $BTD_{11-12}$

The composition (i.e. refractive index) and the microphysical properties are used to calculate the optical properties (mass extinction coefficient, single scattering albedo and asymmetry parameter). To calculate these properties we use the tool *MOPSMAP* version 1.0 (Gasteiger and Wiegner, 2018). It comprises a precalculated data set of optical properties for single particles in random orientation, using Mie theory for spheres and the T-matrix method for spheroids. Then MOPSMAP computes the optical properties for a given ensemble of different single particles by averaging their properties. The input consists of the particle size and shape distribution, the refractive index and the bulk density. Wavelengths between 5 and 15 μm are considered at a resolution of 0.1 μm.

Using the optical properties one can calculate the brightness temperature difference $BTD_{11-12}$ as measured from satellite. Here we adapt a simple model of a single homogeneous volcanic ash layer as described by Prata and Grant (2001) (and applied in Prata and Prata, 2012; Prata et al., 2019). Only two wavelengths (11 and 12 μm) at nadir are considered and scattering effects are neglected. For theses wavelengths surface emissivities range roughly between 0.95 and and 1, depending on the surface type and the exact wavelength (Zhou et al., 2013). However, for simplicity we assume that the Earth's surface behaves like a black body and that the atmosphere is transparent except for the ash cloud; thus, we obtain Eqs. (11) and (12).

$$I_{11} = (1-t_{11})\, B_{11}(T_c) + t_{11}\, B_{11}(T_s) \tag{11}$$

$$I_{12} = (1-t_{12})\, B_{12}(T_c) + t_{12}\, B_{12}(T_s) \tag{12}$$

Here $I_\lambda$ denotes the spectral radiance measured at the top of the atmosphere, $B_\lambda$ the Planck function, $T_s$ and $T_c$ the temperatures of the Earth's surface and the cloud top, respectively. $t_\lambda = \exp(-\beta_\lambda \rho L)$ is the transmissivity with the mass extinction coefficient $\beta_\lambda$, the mass concentration $\rho$ and the geometrical cloud thickness $L$. We consider a test case with typical values of $L = 1000$ m and $\rho = 0.5$ mg m$^{-3}$ (e.g. Schumann et al., 2011), $T_s = 290$ K and $T_c = 220$ K (about 10 km).

## 3. Results

### 3.1. Refractive indices

To begin we consider the potential impact of the parameters $f_{\mathrm{glass}}$, $f_{\mathrm{void}}$ and $x_s$ on the derivation of volcanic glass refractive indices. Fig. 3 shows example calculations for the refractive index of volcanic glass derived from the the bulk refractive index of Eyjafjallajökull ash by Deguine et al., 2020, which lies with 58.6 wt.% in the center of the regime of typical silica contents. The corresponding densities are given in Table 3. A reference calculation is shown ($f_{\mathrm{glass}} = 0.59$, $f_{\mathrm{void}} = 0$, $x_s = 60$ wt.%) and the results for different variations of the reference settings. A change of $f_{\mathrm{glass}}$ by ±0.05% leads only to minor changes of the volcanic glass refractive index and density. However, for the extreme case $f_{\mathrm{glass}} = 1$ the imaginary part of the refractive index increases partly by up to 0.5 and the density by 7%. The variation of $x_s$ by ±5 wt.% can lead to changes of the refractive index up to about ±0.2, whereas the change in the density is of the order of 1%. $f_{\mathrm{void}}$ has the largest impact:

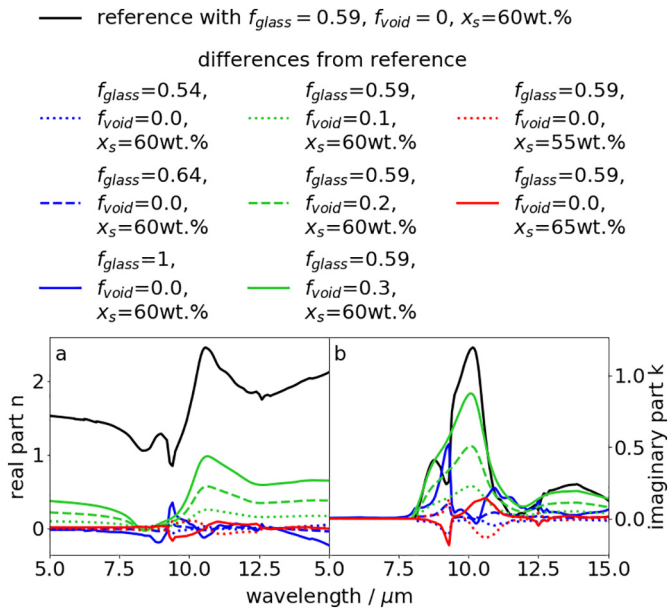


**Fig. 3.** Wavelength dependence of the real and imaginary part of the refractive index of volcanic glass derived from the bulk refractive index of Eyjafjallajökull ash by Deguine et al., 2020; a reference value is given (black), whereas for the other settings the reference is subtracted, i.e. the difference with respect to this reference is shown (blue, green, red); the parameters $f_{\mathrm{glass}}$, $f_{\mathrm{void}}$ and $x_s$ are varied.

**Table 3**
Density of volcanic glass derived from the bulk properties of Eyjafjallajökull ash by Deguine et al. (2020), varying the parameters $f_{\mathrm{glass}}$, $f_{\mathrm{void}}$ and $x_s$; the reference calculation is given in the first line, for the other settings the relative deviation of the density with respect to the reference density is given as well.

| $x_s$ / wt.% | $f_{\mathrm{glass}}$ | $f_{\mathrm{void}}$ | $\rho_{\mathrm{glass}}$ / g cm$^{-3}$ | |
|---|---|---|---|---|
| 60 | 0.59 | 0.00 | 2.61 | (ref.) |
| 60 | 0.54 | 0.00 | 2.56 | (−2%) |
| 60 | 0.64 | 0.00 | 2.64 | (1%) |
| 60 | 1.00 | 0.00 | 2.79 | (7%) |
| 60 | 0.59 | 0.10 | 3.14 | (20%) |
| 60 | 0.59 | 0.20 | 3.80 | (46%) |
| 60 | 0.59 | 0.30 | 4.65 | (78%) |
| 55 | 0.59 | 0.00 | 2.59 | (−1%) |
| 65 | 0.59 | 0.00 | 2.61 | (0%) |

for $f_{\mathrm{void}} = 0.3$ the real part of the refractive index increases by up to 1 and the imaginary part by about 0.8; also the density exhibits an increase of close to 80%.

Next the refractive indices for volcanic glasses calculated from all measurements of bulk volcanic ashes by Reed et al. (2018) and Deguine et al. (2020) are considered in Figs. 4 and 5, respectively; the latter are extrapolated from 14.49 μm up to 15 μm. Also shown are the refractive indices for obsidian, basaltic and quartz glass. Noteworthy are the dips between 9 and 10 μm for both $n$ and $k$ in the calculated refractive indices, Figs. 4 (a, b) and 5 (a, b). For the felsic cases this is probably due to the high peaks of crystalline quartz, whereas for the mafic cases a similar (although weaker) peak was visible in the diopside sample, Fig. 1. Interestingly, these dips are present for the measured volcanic glass refractive indices, such that these exhibit more features than the smoother bulk refractive indices (Reed et al., 2018; Deguine et al., 2020). In Fig. 4 (b) the imaginary part of the refractive index becomes negative for the samples of Aso and Tongario for wavelengths of 10 to 12 μm, and therefore is set to zero here. Similarly, the imaginary parts of some refractive indices are set to zero for wavelengths < 8 μm, Figs. 4 (b) and 5 (b).

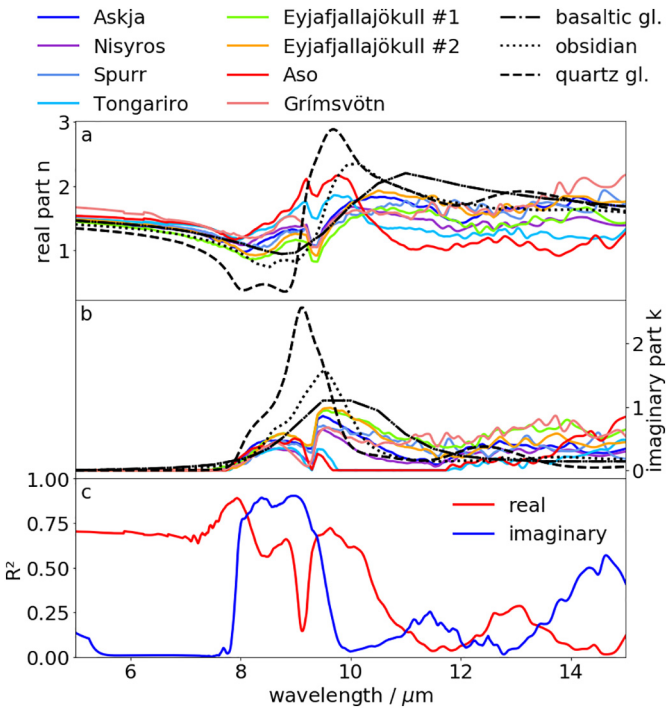


**Fig. 4.** Wavelength dependence of the real (a) and imaginary part (b) of the refractive indices of the volcanic glasses calculated from refractive indices of Reed et al. (2018) for bulk volcanic ash samples of different volcanos; (c) shows the corresponding $R^2$ value for the linear regression result at each wavelength.

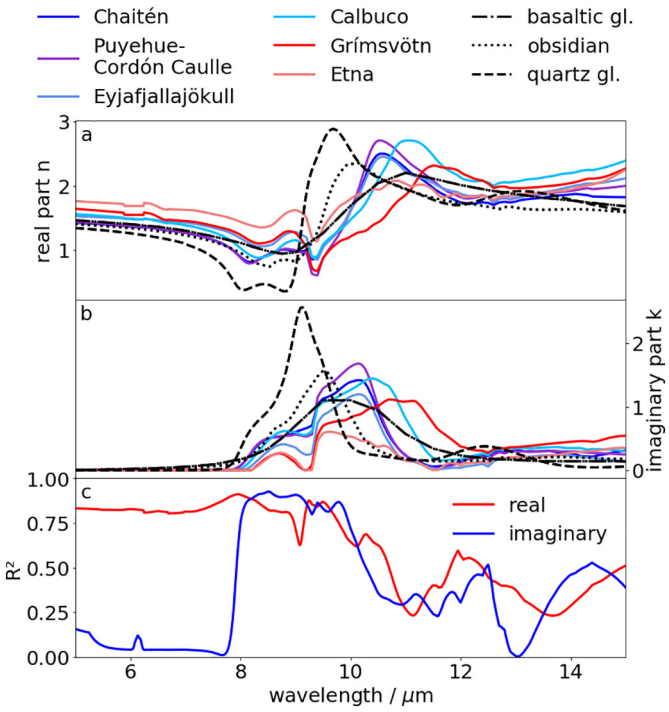


**Fig. 5.** As Fig. 4 but using refractive indices of Deguine et al. (2020).

Figs. 4 (c) and 5 (c) show the coefficient of determination $R^2$ for the wavelength-dependent linear regression. A perfect fit results in $R^2 = 1$, whereas a constant fit function returning the mean leads to $R^2 = 0$. The latter might happen if there is no clear functional dependence between the refractive index and the silica content. In Fig. 4 (c) $R^2$ of the real part is mostly around 0.7 up to 10 μm, except for a dip between 9 μm and 9.5 μm. Between 11 μm and 15 μm it is mostly < 0.25; this is because of the missing quadratic relationship between the refractive index and the silica content (e.g. the real parts of the volcanic glasses of Nisyros and Tongariro are between those of Grímsvötn and Aso, although the last two both have lower silica contents than the first two). For the imaginary part $R^2$ is roughly zero up to 8 μm as the imaginary parts of the volcanic glasses are mostly zero (or are set to zero if they become negative). $R^2$ rises to values of approximately 0.8 at wavelengths of 8 to 9.5 μm. Beyond that it remains < 0.25 up to roughly 13.5 μm; this might be partly due to the vanishing imaginary parts of the refractive indices of the volcanic glasses of Aso and Tongariro. Fig. 5 (c) shows similar values for $R^2$ as Fig. 4 (c) up to 9.5 μm. Beyond that $R^2$ decreases for the real and imaginary part to values mostly between 0.25 and 0.5, except for a dip of $R^2$ of the imaginary part to zero at 13 μm, where the imaginary part of quartz glass intersects all other imaginary parts. Calculating the average $R^2$ of the real and imaginary part between 8 μm and 12 μm gives 0.41 and 0.4 using Reed et al. (2018), and 0.64 and 0.62 using Deguine et al. (2020). This shows that the linear regression performs significantly better using the data of Deguine et al. (2020) compared to Reed et al. (2018). Therefore, we will use only the data derived from Deguine et al. (2020) from now on. In the next step we use the linear regression results to calculate the wavelength dependence of the refractive indices of volcanic glasses for bulk silica contents $x_s$ between 45 and 100 wt.%, Fig. 6. Fig. 7 shows the calculated glass densities. The linear regression yields $R^2 = 0.88$.

Mathematically $n$ and $k$ are connected by the Kramers-Kronig relation (Lucarini et al., 2005). Its singly subtractive version is given as Eq. (13).

$$\frac{n(\omega)-n(\omega_a)}{\omega^2-\omega_a^2} = \frac{2}{\pi}\mathcal{P}\int_0^\infty \frac{\overline{\omega}k(\overline{\omega})}{\left(\overline{\omega}^2-\omega^2\right)\left(\overline{\omega}^2-\omega_a^2\right)}\mathrm{d}\overline{\omega} \tag{13}$$

$\omega$ and $\omega_a$ are two wavenumbers and $\mathcal{P}$ denotes the Cauchy principal value of the integral. To check the consistency of the retrieved volcanic glass refractive indices we evaluate if the Kramers-Kronig relation is still fulfilled (Deguine et al. (2020) used a similar approach to determine the real parts of the refractive indices). We extend the imaginary part $k$ of the refractive index assuming $k \propto \lambda^{-1}$ for wavelengths $\lambda > 15$ μm and $k \propto \lambda^3$ for $\lambda < 5$ μm (Herbin et al., 2017). The choice of the anchor point $n(\omega_a)$ is crucial for the method (Herbin et al., 2017); we choose $\omega_a = 1000\,\mathrm{cm}^{-1}$ such that the integrand in Eq. (13) becomes largest in the center of the considered spectral regime where also the main

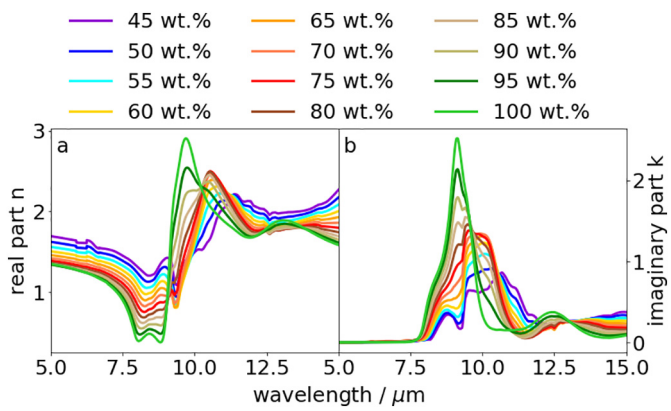


**Fig. 6.** Wavelength dependence of the real and imaginary part of the refractive indices of the volcanic glasses calculated from the linear regression results for different bulk silica contents.

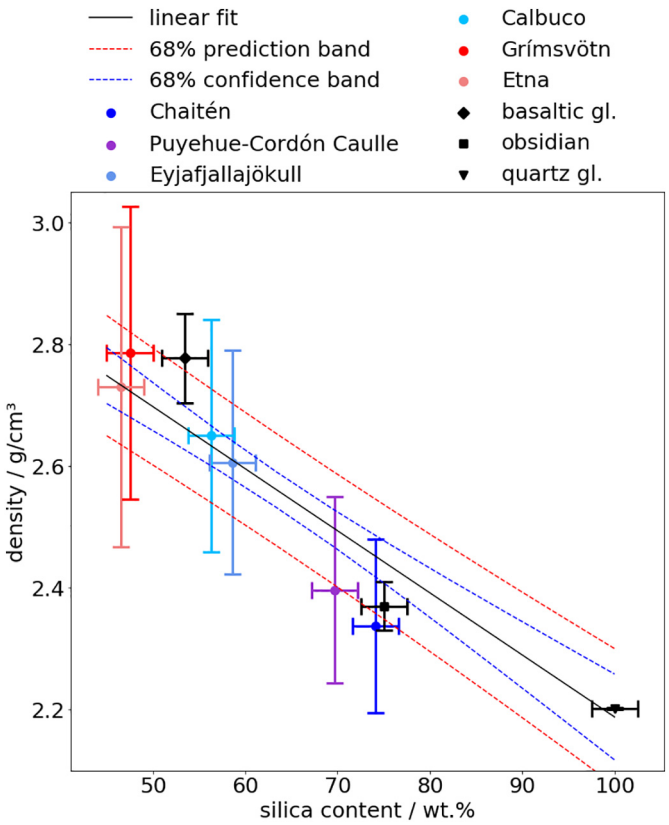


**Fig. 7.** Density of the volcanic glasses calculated from the bulk samples of different silica contents, typical densities for basaltic, obsidian and quartz glass, and the linear fit for these data.

absorption feature is located, Fig. 5 (b). $n(\omega_a)$ is taken from the individual regression results. The relative deviation of $n$ by Kramers-Kronig and linear regression relative to the latter is up to $\pm 10\%$ for 5 to 14 μm. For wavelengths > 10 μm the deviation increases for larger wavelengths and lower silica contents. At 15 μm the deviation for $x_s = 45$ wt.% is $-17\%$. Note that this might be at least partially connected to the fact that an assumption was used for $k$ for wavelengths > 15 μm instead of real measurements.

Next we can calculate the refractive indices for different mixtures of volcanic glasses, minerals and bubbles, Fig. 8. We vary different parameters within realistic ranges in order to investigate their impact on the refractive indices of volcanic ashes, i.e. $x_s$ from 45 to 75 wt.%, $f_{\mathrm{glass}}$ from $x_s/100$ wt.% to 1 and $f_{\mathrm{void}}$ from 0 to 0.75. In pink, the refractive index for $f_{\mathrm{glass}} = 0$ is shown, i.e. the pure mineral case. The grey shaded area shows the 68% prediction band for the pure volcanic glass case, i.e. for $f_{\mathrm{glass}} = 1$ and $f_{\mathrm{void}} = 0$. This band shows a significant spread, which in many cases is of the same order or even larger than the variability due to minerals.

### 3.2. Optical properties

Next we quantify the impact of the different microphysical properties and the composition on the optical properties. The largest spread and the corresponding wavelength are given for each property in Table 4. Considering the size distributions described in Sec. 2.2.1 (limited within MOPSMAP to $r \in [0.001, 30]$μm) for spherical particles and using the refractive index of Eyjafjallajökull ash of Deguine et al. (2020) and a density of 2.79 g cm$^{-3}$ (calculated from the silica content and the linear relation of Vogel et al., 2017) we obtain the optical properties shown in Fig. 9. $r_{\mathrm{eff}}$ as well as $s$ have a great influence on the optical properties, with $r_{\mathrm{eff}}$ dominating over $s$. The single scattering albedo,

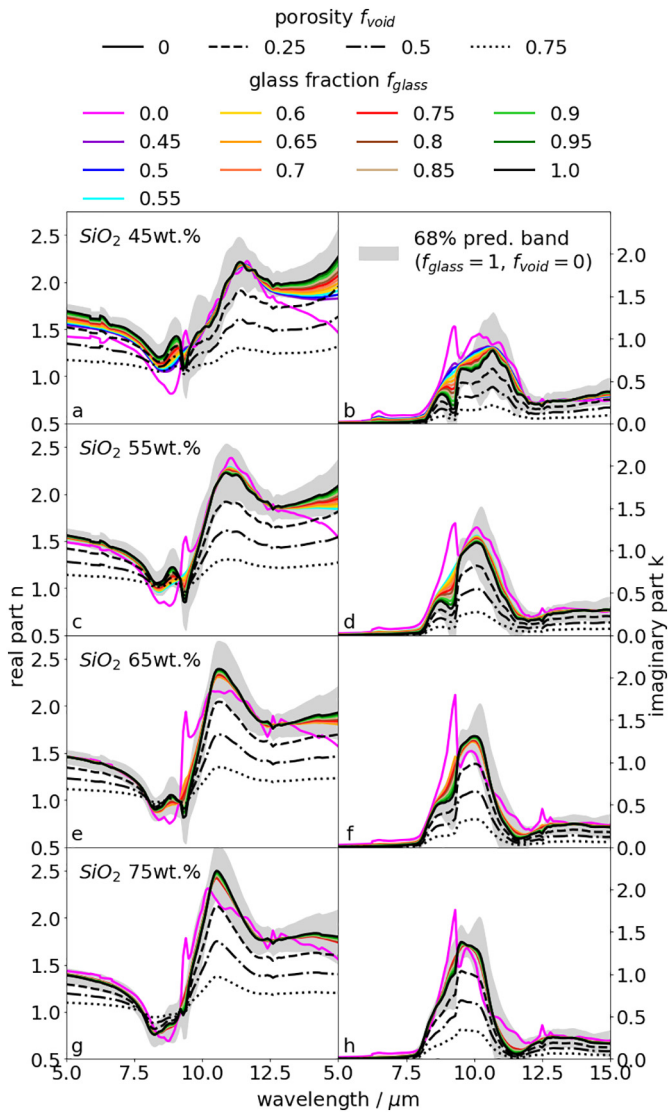


**Fig. 8.** Wavelength dependence of the real and imaginary part of the refractive indices of volcanic ash mixtures of glasses, minerals and voids with different compositions. $f_{\mathrm{glass}}$ is indicated by the color, $f_{\mathrm{void}}$ by the linestyle. $x_s$ has values of 45 wt.% (a, b), 55 wt.% (c, d), 65 wt.% (e, f) and 75 wt.% (g, h). Grey shaded is the 68% prediction band for the pure volcanic glass, i.e. for $f_{\mathrm{glass}} = 1$ and $f_{\mathrm{void}} = 0$.

Fig. 9 (b), shows that for small $r_{\mathrm{eff}}$ (0.6 μm) absorption dominates over scattering for wavelengths above 8 μm, whereas absorption and scattering are of similar importance for larger $r_{\mathrm{eff}}$ (≥ 1.8 μm). The asymmetry parameter, Fig. 9 (c), increases with increasing $r_{\mathrm{eff}}$, i.e. forward scattering becomes dominant.

Next we consider different particle shapes (spheres, pro- and oblate spheroids; $r \in [0.001, 30]$μm) and shape distributions (log-normal distributions of spheroids as described in Sec. 2.2.2; $r \in [0.001, 13]$μm). For aspect ratio distributions $\varepsilon$ is limited to [1,5], split in 10 intervals. Pro- and oblate spheroids are used in equal parts. Considering different sizes (log-normal distribution with $r_{\mathrm{eff}} \in \{0.6, 3, 6\}$μm, $s = 1.5$) we find that the shape has small influence on the optical properties with differences up to 10%, see Fig. 10 and Table 4.

To study the sensitivity with respect to the radius definition, we consider different possibilities (with $r \in [0.001, 13/12/9]$μm for $r_c$, $r_v$ and $r_{\mathrm{vcr}}$, respectively) for different sizes (log-normal distribution with $r_{\mathrm{eff}} \in \{0.6, 3, 6\}$μm, $s = 1.5$) and a non-spherical shape (pro- and oblate spheroids with log-normal aspect ratio distribution with $\varepsilon_0 = 1.5$ and $\sigma_{\mathrm{ar}} = 0.45$), Fig. 11. The absolute differences are rather small although

**Table 4**
Maximal spreads (Δ) in the optical properties mass extinction coefficient (*Ext.*), single scattering albedo (SSA) and asymmetry parameter, and the corresponding wavelengths (λ) for the variation of different properties.

| $r_{eff}$ / μm | Ext. / $\frac{m^2}{kg}$ | | SSA | | Asym. param. | |
|---|---|---|---|---|---|---|
| | Δ | λ / μm | Δ | λ / μm | Δ | λ / μm |
| | | | *Size* | | | |
| – | 301 | 9.6 | 0.64 | 7.9 | 0.79 | 8.1 |
| | | | *Shape* | | | |
| 0.6 | 39 | 10.1 | 0.04 | 7.6 | 0.02 | 11.0 |
| 3.0 | 23 | 10.6 | 0.02 | 7.9 | 0.02 | 8.1 |
| 6.0 | 29 | 5.0 | 0.03 | 11.7 | 0.04 | 5.0 |
| | | | *Radius definition* | | | |
| 0.6 | 10 | 10.4 | 0.03 | 7.6 | 0.02 | 5.0 |
| 3.0 | 11 | 10.3 | 0.01 | 7.9 | 0.02 | 10.0 |
| 6.0 | 12 | 6.9 | 0.01 | 8.0 | 0.01 | 5.1 |
| | | | *Composition (Refractive Index)* | | | |
| 0.6 | 564 | 9.2 | 0.64 | 7.2 | 0.07 | 10.8 |
| 3.0 | 184 | 9.3 | 0.80 | 7.8 | 0.20 | 5.0 |
| 6.0 | 117 | 7.7 | 0.73 | 7.8 | 0.25 | 6.3 |

the relative differences can go up to about 17.5%. Generally, $r_{vcr}$ leads to larger differences from $r_c$ than $r_v$. The differences tend to decrease with increasing $r_{eff}$.

Finally, we consider the influence of the volcanic ash composition (i.e. the refractive index and the corresponding bulk density) on the optical properties. Therefore, we consider spheres of different sizes (log-normal distribution with $r_{eff} \in \{0.6, 3, 6\}$μm, $s = 1.5$; $r \in [0.001, 20]$μm) and the refractive indices from Fig. 8 (but only $f_{void} = 0$ and $f_{glass} > 0$; 63 compositions in total). Note that this computation corresponds to assuming an internal mixture, since we use an effective refractive index for all particles in an ensemble, instead of different refractive indices of different glasses/minerals for the single particles. Although the main behavior of the optical properties is determined by $r_{eff}$, the refractive indices introduce a significant variability, see Fig. 12 and Table 4.

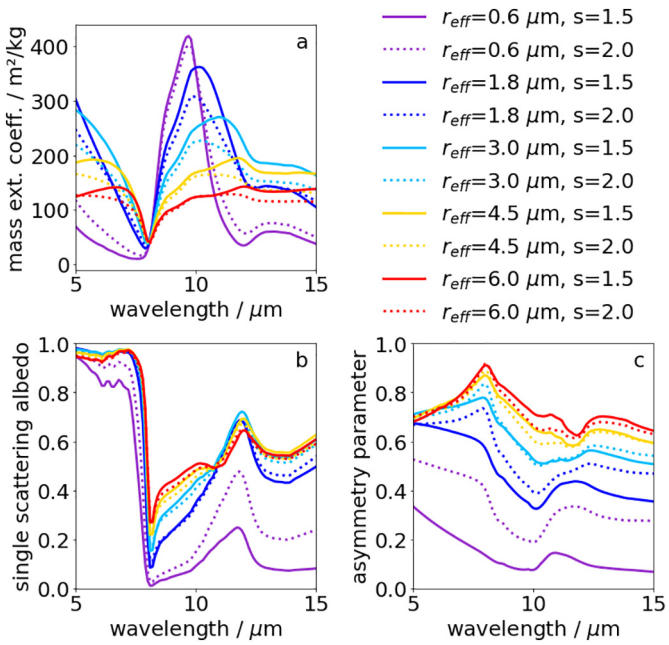


**Fig. 9.** Mass extinction coefficient (a), single scattering albedo (b) and asymmetry parameter (c) for ensembles of spherical particles with a log-normal size distribution with different $r_{eff}$ and $s$ with the refractive index of Eyjafjallajökull ash Deguine et al. (2020).

## 4. Discussions

Considering the refractive indices of volcanic glasses in Fig. 6, there are some general features observable. Up to 8 μm there is relatively little variation in the imaginary part, Fig. 6 (b), but significant variation for larger wavelengths. Similar results have been found by Reed et al. (2018). In the real part there is small variability approximately at 11 μm and 13 μm, Fig. 6 (a). Similar points appeared in the models of the refractive index of Prata et al. (2019). The peak of the imaginary part (of the broad feature, neglecting the small troughs due to single minerals) varies between roughly 10 μm for 75 wt.% and 11 μm for 45 wt.%, Fig. 6 (b). For comparison, in laboratory measurements peaks were found to be in the range 9 to 10 μm (Reed et al., 2018) or 10 to 10.5 μm (Deguine et al., 2020). The width of the peak varies also depending on the composition. In Prata et al. (2019) and Deguine et al. (2020), a shift of the peak towards higher wavelengths and an increase of width was shown to be connected to a lower silica content. Fig. 6 (b) shows a similar behavior for our volcanic glasses. Also the real part shows a similar dependence on the silica content as in Prata et al. (2019) and Deguine et al. (2020), e.g. a negative correlation of the refractive index and the silica content for wavelengths 5 to 8.5 μm and 11 to 15 μm, but a positive correlation for 9.5 to 11 μm, Fig. 6 (a). However, the amplitudes of the refractive indices are much smaller in Reed et al. (2018) and Prata et al. (2019). The comparison indicates that the qualitative behavior of volcanic glass and the the bulk volcanic ash are similar. Note that we calculated the refractive indices of volcanic glasses using the data of Deguine et al. (2020) instead of the results of Reed et al. (2018), as $R^2$ using the latter is generally lower, Figs. 4 (c) and 5 (c). Deguine et al. (2020) also showed that their results are in better agreement with the glass refractive indices from Pollack et al. (1973) than the results by Reed et al. (2018). As pointed out by Deguine et al. (2020) different assumptions with respect to the shape (spheres and ellipsoids) might be the reason for the large differences in the refractive indices.

Fig. 8 allows us to estimate the importance of different compositional properties regarding the refractive indices. For instance the difference between the pure minerals (pink in Fig. 8) and the pure glass (solid black) is generally small, except for the typical quartz peaks between 9 and 10 μm. Also the influence of the minerals is more visible for volcanic ashes with $x_s = 45$ wt.%, Fig. 8 (a, b), which can also have more crystals, i.e. a lower $f_{glass}$. However, the porosity is significant, leading to a flattening of the real part $n$ of the refractive index, Fig. 8 (a, c, e, g), and a lowering of the peak amplitude in the imaginary part $k$, Fig. 8 (b, d, f, h). Also the silica content $x_s$ has a large impact: whereas the imaginary part $k$ of the refractive index reaches up to about 1 for $x_s = 45$ wt.%, Fig. 8 (b), it increases up to about 1.5 for $x_s = 75$ wt.%, Fig. 8 (h).

We note that these results should be treated with some caution: we make various assumptions, each of them having a non-negligible impact. For instance the calculations are based on different refractive index measurements of minerals using different techniques and instruments, and some may be less accurate than others (e.g. anorthite does not become zero for small wavelengths, diopside exhibits some features that are very similar to quartz, Fig. 1). Also, all the minerals are investigated in form of KBr pellets or pure crystalline slabs, whereas the volcanic ash samples were measured in suspension in nitrogen gas (Reed et al., 2018; Deguine et al., 2020). Furthermore, we considered only a subset of all possible minerals in volcanic ash and assumed that all ashes of the same silica content have the same mineral phase distribution. Both assumptions might fail in specific cases. The volume weighted averaging is certainly valid for the density, but might have its limits for the refractive index. For instance, the refractive index of a particle consisting of a crystal covered by glass might be stronger influenced by the glass than by the mineral. Our assumptions for $f_{void}$ and $f_{glass}$

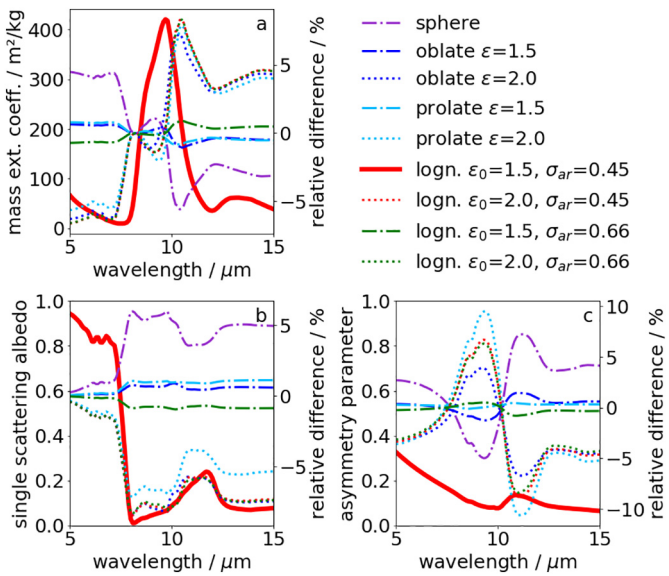


**Fig. 10.** Mass extinction coefficient (a), single scattering albedo (b) and asymmetry parameter (c) for particle ensembles with a log-normal size distribution with $r_{\mathrm{eff}} = 0.6$ μm and $s = 1.5$ with the refractive index of the Eyjafjallajökull ash by Deguine et al. (2020). Different shapes (spheres, spheroids) and aspect ratio distributions are considered. The latter are modified log-normal distributions consisting of ob- and prolate particles in equal parts with different $\varepsilon_0$ and $\sigma_{\mathrm{ar}}$. One case (thick red line) is shown as reference (left axis), whereas for the others the relative differences are shown (right axis).

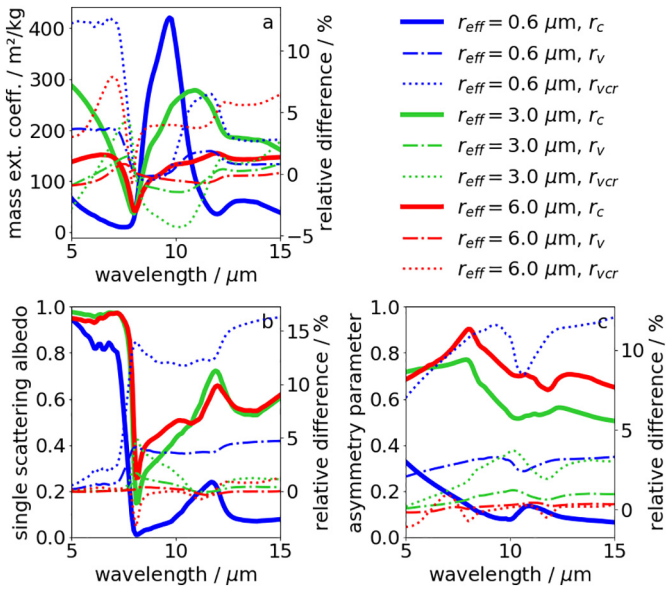


**Fig. 11.** Mass extinction coefficient (a), single scattering albedo (b) and asymmetry parameter (c) for ensembles of particles with a log-normal size distribution with different $r_{\mathrm{eff}}$ and $s = 1.5$, a log-normal aspect ratio distribution with $\varepsilon_0 = 1.5$, $\sigma_{\mathrm{ar}} = 0.45$ of spheroids, with the refractive index of the Eyjafjallajökull ash by Deguine et al. (2020). For the different $r_{\mathrm{eff}}$ different definitions of the radius are shown. One case (thick solid line) is shown as reference (left axis), whereas for the others the relative differences are shown (right axis).

are based on statistical analyses rather than on individual measurements. Especially a non-neglibile porosity might significantly alter the derived refractive indices of volcanic glasses, Fig. 3 and Table 3. Also the assumption of bubbles filled with air instead of specific gases resulting in the approximations $m_{\mathrm{void}} = 1$ and $\rho_{\mathrm{void}} = 0$ should be mentioned here. For the calculation of the volcanic glasses we relied on the measurements of Deguine et al. (2020). However, comparing these with Reed et al. (2018) shows that very similar measurement techniques might still result in different refractive indices. Also the refractive indices from both, Reed et al. (2018) and Deguine et al. (2020), do not show the large peaks of crystalline quarz, which leads to troughs in our volcanic glass refractive indices.

Comparing the results in Table 4 for the spreads in optical properties we see that with respect to the mass extinction coefficient the radius definition leads to the smallest variability, followed by the shape. Size and composition have a similar large impact in general, with the impact of the composition increasing with decreasing $r_{\mathrm{eff}}$. Note that the maximum spread due to the composition is located at a wavelength of 9.2 to 9.3 μm for $r_{\mathrm{eff}} = 0.6$ μm and 3.0 μm, respectively, which is where the major quartz peak is located, Fig. 12 (a, b). Thus, a single crystal leads to this large impact. Considering the single scattering albedo the ranking of importance is the same. Here most maximum spreads are located at 7.3 to 8.0 μm. At this point the single scattering albedo drops from close to 1 to below 0.5. This drop can be slightly shifted, Fig. 9 (b), such that the maximum spread in this regime can be larger than the general variability. Finally, with respect to the asymmetry parameter the size leads to the largest spread, followed by the composition, followed by the shape and the radius definition. Based on these rankings we decide to incorporate the full variability due to size and composition to create our representative data set of optical properties for volcanic ash. Thus, the size distributions for all $r_{\mathrm{eff}}$ and $s$ are considered, as well as all refractive indices. For shape and radius definition the impacts are relatively small such that a single setting is indeed sufficient. Thus, for the shape a log-normal distribution with $\varepsilon_0 = 1.5$ and $\sigma_{\mathrm{ar}} = 0.45$ and the radius definition $r_{\mathrm{c}}$ are used. The ranking also indicates that

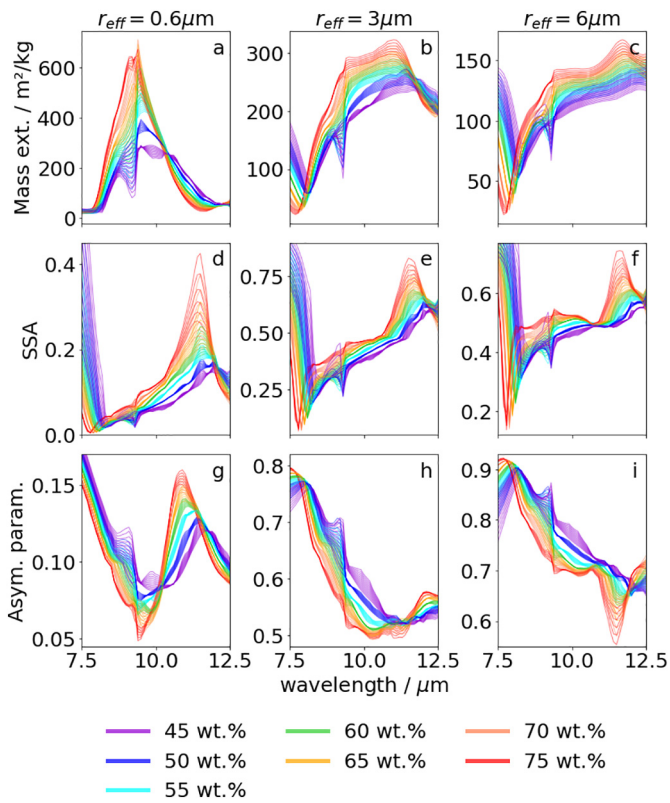


**Fig. 12.** Mass extinction coefficient (a, b, c), single scattering albedo (d, e, f) and asymmetry parameter (g, h, i) for ensembles of spherical particles with a log-normal size distribution with different $r_{\mathrm{eff}}$ and $s = 1.5$ for different refractive indices (see text). The different silica contents are marked by color.

mainly size and composition are needed for a fast calculation of the refractive index and the optical properties of a specific volcanic ash.

Regarding satellite remote sensing two further points should be stressed: First, the dominant peak of the mass extinction coefficient around 10 μm decreases with increasing $r_{\mathrm{eff}}$, Fig. 9 (a), and finally vanishes, leading to a strong dependence of $BTD_{11-12}$ on $r_{\mathrm{eff}}$; for $r_{\mathrm{eff}} \geq 6$ μm the signal in $BTD_{11-12}$ might disappear or even become positive. This dependence has also been pointed out by Prata (1989); Wen and Rose (1994); Stevenson et al. (2015). Second, the dependency of the optical properties on the silica content is visible in Fig. 12. For instance for large particles ($r_{\mathrm{eff}} = 6$ μm) the mass extinction coefficient correlates roughly with the silica content for 8.5 to 12 μm, Fig. 12 (c). However, for small particles ($r_{\mathrm{eff}} = 0.6$ μm) the behavior changes in the regime 10 to 12 μm: here the quantities anti-correlate, Fig. 12 (a). Similar dependencies are visible for the single scattering albedo, Fig. 12 (d, e, f) and the asymmetry parameter, Fig. 12 (g, h, i). In particular the silica dependencies of the mass extinction coefficient, Fig. 12 (a, b, c), indicate that there might be a possibility to retrieve the silica content as a proxy for the composition by satellite.

As noted in the introduction, $BTD_{11-12}$ can be considered for the detection of volcanic clouds via satellite. Using our representative set of optical properties (as outlined above and calculated for $r \in [0.001, 12]$μm) we determine $BTD_{11-12}$ for an example (Sec. 2.3) of small particles ($r_{\mathrm{eff}} = 0.6$ μm, $s = 1.5$). In this case neglecting scattering effects (Sec. 2.3) is valid as the single scattering albedo for these particles is below roughly 0.4, but there is large variability with respect to the composition, Fig. 12(a, d, g). $BTD_{11-12}$ is then $-1.9 \pm 0.7$ K and ranges from $-2.8$ to $-0.7$ K, i.e. all $BTD_{11-12}$ are negative for the specific size, Fig. 13. Note that the standard deviation is already larger than for instance the instrumental uncertainties of the 10.8 μm and 12.0 μm channels of the radiometer MSG-SEVIRI, which are of the order of 0.06 K and 0.10 to 0.16 K in-flight at 95 K (EUMETSAT, 2019; Schmetz et al., 2002b), stressing the importance to consider the correct composition in remote sensing retrieval applications. Fig. 13 shows that in this case different silica contents (indicated by the color) might be separable up to a certain degree. The size of the markers also indicates $f_{\mathrm{glass}}$. Within this model an increase in $f_{\mathrm{glass}}$ leads to an increase in $BTD_{11-12}$. However, the differences from $f_{\mathrm{glass}}$ are much smaller than those due to $x_s$, and of a similar order as the instrumental noise. Crosses indicate the results for the refractive indices of Deguine et al. (2020). They are aligned along the results of our representative data set, but some show large deviations from our calculations of similar silica content, e.g. Grímsvötn. Its peak in the imaginary part is shifted to larger wavelengths, Fig. 5 and Deguine et al. (2020), which results in a more negative $BTD_{11-12}$. This shows that the variability of the refractive index of volcanic ash might be even larger than what is covered by our method.

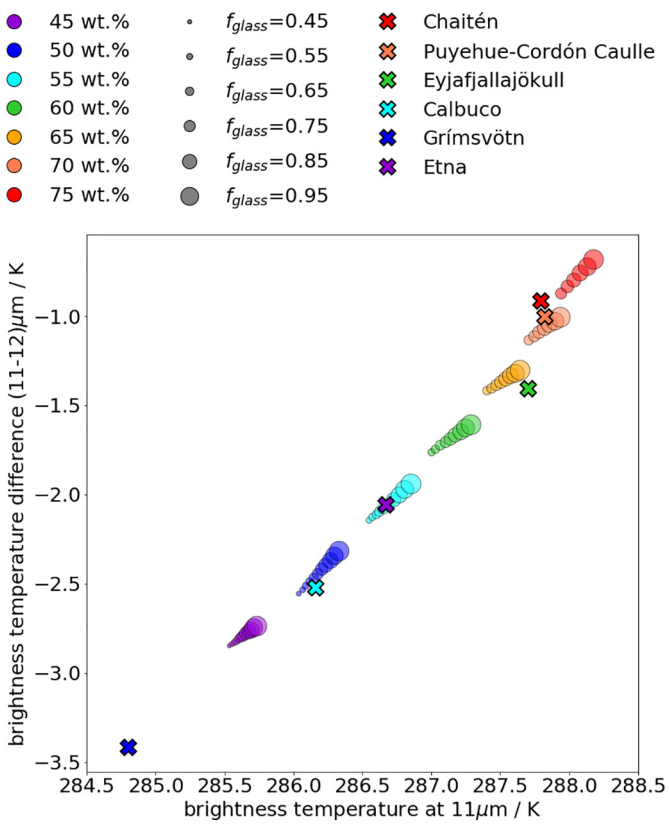


**Fig. 13.** Brightness temperature at 11 μm vs. brightness temperature difference at 11 μm and 12 μm for different compositions (as derived in Sec. 3.1), a log-normal size distribution ($r_{\mathrm{eff}} = 0.6$ μm, $s = 1.5$), and a ob−/prolate spheroidal shape with a modified log-normal aspect ratio distribution ($\varepsilon_0 = 1.5$, $\sigma_{\mathrm{ar}} = 0.45$). Also marked are the results for the refractive indices from Deguine et al. (2020) for the same microphysical properties.

## 5. Conclusions

Monitoring and initializing of nowcastings for volcanic ash clouds is regularly performed using satellite-borne passive infrared imagers. As these retrievals often rely on radiative transfer calculations, a good knowledge of the microphysical properties and the complex refractive index of volcanic ash is necessary. In this work we describe a method to calculate the complex refractive index of volcanic ash in the infrared (5 to 15 μm). This can be done for different volcanic ash compositions with respect to volcanic glasses, crystalline minerals and vesicles. The main parameters are the silica content, the glass fraction and the porosity. We compose a set of complex refractive indices in the infrared of the individual crystalline components as well as their densities. Combining these according to a typical silica dependent distribution from the literature we get effective refractive indices for the mineral part. These are used to determine the refractive indices of various volcanic glasses from the refractive indices of corresponding bulk samples from the literature. A wavelength dependent linear regression between the refractive indices of the volcanic glasses and the bulk silica content is performed. Subsequently, the refractive indices of the minerals and the glasses are combined for different compositions (varying silica content, glass fraction and porosity). Our results indicate that the impact of the glass fraction seems to be rather negligible compared to the impact of the silica content, which in turn may have less influence than the porosity. However, a short literature review indicates that the last might be negligible for particle sizes of the order of 1 μm, although this is not fully settled. The density of the volcanic ash was determined similar to the refractive index.

Furthermore, we review typical microphysical properties (size and shape) of volcanic ash. Calculating the resulting optical properties we show that the size and the composition lead to the largest variations with similar impact, whereas the considered shapes and radius definitions play a minor role. We show that the extinctions for 11 to 12 μm exhibit a size dependence such that the corresponding brightness temperature difference $BTD_{11-12}$ might become non-negative, and thus the criterion $BTD_{11-12} < 0$ regularly applied for volcanic ash detection by satellite might not be applicable for roughly $r_{\mathrm{eff}} \geq 6$ μm. A small single scattering albedo is observed for small particles, whereas scattering and absorption are more balanced for larger particles. Applying a simple model we estimate the range of $BTD_{11-12}$ and find a strong dependence on the composition which is non-negligible for modern satellite instruments.

To improve our method further laboratory measurements of bulk volcanic ashes and volcanic glasses would be needed, preferably together with measurements of mineral compositions, glass fractions and porosities. The latter would enable us to further validate our calculations. But already now our work shows that the composition of volcanic ash and, therefore, a proper assumption of the refractive index is

necessary for trustworthy satellite retrievals in the infrared. The results can be used for the development of new retrieval algorithms or to quantify the uncertainties in radiative transfer calculation-based retrievals due to the usage of a single refractive index for the volcanic ash. Also noteworthy is the fact that a dependence on the silica content (and to a much smaller extent on the glass fraction) is observable in the refractive index, the mass extinction coefficient and $BTD_{11-12}$, indicating that composition might be retrievable to some degree by remote sensing methods.

## Data availability

The created complex refractive indices of volcanic ash as well as the optical properties are available as supplementary data (Piontek et al., 2021).

## Declaration of Competing Interest

None.

## Acknowledgments

D. Piontek was supported by the European Unions's Horizon 2020 research and innovation program under grant agreement no. 723986 (EUNADICS-AV), J. Gasteiger under grant agreement no. 640458 (A-LIFE) and A. Hornby by grant agreement no. 753900 (Marie Skłodowska-Curie Action AVAST). C. Voigt acknowledges funding by the Helmholtz Association under contract HGF W2/W3-60. Work by D. Piontek, A. Hornby and C. Voigt was linked to and partially funded by the TeMaS research cluster (University Mainz). The volcanic ash refractive indices by Reed et al. (2018) and Deguine et al. (2020) have been made available through the ARIA database. We like to thank M. Vázquez-Navarro, M. Rapp, B. Mayer and D. Dingwell for the constructive discussions and valuable feedback, as well as R. Meerkötter, U. Schumann and two reviewers for their helpful comments to improve the manuscript.

## References

Arnold, J.A., Glotch, T.D., Plonka, A.M., 2014. Mid-infrared optical constants of clinopyroxene and orthoclase derived from oriented single-crystal reflectance spectra. Am. Mineral. 99, 1942–1955. https://doi.org/10.2138/am-2014-4828.

Aronson, J.R., Strong, P.F., 1975. Optical constants of minerals and rocks. Appl. Opt. 14, 2914–2920. https://doi.org/10.1364/AO.14.002914.

Ball, J.G.C., Reed, B.E., Grainger, R.G., Peters, D.M., Mather, T.A., Pyle, D.M., 2015. Measurements of the complex refractive index of volcanic ash at 450, 546.7, and 650 nm. J. Geophys. Res. Atmos. 120, 7747–7757. https://doi.org/10.1002/2015JD023521.

Bessho, K., Date, K., Hayashi, M., Ikeda, A., Imai, T., Inoue, H., Kumagai, Y., Miyakawa, T., Murata, H., Ohno, T., Okuyama, A., Oyama, R., Sasaki, Y., Shimazu, Y., Shimoji, K., Sumida, Y., Suzuki, M., Taniguchi, H., Tsuchiyama, H., Uesawa, D., Yokota, H., Yoshida, R., 2016. An Introduction to Himawari-8/9 - Japan's New-Generation Geostationary Meteorological Satellites. J. Meteorol. Soc. Jpn. Ser. II 94, 151–183. https://doi.org/10.2151/jmsj.2016-009.

Best, M.G., 2003. Igneous and Metamorphic Petrology. 2nd ed. Blackwell Science, Malden.

Budd, L., Griggs, S., Howarth, D., Ison, S., 2011. A Fiasco of Volcanic Proportions? Eyjafjallajökull and the Closure of European Airspace. Mobilities 6, 31–40. https://doi.org/10.1080/17450101.2011.532650.

Casadevall, T.J., 1994. The 1989–1990 eruption of Redoubt Volcano, Alaska: impacts on aircraft operations. J. Volcanol. Geotherm. Res. 62, 301–316. https://doi.org/10.1016/0377-0273(94)90038-8.

Casas, A.S., Wadsworth, F.B., Ayris, P.M., Delmelle, P., Vasseur, J., Cimarelli, C., Dingwell, D.B., 2019. $SO_2$ scrubbing during percolation through rhyolitic volcanic domes. Geochim. Cosmochim. Acta 257, 150–162. https://doi.org/10.1016/j.gca.2019.04.013.

Cioni, R., Pistolesi, M., Bertagnini, A., Bonadonna, C., Hoskuldsson, A., Scateni, B., 2014. Insights into the dynamics and evolution of the 2010 Eyjafjallajökull summit eruption (Iceland) provided by volcanic ash textures. Earth Planet. Sci. Lett. 394, 111–123. https://doi.org/10.1016/j.epsl.2014.02.051.

Clarisse, L., Prata, F., Lacour, J.L., Hurtmans, D., Clerbaux, C., Coheur, P.F., 2010. A correlation method for volcanic ash detection using hyperspectral infrared measurements. Geophys. Res. Lett. 37. https://doi.org/10.1029/2010GL044828.

Clark, S.P., 1966. Handbook of Physical Constants. Geological Society of America, New York.

Colucci, S., Palladino, D.M., Mulukutla, G.K., Proussevitch, A.A., 2013. 3-D reconstruction of ash vesicularity: Insights into the origin of ash-rich explosive eruptions. J. Volcanol. Geotherm. Res. 255, 98–107. https://doi.org/10.1016/j.jvolgeores.2013.02.002.

Cooper, B.L., Salisbury, J.W., Killen, R.M., Potter, A.E., 2002. Midinfrared spectral features of rocks and their powders. J. Geophys. Res. Planets 107. https://doi.org/10.1029/2000JE001462 1–1–1–17.

Dacre, H.F., Harvey, N.J., Webley, P.W., Morton, D., 2016. How accurate are volcanic ash simulations of the 2010 Eyjafjallajökull eruption? J. Geophys. Res. Atmos. 121, 3534–3547. https://doi.org/10.1002/2015JD024265.

Deguine, A., Petitprez, D., Clarisse, L., Gudmundsson, S., Outes, V., Villarosa, G., Herbin, H., 2020. Complex refractive index of volcanic ash aerosol in the infrared, visible, and ultraviolet. Appl. Opt. 59, 884–895. https://doi.org/10.1364/AO.59.000884.

Delmelle, P., Villiéras, F., Pelletier, M., 2005. Surface area, porosity and water adsorption properties of fine volcanic ash particles. Bull. Volcanol. 67, 160–169. https://doi.org/10.1007/s00445-004-0370-x.

Ebert, M., Weinbruch, S., Rausch, A., Gorzawski, G., Helas, G., Hoffmann, P., Wex, H., 2002. Complex refractive index of aerosols during LACE 98 as derived from the analysis of individual particles. J. Geophys. Res. Atmos. 107. https://doi.org/10.1029/2000JD000195 LAC 3–1–LAC 3–15.

EUMETSAT, 2019. Typical Radiometric Noise, Calibration Bias and Stability for Meteosat-8, −9, −10 and −11 SEVIRI.

Farlow, N.H., Orberbeck, V.R., Snetsinger, K.G., Ferry, G.V., Polkowski, G., Hayes, D.M., 1981. Size Distributions and Mineralogy of Ash Particles in the Stratosphere from Eruptions of Mount St. Helens. Science 211, 832–834. https://doi.org/10.1126/science.211.4484.832.

Francis, P.N., Cooke, M.C., Saunders, R.W., 2012. Retrieval of physical properties of volcanic ash using Meteosat: A case study from the 2010 Eyjafjallajökull eruption. J. Geophys. Res. Atmos., 117 https://doi.org/10.1029/2011JD016788.

Freundt, A., Schmincke, H.U., 1992. Mixing of rhyolite, trachyte and basalt magma erupted from a vertically and laterally zoned reservoir, composite flow P1, Gran Canaria. Contrib. Mineral. Petrol. 112, 1–19. https://doi.org/10.1007/BF00310952.

Gangale, G., Prata, A., Clarisse, L., 2010. The infrared spectral signature of volcanic ash determined from high-spectral resolution satellite measurements. Remote Sens. Environ. 114, 414–425. https://doi.org/10.1016/j.rse.2009.09.007.

Gasteiger, J., Wiegner, M., 2018. MOPSMAP v1.0: a versatile tool for the modeling of aerosol optical properties. Geosci. Model Dev. 11, 2739–2762. https://doi.org/10.5194/gmd-11-2739-2018.

Genareau, K., Proussevitch, A.A., Durant, A.J., Mulukutla, G., Sahagian, D.L., 2012. Sizing up the bubbles that produce very fine ash during explosive volcanic eruptions. Geophys. Res. Lett. 39. https://doi.org/10.1029/2012GL052471.

Genareau, K., Mulukutla, G.K., Proussevitch, A.A., Durant, A.J., Rose, W.I., Sahagian, D.L., 2013. The size range of bubbles that produce ash during explosive volcanic eruptions. J. Appl. Volcanol. 2, 4. https://doi.org/10.1186/2191-5040-2-4.

Glotch, T.D., Rossman, G.R., 2009. Mid-infrared reflectance spectra and optical constants of six iron oxide/oxyhydroxide phases. Icarus 204, 663–671. https://doi.org/10.1016/j.icarus.2009.07.024.

Grainger, R.G., Peters, D.M., Thomas, G.E., Smith, A.J.A., Siddans, R., Carboni, E., Dudhia, A., 2013. Measuring volcanic plume and ash properties from space. Geol. Soc. Spec. Publ. 380, 293–320. https://doi.org/10.1144/SP380.7.

Gudmundsson, M.T., Thordarson, T., Höskuldsson, Á., Larsen, G., Björnsson, H., Prata, F.J., Oddsson, B., Magnússon, E., Högnadóttir, T., Petersen, G.N., Hayward, C.L., Stevenson, J.A., Jónsdóttir, I., 2012. Ash generation and distribution from the April-May 2010 eruption of Eyjafjallajökull, Iceland. Sci. Rep. 2, 572. https://doi.org/10.1038/srep00572.

Guéhenneux, Y., Gouhier, M., Labazuy, P., 2015. Improved space borne detection of volcanic ash for real-time monitoring using 3-Band method. J. Volcanol. Geotherm. Res. 293, 25–45. https://doi.org/10.1016/j.jvolgeores.2015.01.005.

Guffanti, M., Casadevall, T.J., Budding, K., 2010. Encounters of aircraft with volcanic ash clouds; A compilation of known incidents, 1953–2009. U.S. Geological Survey Data Series 545, ver. 1.0, 12 p., plus 4 appendixes including the compilation database. U.S. Geological Survey http://pubs.usgs.gov/ds/545.

Haldar, S.K., Tišljar, J., 2014. Introduction to Mineralogy and Petrology. 1st ed. Elsevier, Amsterdam.

Hansell Jr., R.A., Reid, J.S., Tsay, S.C., Roush, T.L., Kalashnikova, O.V., 2011. A sensitivity study on the effects of particle chemistry, asphericity and size on the mass extinction efficiency of mineral dust in the earth's atmosphere: from the near to thermal IR. Atmos. Chem. Phys. 11, 1527–1547. https://doi.org/10.5194/acp-11-1527-2011.

Heiken, G., 1974. An Atlas of Volcanic Ash. Smithson. Contrib. Earth Sci. 12. https://doi.org/10.5479/si.00810274.12.1.

Herbin, H., Pujol, O., Hubert, P., Petitprez, D., 2017. New approach for the determination of aerosol refractive indices – Part I: Theoretical bases and numerical methodology. J. Quant. Spectrosc. Radiat. Transf. 200, 311–319. https://doi.org/10.1016/j.jqsrt.2017.03.005.

Hornby, A.J., Lavallée, Y., Kendrick, J.E., Rollinson, G., Butcher, A.R., Clesham, S., Kueppers, U., Cimarelli, C., Chigna, G., 2019. Phase partitioning during fragmentation revealed by QEMSCAN Particle Mineralogical Analysis of volcanic ash. Sci. Rep. 9, 126. https://doi.org/10.1038/s41598-018-36857-4.

Inoue, T., 1985. On the Temperature and Effective Emissivity Determination of Semi-Transparent Cirrus Clouds by Bi-Spectral Measurements in the 10 $\mu$m Window Region. J. Meteorol. Soc. Jpn. 63, 88–99. https://doi.org/10.2151/jmsj1965.63.1_88.

Ishimoto, H., Masuda, K., Fukui, K., Shimbori, T., Inazawa, T., Tuchiyama, H., Ishii, K., Sakurai, T., 2016. Estimation of the refractive index of volcanic ash from satellite infrared sounder data. Remote Sens. Environ. 174, 165–180. https://doi.org/10.1016/j.rse.2015.12.009.

Jerram, D., Petford, N., 2011. The Field Description of Igneous Rocks. 2nd ed. Wiley and Blackwell, Chichester.

Kandler, K., Benker, N., Bundke, U., Cuevas, E., Ebert, M., Knippertz, P., Rodríguez, S., Schütz, L., Weinbruch, S., 2007. Chemical composition and complex refractive index of Saharan Mineral Dust at Izaña, Tenerife (Spain) derived by electron microscopy. Atmos. Environ. 41, 8058–8074. https://doi.org/10.1016/j.atmosenv.2007.06.047.

Kitamura, R., Pilon, L., Jonasz, M., 2007. Optical constants of silica glass from extreme ultraviolet to far infrared at near room temperature. Appl. Opt. 46, 8118–8133. https://doi.org/10.1364/AO.46.008118.

Klug, C., Cashman, K.V., 1994. Vesiculation of May 18, 1980, Mount St. Helens magma. Geology 22, 468–472. https://doi.org/10.1130/0091-7613(1994)022¡0468:VOMMSH¿2.3.CO;2.

Klüser, L., Erbertseder, T., Meyer-Arnek, J., 2013. Observation of volcanic ash from Puyehue–Cordón Caulle with IASI. Atmos. Meas. Tech. 6, 35–46. https://doi.org/10.5194/amt-6-35-2013.

Koike, C., Hasegawa, H., Asada, N., Komatuzaki, T., 1989. Optical constants of fine particles for the infrared region. Mon. Not. R. Astron. Soc. 239, 127–137. https://doi.org/10.1093/mnras/239.1.127.

Kylling, A., Kahnert, M., Lindqvist, H., Nousiainen, T., 2014. Volcanic ash infrared signature: porous non-spherical ash particle shapes compared to homogeneous spherical ash particles. Atmos. Meas. Tech. 7, 919–929. https://doi.org/10.5194/amt-7-919-2014.

Langmann, B., 2013. Volcanic Ash versus Mineral Dust: Atmospheric Processing and Environmental and Climate Impacts. ISRN Atmos. Sci. 2013. https://doi.org/10.1155/2013/245076.

Lee, K.M., Park, J.H., 2014. Optical constants for Asian dust in midinfrared region. J. Geophys. Res. Atmos. 119, 927–942. https://doi.org/10.1002/2013JD020207.

Lee, K.H., Wong, M.S., Chung, S.R., Sohn, E., 2014. Improved volcanic ash detection based on a hybrid reverse absorption technique. Atmos. Res. 143, 31–42. https://doi.org/10.1016/j.atmosres.2014.01.019.

Lesins, G., Chylek, P., Lohmann, U., 2002. A study of internal and external mixing scenarios and its effect on aerosol optical properties and direct radiative forcing. J. Geophys. Res. Atmos. 107. https://doi.org/10.1029/2001JD000973 AAC 5–1–AAC 5–12.

Limpert, E., Stahel, W.A., Abbt, M., 2001. Log-normal Distributions across the Sciences: Keys and Clues. BioScience 51, 341–352. https://doi.org/10.1641/0006-3568(2001)051[0341,LNDATS]2.0.CO;2.

Lucarini, V., Saarinen, J.J., Peiponen, K., Vartiainen, E., 2005. Kramers-Kronig Relations in Optical Materials Research. Springer Science+Business Media, Berlin https://doi.org/10.1007/b138913.

Mackie, S., Cashman, K., Ricketts, H., Rust, A., Watson, M. (Eds.), 2016. Volcanica Ash: Hazard Observation, 1st ed. Elsevier, Amsterdam.

Mills, O.P., Rose, W.I., 2010. Shape and surface area measurements using scanning electron microscope stereo-pair images of volcanic ash particles. Geosphere 6, 805–811. https://doi.org/10.1130/GES00558.1.

Miwa, T., Shimano, T., Nishimura, T., 2015. Characterization of the luminance and shape of ash particles at Sakurajima volcano, Japan, using CCD camera images. Bull. Volcanol. 77, 5. https://doi.org/10.1007/s00445-014-0886-7.

Mukai, T., Koike, C., 1990. Optical Constants of Olivine Particles between Wavelengths of 7 and 200 $\mu$m. Icarus 87, 180–187. https://doi.org/10.1016/0019-1035(90)90027-7.

Mutschke, H., Begemann, B., Dorschner, J., Guertler, J., Gustafson, B., Henning, T., Stognienko, R., 1998. Steps toward interstellar silicate mineralogy. III. The role of aluminium in circumstellar amorphous silicates. Astron. Astrophys. 333, 188–198.

Nakagawa, M., Ohba, T., 2002. Minerals in Volcanic Ash 1: Primary Minerals and Volcanic Glass. Glob. Environ. Res. 6, 41–51.

Newman, S.M., Clarisse, L., Hurtmans, D., Marenco, F., Johnson, B., Turnbull, K., Havemann, S., Baran, A.J., O'Sullivan, D., Haywood, J., 2012. A case study of observations of volcanic ash from the Eyjafjallajökull eruption: 2. Airborne and satellite radiative measurements. J. Geophys. Res. Atmos. 117. https://doi.org/10.1029/2011JD016780.

Pavolonis, M.J., Feltz, W.F., Heidinger, A.K., Gallina, G.M., 2006. A Daytime Complement to the Reverse Absorption Technique for Improved Automated Detection of Volcanic Ash. J. Atmos. Ocean. Technol. 23, 1422–1444. https://doi.org/10.1175/JTECH1926.1.

Pavolonis, M.J., Heidinger, A.K., Sieglaff, J., 2013. Automated retrievals of volcanic ash and dust cloud properties from upwelling infrared measurements. J. Geophys. Res. Atmos. 118, 1436–1458. https://doi.org/10.1002/jgrd.50173.

Pavolonis, M.J., Sieglaff, J., Cintineo, J., 2015. Spectrally Enhanced Cloud Objects—A generalized framework for automated detection of volcanic ash and dust clouds using passive satellite measurements: 1. Multispectral analysis. J. Geophys. Res. Atmos. 120, 7813–7841. https://doi.org/10.1002/2014JD022968.

Peterson, J.T., Weinman, J.A., 1969. Optical Properties of Quartz Dust Particles at Infrared Wavelengths. J. Geophys. Res. 74, 6947–6952. https://doi.org/10.1029/JC074i028p06947.

Piontek, D., Hornby, A.J., Voigt, C., Bugliaro, L., Gasteiger, J., 2021. Determination of complex refractive indices and optical properties of volcanic ashes in the thermal infrared based on generic petrological compositions: supplementary material. Zenodo https://doi.org/10.5281/zenodo.4447877.

Piscini, A., Picchiani, M., Chini, M., Corradini, S., Merucci, L., Del Frate, F., Stramondo, S., 2014. A neural network approach for the simultaneous retrieval of volcanic ash parameters and $SO_2$ using MODIS data. Atmos. Meas. Tech. 7, 4023–4047. https://doi.org/10.5194/amt-7-4023-2014.

Polacci, M., Andronico, D., de Michieli Vitturi, M., Taddeucci, J., Cristaldi, A., 2019. Mechanisms of Ash Generation at Basaltic Volcanoes: The Case of Mount Etna, Italy. Front. Earth Sci. 7, 193. https://doi.org/10.3389/feart.2019.00193.

Pollack, J.B., Toon, O.B., Khare, B.N., 1973. Optical Properties of Some Terrestrial Rocks and Glasses. Icarus 19, 372–389. https://doi.org/10.1016/0019-1035(73)90115-2.

Prata, A.J., 1989. Infrared radiative transfer calculations for volcanic ash clouds. Geophys. Res. Lett. 16, 1293–1296. https://doi.org/10.1029/GL016i011p01293.

Prata, A.J., Grant, I.F., 2001. Retrieval of microphysical and morphological properties of volcanic ash plumes from satellite data: Application to Mt Ruapehu, New Zealand. Q. J. R. Meteorol. Soc. 127, 2153–2179. https://doi.org/10.1002/qj.49712757615.

Prata, A.J., Prata, A.T., 2012. Eyjafjallajökull volcanic ash concentrations determined using Spin Enhanced Visible and Infrared Imager measurements. J. Geophys. Res. Atmos. 117. https://doi.org/10.1029/2011JD016800.

Prata, G.S., Ventress, L.J., Carboni, E., Mather, T.A., Grainger, R.G., Pyle, D.M., 2019. A New Parameterization of Volcanic Ash Complex Refractive Index Based on NBO/T and $SiO_2$ Content. J. Geophys. Res. Atmos. 124, 1779–1797. https://doi.org/10.1029/2018JD028679.

Pugnaghi, S., Guerrieri, L., Corradini, S., Merucci, L., Arvani, B., 2013. A new simplified approach for simultaneous retrieval of $SO_2$ and ash content of tropospheric volcanic clouds: an application to the Mt Etna volcano. Atmos. Meas. Tech. 6, 1315–1327. https://doi.org/10.5194/amt-6-1315-2013.

Querry, M.R., 1983. Optical Properties of Natural Minerals and Other Materials in the 350–50,000 $cm^{-1}$ Spectral Region. Technical Report. University of Missouri Kansas City, Department of Physics.

Ralph, J., 2020a. Mindat.org. https://www.mindat.org/min-3231.html (Online; accessed 17-July-2020).

Ralph, J., 2020b. Mindat.org. https://www.mindat.org/min-96.html (Online; accessed 17-July-2020).

Ralph, J., 2020c. Mindat.org. https://www.mindat.org/min-246.html (Online; accessed 17-July-2020).

Ralph, J., 2020d. Mindat.org. https://www.mindat.org/min-2815.html (Online; accessed 17-July-2020).

Ralph, J., 2020e. Mindat.org. https://www.mindat.org/min-2538.html (Online; accessed 17-July-2020).

Reed, B.E., Peters, D.M., McPheat, R., Grainger, R.G., 2018. The Complex Refractive Index of Volcanic Ash Aerosol Retrieved From Spectral Mass Extinction. J. Geophys. Res. Atmos. 123, 1339–1350. https://doi.org/10.1002/2017JD027362.

Reubi, O., Blundy, J., 2009. A dearth of intermediate melts at subduction zone volcanoes and the petrogenesis of arc andesites. Nature 461, 1269–1273. https://doi.org/10.1038/nature08510.

Riley, C.M., Rose, W.I., Bluth, G.J.S., 2003. Quantitative shape measurements of distal volcanic ash. J. Geophys. Res. Solid Earth 108. https://doi.org/10.1029/2001JB000818.

Rogers, N., 2015. The Composition and Origin of Magma. In: Sigurdssonn, H., Houghton, B., McNutt, S.R., Rymer, H., Stix, J. (Eds.), The Encyclopedia of Volcanoes, 2nd ed. Academic Press, London, pp. 93–112.

Rose, William I.J., 1977. Scavenging of volcanic aerosol by ash: Atmospheric and volcanologic implications. Geology 5, 621–624. https://doi.org/10.1130/0091-7613(1977)5¡621:SOVABA¿2.0.CO;2.

Rose, W.I., Chuan, R.L., Cadle, R.D., Woods, D.C., 1980. Small Particles in Volcanic Eruption Clouds. Am. J. Sci. 280, 671–696. https://doi.org/10.2475/ajs.280.8.671.

Rose, W.I., Riley, C.M., Dartevelle, S., 2003. Sizes and Shapes of 10-Ma Distal Fall Pyroclasts in the Ogallala Group, Nebraska. J. Geol. 111, 115–124. https://doi.org/10.1086/344668.

Roush, T., Pollack, J., Orenberg, J., 1991. Derivation of Midinfrared (5–25 $\mu$m) Optical Constants of Some Silicates and Palagonite. Icarus 94, 191–208. https://doi.org/10.1016/0019-1035(91)90150-R.

Schmetz, J., Pili, P., Tjemkes, S., Just, D., Kerkmann, J., Rota, S., Ratier, A., 2002a. An introduction to Meteosat Second Generation (MSG). Bull. Am. Meteorol. Soc. 83, 977–992. https://doi.org/10.1175/1520-0477(2002)083¡0977:AITMSG¿2.3.CO;2.

Schmetz, J., Pili, P., Tjemkes, S., Just, D., Kerkmann, J., Rota, S., Ratier, A., 2002b. Radiometric performance of SEVIRI. Bull. Am. Meteorol. Soc. 83, ES50–ES51. https://doi.org/10.1175/BAMS-83-7-Schmetz-1.

Schmit, T.J., Gunshor, M.M., Menzel, W.P., Gurka, J.J., Li, J., Bachmeier, A.S., 2005. Introducing the Next-Generation Advanced Baseline Imager on GOES-R. Bull. Am. Meteorol. Soc. 86, 1079–1096. https://doi.org/10.1175/BAMS-86-8-1079.

Schumann, U., Weinzierl, B., Reitebuch, O., Schlager, H., Minikin, A., Forster, C., Baumann, R., Sailer, T., Graf, K., Mannstein, H., Voigt, C., Rahm, S., Simmet, R., Scheibe, M., Lichtenstern, M., Stock, P., Rüba, H., Schäuble, D., Tafferner, A., Rautenhaus, M., Gerz, T., Ziereis, H., Krautstrunk, M., Mallaun, C., Gayet, J.F., Lieke, K., Kandler, K., Ebert, M., Weinbruch, S., Stohl, A., Gasteiger, J., Groß, S., Freudenthaler, V., Wiegner, M., Ansmann, A., Tesche, M., Olafsson, H., Sturm, K., 2011. Airborne observations of the Eyjafjalla volcano ash cloud over Europe during air space closure in April and May 2010. Atmos. Chem. Phys. 11, 2245–2279. https://doi.org/10.5194/acp-11-2245-2011.

Sen, G., 2014. Petrology: Principles and Practice. 1st ed. Springer-Verlag, Berlin Heidelberg.

Shcherbakov, V., Jourdan, O., Voigt, C., Gayet, J.F., Chauvigne, A., Schwarzenboeck, A., Minikin, A., Klingebiel, M., Weigel, R., Borrmann, S., Jurkat, T., Kaufmann, S., Schlage, R., Gourbeyre, C., Febvre, G., Lapyonok, T., Frey, W., Molleker, S., Weinzierl, B., 2016. Porous aerosol in degassing plumes of Mt. Etna and Mt. Stromboli. Atmos. Chem. Phys. 16, 11883–11897. https://doi.org/10.5194/acp-16-11883-2016.

Shipley, S., Sarna-Wojcicki, A.M., 1982. Distribution, thickness, and mass of late pleistocene and holocene tephra from major volcanoes in the northwestern United States: a preliminary assessment of hazards from volcanic ejecta to nuclear reactors in the Pacific northwest. U.S. Geol. Surv. Misc. Field Stud. Map MF-1435.

Sokolik, I.N., Toon, O.B., 1999. Incorporation of mineralogical composition into models of the radiative properties of mineral aerosol from UV to IR wavelengths. J. Geophys. Res. Atmos. 104, 9423–9444. https://doi.org/10.1029/1998JD200048.

Sparks, R., 1978. The dynamics of bubble formation and growth in magmas: A review and analysis. J. Volcanol. Geotherm. Res. 3, 1–37. https://doi.org/10.1016/0377-0273(78)90002-1.

Spitzer, W.G., Kleinman, D.A., 1961. Infrared Lattice Bands of Quartz. Phys. Rev. 121, 1324–1335. https://doi.org/10.1103/PhysRev.121.1324.

Stevenson, J.A., Millington, S.C., Beckett, F.M., Swindles, G.T., Thordarson, T., 2015. Big grains go far: understanding the discrepancy between tephrochronology and satellite infrared measurements of volcanic ash. Atmos. Meas. Tech. 8, 2069–2091. https://doi.org/10.5194/amt-8-2069-2015.

Stohl, A., Prata, A.J., Eckhardt, S., Clarisse, L., Durant, A., Henne, S., Kristiansen, N.I., Minikin, A., Schumann, U., Seibert, P., Stebel, K., Thomas, H.E., Thorsteinsson, T., Tørseth, K., Weinzierl, B., 2011. Determination of time- and height-resolved volcanic ash emissions and their use for quantitative ash dispersion modeling: the 2010 Eyjafjallajökull eruption. Atmos. Chem. Phys. 11, 4333–4351. https://doi.org/10.5194/acp-11-4333-2011.

Vedder, W., 1964. Correlations between infrared spectrum and chemical composition of mica. Am. Mineral. 49, 736–768.

Vogel, A., Diplas, S., Durant, A.J., Azar, A.S., Sunding, M.F., Rose, W.I., Sytchkova, A., Bonadonna, C., Krüger, K., Stohl, A., 2017. Reference data set of volcanic ash physicochemical and optical properties. J. Geophys. Res. Atmos. 122, 9485–9514. https://doi.org/10.1002/2016JD026328.

Volz, F.E., 1973. Infrared Optical Constants of Ammonium Sulfate, Sahara Dust, Volcanic Pumice, and Flyash. Appl. Opt. 12, 564–568. https://doi.org/10.1364/AO.12.000564.

Wakaki, M., Kudo, K., Shibuya, T., 2007. Physical Properties and Data of Optical Materials. 1st ed. CRC Press, Boca Raton.

Watkin, S.C., 2003. The application of AVHRR data for the detection of volcanic ash in a Volcanic Ash Advisory Centre. Meteorol. Appl. 10, 301–311. https://doi.org/10.1017/S1350482703001063.

Watson, I., Realmuto, V., Rose, W., Prata, A., Bluth, G., Gu, Y., Bader, C., Yu, T., 2004. Thermal infrared remote sensing of volcanic emissions using the moderate resolution imaging spectroradiometer. J. Volcanol. Geotherm. Res. 135, 75–89. https://doi.org/10.1016/j.jvolgeores.2003.12.017.

Wen, S., Rose, W.I., 1994. Retrieval of sizes and total masses of particles in volcanic clouds using AVHRR bands 4 and 5. J. Geophys. Res. Atmos. 99, 5421–5431. https://doi.org/10.1029/93JD03340.

Western, L.M., Watson, M.I., Francis, P.N., 2015. Uncertainty in two-channel infrared remote sensing retrievals of a well-characterised volcanic ash cloud. Bull. Volcanol. 77, 67. https://doi.org/10.1007/s00445-015-0950-y.

Wilson, T.M., Stewart, C., Sword-Daniels, V., Leonard, G.S., Johnston, D.M., Cole, J.W., Wardman, J., Wilson, G., Barnard, S.T., 2012. Volcanic ash impacts on critical infrastructure. Phys. Chem. Earth 45-46, 5–23. https://doi.org/10.1016/j.pce.2011.06.006.

Wohletz, K.H., Sheridan, M.F., Brown, W.K., 1989. Particle Size Distributions and the Sequential Fragmentation/Transport Theory Applied to Volcanic Ash. J. Geophys. Res. Solid Earth 94, 15703–15721. https://doi.org/10.1029/JB094iB11p15703.

Ye, C., Rucks, M.J., Arnold, J.A., Glotch, T.D., 2019. Mid-Infrared Optical Constants of Labradorite, a Triclinic Plagioclase Mineral. Earth Space Sci. 6, 2410–2422. https://doi.org/10.1029/2019EA000915.

Yu, T., Rose, W.I., Prata, A.J., 2002. Atmospheric correction for satellite-based volcanic ash mapping and retrievals using "split window" IR data from GOES and AVHRR. J. Geophys. Res. Atmos. 107. https://doi.org/10.1029/2001JD000706 AAC 10–1–AAC 10–19.

Zhou, D.K., Larar, A.M., Liu, X., 2013. MetOp-A/IASI Observed Continental Thermal IR Emissivity Variations. IEEE J. Sel. Top. Appl. Earth Obs. Remote Sens. 6, 1156–1162.

## 3.2 P2: Development of the new volcanic ash retrieval VACOS

### The New Volcanic Ash Satellite Retrieval VACOS Using MSG/SEVIRI and Artificial Neural Networks: 1. Development

**Dennis Piontek**, Luca Bugliaro, Marius Schmidl, Daniel K. Zhou, Christiane Voigt
Remote Sensing 2021, 13, 3112.

**Overview** This paper describes the development of the new volcanic ash retrieval VACOS using thermal satellite measurements of the passive imager MSG/SEVIRI and applying artificial neural networks. For the last, a training data set of synthetic observations is created by composing one-dimensional atmospheric gas, cloud and temperature profiles and performing radiative transfer simulations for them with and without a single homogeneous volcanic ash layer. The ash-free simulations are compared to real measurements, showing a reasonable overall agreement but some deviations for cloudy cases and for land surfaces. The former can be explained by inaccuracies in the cloud properties or differences in the cloudiness introduced also by a random element in the method; the latter might be caused by inaccuracies in the ECMWF skin temperatures as already reported elsewhere. Using this data set, different artificial neural networks are trained for the retrieval of a pixel classification, the optical depth at 10.8 µm due to volcanic ash, the top height and the effective particle radius of an ash cloud.

**Author contribution** I conceptualized the algorithm development with LB. MS wrote the original software RTSIM to compile vertical atmospheric profiles based on various input data sets and to perform radiative transfer calculations using libRadtran. MS prepared the input data on nitrogen dioxide. DZ provided data on surface emissivities. I collected atmospheric data from ECMWF, prepared the volcanic ash optical properties, adapted RTSIM for the input data and introduced the dependency of the sea surface emissivity on wind speed and viewing zenith angle. I applied RTSIM to calculate the training data, validated the ash-free simulations, investigated the gas absorption parameterization, trained the artificial neural networks, developed the software VACOS, prepared all figures and wrote the manuscript. LB and CV supervised the research. All authors reviewed manuscript drafts.

remote sensing

MDPI

Article

# The New Volcanic Ash Satellite Retrieval VACOS Using MSG/SEVIRI and Artificial Neural Networks: 1. Development

**Dennis Piontek [1,*], Luca Bugliaro [1], Marius Schmidl [1,†], Daniel K. Zhou [2] and Christiane Voigt [1,3]**

[1] Deutsches Zentrum für Luft- und Raumfahrt (DLR), Institut für Physik der Atmosphäre, 82234 Weßling-Oberpfaffenhofen, Germany; luca.bugliaro@dlr.de (L.B.); marius.schmidl@mtu.de (M.S.); christiane.voigt@dlr.de (C.V.)
[2] NASA Langley Research Center, Hampton, VA 23681, USA; daniel.k.zhou@nasa.gov
[3] Institut für Physik der Atmosphäre, Johannes Gutenberg-Universität Mainz, 55099 Mainz, Germany
* Correspondence: dennis.piontek@dlr.de
† Current address: MTU Aero Engines AG, 80995 Munich, Germany.

**Abstract:** Volcanic ash clouds are a threat to air traffic security and, thus, can have significant societal and financial impact. Therefore, the detection and monitoring of volcanic ash clouds to enhance the safety of air traffic is of central importance. This work presents the development of the new retrieval algorithm VACOS (*Volcanic Ash Cloud properties Obtained from SEVIRI*) which is based on artificial neural networks, the thermal channels of the geostationary sensor MSG/SEVIRI and auxiliary data from a numerical weather prediction model. It derives a pixel classification as well as cloud top height, effective particle radius and, indirectly, the mass column concentration of volcanic ash clouds during day and night. A large set of realistic one-dimensional radiative transfer calculations for typical atmospheric conditions with and without generic volcanic ash clouds is performed to create the training dataset. The atmospheric states are derived from ECMWF data to cover the typical diurnal, annual and interannual variability. The dependence of the surface emissivity on surface type and viewing zenith angle is considered. An extensive dataset of volcanic ash optical properties is used, derived for a wide range of microphysical properties and refractive indices of various petrological compositions, including different silica contents and glass-to-crystal ratios; this constitutes a major innovation of this retrieval. The resulting ash-free radiative transfer calculations at a specific time compare well with corresponding SEVIRI measurements, considering the individual pixel deviations as well as the overall brightness temperature distributions. Atmospheric gas profiles and sea surface emissivities are reproduced with a high agreement, whereas cloudy cases can show large deviations on a single pixel basis (with 95th percentiles of the absolute deviations >30 K), mostly due to different cloud properties in model and reality. Land surfaces lead to large deviations for both the single pixel comparison (with median absolute deviations >3 K) and more importantly the brightness temperature distributions, most likely due to imprecise skin temperatures. The new method enables volcanic ash-related scientific investigations as well as aviation security-related applications.

**Keywords:** volcanic ash cloud; passive satellite remote sensing; artificial neural network; radiative transfer calculation

check for updates

**Citation:** Piontek, D.; Bugliaro, L.; Schmidl, M.; Zhou, D.K.; Voigt, C. The New Volcanic Ash Satellite Retrieval VACOS Using MSG/SEVIRI and Artificial Neural Networks: 1. Development. *Remote Sens.* **2021**, *13*, 3112. https://doi.org/10.3390/rs13163112

Academic Editor: Carmine Serio

Received: 2 July 2021
Accepted: 3 August 2021
Published: 6 August 2021

**Publisher's Note:** MDPI stays neutral with regard to jurisdictional claims in published maps and institutional affiliations.

**Copyright:** © 2021 by the authors. Licensee MDPI, Basel, Switzerland. This article is an open access article distributed under the terms and conditions of the Creative Commons Attribution (CC BY) license (https://creativecommons.org/licenses/by/4.0/).

## 1. Introduction

Large, explosive volcanic eruptions might happen relatively infrequently [1], but their emissions can have massive impacts: volcanic ash can significantly interfere with critical, ground-based infrastructure [2] and can damage aircraft or even cause engine failure [3]. Aviation incidents have been reported more than 1000 km from the volcanic ash source [4], as potentially hazardous ash concentrations might not be visually observable by flight crews [5]. In the case of the eruption of Eyjafjallajökull in 2010, major parts of the European airspace were closed for extended periods of time [6], leading to estimated economic losses of US$1.7 billion for the aviation industry [7].

To mitigate the impact of future eruptions, satellite remote-sensing methods have been developed to monitor volcanic ash clouds, using both polar orbiting and geostationary passive optical imagers (e.g., [8]). Their results can be used to directly assess whether an airspace is safe to be traversed by jet planes (according to thresholds stated by the *International Civil Aviation Organization* (ICAO) [9]), to investigate aerosol–cloud interactions [10] or to calibrate/validate volcanic ash transport and dispersion models as applied by the *Volcanic Ash Advisory Centers* [11–13]. The latter are the main providers of information on atmospheric contamination by volcanic ash in the case of an eruption [9].

Active remote sensing instruments such as lidars provide highly resolved vertical profiles of the aerosol load [14]. However, lidars have a limited spatial and temporal coverage, e.g., the instrument aboard the polar orbiting *Cloud-Aerosol Lidar and Infrared Pathfinder Satellite Observations* (CALIPSO) has a small footprint of 90 m × 335 m and a 16-day repeat cycle [15]. Ground instruments are fixed and airborne measurements are performed only in exceptions (e.g., [6,16–21]). Therefore, none of those instruments is able to provide global data as are necessary in the case of volcanic ash monitoring. In this respect, geostationary radiometers, especially of the second generation, come in handy: such instruments not only provide near-global coverage, but their infrared channels also allow operation during day and night. Examples are the *Geostationary Operational Environmental Satellites* (GOES) covering North and South America, the *Meteosat Second Generation* (MSG) satellites for Europe and Africa and *Himawari* for Eastern Asia and Australia.

The difference between the brightness temperature at 11 µm ($BT_{11}$) and 12 µm ($BT_{12}$), in short $BTD_{11-12}$, can be negative for clouds consisting of small volcanic ash particles (smaller than ~5 µm [22,23]) and mixtures of volcanic ash and sulfuric acid ($H_2SO_4$ [24,25]), whereas for ice clouds $BTD_{11-12}$ tends to be positive [26]. Therefore, this quantity is often used for volcanic ash detection. However, volcanic ash can be hidden by water or ice either within the volcanic ash cloud or as separated clouds, as well as water vapor, especially if the ash cloud itself is at low altitude [11,27]. Furthermore, large ash particles or opaque plumes do not lead to a negative $BTD_{11-12}$ [11,22]. False alarms might be produced by mineral dust aerosol [28], which has similar spectral properties as volcanic ash [11,29,30], or by non-vegetated, quartz-rich surfaces due to their emissivity [11,28].

As a consequence, more sophisticated detection schemes have been proposed: to correct for the presence of water vapor, a $BTD_{11-12}$ threshold depending on $BT_{11}$ has been suggested where the exact function depends on the atmospheric conditions [27]; this resulted in retrievals of larger contaminated areas. Multiple threshold tests were proposed, incorporating, for instance, also $BT_{8.7}$ measurements (e.g., [31,32]) or simulated clear-sky brightness temperatures $BT_{11}$ and $BT_{12}$ from numerical weather predictions (e.g., [31]). Furthermore, it was shown that reflectances in the visible and the near-infrared as well as their ratio can further help to separate volcanic ash clouds from water and ice clouds, especially for optically thick plumes for which $BTD_{11-12}$ tends to vanish (e.g., [33–35]).

As radiance measurements are affected not only by the volcanic ash cloud but also by the atmospheric state, other meteorological clouds and the surface properties, it was suggested to derive quantities that are closer linked to the target cloud's properties. An example is the ratio of effective absorption optical depths at different wavelengths, called $\beta$ ratio, which can be approximately expressed by single scattering properties (e.g., [8,36,37]). For the calculation of $\beta$ ratios, clear sky properties have to be determined by radiative transfer calculations. The combination of multiple $\beta$ ratios of different infrared channels is a good discriminator of volcanic and meteorological clouds [37]. A high spectral resolution can allow for new detection schemes, either directly based on the functional behavior of the brightness temperature spectra, thereby also enabling the separation of volcanic ash from mineral dust (e.g., [29,30]), or by performing singular vector decompositions with some vectors representing clear sky conditions, whereas others describe the volcanic ash influence. A linear decomposition of a measurement with respect to these basis vectors then reveals whether volcanic ash is present or not [38]. An alternative approach is to detect sulfur dioxide ($SO_2$) as a proxy for volcanic ash as both are often emitted

simultaneously [39]. Although both detections can show reasonable spatial agreement, they might differ in some cases [40], sometimes with more than 80% of the volcanic ash remaining undetected [41]. This might be rooted in the presence of distinct volcanic ash and $SO_2$ layers that get separated due to vertical wind shear [42].

To retrieve microphysical (especially the effective particle radius $r_{\mathrm{eff}}$) and macrophysical properties (optical depth $\tau$ and mass column concentration $m_{\mathrm{col}}$), brightness temperatures (usually $BT_{11}$ and $BTD_{11-12}$ or similar) have been precalculated for generic atmospheric settings including only a volcanic ash layer and used as look-up tables (e.g., [22,33,43]). More complex atmospheres were assumed to correct for water vapor, based on either measurements of the surrounding of the volcanic ash clouds or radiative transfer calculations (e.g., [27,43]). The optimal estimation method aims to minimize a cost function (here principally an uncertainty weighted difference between an atmospheric state vector and an a priori assumption, as well as an observation vector and corresponding estimates), usually iteratively for non-linear problems, incorporating radiative transfer calculations [37,44]. For example, Francis et al. [31] applied this approach to retrieve pixelwise the ash layer pressure, mass loading $m_{\mathrm{col}}$ and effective radius $r_{\mathrm{eff}}$ based on observations at 10.8 µm, 12 µm and 13.4 µm, whereas Pavolonis et al. [37] used the same observations to determine different $\beta$ ratios, emissivities and temperatures, later on converting these to microphysical properties. Retrievals can also be performed by making use of the surrounding ash-free area; e.g., Pugnaghi et al. [45] interpolated the radiances across a volcanic ash plume between the edges to obtain an ash-free image. Combining the radiances measured with and without ash, the transmittance of the ash plume could be calculated for different wavelengths. Finally, the effective radius $r_{\mathrm{eff}}$ and the optical depth $\tau$ were determined from the transmittances using conversions from radiative transfer calculations. There are further methods to determine the volcanic ash cloud top height $z_{\mathrm{top}}$. The brightness temperature of opaque parts of a cloud can be assumed to approximately correspond to the ambient temperature. A nearby temperature profile (e.g., using a numerical weather prediction or a radiosonde measurement) can be applied to convert the brightness temperature into an altitude [33,43,46]. During daytime, the difference in the cloud position as seen by the satellite and the sun induced cloud shadow can be used to geometrically calculate $z_{\mathrm{top}}$ [33,43]. Stereoscopic instruments allow inferring $z_{\mathrm{top}}$ from the spatial shift between the projection of a cloud in images retrieved under different viewing angles [33,38,43,47]. The carbon dioxide ($CO_2$) slicing method compares multiple channels around the $CO_2$ absorption feature which have weighting functions peaking at different heights [48,49].

A different approach is the application of artificial neural networks (ANNs), which can be considered as universal approximators for unknown functions [50]. Based on initial research in the 1940s, this method has gained much attention and has significantly advanced in recent decades [51]. It has been used for prediction, functional approximation and classification tasks for numerous problems of atmospheric sciences [52]. With respect to satellite remote sensing, some examples are the retrieval of properties of water clouds [53,54], ice clouds [55,56], ozone profiles [57], volcanic $SO_2$ [58–60] and surface reflectivity [61]. Often, the utilized training datasets either consist of collocated measurements of different instruments [54–56] or are created using radiative transfer calculations [53,57,59–61]. One of the major advantages of ANNs is that, once they are trained, they are fast in application compared to other methods using time-consuming radiative transfer calculations during the retrieval. Gray and Bennartz [62] trained two ANNs for the detection of volcanic ash and $SO_2$-rich ash, respectively, using *Moderate Resolution Imaging Spectroradiometer* (MODIS, e.g., [63]) measurements. The training data were composed of MODIS images of different volcanic eruptions with the target classification performed based on *Hybrid Single Particle Lagrangian Integrated Trajectory* (HYSPLIT) simulations of the volcanic emissions. The input data consisted of brightness temperature (differences) of channels between 7.3 µm and 12 µm. Picchiani et al. [64] trained separated ANNs for volcanic ash detection and ash mass loading $m_{\mathrm{col}}$ retrieval from MODIS measurements. The training data consisted of MODIS images from Etna eruptions with the target classification performed by applying

the $BTD_{11-12} < 0$ criterion, whereas the target mass loading was determined by a look-up table approach. The channels centered at 7.3 µm, 11 µm and 12 µm were used as input. A more detailed classification ANN was trained by Picchiani et al. [65], labeling ash above sea and above meteorological clouds, meteorological clouds themselves and sea, ice and land surfaces using MODIS data. The training data consisted of MODIS images from the Eyjafjallajökull 2010 and Grimsvötn 2011 eruptions with the target classes derived from the $BTD_{11-12} < 0$ criterion, the MODIS land/sea mask, cloud products and $BT_{2.13}$ (band 7) for detection of ice surfaces. The input features include 14 MODIS channels in the visible and infrared and a land/sea mask. The method was further developed by Piscini et al. [66], training individual ANNs for the retrieval of the mass load $m_{\mathrm{col}}$, the effective radius $r_{\mathrm{eff}}$, the optical depth at 11 µm ($\tau_{11}$) and the $SO_2$ column concentration using MODIS observations. Training data were MODIS images from the Eyjafjallajökull 2010 eruption with the target values determined by other retrievals based on radiative transfer calculations, similar to [64]. Initially, all MODIS channels were used as input features, with a pruning procedure performed after the training to find the most important inputs. The ANN ansatz by Picchiani et al. [64] and Piscini et al. [66] was compared to the look-up table and the volcanic plume removal procedure, finding that the look-up table method can be more accurate, but the ANN approach can be less sensitive to perturbations in the satellite measurements [67]. Zhu et al. [68] developed a method to retrieve volcanic cloud top heights $z_{\mathrm{top}}$ combining a stacked denoising autoencoder for feature extraction followed by a least squares support vector regression to derive $z_{\mathrm{top}}$. The training data consisted of collocated *Spinning Enhanced Visible and Infrared Imager* (SEVIRI, aboard MSG [69]) brightness temperatures and *Cloud-Aerosol Lidar with Orthogonal Polarization* (CALIOP, aboard CALIPSO [15]) derived $z_{\mathrm{top}}$ for volcanic ash clouds from the Eyjafjallajökull 2010 and Puyehue-Cordón Caulle 2011 eruptions. Adding vertical temperature profiles from *European Centre for Medium-Range Weather Forecasts* (ECMWF) simulations further improved the retrieval performance.

The aforementioned volcanic ash algorithms used real satellite images as training data, with target values coming either from other retrievals, other sensors or trajectory models. In contrast, the algorithm *Volcanic Ash Detection Utilizing Geostationary Satellites* (VADUGS), applying a single ANN for the retrieval of $m_{\mathrm{col}}$ and $z_{\mathrm{top}}$, was based on a fully simulated training dataset. The input data consisted of the thermal infrared channels of MSG/SEVIRI and auxiliary data such as a land/sea mask, the skin temperature and the viewing zenith angle [70,71]. The ANN architecture followed the development of the cirrus cloud retrieval *Cirrus Optical Properties derived from CALIOP and SEVIRI Algorithm during Day and Night* (COCS, [55]), which was trained with collocated CALIOP and SEVIRI measurements to retrieve cirrus optical depths and cloud top heights. Since 2015, VADUGS runs operationally at the German weather service [72]. Although it produces reasonable results upon visual inspection, a validation against simulated samples has shown that the retrievals are reliable in certain subsets of the test dataset, but not in general [71]. An intercomparison of satellite products exhibited overall low correlations between the retrieval of $m_{\mathrm{col}}$ by VADUGS and other algorithms and found a strong underestimation of $z_{\mathrm{top}}$ when compared with CALIOP results [73]. In addition, note that VADUGS was developed focusing on the Eyjafjallajökull 2010 eruption as only the refractive index of the corresponding volcanic ash was used for the training data [71]. However, the refractive index can vary significantly for different volcanic ashes [74,75] and retrievals are sensitive to it [22,76,77]. Technically, potential improvements can be derived from the development of *Cirrus Properties from SEVIRI* (CiPS [78,79]), which is the successor of COCS. It is based on a similar training dataset but uses a new ANN architecture and training procedure, additional input features and updated CALIOP data. CiPS exhibited a better performance compared to COCS and retrieved additional quantities, e.g., the ice water path.

Building upon VADUGS, a new algorithm called *Volcanic Ash Cloud properties Obtained from SEVIRI* (VACOS) is developed and described in two papers (Figure 1). In Part 1 (this paper), a training dataset consisting of simulated MSG/SEVIRI measurements is created using modeled atmospheric profiles and a climatology of the surface emissivity.

A parameterization of the sea surface emissivity is applied that depends on the viewing zenith angle and wind speed. To cover the variability of volcanic ash clouds, the extensive set of volcanic ash refractive indices and optical properties from Piontek et al. [23] is used together with a wide range of possible ash cloud top heights, geometrical thicknesses and mass concentrations. This constitutes a major advantage compared to the previously mentioned ANN-based volcanic ash retrievals, which were trained on satellite images of only one [64,66], two [65,68] or seven [62] volcanic eruptions or used only a single volcanic ash type [71]. Methodologically, we train four separated ANNs for the classification and the retrieval of the optical depth at 10.8 µm ($\tau_{10.8}$), ash cloud top height ($z_{top}$) and effective particle radius ($r_{eff}$) of the volcanic ash clouds. The ANNs have individual input features and training datasets. Part 2 [80] contains a validation of the retrievals with respect to simulated test datasets, a sensitivity study of the algorithms with respect to the vertical mass profile of volcanic ash layers, case studies comparing the results of the new retrievals with independent lidar and in situ measurements as well as model results and an analysis of the working principles of the ANNs.

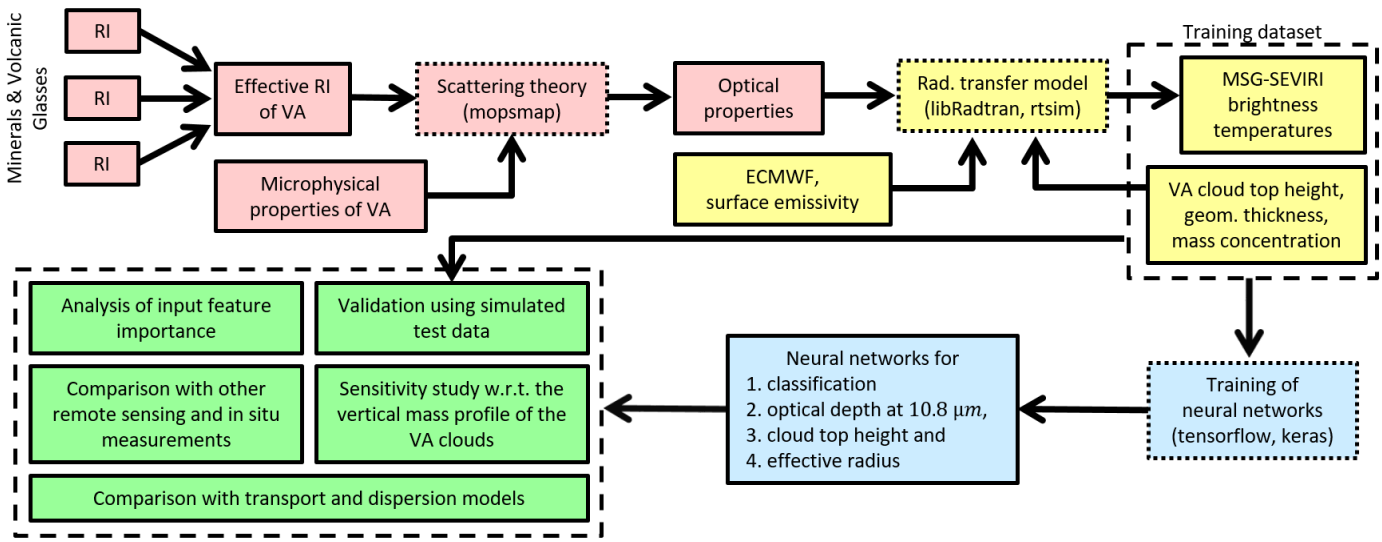


**Figure 1.** Scheme of the algorithm development and validation: (red) calculation of typical refractive indices (RIs) of volcanic ashes (VAs) and the corresponding optical properties [23], (yellow) radiative transfer calculations to compose a training dataset and (blue) training of different ANNs (both in this paper) and (green) validation against simulated test data and other independent measurements and model results [80].

The rest of this paper is organized as follows. We introduce the observation instrument MSG/SEVIRI (Section 2) and the predecessor retrieval VADUGS, including a short, general description of ANNs (Section 3). Next, the training dataset is sketched including its analysis (Section 4), followed by the description of the new ANNs, their input features and their training (Section 5) as well as their application (Section 6). Finally, we give a conclusion and an outlook (Section 7).

## 2. MSG/SEVIRI

VACOS is tailored for the *Spinning Enhanced Visible and Infrared Imager* (SEVIRI) carried by the geostationary *Meteosat Second Generation* (MSG) satellites. SEVIRI is a passive 12-channel imager, measuring radiation in the visible and infrared part of the spectrum. The radiances in the different thermal channels are converted to brightness temperatures ($BT$). For the retrieval, we consider only the seven infrared channels such that it can be applied during day and night. Three of them are window channels (centered at 8.7 µm, 10.8 µm and 12 µm), two are strongly sensitive to water vapor ($H_2O$, 6.2 µm and 7.3 µm) and another two (9.7 µm and 13.4 µm) to ozone ($O_3$) and carbon dioxide ($CO_2$), respectively. The temporal resolution of SEVIRI is 15 min for the full disc and 5 min in rapid scan mode,

which covers mainly Europe. The spatial resolution is 3 km at nadir. The channels are rather broad (spectral bands up to 2 µm) and instrument specific [69]. Figure 2 shows a red-green-blue composite of the SEVIRI disc. There are multiple MSG satellites deployed at different coordinates. In the following, we focus on Meteosat-9/MSG2. From 11 April 2007 to 21 January 2013, it was located at 0°E as the primary operational satellite and covered the prominent eruptions of Eyjafjallajökull 2010, Grimsvötn 2011 and the volcanic ash clouds of Puyehue-Cordón Caulle 2011. From 9 April 2013 to 20 March 2018, it provided the rapid scanning service at 9.5°E. As of 29 June 2020, it is located at 3.5°E as a back-up spacecraft [81,82]. Note that other current or future imagers aboard geostationary satellites have similar spectral channels, e.g., the *Advanced Baseline Imager* on GOES-R, the *Advanced Himawari Imager* on Himawari-8/9, the *Advanced Meteorological Imager* on GEO-KOMPSAT-2A, the *Advanced Geosynchronous Radiation Imager* on Fengyun-4A or the *Flexible Combined Imager* on the Meteosat Third Generation satellites [83–86]. Thus, the method described here can in principle be extended to those as well.

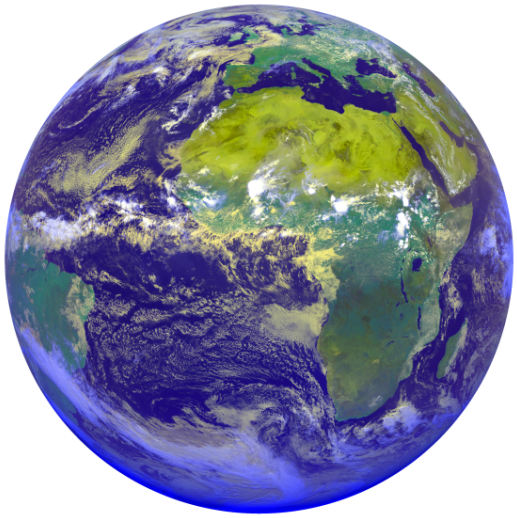

**Figure 2.** Overview red-green-blue composite of MSG/SEVIRI measurements for 15 July 2015 at 12:00 UTC.

## 3. VADUGS

The algorithm VADUGS (*Volcanic Ash Detection Utilizing Geostationary Satellites*) allows pixelwise retrieval of volcanic ash cloud properties using SEVIRI measurements and ANNs [71]. ANNs have been developed based on biological insights on the behavior of the human brain. The feed-forward configuration is made up of multiple layers, with the first one (called input layer) consisting of the input features, and the last one the output layer. In between is an arbitrary number of so-called hidden layers. Hidden and output layers consist of so-called neurons. Those are (usually non-linear) functions receiving the weighted sum of the results of the previous layer's neurons (or input features in the case of the first hidden layer) as an argument. The weights between all pairs of neurons of successive layers are different. They are chosen such that the $n$ input features are (approximately) mapped to the corresponding $m$ target values; thus, an ANN is a function mapping $\mathbb{R}^n \to \mathbb{R}^m$. Using the backpropagation algorithm, the weights are determined in an iterative procedure (called training) by changing their values such that the loss function (a metric quantifying the difference between the output of the ANN for a set of input data samples and the associated target outputs) is minimized. Thus, a training dataset is needed for which the target values are known for all samples. The loss function evaluated on a separate validation dataset is monitored during training to prevent overfitting, i.e., to avoid learning the noise of the training dataset [51,52,87].

VADUGS is a single ANN with one hidden layer with 600 neurons. The input data consist of the infrared brightness temperatures measured by SEVIRI, the skin temperature

from ECMWF and a land/sea mask and the viewing zenith angle. The output layer gives $m_{\mathrm{col}}$ and $z_{\mathrm{top}}$. Radiative transfer simulations were performed to calculate the brightness temperatures for generic atmospheric settings, leading to a dataset of properly tagged samples used for the training. For the simulations, realistic atmospheric conditions were chosen based on ECMWF reanalysis data; to cover seasonal variations, 12 UTC of the 15th day for the months February 2010 to January 2011 was considered. Meteorological cloud layers were incorporated based on the layer-resolved cloud fractions given by ECMWF and parameterized as either liquid or ice water cloud (see also Section 4.1.2). Single homogeneous volcanic ash layers were simulated using the complex refractive index of ash from the Eyjafjallajökull eruption 2010, spherical and spheroidal particle shapes and two different lognormal particle size distributions [71].

## 4. Training Dataset

This section covers the creation of the new training dataset, including a description of the input data of the radiative transfer calculations (Section 4.1) and the calculations themselves (Section 4.2), a validation of the ash-free case (Section 4.3) and the selection of training, validation and test subsets (Section 4.4).

### *4.1. Input Data*

In the following, we describe different input data for the radiative transfer calculations, their variability and the settings. More specifically, we discuss the surface emissivity (Section 4.1.1), the vertical profiles of atmospheric clouds and gases (Section 4.1.2) and the volcanic ash clouds (Section 4.1.3).

#### 4.1.1. Surface Emissivity

For the surface emissivity, we use data from Zhou et al. [88–90]. Those were calculated using measurements of the polar-orbiting IASI instrument over ten years (2007-06 to 2017-05), covering the full globe. The emissivities were averaged over the ten years and for each month. The final spatial resolution is 0.25° and the spectral resolution is 0.25 $\mathrm{cm}^{-1}$ for 645 to 2760 $\mathrm{cm}^{-1}$ (roughly the wavelength range 3.6 to 15.5 µm). For sea surfaces, the emissivity exhibits also a strong dependence on the viewing zenith angle $\theta_{\mathrm{vza}}$ and the wind speed $w_{\mathrm{ws}}$: an increase of $\theta_{\mathrm{vza}}$ reduces the emissivity, whereas an increase of $w_{\mathrm{ws}}$ reduces the emissivity at small $\theta_{\mathrm{vza}}$ but increases it at large $\theta_{\mathrm{vza}}$ [91–93]. The impact can be on the order of 10%. Here, $\theta_{\mathrm{vza}}$ is determined from the geographic coordinates for MSG2, whereas the wind speed $w_{\mathrm{ws}} = \sqrt{U^2 + V^2}$ is based on the horizontal wind speeds at 10 m above the surface, $U$ and $V$, as given by ECMWF (Section 4.1.2). We use the calculations by Masuda [94] which incorporate the surface-emitted surface-reflected radiation into the sea surface emissivity for different wavelengths $\lambda$ (3.7 µm, 11 µm and 12 µm), $\theta_{\mathrm{vza}}$ (0 to 85°) and $w_{\mathrm{ws}}$ (0 to 15 $\mathrm{m\,s}^{-1}$). We divide the calculated emissivities by the value for $\theta_{\mathrm{vza}} = w_{\mathrm{ws}} = 0$. Then, for each wavelength, a function of the form

$$f(\theta_{\mathrm{vza}}, w_{\mathrm{ws}}; \lambda) = g(\theta_{\mathrm{vza}}; \lambda) \cdot h(\theta_{\mathrm{vza}}, w_{\mathrm{ws}}; \lambda) \quad (1)$$

is fitted, with $f$ describing the reduction of the emissivity relative to the case $\theta_{\mathrm{vza}} = w_{\mathrm{ws}} = 0$ at $\lambda$ and $g$ and $h$ being polynomials of sixth degree. $g$ describes mainly the dependence on $\theta_{\mathrm{vza}}$, $h$ is the correction due to $w_{\mathrm{ws}}$ and $f$ is interpolated among the three wavelengths and constantly extrapolated beyond. For sea surfaces, the IASI-measured emissivities are multiplied by $f$ as the data of Zhou et al. [88–90] do not include the dependence on $\theta_{\mathrm{vza}}$ and $w_{\mathrm{ws}}$ explicitly. Note that Masuda [94] considered $w_{\mathrm{ws}}$ at a height of 12.5 m. However, the difference to $w_{\mathrm{ws}}$ derived from ECMWF ERA5 data is assumed to be negligible. During application, $\theta_{\mathrm{vza}} > 85°$ and $w_{\mathrm{ws}} > 15\,\mathrm{m\,s}^{-1}$ are set to these limiting values.

Similar to water, the emissivity of land surfaces decreases with increasing $\theta_{\mathrm{vza}}$. However, the relations depend strongly on the soil type and the wavelength, and the results vary between different experiments. For instance, significant decreases of the emissivity

have been observed for sand: Labed and Stoll [95] found changes of ~6% for wavelengths of 10.6 µm and 12 µm between $\theta_{\mathrm{vza}} = 0°$ and 80°; Snyder et al. [96] reported differences up to ~4% for 8 to 10 µm and ~2% for 10 to 14 µm between $\theta_{\mathrm{vza}} = 10°$ and 53°; Sobrino and Cuenca [97] measured decreases of ~3% between $\theta_{\mathrm{vza}} = 0°$ and 65° for a spectral band at 8 to 14 µm; Cuenca and Sobrino [98] found a reduction of ~5.8% between $\theta_{\mathrm{vza}} = 0°$ and 60° for a channel covering 8.2 to 9.2 µm; McAtee et al. [99] indicated a decrease by up to ~8% comparing $\theta_{\mathrm{vza}} = 0°$ to 70° for the spectral range of 8 to 12 µm; García-Santos et al. [100] got a difference larger than 10% between $\theta_{\mathrm{vza}} = 0°$ and 70° for a spectral band at 8.2 to 8.7 µm. On the other hand, Sobrino and Cuenca [97] did not find a dependency of emissivity on $\theta_{\mathrm{vza}}$ for grass and Snyder et al. [96] mostly less than 1% for a sample of compost with grass and leaves. In addition, for $\theta_{\mathrm{vza}}$ up to 30°, the changes in the emissivity are mostly negligible [97,98,100]. Therefore, we neglect the dependence of the emissivity on $\theta_{\mathrm{vza}}$ for land surface in the following.

#### 4.1.2. Atmospheric Data

Every radiative transfer calculation needs an atmospheric state as input. We use ECMWF ERA5 reanalysis data [101], in particular the skin temperature, temperature profile, logarithm of surface pressure, 10 m U and V wind components, specific humidity, ozone mass mixing ratio, fraction of cloud cover, specific cloud liquid and ice water contents and land/sea mask. Additionally, the total column water, water vapor and ozone are included in the training dataset; those quantities are not needed for the radiative transfer calculations, but they are used as input features for the ANNs.

Data of three arbitrary, recent years are collected: 2010, 2013 and 2015. For each year, the 15th day of each month is considered. Compared to the data used for VADUGS, we have an increased vertical resolution (137 instead of 91 model levels) and temporal resolution (1 h instead of only 12 UTC [102]).

Figure 3 shows exemplarily the variability of the skin temperature. The daily mean skin temperature exhibits an annual variability of ~20 K in central Europe, whereas skin temperature within a single day might vary about 10 K in central Europe but ~40 K in Northern Africa. This stresses the necessity to cover the full yearly as well as daily variability of the atmospheric state in a sufficient temporal resolution. Figure 3c shows the differences in daily mean skin temperature between 2010 and 2015 for a single day. These can lead to temperature differences of roughly −10 to 10 K, which is why we base our calculations on data of three different years. Furthermore, the high temporal resolution allows to capture the full daily cycle of the atmospheric properties. Figure 4 shows that a coarser resolution of, e.g., 6 h might miss a part of the skin temperature variability. When considering a location close to a longitude of 0°E, the 6 h resolution can reproduce the minima and maxima in the daily course of the skin temperature. However, when considering a larger longitude, this might change as the sun is in zenith at a different time with respect to UTC. For instance, at 20°N, 30°E, the local minimum is ~3 K lower than the temperature at 0 UTC, while, at 20°N, 55°E, the local maximum is ~3 K higher than the temperature at 12 UTC. Thus, the hourly resolution helps to create a training dataset that enables the resulting retrieval to work at all longitudes at all times of day, as required by a geostationary sensor.

Based on the ECMWF data, the atmospheric state is composed similarly to the method of Bugliaro et al. [71], i.e., vertical temperature profile, skin temperature, wind speed at 10 m altitude and densities of gaseous water ($H_2O$) and ozone ($O_3$). Oxygen ($O_2$) and carbon dioxide ($CO_2$) are derived from the air density using constant mixing ratios of 0.20948 [103] and 0.0004 [104], respectively, whereas, for nitrogen dioxide ($NO_2$), the mixing ratios stem from a chemical transport model with 72 model levels and a latitudinal and longitudinal resolution of 2° and 2.5°, respectively, simulating November 2012 to October 2013; the daily average of the 15th of each month was used [105,106]. Those five gases are required to perform corresponding radiative transfer calculations [107]; especially $H_2O$, $CO_2$ and $O_3$ have strong absorption features in the thermal infrared MSG/SEVIRI channels [108].

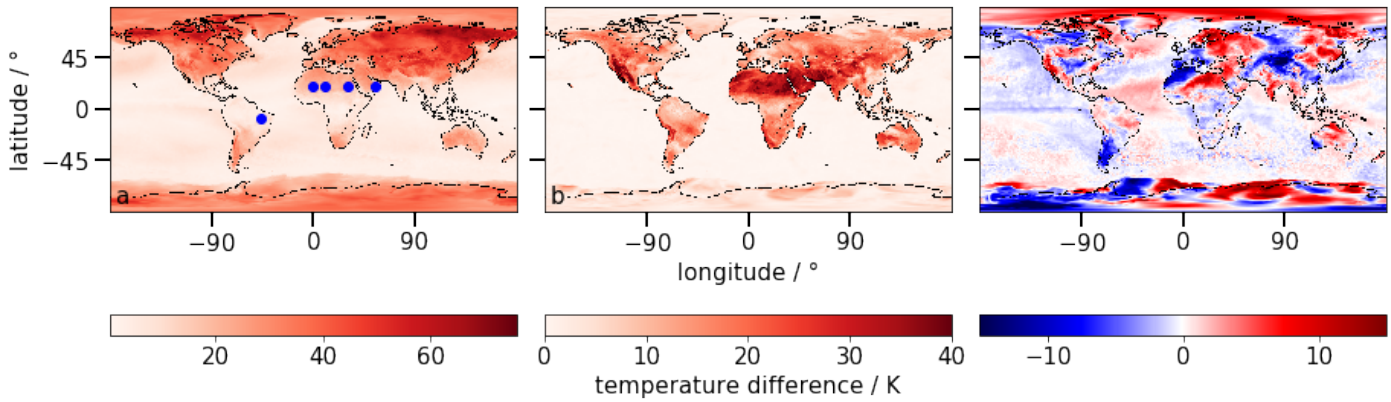


**Figure 3.** Differences in the skin temperature (from ECMWF ERA5): between the maxima and minima of the daily means of the 15th of each month in 2010, i.e., the annual variability (**a**); between the maxima and the minima of the 15 May 2010, i.e., the daily variability (**b**); between the daily means of 15 May 2010 and 2015 at 12:00 UTC, i.e., the inter-annual variability (**c**). The blue dots mark the locations shown in Figure 4.

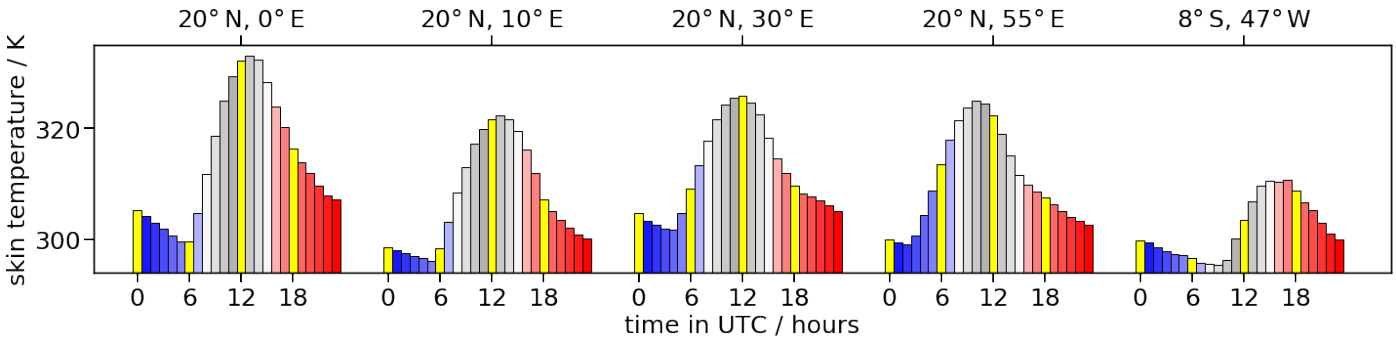


**Figure 4.** Daily course of the skin temperature (from ECMWF ERA5) for five different locations (see marker in Figure 3); the yellow columns represent the temperatures at 0, 6, 12 and 18 UTC.

Meteorological clouds are extracted from ECMWF data as well; however, the maximum random overlap rule of ECMWF cannot be implemented in a one-dimensional (1D) radiative transfer model. Thus, using the cloud fractions for each layer, a random set of 1D clouds is created. No partial cloudiness is considered and vertically adjacent cloud layers are assumed to overlap as much as possible (for details, see [71]). For liquid water clouds, the parameterizations by Bugliaro et al. [109] and Hu and Stamnes [110] are used to create the $r_{\mathrm{eff}}$ profiles and the optical properties, respectively. For ice water clouds, the parameterization by Wyser [111] and the rough-aggregate habit [107] with the parameterization by Heymsfield et al. [112], Yang et al. [113], Baum et al. [114] are applied for $r_{\mathrm{eff}}$ and the optical properties, respectively. Note that the composed atmospheres are fully consistent, i.e., the vertical temperature and gas profiles match the cloud profiles (i.e., humidity saturation at the correct altitudes). The atmospheres, in turn, match the surface emissivities and the viewing zenith angles. This distinguishes our approach from radiative transfer calculations by Krebs et al. [115] or Vázquez-Navarro et al. [116], who also created comprehensive simulated datasets of MSG/SEVIRI observations, but combined atmospheric profiles with random cloud layers, constant surface emissivities and arbitrary viewing zenith angles. In the case of the VADUGS training data, atmospheric profiles and clouds were consistent, but not the viewing zenith angles [71].

#### 4.1.3. Volcanic Ash Clouds

Volcanic ash clouds exhibit a significant amount of variability. The volcanic ash cloud top height $z_{\mathrm{top}}$ depends on the intensity of the eruption: whereas weak eruptions emit ash only up to a few hundred meters [117], affecting mainly the direct surrounding of the vent,

Eyjafjallajökull 2010 injected volcanic ash at heights of 3 to 10 km above sea level [118], Puyehue-Cordón Caulle 2011 injected ash up to 15 km high [38,119]. Even heights > 25 km are possible [120,121], although much rarer [1]. The cloud height also depends on the atmospheric conditions [122] and changes during the ash cloud's lifecycle, e.g., the height decreases due to gravitational settling [10]. Thus, in the following, $z_{\mathrm{top}} \in [0.3, 18]$ km is considered.

The vertical mass profile can be quite complicated, especially for aged clouds, e.g., with a non-uniform distribution and multiple layers [6,18,123]. As SEVIRI offers only limited possibilities for sounding, we consider only the simplest profile of a single, homogeneous layer (as in [71,124]). In addition, the vertical extent $z_{\mathrm{ext}}$ shows a large variability from some hundred meters up to some kilometers [6,18]. Marenco et al. [18] proposed $z_{\mathrm{ext}} = \sqrt{2}\, m_{\mathrm{col,\,meas}} / c_{\mathrm{max,\,meas}}$ with $m_{\mathrm{col,\,meas}}$ being the measured mass load and $c_{\mathrm{max,\,meas}}$ the measured peak mass concentration, arguing that this leads (together with the assumption of a homogeneous layer with the concentration $c$ being $c_{\mathrm{max,\,meas}} / \sqrt{2}$) to a good representation of real ash clouds for radiative transfer. Another approach based on plume rise calculations for stable stratified atmospheres suggests $z_{\mathrm{ext}} = 0.4 z_{\mathrm{top}}$ for the depth [125,126] and has been applied to volcanic ash cloud retrievals [33,43,127]. The latter relation is also assumed for VACOS. Thus, after choosing $z_{\mathrm{top}}$, the vertical extent is $z_{\mathrm{ext}} \in [100\,\mathrm{m}, 0.4 z_{\mathrm{top}}]$.

For the mass volume concentration $c$, typical values depend again on the eruption strength and the ash cloud's lifecycle, as sedimentation and dispersion may lead to a thinning of the cloud. Przedpelski and Casadevall [128] estimated $2\,\mathrm{g\,m^{-3}}$ from inspections of KLM 867's engines after encountering an ash cloud of Redoubt Volcano in 1989. Weber et al. [19] reported in situ measured concentrations of the Eyjafjallajökull 2010 ash plume of 500 to 2000 $\mathrm{\mu g\,m^{-3}}$ at distances of 15 to 60 km from the vent. Marenco et al. [18] found from lidar data mean concentrations of 300 to 650 $\mathrm{\mu g\,m^{-3}}$ with maxima of 800 to 1900 $\mathrm{\mu g\,m^{-3}}$ above Great Britain on 14–17 May, about 1400 km from the source. Schumann et al. [6] measured in situ averages of 105 to 283 $\mathrm{\mu g\,m^{-3}}$ with maxima (of 10 s mean values) of 282 to 830 $\mathrm{\mu g\,m^{-3}}$ above the North Sea on 17 May, roughly at a distance of 1760 km from the vent. With respect to aviation, three regimes of ash contamination are differentiated: low contaminations for concentrations $\leq 2\,\mathrm{mg\,m^{-3}}$, medium contaminations for concentrations of 2 to $4\,\mathrm{mg\,m^{-3}}$ and high contaminations for concentrations $\geq 4\,\mathrm{mg\,m^{-3}}$ [9]. In the following, mass column concentrations of 0 (no ash) to $30\,\mathrm{g\,m^{-2}}$ are considered. Thus, after choosing $z_{\mathrm{ext}}$, the mass volume concentration is $c \in [0\,\mathrm{g\,m^{-3}}, \frac{30\,\mathrm{g\,m^{-2}}}{z_{\mathrm{ext}}}]$; for a typical cloud thickness of $z_{\mathrm{ext}} = 1$ km, this would cover mass volume concentrations up to $30\,\mathrm{mg\,m^{-3}}$, covering all three contamination regimes according to ICAO.

Volcanic ashes themselves can also differ significantly with respect to chemical composition, particle size and shape. Here, we consider the comprehensive set of optical properties covering the variability of all three properties described by Piontek et al. [23]. The refractive indices of volcanic ashes, as shown in Figure 5, were calculated by averaging the refractive indices of different components of volcanic ash (i.e., minerals and glasses) according to typical petrological compositions; the last depends on the silica content $x_s$, which was varied from 45 to 75 wt.%, and the ratio between volcanic glass and minerals, $f_{\mathrm{glass}}$, which varied between $x_s/100$ wt.% and 1. Focusing on distal ash, the porosity of volcanic ash [21] is neglected.

The microphysical properties were chosen based on a literature review: a log-normal particle size distribution (Equation (7) in [23]) was assumed with $r_{\mathrm{eff}} \in \{0.6, 1.8, 3, 4.5, 6\}$ and geometric standard deviations $s \in \{1.5, 2.0\}$. Pro- and oblate spheroids were assumed in equal parts, with the aspect ratio following a modified log-normal distribution (Equation (9) in [23]) with median aspect ratio $\epsilon_0 = 1.5$ and a spread $\sigma_{\mathrm{ar}} = 0.45$. Using Mie theory and the T-matrix method [129], the optical properties were derived for wavelengths of 5 to 15 µm, as shown in Figure 6.

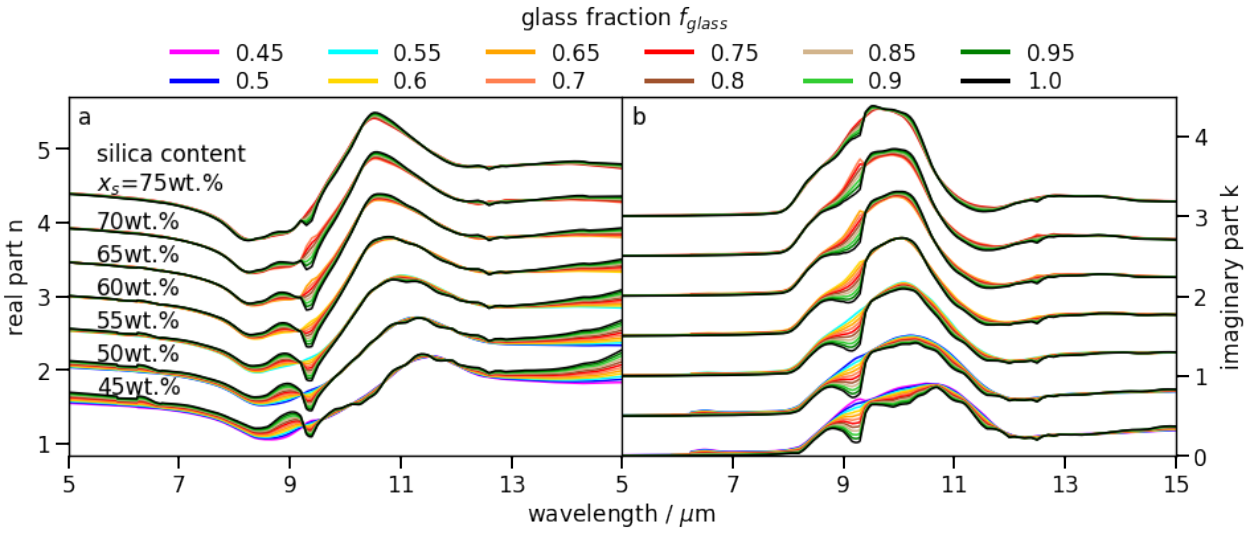


**Figure 5.** Real (**a**) and imaginary (**b**) parts of the complex refractive indices of the volcanic ash types derived by Piontek et al. [23]. Different glass fractions $f_{\text{glass}}$ are denoted by the color. For visibility reasons, different silica contents $x_s$ are shifted by 0.5 with respect to each other.

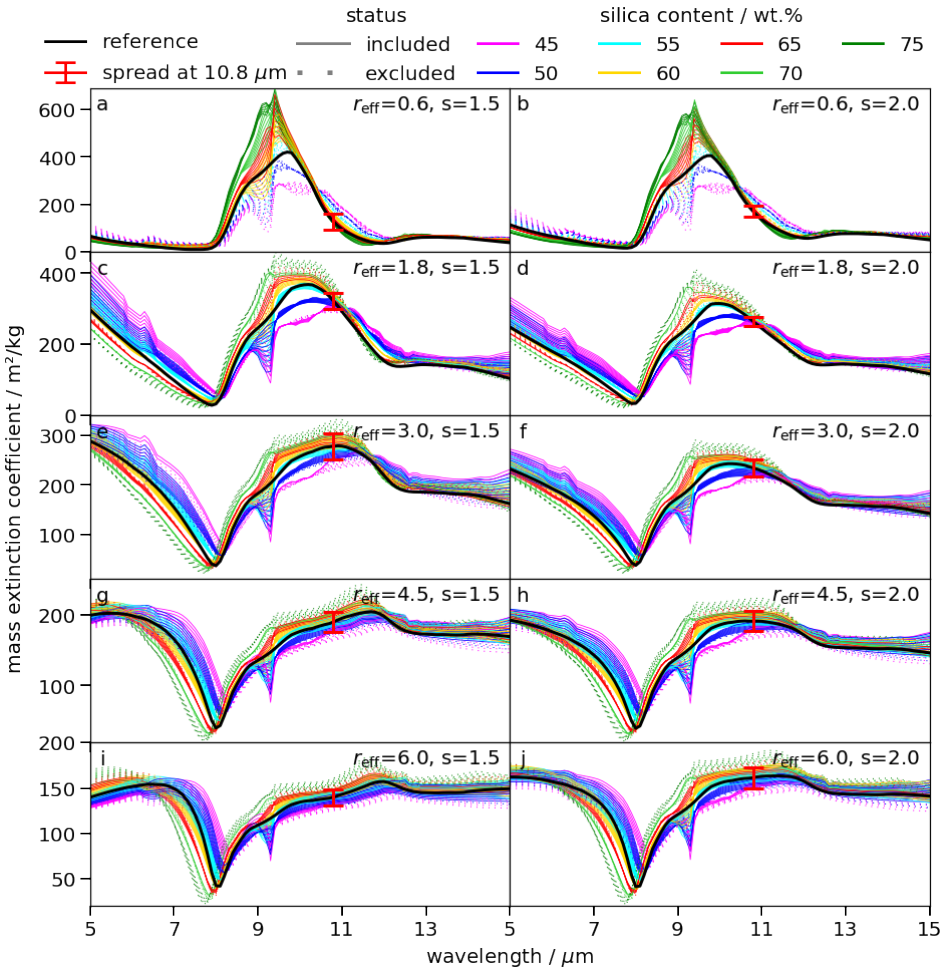


**Figure 6.** Mass extinction coefficient of the volcanic ash types derived by Piontek et al. [23] and (in black) for Eyjafjallajökull ash [75] as reference. The silica content $x_s$ is denoted by the color and the status (included or excluded with respect to the simulated dataset) by the linestyle. The mass extinction coefficient at 10.8 µm of Eyjafjallajökull ash and the standard deviation of all mass extinction coefficients at 10.8 µm are given by the red marker. The panels show subsets of different $r_{\text{eff}}$ and $s$.

To exclude outliers as potentially unphysical volcanic ashes, only a selection of ash types is used for the training below (see Figure 6). Therefore, the standard deviation $\sigma(r_{\text{eff}}, s)$ of the mass extinction coefficient at 10.8 µm, $k_{10.8}$, of all volcanic ashes is calculated. Next, the mass extinction coefficient $k_{\text{Eyja}}(r_{\text{eff}}, s)$ at 10.8 µm for Eyjafjallajökull ash from Deguine et al. [75] is determined for the same microphysical properties $r_{\text{eff}}$, $s$ and shape [23]. Finally, we keep only those volcanic ashes that are $1\sigma$ close to the Eyjafjallakökull ash, i.e., that fulfill $\left|k_{10.8} - k_{\text{Eyja}}(r_{\text{eff}}, s)\right| \leq \sigma(r_{\text{eff}}, s)$. Overall, 57% of the ash types pass this test. Figure 6 shows that for $r_{\text{eff}} = 0.6$ µm mostly ashes of low $x_s$ are excluded, whereas for $r_{\text{eff}} = 1.8$ µm mainly high $x_s$ are dismissed. For the other $r_{\text{eff}}$, the selection is relatively balanced with respect to $x_s$.

### 4.2. Radiative Transfer Calculations

To create the input files of the radiative transfer calculation, the algorithm RTSIM [71] randomly picks uniformly distributed times among those covered by the ECMWF data (Section 4.1.2), coordinates with respect to the SEVIRI disc and compiles the corresponding surface properties and atmospheric, cloud and ash profiles; meteorological clouds can be created in ~51% of the cases. For each set of input parameters, four calculations are performed if possible: clear-sky conditions; only meteorological clouds; only volcanic ash clouds; meteorological and volcanic ash clouds. The ash cloud parameters (i.e., $z_{\text{top}}$, $c$, $\tau_{10.8}$ and $r_{\text{eff}}$) and the simulated brightness temperatures together enter the training data.

1D radiative transfer calculations of the thermal infrared brightness temperatures as measured by SEVIRI are performed using libRadtran version 2.0.3 [130,131] and the C-version of the *Discrete Ordinate Radiative Transfer Solver* (DISORT [132,133]) with 16 streams. The *Cluster for Advanced Research in Aerospace* (CARA) of the Deutsches Zentrum für Luft- und Raumfahrt (DLR) is used, allowing the calculation of 1000 samples with 7 simulated brightness temperatures each on a single node within approximately 100 s.

To account for gas absorption, a method by Buehler et al. [134] is used in the implementation by Gasteiger et al. [135], called REPTRAN. It performs radiative transfer simulations at representative wavelengths within a given spectral interval (on average 3 and typically <10) and calculates a weighted sum of them as an approximation of the integral of the top of atmosphere radiance over a satellite channel's spectral response function/a narrow spectral band. The representative wavelengths and the weights were determined such that the approximation for the integrated top of atmosphere radiance has an error < 1%, using a training dataset of simulated top of atmosphere radiances with a high spectral resolution covering a large variety of atmospheric states. Four different parameterizations are available: *channel* (optimized for SEVIRI's spectral channels), *coarse* (band width of 15 $\text{cm}^{-1}$), *medium* (5 $\text{cm}^{-1}$) and *fine* (1 $\text{cm}^{-1}$). *channel* uses the least number of spectral sampling points and is fastest. However, Gasteiger et al. [135] pointed out that the applicability of the parameterization might cease if a significant spectral variability is introduced which has not been considered in their training dataset. For instance, surface emissivity was assumed wavelength-independent by Gasteiger et al. [135]. In our simulations, surface emissivity shows a strong spectral variability, especially for sand [88]. Furthermore, the refractive index of the volcanic ash, which has imaginary values between 0 and about 1.4 (Figure 5), was assumed wavelength-independent and between 0.001 and 0.1 by Gasteiger et al. [135].

To select accurate parameterizations, we performed test calculations of the brightness temperatures for the REPTRAN modes *channel*, *coarse*, *medium* and *fine*. Cases with and without meteorological clouds/volcanic ash were considered with the ash cloud parameters as described in Section 4.1.3 and an example ash with the refractive index of Eyjafjallajökull ash from Deguine et al. [75], a log-normal size distribution with $r_{\text{eff}} = 0.6$ µm, $s = 1.5$ and the previously described shape distribution. In total, for each parameterization, 500 atmospheric states were simulated with each up to four cloud states as described above. The differences to the *fine* calculations are shown in Figure 7, assuming that those represent the most accurate approximation to a line-by-line calculation. This is supported by the fact that the spread decreases when considering a higher-resolution approximation

(except for $BT_{9.7}$). Median differences for *channel* are the largest for all channels but $BT_{9.7}$. This might reflect the fact that $BT_{9.7}$ is sensitive to ozone, which is mainly present in the stratosphere and, thus, might hide the impact of the additional spectral variability due to the surface emissivity and the volcanic ash refractive index. Outliers reach absolute differences >2 K (not shown). In some cases (e.g., $BT_{6.2}$ and $BT_{10.8}$), the differences between *coarse* and *medium* are rather small, such that the lower resolution parameterization is applied. Overall, we conclude to use the *channel* parameterization for $BT_{9.7}$; *coarse* for $BT_{6.2}$, $BT_{10.8}$ and $BT_{12.0}$; *medium* for $BT_{7.3}$, $BT_{8.7}$ and $BT_{13.4}$.

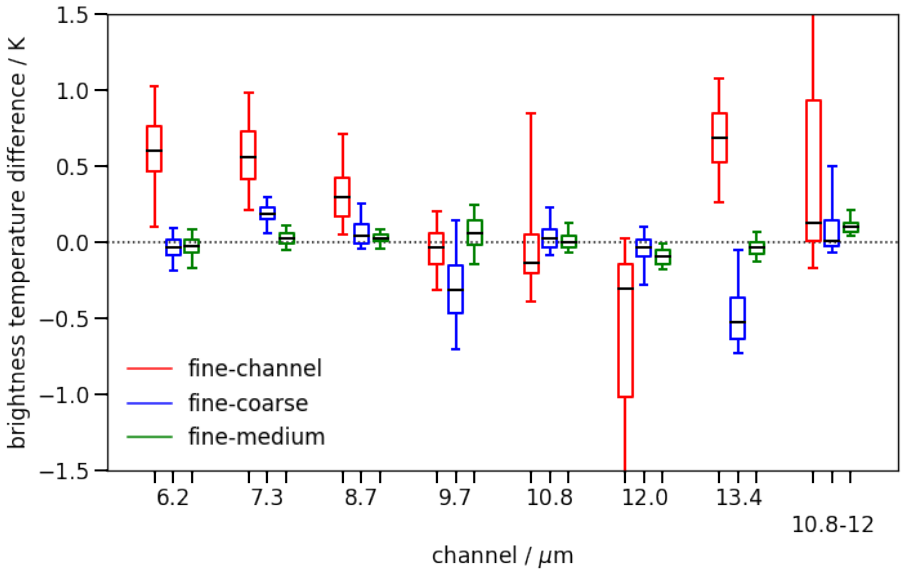


**Figure 7.** Brightness temperature differences for radiative transfer calculations of different REPTRAN parameterizations. The considered test dataset is described in the text. The boxplot shows the median, first and third quartile (box) and the 5th and 95th percentile (whiskers).

### *4.3. Test of the Ash-Free Training Data*

The presented method is not expected to reproduce observations on a single pixel basis as, for example, spatial resolution is too coarse, averaged surface emissivities are used and the ECMWF model might not represent reality, especially clouds, accurately enough. However, the aim of the setup is to create a dataset that statistically approximates the reality. To validate this, 49,701 simulations without ash for 15 July 2015 at 12:00 UTC were performed, randomly scattered over the SEVIRI disc and compared with the corresponding SEVIRI measurements (see Figure 2). If RTSIM created no clouds in the atmosphere, the cloud-free simulation was used, otherwise the simulation containing clouds. The distributions of the simulated and the corresponding measured brightness temperatures should be similar, and thereby would indicate that RTSIM creates atmospheric profiles and libRadtran derives brightness temperatures that generally approximate reality, although individual samples might deviate from the measurements. Thus, simulations can then be viewed as a strong training dataset.

Figure 8 shows a two-dimensional histogram for the full dataset of measured against simulated $BT_{10.8}$. Most samples are located close to the identity, with slightly more points above the identity than below, i.e., the simulation tends to overestimate the brightness temperature. Single points show large differences up to about 80 K between simulation and measurements, probably when the simulation is cloud-free and reality shows a high cold ice cloud. Figure 9 shows the median and the 95th percentile of the absolute difference between the simulated and the measured brightness temperatures. Different subsets are considered: (a) all samples as well as land and sea samples for clear conditions; (b) clear and cloudy samples for sea surfaces; (c) viewing zenith angle $\theta_{\mathrm{vza}}$ separated by 40° and 55° for clear conditions over sea; (d) viewing zenith angle $\theta_{\mathrm{vza}}$ separated by 40° and 55° for

clear conditions over land. Clear conditions are determined by the fact that no cloud layers were created by RTSIM and that the total cloud cover by ECMWF is below 25%; of course, observations might still contain meteorological clouds. The statistical distributions of the measured and simulated brightness temperatures (and brightness temperature differences $BTD_{8.7-10.8}$ and $BTD_{10.8-12.0}$) are shown as histograms in Figure 10. Figure 11 shows as an example the distribution of $BT_{10.8}$ for the subsets of clear sky land/sea samples and clear/cloudy samples of sea surfaces.

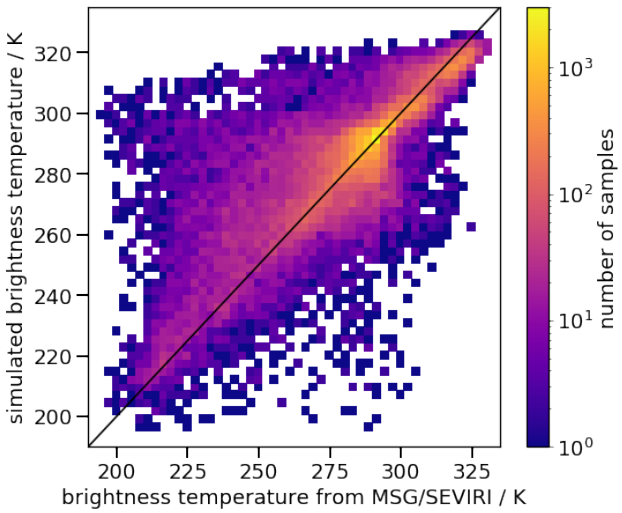


**Figure 8.** $BT_{10.8}$ measured by MSG/SEVIRI against corresponding RTSIM and libRadtran results for the corresponding coordinates.

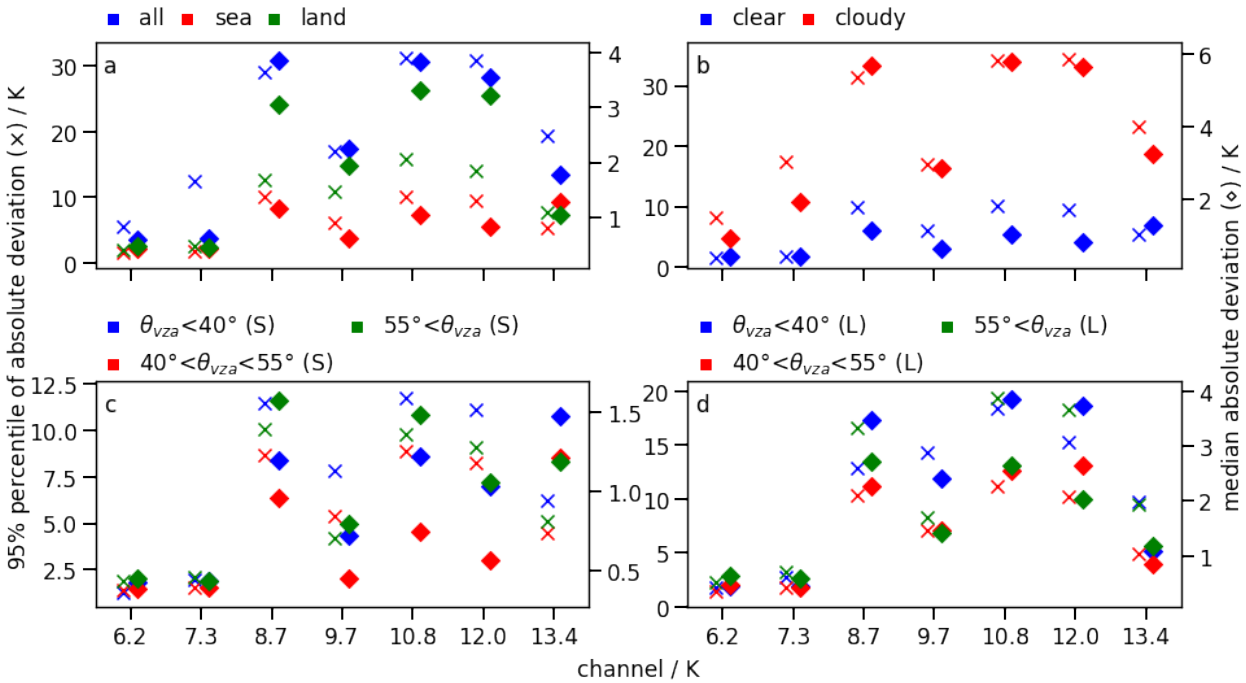


**Figure 9.** The 95th percentile (cross) and median (diamond) of the absolute deviation between the simulated brightness temperatures and the corresponding MSG/SEVIRI measurements; considered is the full dataset (*all*) (**a**) as well as subsets, i.e., (**a**) land and sea for cloud-free samples (i.e., no cloud layers simulated, total cloud cover $\leq 0.25$), (**b**) clear and cloudy (i.e., at least one cloud layer simulated and total cloud cover $\geq 0.25$) for sea surfaces and (**c**) different $\theta_{\mathrm{vza}}$ above sea and (**d**) land.

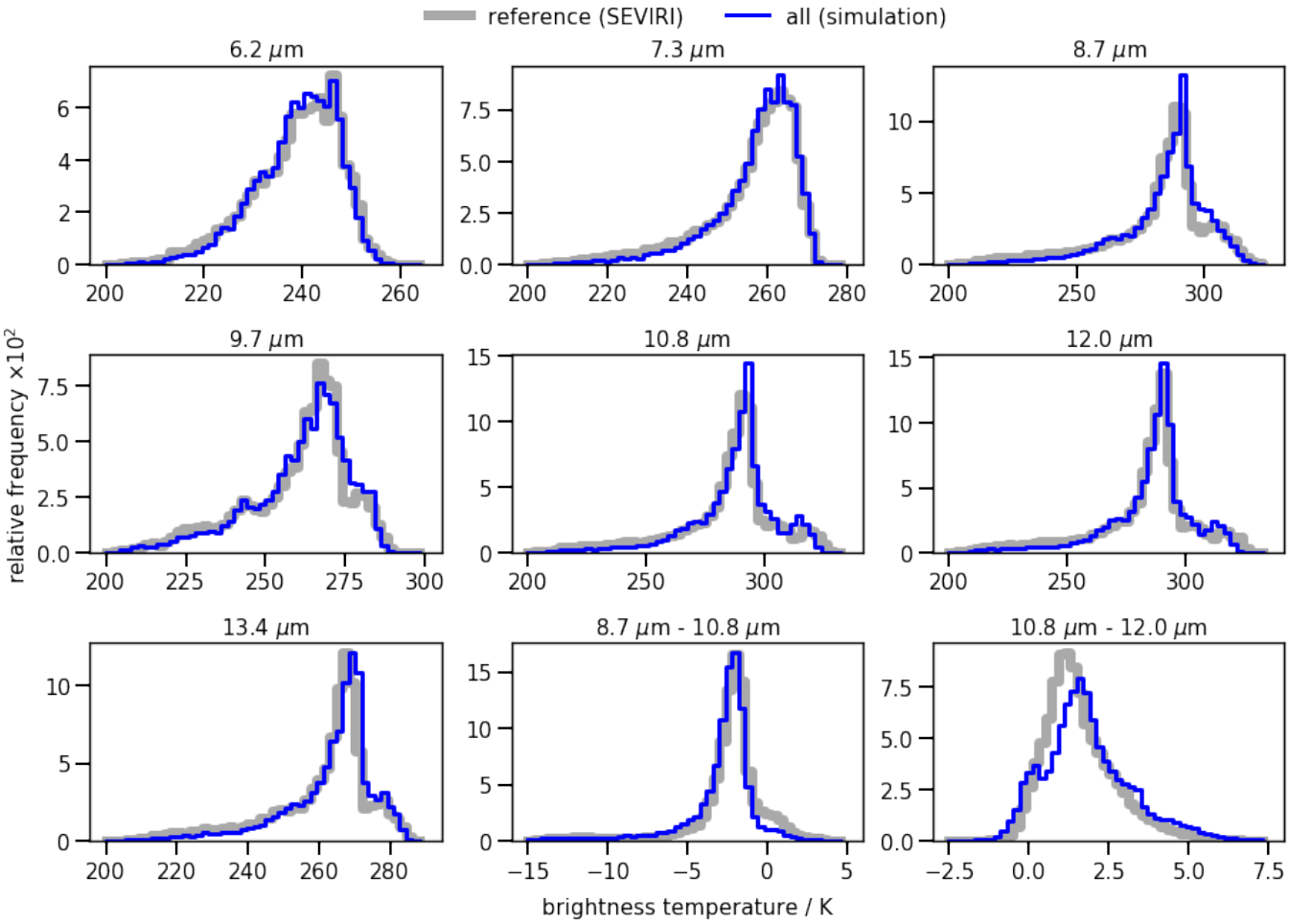


**Figure 10.** Distributions of the brightness temperature in different MSG/SEVIRI channels as measured from space and as simulated using RTSIM and libRadtran, separated into 50 bins.

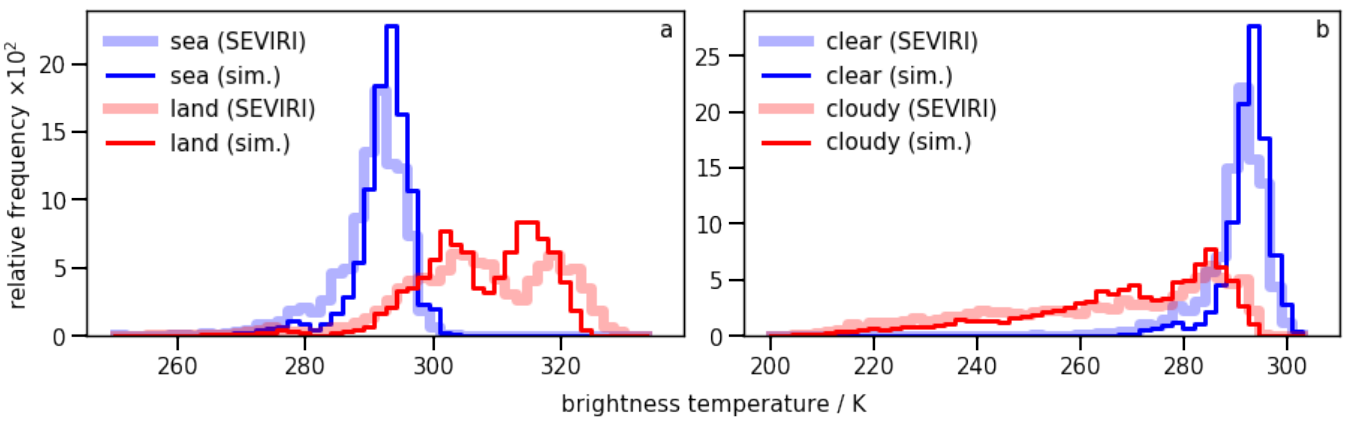


**Figure 11.** Distributions of $BT_{10.8}$ as measured by MSG/SEVIRI and as simulated using RTSIM and libRadtran: (**a**) sea and land surfaces for clear sky conditions; (**b**) sea surfaces for clear and cloudy conditions.

Atmospheric gases, meteorological clouds and the surface properties are the main aspects that determine the quality of the simulations. Water vapor is mainly visible in $BT_{6.2}$ and $BT_{7.3}$, with the latter being sensitive at least down to the mid-troposphere [69]. Their brightness temperature distributions in Figure 10 show a good agreement, and, even on a single pixel basis, the deviations are small, with median absolute deviations mostly below 1 K. The effect of $H_2O$ on the atmospheric window channels $BT_{8.7}$, $BT_{10.8}$ and $BT_{12}$

is small [108,136]. However, the single pixel deviations of the window channels are larger than those of $BT_{6.2}$ and $BT_{7.3}$ when considering only clear sky samples, indicating that other effects dominate the former. $O_3$ and $CO_2$ mainly impact $BT_{9.7}$ and $BT_{13.4}$, respectively. Their distributions in Figure 10 generally agree well up to a small peak on the right side that is not fully reproduced. However, as this minor peak is also present in the distributions of the window channels, it can be expected to stem from the surface properties, particularly from land surfaces that produce multiple peaks. The single pixel median absolute deviation for all samples is generally around 2 K.

Meteorological clouds impact the atmospheric window channels. Individual pixel deviations are remarkable: the median absolute deviation of cloudy samples is ~6 K, with the 95th percentile of the absolute deviation even beyond 30 K. This indicates that the largest deviations in Figure 8 could be caused by the occurrence of meteorological clouds, for instance, if they are present in reality but missing in the simulation, or if the there are significant differences in the cloud top heights. The size of the smaller deviations might be related to inaccuracies in the cloud properties, e.g., the cloud top height, the liquid and ice water content derived from the ECMWF model or $r_{\mathrm{eff}}$ derived from parameterizations. In addition, clouds are described differently in the 1D radiative transfer calculations than in nature, which has an impact especially in the case of partial cloudiness, and a random element is applied for the creation of the cloud layers [71]. However, the resulting brightness temperature distributions in Figures 10 and 11 agree with the SEVIRI measured distributions.

The surface properties (emissivity and skin temperature) influence the atmospheric window channels as well. As pointed out above, their brightness temperature distributions show a good agreement (Figure 10). The distributions of $BT_{10.8}$ for sea surfaces and clear sky pixels roughly agree, whereas for land surfaces two peaks of similar height are visible with the right flank of the simulated distribution shifted towards lower temperatures (Figure 11a). The single pixel comparison exhibits generally low median absolute deviations (<2 K) for clear sky sea surfaces, but the deviation is larger for land than for sea. Considering the $\theta_{\mathrm{vza}}$-dependence for sea surfaces, the median absolute deviation is largest for $55° < \theta_{\mathrm{vza}}$, which might be related to the strong $\theta_{\mathrm{vza}}$-dependence of the water surface emissivity for large viewing zenith angles. On the contrary, for land surfaces, the median absolute deviation is largest for $\theta_{\mathrm{vza}} < 40°$. This seems reasonable as the $\theta_{\mathrm{vza}}$-dependence is smaller for land surfaces than for water surfaces. Furthermore, a higher $\theta_{\mathrm{vza}}$ leads to a larger gas column along the optical path, thereby effectively hiding deviations due to inaccurate surface properties.

The surface emissivity is a climatology over 10 years, whereas the actual emissivity in the present scene might slightly deviate, e.g., due to wetter or dryer surfaces, more or less vegetation, etc. [89]. Could this cause the deviations observed for land surfaces? Neglecting all atmospheric effects, we can estimate the deviation of the surface emissivity corresponding to the deviation in the simulated brightness temperatures using Planck's law. For the wavelength $\lambda$, let the measured brightness temperature $BT_{\lambda,\mathrm{m}}$ be related to an emissivity $\epsilon_{\lambda,\mathrm{m}}$ and the simulated one $BT_{\lambda,\mathrm{s}}$ to $\epsilon_{\lambda,\mathrm{s}}$. Their ratio $r$ is

$$r = \frac{\epsilon_{\lambda,\mathrm{s}}}{\epsilon_{\lambda,\mathrm{m}}} = \frac{\exp(c/\lambda/BT_{\lambda,\mathrm{m}}) - 1}{\exp(c/\lambda/BT_{\lambda,\mathrm{s}}) - 1} \tag{2}$$

with $c = 0.0145$ m K [108]. For $BT_{\lambda,\mathrm{m}}$ between 263 K and 303 K and $BT_{\lambda,\mathrm{m}} - BT_{\lambda,\mathrm{s}} = \pm 4$ K, the difference $|1 - r|$ is ca. 0.1, 0.08 and 0.07 for $\lambda$ of 8.7 µm, 10.8 µm and 12 µm, respectively. For $BT_{8.7}$, such deviations are possible, as the spread in emissivities of typical surfaces is large in the corresponding spectral regime (sand has emissivities down to 0.7, whereas water and vegetated surfaces have values close to 1). Around 10.8 µm and 12 µm, the differences in typical surface emissivities are <0.05 [88,89]. Therefore, it seems unlikely that an error in the surface emissivity is the single cause for the differences in the brightness temperatures above land surfaces, as their median absolute deviation in the three window channels are similar.

Another possible reason might be inaccuracies in the skin temperature. For instance, it is known that ECMWF underestimates skin temperatures for land at daytime and overestimates during night: Trigo et al. [137] found errors of the order of 2 to 5 K, especially for semiarid regions (North Africa, Sahara and Namibia), and Johannsen et al. [138] found in parts underestimations in the order of 5 K for the Iberian peninsula when comparing ECMWF data with satellite retrievals. The ECMWF data and the surface emissivity have a spatial resolution of 0.25°, corresponding to roughly 28 km at the SEVIRI sub-satellite point. However, SEVIRI itself has a resolution of 3 km at nadir. Due to this difference, small-scale features and sudden changes in the surface type (e.g., at coastlines) can lead to inaccuracies.

To sum up, the comparison indicates that gas profiles are reproduced correctly on a single pixel basis, similar to sea surfaces in the absence of clouds. For cloudy samples, the measured and simulated brightness temperature distributions agree well, but considering individual pixels we find notable deviations. Land surfaces lead to deviations for both, single pixels (<4 K) and the brightness temperature distributions. Especially the good agreement of the distributions of $BTD_{8.7-10.8}$ and $BTD_{10.8-12.0}$ highlights that relative deviations within single spectra are small, with only a minor positive bias for $BTD_{10.8-12.0}$. Thus, we conclude that the simulations can be used as a training dataset.

### 4.4. Training, Validation and Test Data

We performed simulations for ~30 million samples. Then, two selections are made: First, for ash-loaded samples, only those that have $BTD_{10.8-12} < 0$ are kept. This threshold criterion is typical for volcanic ash detection and has been used for VADUGS as well [71]. It reduces the amount of samples with overlapping signals from meteorological and volcanic ash clouds, thereby effectively making the classification task slightly simpler for the ANNs. Second, the selection of ash types similar to Eyjafjallajökull ash is applied to reduce the complexity of the training datasets. From the remaining data, two sets are formed: the full dataset (Dataset A) and a subset containing only the ash-loaded samples (Dataset B). Dataset A is used for the ANNs for classification and the retrieval of $\tau_{10.8}$, i.e., the algorithms that are applied to all satellite measurements. Dataset B is used for the ANNs of $z_{\text{top}}$ and $r_{\text{eff}}$, which are only applied to ash-loaded pixels. Dataset A and B are randomly grouped into a training (70%), a validation (20%) and a test (10%) dataset, as shown in Table 1. Training and validation datasets are used for the training of the ANNs; the test dataset is used to characterize the final algorithms in Piontek et al. [80]. Distributions of the target values in the training datasets are sketched in Figure 12. Note that they are not uniformly distributed due to the selections performed as well as the usage of different volcanic ash types.

**Table 1.** Information on the different simulated datasets.

| Dataset | Description | Samples | Ash Fraction |
|---|---|---|---|
| Training A | clear + ash | 8,725,531 | 32.1% |
| Validation A | clear + ash | 2,493,719 | 32.1% |
| Test A | clear + ash | 1,252,470 | 32.3% |
| Training B | only ash | 2,798,004 | 100.0% |
| Validation B | only ash | 800,117 | 100.0% |
| Test B | only ash | 405,556 | 100.0% |

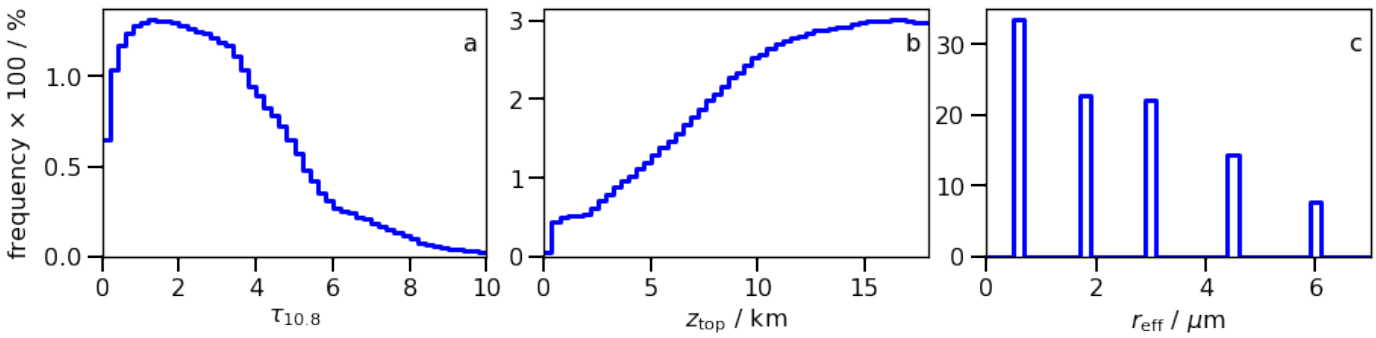


**Figure 12.** Distributions of: (**a**) $\tau_{10.8}$ in *Training A*; (**b**) $z_{top}$ in *Training B*; (**c**) $r_{eff}$ in *Training B*. In (**a**), only non-zero values are shown.

## 5. Training of the ANNs

For the ANNs, TensorFlow version 1.14.0 [139,140] and Keras version 2.3.1 [141] are used. Individual ANNs are trained for the classification, the retrieval of volcanic ash-induced optical depths at 10.8 µm ($\tau_{10.8}$), cloud top heights ($z_{top}$, in meters) and effective particle radii ($r_{eff}$, in micrometers). The classification ANN differentiates four categories: clear sky; only meteorological clouds; only volcanic ash clouds; both meteorological and volcanic ash clouds.

VADUGS directly retrieved $m_{col}$, whereas VACOS derives $\tau_{10.8}$ as this quantity is more closely related to the observational data as SEVIRI measures radiances. It can be converted into $m_{col}$ using $k_{10.8}$. The wavelength 10.8 µm was chosen (as in [66]) as it corresponds to one of the SEVIRI channels, is in the atmospheric window, is less influenced by $H_2O$ and volcanic $SO_2$ emissions (compared to 8.7 µm, see [29]) and experiences relatively large extinctions (compared to 12 µm). The ANNs for the classification and $\tau_{10.8}$ are trained with the full training dataset (Dataset A in Table 1), whereas the ANNs for $z_{top}$ and $r_{eff}$ are trained only with ash-containing samples (Dataset B). The input features (in Table 2) contain the seven infrared brightness temperatures from SEVIRI, including $BT_{10.8}$ and $BT_{12}$ that are often used for volcanic ash detection [24,25], as well as $BT_{8.7}$ [31]. Prata and Grant [33] showed that $BTD_{8.7–12}$ can be even more negative than $BTD_{10.8–12}$. As water vapor can hide the volcanic ash [27,43], $BT_{6.2}$ and $BT_{7.3}$ are included, which are sensitive to water vapor [69]. Similarly, $BT_{9.7}$ and $BT_{13.4}$ are included to treat $O_3$ and $CO_2$ [69]. From ECMWF, the skin temperature is included as a reference for the temperature profile, as well as estimates of the total column water, water vapor and ozone to account for the influence of gases and meteorological clouds on the satellite measurements and thereby to extract the impact of the volcanic ash. Latitude and longitude allow the ANNs to learn the geography to some extent and latitudinal dependencies of the atmospheric profile. The land/sea-mask partly encodes the very different emissivities [88,89] as well as differences of the atmosphere and cloud layers above land and sea. Day of year and hour of day are included to consider seasonal and diurnal variations in the atmospheric properties, respectively. Their sine and cosine are used to avoid discontinuities (e.g., between 31 December and 1 January or 24:00 and 0:00) and make the encoding unambiguous [78]. The satellite viewing zenith angle is included to correct slant observations, leading to longer optical paths through the atmosphere for higher $\theta_{vza}$. $\tau_{10.8}$ is included as an input feature for the ANNs of $z_{top}$ and $r_{eff}$ to make use of the previously retrieved information. Finally, the "clear" brightness temperatures $BT_{8.7,clr}$, $BT_{10.8,clr}$ and $BT_{12,clr}$ are given as input. Those correspond to the brightness temperatures that would be measured in absence of the volcanic ash clouds (but with meteorological clouds if present) to quantify the surroundings [27,31,45].

**Table 2.** Model settings and input features for the ANNs retrieving the classification, $\tau_{10.8}$, $z_{\text{top}}$ and $r_{\text{eff}}$. $\sigma$ denotes the standard deviation. The ANN architectures are given as lists of neurons per layer, with the first number giving the amount of input neurons, the second number the amount of neurons in the first hidden layer and the last number the amount of output neurons.

| | **Classification** | $\tau_{10.8}$ | $z_{\text{top}}$ | $r_{\text{eff}}$ |
|---|---|---|---|---|
| **Model setting** | | | | |
| Input/output standardization | × | × | × | × |
| LeCun normal distributed initialization | × | × | × | × |
| Add Gaussian noise to input ($\sigma = 0.1$) | | | × | × |
| Architecture | 19-100-100-100-4 | 19-100-100-100-1 | 23-100-100-100-1 | 23-100-100-100-1 |
| Activation function (hidden neurons) | tanh | tanh | tanh | tanh |
| Activation function (output neurons) | softmax | linear | linear | linear |
| Loss function | cross entropy | mean squared error | mean squared error | mean squared error |
| Sample weighting | | × | | |
| Nadam training algorithm | × | × | × | × |
| Epochs trained | 60,000 | 2000 | 2000 | 2000 |
| **Feature (unit/range)** | | | | |
| $BT_{6.2}$ (K) | × | × | × | × |
| $BT_{7.3}$ (K) | × | × | × | × |
| $BT_{8.7}$ (K) | × | × | × | × |
| $BT_{9.7}$ (K) | × | × | × | × |
| $BT_{10.8}$ (K) | × | × | × | × |
| $BT_{12}$ (K) | × | × | × | × |
| $BT_{13.4}$ (K) | × | × | × | × |
| Skin temperature (K) | × | × | × | × |
| Binary land/sea mask | × | × | × | × |
| Total column water vapor (kg m$^{-2}$) | × | × | × | × |
| Total column water (kg m$^{-2}$) | × | × | × | × |
| Total column ozone (kg m$^{-2}$) | × | × | × | × |
| Latitude (−90 to 90°) | × | × | × | × |
| Longitude (−180 to 180°) | × | × | × | × |
| Sine of day of year | × | × | × | × |
| Cosine of day of year | × | × | × | × |
| Sine of hour of day | × | × | × | × |
| Cosine of hour of day | × | × | × | × |
| Cosine of satellite zenith angle | × | × | × | × |
| $\tau_{10.8}$ (retrieved) | | | × | × |
| $BT_{8.7,\text{clr}}$ (K) | | | × | × |
| $BT_{10.8,\text{clr}}$ (K) | | | × | × |
| $BT_{12,\text{clr}}$ (K) | | | × | × |

Input and output data are standardized. As $\tau_{10.8}$ is the result of a previous retrieval and $BT_{\lambda,\text{clr}}$ is estimated from the surrounding satellite measurements for application to real data (Section 6), those values are prone to errors. Therefore, the ANNs for $z_{\text{top}}$ and $r_{\text{eff}}$ apply a Gaussian noise with standard deviation of 0.1 on the input layer during training. Each ANN consists of three hidden layers with 100 neurons each. This choice is motivated by Strandgren et al. [78], who investigated different ANN structures when developing CiPS, i.e., a retrieval similar to VACOS but for cirrus clouds. They found the best performance for their most complex ANN, having three hidden layers with 64 neurons each. The output layers of our ANNs have a single neuron for regressions or four neurons for the classification. Note that the ANNs now have roughly twice as many trainable parameters as VADUGS: For example, an ANN with 19 inputs, $3 \times 100$ hidden neurons and a single output has 22,301 parameters, whereas the VADUGS architecture with 17 inputs, $1 \times 600$ hidden neurons and 2 outputs has 12,002 free parameters. The hidden layers use the hyperbolic tangent as activation function, while the output layer uses a linear function for regressions and a softmax function for classification [142]. The last allows the

classification ANN to produce a normalized four-dimensional output vector, where each component can be roughly interpreted as the probability of the corresponding category. All neurons use bias neurons and are initialized by a LeCun normal distribution [87]. The mean squared error is utilized as loss function for regressions and the categorical cross entropy for classifications [142]. For the training of classification, $z_{\text{top}}$ and $r_{\text{eff}}$ retrievals, all samples are weighted equally (with 1) when calculating the total loss of a batch of samples. For the ANN of $\tau_{10.8}$, the following sample weighting with respect to the true $\tau_{10.8}$ is applied to increase the importance of the few samples with small $\tau_{10.8}$ (e.g., less than 3% of the samples in the training subset of Dataset A have $\tau_{10.8} < 0.6$) in comparison to the many ash-free and very ash-loaded samples:

$$\begin{aligned} 0 \leq \tau_{10.8} \leq 0.001 &: 0.3 \\ 0.001 < \tau_{10.8} \leq 0.2 &: 5 \\ 0.2 < \tau_{10.8} \leq 0.5 &: 3 \\ 0.5 < \tau_{10.8} \leq 1 &: 0.01 \\ 1 < \tau_{10.8} &: 0.001 \end{aligned}$$

The weight for $\tau_{10.8} \leq 0.001$ is introduced to reduce the focus on very low concentrations that might be hardly retrievable anyway. With the weights for $0.001 < \tau_{10.8} \leq 0.5$ the focus on usual concentrations is increased. To avoid a general overestimation due to the many samples with large $\tau_{10.8}$ (see Figure 12), lower weights for $\tau_{10.8} > 0.5$ are applied. The numerical values are determined by testing different settings. The Nadam (short for *Nesterov-accelerated Adaptive Moment Estimation*) algorithm is applied during the training with recommended parameters (learning rate = 0.001, $\beta_1 = 0.9$ and $\beta_2 = 0.999$ [143,144]), with batch sizes of 1000. For regressions, the learning rate is reduced by a factor 100 every 500 epochs, with 2000 epochs in total, reaching a minimum of the loss function evaluated on the validation dataset, with the loss function remaining constant for several hundred epochs. For the classification ANN, the learning rate is reduced once after 500 epochs and training is stopped after 60,000 epochs, as accuracy (assuming a threshold of 0.5 for the four categories) calculated for the validation dataset decreases by <0.065% in the last 10,000 epochs.

Reality (i.e., atmospheric and volcanic ash properties) is very complex and variable and has only been approximated by the simulated data. A possible pitfall of this approach is that ANNs might overfit with respect to both the simulated training and the validation data. For example, some of the first ANNs we created here were trained successfully considering the simulated datasets, but revealed weaknesses when applied to real satellite data, such as misinterpretation of meteorological clouds as volcanic ash or wrong retrievals for thin ash clouds. To overcome these issues, we applied different selections with respect to the simulated datasets when training the final ANNs and introduced Gaussian noise layers and sample weightings as outlined above.

## 6. Notes on the Application

To perform the VACOS retrieval, the ANNs are applied in two steps: First, the classification ANN is used to detect volcanic ash. Alternatively, $\tau_{10.8}$ is retrieved to find ash clouds; reasonable thresholds are found in [80]. Second, $r_{\text{eff}}$ and $z_{\text{top}}$ are retrieved for all ash-containing pixels. In order to apply the ANNs, the input features as given in Table 2 have to be composed. For the training, $\tau_{10.8}$ and $BT_{\lambda,\text{clr}}$ at wavelength $\lambda$ are simulated and, therefore, exact. However, for the application on satellite data, the input feature $\tau_{10.8}$ is obtained from the retrieval result of the corresponding ANN, whereas $BT_{\lambda,\text{clr}}$ is estimated from the SEVIRI images. We assume that the ash clouds are spatially limited and the highest $BT_\lambda$ in the close surrounding of a specific pixel corresponds to the value that would be measured in absence of the volcanic ash cloud [115]. Therefore, for each pixel, the maximum $BT_\lambda$ within a radius of 12 pixels is determined, denoted $BT_\lambda^{12\,\text{px}}$; similar pixel areas were considered by Krebs et al. [115]. Assuming a pixel size of 3 km, a surrounding

of at least 36 km would be considered, which is sufficient for ash plumes close to the volcano [19]. At greater distance, ash clouds can become wider [6]; thus, an additional step is implemented. The SEVIRI disc is split in 10 × 10 boxes and the maximum of $BT_{\lambda}^{12\,\mathrm{px}}$ of all presumably ash-free pixels, i.e., pixels with

$$BT_{10.8\,\mu\mathrm{m}}^{12\,\mathrm{px}} - BT_{12.0\,\mu\mathrm{m}}^{12\,\mathrm{px}} \geq 0 \tag{3}$$

is determined within each box, called $BT_{\lambda}^{\mathrm{ref}}$. Now, for each pixel in the box, the brightness temperature difference is checked: if Equation (3) is not fulfilled, which indicates that volcanic ash still influences the measurement, the replacement

$$\left(BT_{\lambda}^{12\,\mathrm{px}} + BT_{\lambda}^{\mathrm{ref}}\right)/2 \longrightarrow BT_{\lambda}^{12\,\mathrm{px}} \tag{4}$$

is conducted. This last step is repeated twice in case Equation (3) remains unfulfilled. The final $BT_{\lambda}^{12\,\mathrm{px}}$ is used as an approximation for $BT_{\lambda,\mathrm{clr}}$. A uniform filter of size 5 × 5 pixels is applied for both $BT_{\lambda,\mathrm{clr}}$ and the retrieved $\tau_{10.8}$ (see [80]). Similarly, the total column water vapor and total column water are taken from an external source, e.g., a model, and might be arbitrarily wrong. However, the training dataset includes for a specific atmospheric profile samples with and without meteorological clouds (if those are theoretically possible due to the ECMWF data), both with the same total column quantities. Thus, the ANNs learn a certain robustness with respect to inaccuracies of the total column water and total column water vapor. This is different for the total column ozone and skin temperature, which are also obtained externally. The preferred source is ECMWF ERA5 as this was also used to create the training data.

The results of the ANNs can be treated in different ways. The classification result can either be used directly or a binary ash flag (i.e., ash or no ash) can be calculated by adding the probabilities of the two ash-free and the two ash-containing categories, respectively. Using the retrieved $z_{\mathrm{top}}$ and $z_{\mathrm{ext}} = 0.4 z_{\mathrm{top}}$ [125,126], one can derive an estimate for the geometrical thickness [127]. The retrieved $\tau_{10.8}$ can be converted into $m_{\mathrm{col}}$ using $k_{10.8}$; typical values for different $x_s$ and $r_{\mathrm{eff}}$ are given in Table 3 as derived from all data in Figure 6. Generally, $k_{10.8}$ increases with increasing $x_s$ when $r_{\mathrm{eff}} = \mathrm{const.}$, except for ashes with a $r_{\mathrm{eff}} = 0.6\,\mu\mathrm{m}$, where the opposite is the case. For $x_s = \mathrm{const.}$, $k_{10.8}$ is largest in the case $r_{\mathrm{eff}} = 1.8\,\mu\mathrm{m}$ and decreases with increasing $r_{\mathrm{eff}}$. In practice, to determine $k_{10.8}$, one needs to know $r_{\mathrm{eff}}$ and $x_s$. The former can be approximated by satellite retrievals, the age of an ash cloud or the distance to its source. The latter can be estimated using previous knowledge about the volcanic source or laboratory analyses of volcanic ash samples when considering past eruptions. If none of this information is given, one can simply assume $k_{10.8} = 200\,\mathrm{m^2\,kg^{-1}}$ which produces roughly the mean $m_{\mathrm{col}}$ considering the extremal values $140\,\mathrm{m^2\,kg^{-1}}$ and $328\,\mathrm{m^2\,kg^{-1}}$ of the mean $k_{10.8}$ in Table 3.

**Table 3.** Mean mass extinction coefficients at 10.8 µm ($k_{10.8}$) and their standard deviations for different volcanic ashes (from [23]) given in $\mathrm{m^2\,kg^{-1}}$. Subsets of different effective radii $r_{\mathrm{eff}}$ and silica contents $x_s$ are considered.

| $x_s$/wt.% | $r_{\mathrm{eff}}$/µm | | | | |
|---|---|---|---|---|---|
| | **0.6** | **1.8** | **3.0** | **4.5** | **6.0** |
| 45 | 229 ± 9 | 279 ± 23 | 228 ± 15 | 173 ± 6 | 140 ± 10 |
| 50 | 210 ± 14 | 290 ± 25 | 241 ± 17 | 181 ± 5 | 146 ± 10 |
| 55 | 194 ± 18 | 305 ± 28 | 255 ± 19 | 190 ± 4 | 152 ± 11 |
| 60 | 178 ± 20 | 310 ± 31 | 263 ± 21 | 195 ± 5 | 155 ± 12 |
| 65 | 164 ± 22 | 314 ± 33 | 271 ± 24 | 201 ± 5 | 159 ± 12 |
| 70 | 152 ± 24 | 321 ± 34 | 282 ± 26 | 208 ± 5 | 164 ± 13 |
| 75 | 144 ± 26 | 328 ± 35 | 292 ± 28 | 215 ± 5 | 169 ± 13 |

For the visible spectrum, mass extinction coefficients of 690 $m^2\,kg^{-1}$ at $\lambda = 532$ nm [145] and 637 $m^2\,kg^{-1}$ for $\lambda = 355$ nm [146] were found for Eyjafjallajökull volcanic ash. As the refractive index exhibits only a small variability in the visible spectrum with respect to the chemical composition [75,147], these mass extinction coefficient estimates can also be assumed to be representative for other types of volcanic ash. Thus, the optical depth of a volcanic ash cloud is roughly 3.3 times larger in the visible spectrum when comparing to a typical $k_{10.8}$ of 200 $m^2\,kg^{-1}$ at 10.8 µm. Finally, combining $m_{col}$ and $z_{ext}$ allows estimating the average mass volume concentration $c$.

VACOS can be applied quickly: processing a full MSG/SEVIRI image (3712 × 3712 pixels) on an ordinary desktop personal computer (using a single core of an Intel Core i5-6600 CPU at 3.30 GHz) with an off-the-shelf, uncustomized version of TensorFlow, each ANN needs ~70 s, excluding input/output processing. Performance could be increased by restricting the retrieval, e.g., only $\tau_{10.8}$ could be retrieved for the full disc to detect volcanic ash, whereas $z_{top}$ and $r_{eff}$ could be determined for ash-contaminated pixels only. Thus, it is possible to use VACOS operationally.

## 7. Conclusions

The new retrieval algorithm VACOS (*Volcanic Ash Cloud properties Obtained from SEVIRI*) is introduced. It derives a pixel classification, cloud top height, effective particle radius and (indirectly) the mass column concentration, each of which is done individually by a shallow artificial neural network. The artificial neural networks receive seven brightness temperatures of the infrared channels of the geostationary instrument MSG/SEVIRI as well as auxiliary data from ECMWF. Using MSG/SEVIRI allows for a comparably high temporal and spatial resolution of the retrievals. Focusing on the infrared spectrum allows the application at day and night. After the time-consuming creation of a radiative transfer simulated training dataset and the training itself, artificial neural networks are fast [64,78], have good generalization skills [52] and a high robustness with respect to perturbations [67,68]. The training dataset is of main importance for the development of artificial neural networks. Here, we perform one-dimensional radiative transfer calculations for a large set of typical atmospheric conditions with and without generic volcanic ash clouds. The radiative transfer's input data are described and the central aspects discussed, in particular pointing out the strong dependence of surface emissivities on the surface type and the viewing zenith angle, the significant variability of the atmospheric state between different years and the need for a high temporal resolution to also cover its diurnal variability. A special focus is put on the representation of the volcanic ash clouds. Macrophysical properties are reviewed, and microphysical and optical properties are received from Piontek et al. [23]. The usage of a large set of refractive indices representing different volcanic ash types with respect to their silica content and glass-to-crystal ratio is a major difference to most other artificial neural network-based volcanic ash retrievals using passive imagers: they either rely on a single or a handful of volcanic ash refractive indices or use training datasets consisting of only a few different volcanic ash clouds. We perform a validation of the ash-free radiative transfer calculations by comparing those with real MSG/SEVIRI measurements for a specific scene. An overall agreement of the statistical distributions of the brightness temperatures is found, showing that the composed atmospheric and surface data are representative for the real world. Comparing simulations and measurements on a single pixel basis, we find indications that atmospheric gas profiles and sea surface emissivities are reproduced with a high agreement. For cloudy samples, the measured and simulated brightness temperature distributions agree, but considering individual pixels significant deviations are found (with 95th percentiles of the absolute deviations >30 K), most likely introduced by a random element in the implementation of the maximum-random overlap configuration in a one-dimensional atmosphere and possible different locations of clouds in the model and reality. Land surfaces lead to large deviations, for single pixels (with median absolute deviations >3 K) as well as for the brightness temperature distributions, likely due to inaccurate skin temperatures. Finally,

we describe the architecture of the different artificial neural networks and their technical setup, input features, training and application.

Our work can be extended in different directions: the validation of the ash-free simulations shows that the representation of land surfaces is not fully realistic and could be improved, e.g., by using other model results or satellite retrieved skin temperatures. Volcanic ash plumes close to the vent often carry $SO_2$ [39,42] or ice water [148–150], both of which are neglected for reasons of simplicity. Other aerosols are also noteworthy, especially mineral dust which has similar refractive indices as volcanic ash due to their silica contents [11]. Including both in the training data, it might be possible to train an algorithm to separate volcanic ash from dust. The artificial neural networks could be improved by using additional input data, e.g., model-based vertical temperature profiles [68] or extremal or average brightness temperatures of the surrounding of a pixel [78]. The latter would require the simulation of extended areas, i.e., images of volcanic ash clouds in different atmospheric and surface settings, which would also enable the use of convolutional neural networks for image recognition [151]. As other geostationary passive imagers have similar spectral channels as MSG/SEVIRI [69,83,85,86], the algorithm might be transferable to these instruments [152]. A thorough validation of VACOS is presented in a companion paper [80]. An operational application by the German weather service (DWD) is ongoing.

To conclude, the new volcanic ash retrieval allows detecting and monitoring volcanic ash clouds above Europe, Africa and the Atlantic with high spatial and temporal resolution, enabling volcanic ash-related scientific investigations as well as aviation security-related applications.

**Author Contributions:** Conceptualization, D.P. and L.B.; methodology, D.P. and M.S.; software, D.P. and M.S.; validation, D.P.; formal analysis, D.P.; investigation, D.P.; data sources, D.K.Z.; writing—original draft preparation, D.P.; writing—review and editing, L.B., C.V., M.S. and D.K.Z.; visualization, D.P.; supervision, L.B. and C.V.; project administration, L.B.; funding acquisition, C.V. and L.B. All authors have read and agreed to the published version of the manuscript.

**Funding:** D. Piontek and L. Bugliaro were supported by the European Unions's Horizon 2020 research and innovation program under grant agreement No. 723986 (EUNADICS-AV). C. Voigt acknowledges funding by the Helmholtz Association under contract HGF W2/W3-60.

**Institutional Review Board Statement:** Not applicable.

**Informed Consent Statement:** Not applicable.

**Data Availability Statement:** Data presented in this study is available on request from the corresponding author.

**Acknowledgments:** The MSG/SEVIRI data were provided by EUMETSAT (European Organisation for the Exploitation of Meteorological Satellites) and the auxiliary data were obtained from ECMWF (European Center for Medium-Range Weather Forecasts). Radiative transfer calculations were performed on DLR's CARA (Cluster for Advanced Research in Aerospace). Furthermore, we thank M. Vázquez-Navarro, J. Strandgren, B. Mayer and M. Rapp for constructive discussions and valuable feedback; W. Beer for technical support; G. Dekoutsidis and two reviewers for the helpful comments to improve the manuscript.

**Conflicts of Interest:** The authors declare no conflict of interest.

## References

1. Siebert, L.; Simkin, T.; Kimberly, P. *Volcanoes of the World*, 3rd ed.; University of California Press: Berkeley, CA, USAA; Los Angeles, CA, USA; London, UK, 2011.
2. Wilson, T.M.; Stewart, C.; Sword-Daniels, V.; Leonard, G.S.; Johnston, D.M.; Cole, J.W.; Wardman, J.; Wilson, G.; Barnard, S.T. Volcanic ash impacts on critical infrastructure. *Phys. Chem. Earth* **2012**, *45–46*, 5–23. [CrossRef]
3. Casadevall, T.J. The 1989–1990 eruption of Redoubt Volcano, Alaska: Impacts on aircraft operations. *J. Volcanol. Geotherm. Res.* **1994**, *62*, 301–316. [CrossRef]
4. Guffanti, M.; Casadevall, T.J.; Budding, K. Encounters of aircraft with volcanic ash clouds; A compilation of known incidents, 1953–2009. U.S. Geological Survey Data Series 545, Ver. 1.0, 12 p., Plus 4 Appendixes Including the Compilation Database, 2010. Available online: https://pubs.usgs.gov/ds/545/DS545.pdf (accessed on 5 August 2021).

5. Weinzierl, B.; Sauer, D.; Minikin, A.; Reitebuch, O.; Dahlkötter, F.; Mayer, B.; Emde, C.; Tegen, I.; Gasteiger, J.; Petzold, A.; et al. On the visibility of airborne volcanic ash and mineral dust from the pilot's perspective in flight. *Phys. Chem. Earth Parts A/B/C* **2012**, *45–46*, 87–102. [CrossRef]
6. Schumann, U.; Weinzierl, B.; Reitebuch, O.; Schlager, H.; Minikin, A.; Forster, C.; Baumann, R.; Sailer, T.; Graf, K.; Mannstein, H.; et al. Airborne observations of the Eyjafjalla volcano ash cloud over Europe during air space closure in April and May 2010. *Atmos. Chem. Phys* **2011**, *11*, 2245–2279. [CrossRef]
7. Budd, L.; Griggs, S.; Howarth, D.; Ison, S. A Fiasco of Volcanic Proportions? Eyjafjallajökull and the Closure of European Airspace. *Mobilities* **2011**, *6*, 31–40. [CrossRef]
8. Pavolonis, M.J.; Sieglaff, J.; Cintineo, J. Spectrally Enhanced Cloud Objects—A generalized framework for automated detection of volcanic ash and dust clouds using passive satellite measurements: 1. Multispectral analysis. *J. Geophys. Res. Atmos.* **2015**, *120*, 7813–7841. [CrossRef]
9. Volcanic Ash Contingency Plan: European and North Atlantic Regions, Edition 2.0.0. International Civil Aviation Organization, European and North Atlantic Office. 2016. Available online: https://www.skybrary.aero/bookshelf/books/357.pdf (accessed on 5 August 2021).
10. Langmann, B. Volcanic Ash versus Mineral Dust: Atmospheric Processing and Environmental and Climate Impacts. *ISRN Atmos. Sci.* **2013**, *2013*. [CrossRef]
11. Watkin, S.C. The application of AVHRR data for the detection of volcanic ash in a Volcanic Ash Advisory Centre. *Meteorol. Appl.* **2003**, *10*, 301–311. [CrossRef]
12. Stohl, A.; Prata, A.J.; Eckhardt, S.; Clarisse, L.; Durant, A.; Henne, S.; Kristiansen, N.I.; Minikin, A.; Schumann, U.; Seibert, P.; et al. Determination of time- and height-resolved volcanic ash emissions and their use for quantitative ash dispersion modeling: The 2010 Eyjafjallajökull eruption. *Atmos. Chem. Phys.* **2011**, *11*, 4333–4351. [CrossRef]
13. Dacre, H.F.; Harvey, N.J.; Webley, P.W.; Morton, D. How accurate are volcanic ash simulations of the 2010 Eyjafjallajökull eruption? *J. Geophys. Res. Atmos.* **2016**, *121*, 3534–3547. [CrossRef]
14. Winker, D.M.; Liu, Z.; Omar, A.; Tackett, J.; Fairlie, D. CALIOP observations of the transport of ash from the Eyjafjallajökull volcano in April 2010. *J. Geophys. Res. Atmos.* **2012**, *117*. [CrossRef]
15. Winker, D.M.; Vaughan, M.A.; Omar, A.; Hu, Y.; Powell, K.A.; Liu, Z.; Hunt, W.H.; Young, S.A. Overview of the CALIPSO Mission and CALIOP Data Processing Algorithms. *J. Atmos. Ocean. Technol.* **2009**, *26*, 2310–2323. [CrossRef]
16. Jurkat, T.; Voigt, C.; Arnold, F.; Schlager, H.; Aufmhoff, H.; Schmale, J.; Schneider, J.; Lichtenstern, M.; Dörnbrack, A. Airborne stratospheric ITCIMS measurements of $SO_2$, HCl, and $HNO_3$ in the aged plume of volcano Kasatochi. *J. Geophys. Res. Atmos.* **2010**, *115*. [CrossRef]
17. Schmale, J.; Schneider, J.; Jurkat, T.; Voigt, C.; Kalesse, H.; Rautenhaus, M.; Lichtenstern, M.; Schlager, H.; Ancellet, G.; Arnold, F.; et al. Aerosol layers from the 2008 eruptions of Mount Okmok and Mount Kasatochi: In situ upper troposphere and lower stratosphere measurements of sulfate and organics over Europe. *J. Geophys. Res. Atmos.* **2010**, *115*. [CrossRef]
18. Marenco, F.; Johnson, B.; Turnbull, K.; Newman, S.; Haywood, J.; Webster, H.; Ricketts, H. Airborne lidar observations of the 2010 Eyjafjallajökull volcanic ash plume. *J. Geophys. Res. Atmos.* **2011**, *116*. [CrossRef]
19. Weber, K.; Eliasson, J.; Vogel, A.; Fischer, C.; Pohl, T.; van Haren, G.; Meier, M.; Grobéty, B.; Dahmann, D. Airborne in-situ investigations of the Eyjafjallajökull volcanic ash plume on Iceland and over north-western Germany with light aircrafts and optical particle counters. *Atmos. Environ.* **2012**, *48*, 9–21. [CrossRef]
20. Voigt, C.; Jessberger, P.; Jurkat, T.; Kaufmann, S.; Baumann, R.; Schlager, H.; Bobrowski, N.; Giuffrida, G.; Salerno, G. Evolution of $CO_2$, $SO_2$, HCl, and $HNO_3$ in the volcanic plumes from Etna. *Geophys. Res. Lett.* **2014**, *41*, 2196–2203. [CrossRef]
21. Shcherbakov, V.; Jourdan, O.; Voigt, C.; Gayet, J.F.; Chauvigne, A.; Schwarzenboeck, A.; Minikin, A.; Klingebiel, M.; Weigel, R.; Borrmann, S.; et al. Porous aerosol in degassing plumes of Mt. Etna and Mt. Stromboli. *Atmos. Chem. Phys.* **2016**, *16*, 11883–11897. [CrossRef]
22. Wen, S.; Rose, W.I. Retrieval of sizes and total masses of particles in volcanic clouds using AVHRR bands 4 and 5. *J. Geophys. Res. Atmos.* **1994**, *99*, 5421–5431. [CrossRef]
23. Piontek, D.; Hornby, A.; Voigt, C.; Bugliaro, L.; Gasteiger, J. Determination of complex refractive indices and optical properties of volcanic ashes in the thermal infrared based on generic petrological compositions. *J. Volcanol. Geotherm. Res.* **2021**, *411*, 107174. [CrossRef]
24. Prata, A.J. Infrared radiative transfer calculations for volcanic ash clouds. *Geophys. Res. Lett.* **1989**, *16*, 1293–1296. [CrossRef]
25. Prata, A.J. Observations of volcanic ash clouds in the 10–12 μm window using AVHRR/2 data. *Int. J. Remote Sens.* **1989**, *10*, 751–761. [CrossRef]
26. Inoue, T. On the Temperature and Effective Emissivity Determination of Semi-Transparent Cirrus Clouds by Bi-Spectral Measurements in the 10 μm Window Region. *J. Meteorol. Soc. Jpn.* **1985**, *63*, 88–99. [CrossRef]
27. Yu, T.; Rose, W.I.; Prata, A.J. Atmospheric correction for satellite-based volcanic ash mapping and retrievals using "split window" IR data from GOES and AVHRR. *J. Geophys. Res. Atmos.* **2002**, *107*, AAC 10–1–AAC 10–19. [CrossRef]
28. Ackerman, S.A. Remote sensing aerosols using satellite infrared observations. *J. Geophys. Res. Atmos.* **1997**, *102*, 17069–17079. [CrossRef]
29. Clarisse, L.; Prata, F.; Lacour, J.L.; Hurtmans, D.; Clerbaux, C.; Coheur, P.F. A correlation method for volcanic ash detection using hyperspectral infrared measurements. *Geophys. Res. Lett.* **2010**, *37*. [CrossRef]

30. Gangale, G.; Prata, A.; Clarisse, L. The infrared spectral signature of volcanic ash determined from high-spectral resolution satellite measurements. *Remote Sens. Environ.* **2010**, *114*, 414–425. [CrossRef]
31. Francis, P.N.; Cooke, M.C.; Saunders, R.W. Retrieval of physical properties of volcanic ash using Meteosat: A case study from the 2010 Eyjafjallajökull eruption. *J. Geophys. Res. Atmos.* **2012**, *117*. [CrossRef]
32. Guéhenneux, Y.; Gouhier, M.; Labazuy, P. Improved space borne detection of volcanic ash for real-time monitoring using 3-Band method. *J. Volcanol. Geotherm. Res.* **2015**, *293*, 25–45. [CrossRef]
33. Prata, A.J.; Grant, I.F. Retrieval of microphysical and morphological properties of volcanic ash plumes from satellite data: Application to Mt Ruapehu, New Zealand. *Q. J. R. Meteorol. Soc.* **2001**, *127*, 2153–2179. [CrossRef]
34. Pavolonis, M.J.; Feltz, W.F.; Heidinger, A.K.; Gallina, G.M. A Daytime Complement to the Reverse Absorption Technique for Improved Automated Detection of Volcanic Ash. *J. Atmos. Ocean. Technol.* **2006**, *23*, 1422–1444. [CrossRef]
35. Zhu, L.; Liu, J.; Liu, C.; Wang, M. Satellite remote sensing of volcanic ash cloud in complicated meteorological conditions. *Sci. China Earth Sci.* **2011**, *54*, 1789–1795. [CrossRef]
36. Pavolonis, M.J. Advances in Extracting Cloud Composition Information from Spaceborne Infrared Radiances—A Robust Alternative to Brightness Temperatures. Part I: Theory. *J. Appl. Meteorol. Climatol.* **2010**, *49*, 1992–2012. [CrossRef]
37. Pavolonis, M.J.; Heidinger, A.K.; Sieglaff, J. Automated retrievals of volcanic ash and dust cloud properties from upwelling infrared measurements. *J. Geophys. Res. Atmos.* **2013**, *118*, 1436–1458. [CrossRef]
38. Grainger, R.G.; Peters, D.M.; Thomas, G.E.; Smith, A.J.A.; Siddans, R.; Carboni, E.; Dudhia, A. Measuring volcanic plume and ash properties from space. *Geol. Soc. Lond. Spec. Publ.* **2013**, *380*, 293–320. [CrossRef]
39. Carn, S.A.; Krueger, A.J.; Krotkov, N.A.; Yang, K.; Evans, K. Tracking volcanic sulfur dioxide clouds for aviation hazard mitigation. *Nat. Hazards* **2009**, *51*, 325–343. [CrossRef]
40. Thomas, H.E.; Prata, A.J. Sulphur dioxide as a volcanic ash proxy during the April-May 2010 eruption of Eyjafjallajökull Volcano, Iceland. *Atmos. Chem. Phys.* **2011**, *11*, 6871–6880. [CrossRef]
41. Sears, T.M.; Thomas, G.E.; Carboni, E.; A. Smith, A.J.; Grainger, R.G. $SO_2$ as a possible proxy for volcanic ash in aviation hazard avoidance. *J. Geophys. Res. Atmos.* **2013**, *118*, 5698–5709. [CrossRef]
42. Prata, A.J.; Kerkmann, J. Simultaneous retrieval of volcanic ash and $SO_2$ using MSG-SEVIRI measurements. *Geophys. Res. Lett.* **2007**, *34*. [CrossRef]
43. Prata, A.J.; Grant, I.F. Determination of mass loadings and plume heights of volcanic ash clouds from satellite data. *CSIRO Atmos. Res. Tech. Pap.* **2001**, *48*, pp. 1–41.
44. Rodgers, C.D. *Inverse Methods for Atmospheric Sounding*; World Scientific: Singapore; River Edge, NJ, USA; London, UK, 2000. [CrossRef]
45. Pugnaghi, S.; Guerrieri, L.; Corradini, S.; Merucci, L.; Arvani, B. A new simplified approach for simultaneous retrieval of $SO_2$ and ash content of tropospheric volcanic clouds: An application to the Mt Etna volcano. *Atmos. Meas. Tech.* **2013**, *6*, 1315–1327. [CrossRef]
46. Schneider, D.J.; Van Eaton, A.R.; Wallace, K.L. Satellite observations of the 2016–2017 eruption of Bogoslof volcano: Aviation and ash fallout hazard implications from a water-rich eruption. *Bull. Volcanol.* **2020**, *82*, 29. [CrossRef]
47. Prata, A.; Turner, P. Cloud-top height determination using ATSR data. *Remote Sens. Environ.* **1997**, *59*, 1–13. [CrossRef]
48. Menzel, W.P.; Smith, W.L.; Stewart, T.R. Improved Cloud Motion Wind Vector and Altitude Assignment Using VAS. *J. Clim. Appl. Meteorol.* **1983**, *22*, 377–384. [CrossRef]
49. Taylor, I.A.; Carboni, E.; Ventress, L.J.; Mather, T.A.; Grainger, R.G. An adaptation of the $CO_2$ slicing technique for the Infrared Atmospheric Sounding Interferometer to obtain the height of tropospheric volcanic ash clouds. *Atmos. Meas. Tech.* **2019**, *12*, 3853–3883. [CrossRef]
50. Hornik, K.; Stinchcombe, M.; White, H. Multilayer feedforward networks are universal approximators. *Neural Netw.* **1989**, *2*, 359–366. [CrossRef]
51. Hsieh, W.W.; Tang, B. Applying Neural Network Models to Prediction and Data Analysis in Meteorology and Oceanography. *Bull. Am. Meteorol. Soc.* **1998**, *79*, 1855–1870. [CrossRef]
52. Gardner, M.; Dorling, S. Artificial neural networks (the multilayer perceptron)—A review of applications in the atmospheric sciences. *Atmos. Environ.* **1998**, *32*, 2627–2636. [CrossRef]
53. Cerdeña, A.; González, A.; Pérez, J.C. Remote Sensing of Water Cloud Parameters Using Neural Networks. *J. Atmos. Ocean. Technol.* **2007**, *24*, 52–63. [CrossRef]
54. Minnis, P.; Hong, G.; Sun-Mack, S.; Smith, W.L., Jr.; Chen, Y.; Miller, S.D. Estimating nocturnal opaque ice cloud optical depth from MODIS multispectral infrared radiances using a neural network method. *J. Geophys. Res. Atmos.* **2016**, *121*, 4907–4932. [CrossRef]
55. Kox, S.; Bugliaro, L.; Ostler, A. Retrieval of cirrus cloud optical thickness and top altitude from geostationary remote sensing. *Atmos. Meas. Tech.* **2014**, *7*, 3233–3246. [CrossRef]
56. Holl, G.; Eliasson, S.; Mendrok, J.; Buehler, S.A. SPARE-ICE: Synergistic ice water path from passive operational sensors. *J. Geophys. Res. Atmos.* **2014**, *119*, 1504–1523. [CrossRef]
57. Xu, J.; Schüssler, O.; Rodriguez, D.G.L.; Romahn, F.; Doicu, A. A Novel Ozone Profile Shape Retrieval Using Full-Physics Inverse Learning Machine (FP-ILM). *IEEE J. Sel. Top. Appl. Earth Obs. Remote Sens.* **2017**, *10*, 5442–5457. [CrossRef]

58. Piscini, A.; Carboni, E.; Del Frate, F.; Grainger, R.G. Simultaneous retrieval of volcanic sulphur dioxide and plume height from hyperspectral data using artificial neural networks. *Geophys. J. Int.* **2014**, *198*, 697–709. [CrossRef]
59. Efremenko, D.S.; Loyola, R.D.G.; Hedelt, P.; Spurr, R.J.D. Volcanic SO2 plume height retrieval from UV sensors using a full-physics inverse learning machine algorithm. *Int. J. Remote Sens.* **2017**, *38*, 1–27. [CrossRef]
60. Hedelt, P.; Efremenko, D.S.; Loyola, D.G.; Spurr, R.; Clarisse, L. Sulfur dioxide layer height retrieval from Sentinel-5 Precursor/TROPOMI using FP_ILM. *Atmos. Meas. Tech.* **2019**, *12*, 5503–5517. [CrossRef]
61. Loyola, D.G.; Xu, J.; Heue, K.P.; Zimmer, W. Applying FP_ILM to the retrieval of geometry-dependent effective Lambertian equivalent reflectivity (GE_LER) daily maps from UVN satellite measurements. *Atmos. Meas. Tech.* **2020**, *13*, 985–999. [CrossRef]
62. Gray, T.M.; Bennartz, R. Automatic volcanic ash detection from MODIS observations using a back-propagation neural network. *Atmos. Meas. Tech.* **2015**, *8*, 5089–5097. [CrossRef]
63. Watson, I.; Realmuto, V.; Rose, W.; Prata, A.; Bluth, G.; Gu, Y.; Bader, C.; Yu, T. Thermal infrared remote sensing of volcanic emissions using the moderate resolution imaging spectroradiometer. *J. Volcanol. Geotherm. Res.* **2004**, *135*, 75–89. [CrossRef]
64. Picchiani, M.; Chini, M.; Corradini, S.; Merucci, L.; Sellitto, P.; Del Frate, F.; Stramondo, S. Volcanic ash detection and retrievals using MODIS data by means of neural networks. *Atmos. Meas. Tech.* **2011**, *4*, 2619–2631. [CrossRef]
65. Picchiani, M.; Chini, M.; Corradini, S.; Merucci, L.; Piscini, A.; Frate, F.D. Neural network multispectral satellite images classification of volcanic ash plumes in a cloudy scenario. *Ann. Geophys.* **2014**, *57*. [CrossRef]
66. Piscini, A.; Picchiani, M.; Chini, M.; Corradini, S.; Merucci, L.; Del Frate, F.; Stramondo, S. A neural network approach for the simultaneous retrieval of volcanic ash parameters and $SO_2$ using MODIS data. *Atmos. Meas. Tech.* **2014**, *7*, 4023–4047. [CrossRef]
67. Corradini, S.; Pugnaghi, S.; Piscini, A.; Guerrieri, L.; Merucci, L.; Picchiani, M.; Chini, M. Volcanic Ash and $SO_2$ retrievals using synthetic MODIS TIR data: comparison between inversion procedures and sensitivity analysis. *Ann. Geophys.* **2014**, *57*. [CrossRef]
68. Zhu, W.; Zhu, L.; Li, J.; Sun, H. Retrieving volcanic ash top height through combined polar orbit active and geostationary passive remote sensing data. *Remote Sens.* **2020**, *12*, 953. [CrossRef]
69. Schmetz, J.; Pili, P.; Tjemkes, S.; Just, D.; Kerkmann, J.; Rota, S.; Ratier, A. An Introduction to Meteosat Second Generation (MSG). *Bull. Am. Meteorol. Soc.* **2002**, *83*, 977–992. [CrossRef]
70. Kox, S.; Schmidl, M.; Graf, K.; Mannstein, H.; Buras, R.; Gasteiger, J. A new approach on the detection of volcanic ash clouds. In Proceedings of the 2013 EUMETSAT Meteorological Satellite Conference, 16–20 September 2013, Vienna, Austria, 2013.
71. Bugliaro, L.; Piontek, D.; Kox, S.; Schmidl, M.; Mayer, B.; Müller, R.; Vázquez-Navarro, M.; Gasteiger, J.; Kar, J. Combining radiative transfer calculations and a neural network for the remote sensing of volcanic ash using MSG/SEVIRI. 2021, in preparation.
72. Jahresbericht 2015: Flugwetterdienst. Deutscher Wetterdienst, 2015. Available online: https://www.dwd.de/DE/fachnutzer/luftfahrt/download/jahresberichte_flugwetterdienst/2015.pdf?__blob=publicationFile&v=3 (accessed on 5 August 2021).
73. Meeting on the Intercomparison of Satellite-based Volcanic Ash Retrieval Algorithms, Madison WI, USA, 29 June—2 July 2015, Final Report. World Meteorological Organization. 2015. Available online: https://web.archive.org/web/20171113102551/http://www.wmo.int/pages/prog/sat/documents/SCOPE-NWC-PP2_VAIntercompWSReport2015.pdf (accessed on 5 August 2021).
74. Reed, B.E.; Peters, D.M.; McPheat, R.; Grainger, R.G. The Complex Refractive Index of Volcanic Ash Aerosol Retrieved From Spectral Mass Extinction. *J. Geophys. Res. Atmos.* **2018**, *123*, 1339–1350. [CrossRef]
75. Deguine, A.; Petitprez, D.; Clarisse, L.; Gudmundsson, S.; Outes, V.; Villarosa, G.; Herbin, H. Complex refractive index of volcanic ash aerosol in the infrared, visible, and ultraviolet. *Appl. Opt.* **2020**, *59*, 884–895. [CrossRef] [PubMed]
76. Western, L.M.; Watson, M.I.; Francis, P.N. Uncertainty in two-channel infrared remote sensing retrievals of a well-characterised volcanic ash cloud. *Bull. Volcanol.* **2015**, *77*, 67. [CrossRef]
77. Prata, G.S.; Ventress, L.J.; Carboni, E.; Mather, T.A.; Grainger, R.G.; Pyle, D.M. A New Parameterization of Volcanic Ash Complex Refractive Index Based on NBO/T and $SiO_2$ Content. *J. Geophys. Res. Atmos.* **2019**, *124*, 1779–1797. [CrossRef]
78. Strandgren, J.; Bugliaro, L.; Sehnke, F.; Schröder, L. Cirrus cloud retrieval with MSG/SEVIRI using artificial neural networks. *Atmos. Meas. Tech.* **2017**, *10*, 3547–3573. [CrossRef]
79. Strandgren, J.; Fricker, J.; Bugliaro, L. Characterisation of the artificial neural network CiPS for cirrus cloud remote sensing with MSG/SEVIRI. *Atmos. Meas. Tech.* **2017**, *10*, 4317–4339. [CrossRef]
80. Piontek, D.; Bugliaro, L.; Jayanta, K.; Schumann, U.; Marenco, F.; Plu, M.; Voigt, C. The New Volcanic Ash Retrieval VACOS Using MSG/SEVIRI and Artificial Neural Networks: 2. Validation. *Remote Sens.* **2021**, submitted.
81. ESA. Available online: https://directory.eoportal.org/web/eoportal/satellite-missions/m/meteosat-second-generation (accessed on 29 June 2020).
82. WMO. Available online: https://www.wmo-sat.info/oscar/satellites/view/303 (accessed on 29 June 2020).
83. Schmit, T.J.; Gunshor, M.M.; Menzel, W.P.; Gurka, J.J.; Li, J.; Bachmeier, A.S. Introducing the Next-Generation Advanced Baseline Imager on GOES-R. *Bull. Am. Meteorol. Soc.* **2005**, *86*, 1079–1096. [CrossRef]
84. Durand, Y.; Hallibert, P.; Wilson, M.; Lekouara, M.; Grabarnik, S.; Aminou, D.; Blythe, P.; Napierala, B.; Canaud, J.L.; Pigouche, O.; et al. The flexible combined imager onboard MTG: From design to calibration. In *Sensors, Systems, and Next-Generation Satellites XIX*; Meynart, R.; Neeck, S.P., Shimoda, H., Eds.; International Society for Optics and Photonics, SPIE: Bellingham, WA, USA, 2015; Volume 9639, pp. 1–14. [CrossRef]
85. Bessho, K.; Date, K.; Hayashi, M.; Ikeda, A.; Imai, T.; Inoue, H.; Kumagai, Y.; Miyakawa, T.; Murata, H.; Ohno, T.; et al. An Introduction to Himawari-8/9-Japan's New-Generation Geostationary Meteorological Satellites. *J. Meteorol. Soc. Jpn. Ser. II* **2016**, *94*, 151–183. [CrossRef]

86. Yang, J.; Zhang, Z.; Wei, C.; Lu, F.; Guo, Q. Introducing the New Generation of Chinese Geostationary Weather Satellites, Fengyun-4. *Bull. Am. Meteorol. Soc.* **2017**, *98*, 1637–1658. [CrossRef]
87. Montavon, G.; Orr, G.B.; Müller, K.R. (Eds.) *Neural Networks: Tricks of the Trade*, 2nd ed.; Springer: Berlin/Heidelberg, Germany, 2012. [CrossRef]
88. Zhou, D.K.; Larar, A.M.; Liu, X.; Smith, W.L.; Strow, L.L.; Yang, P.; Schlüssel, P.; Calbet, X. Global Land Surface Emissivity Retrieved From Satellite Ultraspectral IR Measurements. *IEEE Trans. Geosci. Remote Sens.* **2011**, *49*, 1277–1290. [CrossRef]
89. Zhou, D.K.; Larar, A.M.; Liu, X. MetOp-A/IASI Observed Continental Thermal IR Emissivity Variations. *IEEE J. Sel. Top. Appl. Earth Obs. Remote Sens.* **2013**, *6*, 1156–1162. [CrossRef]
90. Zhou, D.K.; Larar, A.M.; Liu, X. On the relationship between land surface infrared emissivity and soil moisture. *J. Appl. Remote Sens.* **2018**, *12*, 1–14. [CrossRef]
91. Masuda, K.; Takashima, T.; Takayama, Y. Emissivity of pure and sea waters for the model sea surface in the infrared window regions. *Remote Sens. Environ.* **1988**, *24*, 313–329. [CrossRef]
92. Wu, X.; Smith, W.L. Emissivity of rough sea surface for 8–13 μm: Modeling and verification. *Appl. Opt.* **1997**, *36*, 2609–2619. [CrossRef]
93. Niclòs, R.; Valor, E.; Caselles, V.; Coll, C.; Sánchez, J.M. In situ angular measurements of thermal infrared sea surface emissivity—Validation of models. *Remote Sens. Environ.* **2005**, *94*, 83–93. [CrossRef]
94. Masuda, K. Infrared sea surface emissivity including multiple reflection effect for isotropic Gaussian slope distribution model. *Remote Sens. Environ.* **2006**, *103*, 488–496. [CrossRef]
95. Labed, J.; Stoll, M.P. Angular variation of land surface spectral emissivity in the thermal infrared: Laboratory investigations on bare soils. *Int. J. Remote Sens.* **1991**, *12*, 2299–2310. [CrossRef]
96. Snyder, W.C.; Wan, Z.; Zhang, Y.; Feng, Y.Z. Thermal Infrared (3–14 μm) bidirectional reflectance measurements of sands and soils. *Remote Sens. Environ.* **1997**, *60*, 101–109. [CrossRef]
97. Sobrino, J.A.; Cuenca, J. Angular variation of thermal infrared emissivity for some natural surfaces from experimental measurements. *Appl. Opt.* **1999**, *38*, 3931–3936. [CrossRef] [PubMed]
98. Cuenca, J.; Sobrino, J.A. Experimental measurements for studying angular and spectral variation of thermal infrared emissivity. *Appl. Opt.* **2004**, *43*, 4598–4602. [CrossRef]
99. McAtee, B.K.; Prata, A.J.; Lynch, M.J. The Angular Behavior of Emitted Thermal Infrared Radiation (8–12 μm) at a Semiarid Site. *J. Appl. Meteorol.* **2003**, *42*, 1060–1071. [CrossRef]
100. García-Santos, V.; Valor, E.; Caselles, V.; Ángeles Burgos, M.; Coll, C. On the angular variation of thermal infrared emissivity of inorganic soils. *J. Geophys. Res. Atmos.* **2012**, *117*. [CrossRef]
101. Hersbach, H.; Bell, B.; Berrisford, P.; Hirahara, S.; Horányi, A.; Muñoz-Sabater, J.; Nicolas, J.; Peubey, C.; Radu, R.; Schepers, D.; et al. The ERA5 global reanalysis. *Q. J. R. Meteorol. Soc.* **2020**, *146*, 1999–2049. [CrossRef]
102. ECMWF. Available online: https://confluence.ecmwf.int/display/CKB/ERA5%3A+data+documentation (accessed on 30 June 2020).
103. Reineke, W.; Schlömann, M. Globale Umwelt. Klima und Mikroorganismen. In *Umweltmikrobiologie*; Springer: Berlin/Heidelberg, Germany, 2020; pp. 1–34. [CrossRef]
104. Friedlingstein, P.; O'Sullivan, M.; Jones, M.W.; Andrew, R.M.; Hauck, J.; Olsen, A.; Peters, G.P.; Peters, W.; Pongratz, J.; Sitch, S.; et al. Global Carbon Budget 2020. *Earth Syst. Sci. Data* **2020**, *12*, 3269–3340. [CrossRef]
105. Chan, K.; Chan, K. Aerosol optical depths and their contributing sources in Taiwan. *Atmos. Environ.* **2017**, *148*, 364–375. [CrossRef]
106. Chan, K. Biomass burning sources and their contributions to the local air quality in Hong Kong. *Sci. Total Environ.* **2017**, *596–597*, 212–221. [CrossRef]
107. Mayer, B.; Kylling, A.; Emde, C.; Buras, R.; Hamann, U.; Gasteiger, J.; Richter, B. libRadtrans Users's Guide, 2019. Available online: https://web.archive.org/web/20200822040829/http://www.libradtran.org/doc/libRadtran.pdf (accessed on 5 August 2021).
108. Wallace, J.; Hobbs, P. *Atmospheric Science: An Introductory Survey*, 2nd ed.; Academic Press: Burlington, MA, USA, 2006.
109. Bugliaro, L.; Zinner, T.; Keil, C.; Mayer, B.; Hollmann, R.; Reuter, M.; Thomas, W. Validation of cloud property retrievals with simulated satellite radiances: A case study for SEVIRI. *Atmos. Chem. Phys.* **2011**, *11*, 5603–5624. [CrossRef]
110. Hu, Y.X.; Stamnes, K. An Accurate Parameterization of the Radiative Properties of Water Clouds Suitable for Use in Climate Models. *J. Clim.* **1993**, *6*, 728–742. [CrossRef]
111. Wyser, K. The Effective Radius in Ice Clouds. *J. Clim.* **1998**, *11*, 1793–1802. [CrossRef]
112. Heymsfield, A.J.; Schmitt, C.; Bansemer, A. Ice Cloud Particle Size Distributions and Pressure-Dependent Terminal Velocities from In Situ Observations at Temperatures from 0° to −86 °C. *J. Atmos. Sci.* **2013**, *70*, 4123–4154. [CrossRef]
113. Yang, P.; Bi, L.; Baum, B.A.; Liou, K.N.; Kattawar, G.W.; Mishchenko, M.I.; Cole, B. Spectrally Consistent Scattering, Absorption, and Polarization Properties of Atmospheric Ice Crystals at Wavelengths from 0.2 to 100 μm. *J. Atmos. Sci.* **2013**, *70*, 330–347. [CrossRef]
114. Baum, B.A.; Yang, P.; Heymsfield, A.J.; Bansemer, A.; Cole, B.H.; Merrelli, A.; Schmitt, C.; Wang, C. Ice cloud single-scattering property models with the full phase matrix at wavelengths from 0.2 to 100 μm. *J. Quant. Spectrosc. Radiat. Transf.* **2014**, *146*, 123–139. [CrossRef]

115. Krebs, W.; Mannstein, H.; Bugliaro, L.; Mayer, B. Technical note: A new day- and night-time Meteosat Second Generation Cirrus Detection Algorithm MeCiDA. *Atmos. Chem. Phys.* **2007**, *7*, 6145–6159. [CrossRef]
116. Vázquez-Navarro, M.; Mayer, B.; Mannstein, H. A fast method for the retrieval of integrated longwave and shortwave top-of-atmosphere upwelling irradiances from MSG/SEVIRI (RRUMS). *Atmos. Meas. Tech.* **2013**, *6*, 2627–2640. [CrossRef]
117. Polacci, M.; Andronico, D.; de' Michieli Vitturi, M.; Taddeucci, J.; Cristaldi, A. Mechanisms of Ash Generation at Basaltic Volcanoes: The Case of Mount Etna, Italy. *Front. Earth Sci.* **2019**, *7*, 193. [CrossRef]
118. Gudmundsson, M.T.; Thordarson, T.; Höskuldsson, R.; Larsen, G.; Björnsson, H.; Prata, F.J.; Oddsson, B.; Magnússon, E.; Högnadóttir, T.; Petersen, G.N.; et al. Ash generation and distribution from the April-May 2010 eruption of Eyjafjallajökull, Iceland. *Sci. Rep.* **2012**, *2*, 572. [CrossRef] [PubMed]
119. Klüser, L.; Erbertseder, T.; Meyer-Arnek, J. Observation of volcanic ash from Puyehue–Cordón Caulle with IASI. *Atmos. Meas. Tech.* **2013**, *6*, 35–46. [CrossRef]
120. Sparks, R.S.J. The dimensions and dynamics of volcanic eruption columns. *Bull. Volcanol.* **1986**, *48*, 3–15. [CrossRef]
121. Sparks, R.J.; Moore, J.G.; Rice, C.J. The initial giant umbrella cloud of the May 18th, 1980, explosive eruption of Mount St. Helens. *J. Volcanol. Geotherm. Res.* **1986**, *28*, 257–274. [CrossRef]
122. Tupper, A.; Textor, C.; Herzog, M.; Graf, H.F.; Richards, M.S. Tall clouds from small eruptions: The sensitivity of eruption height and fine ash content to tropospheric instability. *Nat. Hazards* **2009**, *51*, 375–401. [CrossRef]
123. Turnbull, K.; Johnson, B.; Marenco, F.; Haywood, J.; Minikin, A.; Weinzierl, B.; Schlager, H.; Schumann, U.; Leadbetter, S.; Woolley, A. A case study of observations of volcanic ash from the Eyjafjallajökull eruption: 1. In situ airborne observations. *J. Geophys. Res. Atmos.* **2012**, *117*. [CrossRef]
124. Lee, K.H.; Wong, M.S.; Chung, S.R.; Sohn, E. Improved volcanic ash detection based on a hybrid reverse absorption technique. *Atmos. Res.* **2014**, *143*, 31–42. [CrossRef]
125. Briggs, G.A. Plume Rise Predictions. In *Lectures on Air Pollution and Environmental Impact Analyses*; American Meteorological Society: Boston, MA, USA, 1982; Chapter 3, pp. 59–111.
126. Manins, P. Cloud heights and stratospheric injections resulting from a thermonuclear war. *Atmos. Environ.* **1985**, *19*, 1245–1255. [CrossRef]
127. Schmehl, K.J.; Haupt, S.E.; Pavolonis, M.J. A Genetic Algorithm Variational Approach to Data Assimilation and Application to Volcanic Emissions. *Pure Appl. Geophys.* **2012**, *169*, 519–537. [CrossRef]
128. Przedpelski, Z.J.; Casadevall, T.J. Impact of Volcanic Ash from 15 December 1989 Redoubt Volcano Eruption on GE CF6-80C2 Turbofan Engines. In *Volcanic Ash and Aviation Safety: Proceedings of the First International Symposium on Volcanic Ash and Aviation Safety, U.S. Geological Survey Bulletin 2047*; U.S. Government Printing Office: Washington, DC, USA, 1994; pp. 129–135.
129. Gasteiger, J.; Wiegner, M. MOPSMAP v1.0: A versatile tool for the modeling of aerosol optical properties. *Geosci. Model Dev.* **2018**, *11*, 2739–2762. [CrossRef]
130. Mayer, B.; Kylling, A. Technical note: The libRadtran software package for radiative transfer calculations-description and examples of use. *Atmos. Chem. Phys.* **2005**, *5*, 1855–1877. [CrossRef]
131. Emde, C.; Buras-Schnell, R.; Kylling, A.; Mayer, B.; Gasteiger, J.; Hamann, U.; Kylling, J.; Richter, B.; Pause, C.; Dowling, T.; et al. The libRadtran software package for radiative transfer calculations (version 2.0.1). *Geosci. Model Dev.* **2016**, *9*, 1647–1672. [CrossRef]
132. Stamnes, K.; Tsay, S.C.; Wiscombe, W.; Jayaweera, K. Numerically stable algorithm for discrete-ordinate-method radiative transfer in multiple scattering and emitting layered media. *Appl. Opt.* **1988**, *27*, 2502–2509. [CrossRef] [PubMed]
133. Buras, R.; Dowling, T.; Emde, C. New secondary-scattering correction in DISORT with increased efficiency for forward scattering. *J. Quant. Spectrosc. Radiat. Transf.* **2011**, *112*, 2028–2034. [CrossRef]
134. Buehler, S.; John, V.; Kottayil, A.; Milz, M.; Eriksson, P. Efficient radiative transfer simulations for a broadband infrared radiometer—Combining a weighted mean of representative frequencies approach with frequency selection by simulated annealing. *J. Quant. Spectrosc. Radiat. Transf.* **2010**, *111*, 602–615. [CrossRef]
135. Gasteiger, J.; Emde, C.; Mayer, B.; Buras, R.; Buehler, S.; Lemke, O. Representative wavelengths absorption parameterization applied to satellite channels and spectral bands. *J. Quant. Spectrosc. Radiat. Transf.* **2014**, *148*, 99–115. [CrossRef]
136. Ackerman, S.A.; Smith, W.L.; Revercomb, H.E.; Spinhirne, J.D. The 27–28 October 1986 FIRE IFO Cirrus Case Study: Spectral Properties of Cirrus Clouds in the 8–12 μm Window. *Mon. Weather Rev.* **1990**, *118*, 2377–2388. [CrossRef]
137. Trigo, I.F.; Boussetta, S.; Viterbo, P.; Balsamo, G.; Beljaars, A.; Sandu, I. Comparison of model land skin temperature with remotely sensed estimates and assessment of surface- atmosphere coupling. *J. Geophys. Res. Atmos.* **2015**, *120*, 12096–12111. [CrossRef]
138. Johannsen, F.; Ermida, S.; Martins, J.; Trigo, I.; Nogueira, M.; Dutra, E. Cold Bias of ERA5 Summertime Daily Maximum Land Surface Temperature over Iberian Peninsula. *Remote Sens.* **2019**, *11*, 2570. [CrossRef]
139. Abadi, M.; Agarwal, A.; Barham, P.; Brevdo, E.; Chen, Z.; Citro, C.; Corrado, G.; Davis, A.; Dean, J.; Devin, M.; et al. TensorFlow: Large-Scale Machine Learning on Heterogeneous Distributed Systems. *arXiv* **2015**, arXiv:1603.04467.
140. Abadi, M.; Barham, P.; Chen, J.; Chen, Z.; Davis, A.; Dean, J.; Devin, M.; Ghemawat, S.; Irving, G.; Isard, M.; et al. TensorFlow: A system for large-scale machine learning. In Proceedings of the 12th USENIX Symposium on Operating Systems Design and Implementation (OSDI'16), Savannah, GA, USA, 2–4 November 2016; USENIX Association: Berkeley, CA, USA, 2016; pp. 265–283
141. Keras. 2015. Available online: https://keras.io (accessed on 5 August 2021).
142. Goodfellow, I.; Bengio, Y.; Courville, A. *Deep Learning: Das umfassende Handbuch*, 1st ed.; MITP: Frechen, Germany, 2018.

143. Dozat, T. Incorporating Nesterov Momentum into Adam. 2016. Available online: https://openreview.net/pdf?id=OM0jvwB8jIp57ZJjtNEZ (accessed on 5 August 2021).
144. Ruder, S. An Overview of Gradient Descent Optimization Algorithms. 2016. Available online: https://arxiv.org/pdf/1609.04747.pdf (accessed on 5 August 2021).
145. Gasteiger, J.; Groß, S.; Freudenthaler, V.; Wiegner, M. Volcanic ash from Iceland over Munich: Mass concentration retrieved from ground-based remote sensing measurements. *Atmos. Chem. Phys.* **2011**, *11*, 2209–2223. [CrossRef]
146. Hervo, M.; Quennehen, B.; Kristiansen, N.I.; Boulon, J.; Stohl, A.; Fréville, P.; Pichon, J.M.; Picard, D.; Labazuy, P.; Gouhier, M.; et al. Physical and optical properties of 2010 Eyjafjallajökull volcanic eruption aerosol: Ground-based, Lidar and airborne measurements in France. *Atmos. Chem. Phys.* **2012**, *12*, 1721–1736. [CrossRef]
147. Ball, J.G.C.; Reed, B.E.; Grainger, R.G.; Peters, D.M.; Mather, T.A.; Pyle, D.M. Measurements of the complex refractive index of volcanic ash at 450, 546.7, and 650 nm. *J. Geophys. Res. Atmos.* **2015**, *120*, 7747–7757. [CrossRef]
148. Rose, W.; Gu, Y.; Watson, I.; Yu, T.; Blut, G.; Prata, A.; Krueger, A.; Krotkov, N.; Carn, S.; Fromm, M.; et al. The February–March 2000 Eruption of Hekla, Iceland from a Satellite Perspective. In *Volcanism and the Earth's Atmosphere*; American Geophysical Union: Washington, DC, USA, 2004; pp. 107–132. [CrossRef]
149. Rose, W.I.; Bluth, G.J.S.; Watson, I.M. Ice in Volcanic Clouds: When and Where? In Proceedings of the 2nd International Conference on Volcanic Ash and Aviation Safety, Alexandria, VA, USA, 21–24 June 2004; Office of the Federal Coordinator for Meteorological Services and Supporting Research: Silver Spring, MD, USA, 2004, pp. 3.27–3.33.
150. Durant, A.J.; Shaw, R.A.; Rose, W.I.; Mi, Y.; Ernst, G.G.J. Ice nucleation and overseeding of ice in volcanic clouds. *J. Geophys. Res. Atmos.* **2008**, *113*. [CrossRef]
151. Drönner, J.; Korfhage, N.; Egli, S.; Mühling, M.; Thies, B.; Bendix, J.; Freisleben, B.; Seeger, B. Fast Cloud Segmentation Using Convolutional Neural Networks. *Remote Sens.* **2018**, *10*, 1782. [CrossRef]
152. De Laat, A.; Vazquez-Navarro, M.; Theys, N.; Stammes, P. Analysis of properties of the 19 February 2018 volcanic eruption of Mount Sinabung in S5P/TROPOMI and Himawari-8 satellite data. *Nat. Hazards Earth Syst. Sci.* **2020**, *20*, 1203–1217. [CrossRef]

## 3.3 P3: Validation and application of VACOS

### The New Volcanic Ash Satellite Retrieval VACOS Using MSG/SEVIRI and Artificial Neural Networks: 2. Validation

**Dennis Piontek**, Luca Bugliaro, Jayanta Kar, Ulrich Schumann, Franco Marenco, Matthieu Plu, Christiane Voigt
Remote Sensing 2021, 13, 3128.

**Overview** In this paper, the volcanic ash retrieval VACOS is validated and characterized using a simulated test data set, CALIOP retrievals, airborne lidar and in situ measurements obtained during measurement campaigns of the DLR and the FAAM, and the results of a volcanic ash transport and dispersion model ensemble. A sensitivity study with respect to the volcanic ash cloud profile is conducted to quantify the uncertainty related to the assumption of a single homogeneous ash layer, which was adopted during the algorithm development. The importance of different input features is investigated and inferences are drawn about the working principles of the artificial neural networks.

**Author contribution** I conceptualized the research with LB. JK provided the retrievals of volcanic ash mass loads and cloud top heights from CALIPSO/CALIOP data. US provided airborne in situ measurements of volcanic ash mass concentrations. FM provided airborne lidar-derived volcanic ash mass profiles. MP provided results of a volcanic ash transport and dispersion model ensemble. LB performed cirrus retrievals for MSG/SEVIRI observations. I provided the simulated test data, applied VACOS, conducted the validation of the VACOS retrievals against all available reference data, performed the sensitivity study for volcanic ash cloud profiles, analyzed the input feature importance and discussed the working principles of the artificial neural networks, prepared all figures and wrote the manuscript. LB and CV supervised the research. All authors reviewed manuscript drafts.

remote sensing

MDPI

Article

# The New Volcanic Ash Satellite Retrieval VACOS Using MSG/SEVIRI and Artificial Neural Networks: 2. Validation

**Dennis Piontek [1,*], Luca Bugliaro [1], Jayanta Kar [2,3], Ulrich Schumann [1], Franco Marenco [4,5], Matthieu Plu [6] and Christiane Voigt [1,7]**

1 Deutsches Zentrum für Luft- und Raumfahrt (DLR), Institut für Physik der Atmosphäre, 82234 Weßling-Oberpfaffenhofen, Germany; luca.bugliaro@dlr.de (L.B.); ulrich.schumann@dlr.de (U.S.); christiane.voigt@dlr.de (C.V.)
2 Science Systems and Applications Inc., Hampton, VA 23666, USA; jayanta.kar@nasa.gov
3 Science Directorate, NASA Langley Research Center, Hampton, VA 23666, USA
4 Space Applications and Nowcasting, Met Office, Exeter EX1 3PB, UK; franco.marenco@metoffice.gov.uk
5 Climate and Atmosphere Research Centre (CARE-C), Cyprus Institute, Aglantzia, Nicosia 2121, Cyprus
6 Centre National de Recherches Météorologiques (CNRM), University of Toulouse, Météo-France, CNRS, 31057 Toulouse, France; matthieu.plu@meteo.fr
7 Institut für Physik der Atmosphäre, Johannes Gutenberg-Universität Mainz, 55099 Mainz, Germany
* Correspondence: dennis.piontek@dlr.de

**Abstract:** Volcanic ash clouds can damage aircrafts during flight and, thus, have the potential to disrupt air traffic on a large scale, making their detection and monitoring necessary. The new retrieval algorithm VACOS (*Volcanic Ash Cloud properties Obtained from SEVIRI*) using the geostationary instrument MSG/SEVIRI and artificial neural networks is introduced in a companion paper. It performs pixelwise classifications and retrieves (indirectly) the mass column concentration, the cloud top height and the effective particle radius. VACOS is comprehensively validated using simulated test data, CALIOP retrievals, lidar and in situ data from aircraft campaigns of the DLR and the FAAM, as well as volcanic ash transport and dispersion multi model multi source term ensemble predictions. Specifically, emissions of the eruptions of Eyjafjallajökull (2010) and Puyehue-Cordón Caulle (2011) are considered. For ash loads larger than 0.2 g m$^{-2}$ and a mass column concentration-based detection procedure, the different evaluations give probabilities of detection between 70% and more than 90% at false alarm rates of the order of 0.3–3%. For the simulated test data, the retrieval of the mass load has a mean absolute percentage error of ~40% or less for ash layers with an optical thickness at 10.8 µm of 0.1 (i.e., a mass load of about 0.3–0.7 g m$^{-2}$, depending on the ash type) or more, the ash cloud top height has an error of up to 10% for ash layers above 5 km, and the effective radius has an error of up to 35% for radii of 0.6–6 µm. The retrieval error increases with decreasing ash cloud thickness and top height. VACOS is applicable even for overlaying meteorological clouds, for example, the mean absolute percentage error of the optical depth at 10.8 µm increases by only up to ~30%. Viewing zenith angles >60° increase the mean percentage error by up to ~20%. Desert surfaces are another source of error. Varying geometrical ash layer thicknesses and the occurrence of multiple layers can introduce an additional error of about 30% for the mass load and 5% for the cloud top height. For the CALIOP data, comparisons with its predecessor VADUGS (operationally used by the DWD) show that VACOS is more robust, with retrieval errors of mass load and ash cloud top height reduced by >10% and >50%, respectively. Using the model data indicates an increase in detection rate in the order of 30% and more. The reliability under a wide spectrum of atmospheric conditions and volcanic ash types make VACOS a suitable tool for scientific studies and air traffic applications related to volcanic ash clouds.

**Keywords:** volcanic ash cloud; passive satellite remote sensing; artificial neural network; validation; Eyjafjallajökull; Puyehue-Cordón Caulle; lidar; in situ; transport and dispersion model

check for updates

**Citation:** Piontek, D.; Bugliaro, L.; Kar, J.; Schumann, U.; Marenco, F.; Plu, M.; Voigt, C. The New Volcanic Ash Satellite Retrieval VACOS Using MSG/SEVIRI and Artificial Neural Networks: 2. Validation. *Remote Sens.* **2021**, *13*, 3128. https://doi.org/10.3390/rs13163128

Academic Editor: Carmine Serio

Received: 1 July 2021
Accepted: 3 August 2021
Published: 7 August 2021

**Publisher's Note:** MDPI stays neutral with regard to jurisdictional claims in published maps and institutional affiliations.

**Copyright:** © 2021 by the authors. Licensee MDPI, Basel, Switzerland. This article is an open access article distributed under the terms and conditions of the Creative Commons Attribution (CC BY) license (https://creativecommons.org/licenses/by/4.0/).

## 1. Introduction

A new volcanic ash retrieval using *artificial neural networks* (ANNs) and the *Spinning Enhanced Visible and Infrared Imager* (SEVIRI) aboard the *Meteosat Second Generation* (MSG) satellites is developed and presented; this algorithm is called VACOS (*Volcanic Ash Cloud Properties Obtained from SEVIRI*) and builds upon its predecessor VADUGS (*Volcanic Ash Detection Using Geostationry Satellites* [1]). The companion paper [2] describes the algorithm development: Using a comprehensive set of volcanic ash optical properties [3], surface emissivities [4–6] and atmospheric profiles of pressure, temperature, air density, concentrations of oxygen, water vapor, ozone, carbon dioxide and nitrogen dioxide, liquid and ice water clouds, mostly derived from ECMWF model reanalyses, one-dimensional radiative transfer calculations are performed with and without realistic volcanic ash clouds to create training, validation and test data sets. These three simulated data sets contain the volcanic ash cloud properties, i.e., geometrical vertical extent, mass volume concentration, cloud top height, the brightness temperatures (BTs) of the infrared channels of SEVIRI and various auxiliary quantities. The ash-free simulations are validated by comparing the results of radiative transfer calculations of a specific date with the corresponding SEVIRI measurements. Using the simulated data sets, four different ANNs are trained for the pixelwise retrieval of the optical depth at 10.8 µm due to ash ($\tau_{10.8}$), the ash cloud top height (in m, $z_{\mathrm{top}}$), the effective particle radius (in µm, $r_{\mathrm{eff}}$) and an overall classification in four categories (ash-free and cloud-free; only meteorological clouds; only volcanic ash clouds; both volcanic ash and meteorological clouds present). The ANN for classification returns a normalized four-dimensional vector, where each component can be roughly interpreted as the probability of the corresponding category. The four ANNs perform independently of each other, but the retrievals of $z_{\mathrm{top}}$ and $r_{\mathrm{eff}}$ receive an estimate of $\tau_{10.8}$ as an input. This approach allowed to use different training data sets and ANN settings for each retrieval.

This paper contains an analysis of the retrieval performance: A detailed validation with respect to simulated test data sets is presented (Section 2) and the sensitivity of the retrievals with respect to the volcanic ash cloud profile is given (Section 3). To demonstrate the reliability of the new algorithm and to check its performance with respect to its predecessor, various comparisons with other remote and in situ measurements (Section 4) and model calculations were made (Section 5). The individual features of the final ANNs are analyzed to make some inferences on the functioning of the algorithms (Section 6). Finally, we give a conclusion and an outlook.

## 2. Performance on Simulated Test Data

The development of the VACOS retrieval is described in Piontek et al. [2]. In the following, we systematically quantify the performance of the retrievals with respect to volcanic ash cloud properties, presence of meteorological clouds (defined to include liquid and ice water clouds) and geographic location. Therefore, the ANNs are applied to the test data sets A (1,252,470 samples) or B (405,556 samples) from Piontek et al. [2], depending on their training data set. The samples of the test data sets are the results of independent radiative transfer calculations and can be compared to the situation for single pixels in a SEVIRI image. The VACOS results are compared with these true values, providing references for the error of the retrievals; those might be larger in reality due to more complicated atmospheric conditions (e.g., additional aerosols such as mineral dust), cases that have not been covered by the training data set (e.g., non-homogeneous ash clouds or multiple ash layers, emitted sulfur dioxide) or slight differences between our radiative transfer calculations and the reality (e.g., due to partial cloud covers, inaccuracies due to the applied parameterizations for meteorological clouds). The error metrics *mean absolute percentage error* (MAPE), *mean percentage error* (MPE), *probability of detection* (POD), *false alarm rate* (FAR) and *accuracy* are used and described in Appendix A.

### 2.1. Classification

The classification ANN returns a normalized four-dimensional vector with each component interpreted as the probability of the corresponding category, see Table 1. Defining that a sample is assigned to a given category if the corresponding component is >50%, the accuracy is 92% with 0.012% of the samples remaining unclassified. These values depend on the composition of the test data set with respect to the different categories, as they are retrieved with different accuracy, see Table 1. Whereas clear sky, cloudy and ash-loaded samples are correctly classified with probabilities of more than 90% each, samples with both meteorological and ash clouds are correctly classified in only 49% of the cases. About 47% of those samples were classified as ash only. Again, this might depend on the composition of the test data; samples with thick ash clouds on top of comparably thin meteorological clouds might be misclassified as ash only. Reducing the amount of these samples in the test data set would significantly modify the results in Table 1. Nevertheless, VACOS is able to detect the presence of ash in almost all cases even for this category, with only 4.1% of the ash remaining undetected. Next, only the samples containing ash and meteorological clouds are considered and separated according to the location of the meteorological clouds as *above* or *below* the ash layer, where we define that *above* denotes that no meteorological clouds are below the volcanic ash cloud bottom and *below* that no meteorological cloud is above the ash cloud top. Samples with multiple meteorological clouds located both above and below the ash layer are not included in either class. Again, note that we do not differentiate between liquid and ice water clouds, although ice water clouds can be expected to dominate for altitudes in the upper troposphere and liquid water clouds in the lower troposphere, and although ice water clouds might damp the ash signal, e.g., in $BTD_{11\text{–}12}$. Furthermore, the dependence on the optical depth of the meteorological clouds themselves is not investigated, although expected to be significant. Table 2 shows the classification of the two subsets. Nearly all samples are classified as ash-containing if the meteorological cloud is below, and astonishingly still ~85% if it is above. The amount of correctly classified samples (i.e., both ash and meteorological cloud) is ~15% higher for meteorological clouds below than above, whereas ~15% of the samples are classified as containing only meteorological clouds if those are above but less than 1% if they are below. This represents the well known fact that an optically thick meteorological cloud can effectively hide a below-cloud volcanic ash layer from the satellite observation. More than 48% of the samples are classified as containing only ash, independently of the position of the meteorological clouds. Motivated by the fact that the identification of cases with both ash and meteorological clouds is not very reliable, but that ash is detected in the majority of the situations, a binary ash flag $P_{\text{ash}}$ (i.e., ash or no ash) is introduced by adding the probabilities of the two categories without ash (*clear*, *clouds*) and the two with ash (*ash*, *both*), respectively. Now, if the resulting probability for ash is above 80%, we assume that ash is present, otherwise not; the threshold is motivated in Section 2.3. The binary ash flag will be used in the rest of the section. It has an accuracy of 99.5%, a POD of 98.6% and a FAR of 0.008% for the simulated data.

**Table 1.** Results of the classification ANN with respect to the simulated test data in percent; four categories are differentiated: ash-free and cloud-free (*clear*), only meteorological clouds (*clouds*), only volcanic ash (*ash*), both volcanic ash and meteorological clouds (*both*); the true value is given in the left column, the corresponding number of samples and how they are classified is given in the other columns.

| | | Retrieval/% | | | |
|---|---|---|---|---|---|
| **Truth** | **Samples** | **Clear** | **Clouds** | **Ash** | **Both** |
| clear | 560,713 | 99.7 | 0.3 | <0.1 | <0.1 |
| clouds | 287,740 | 5.6 | 94.3 | <0.1 | <0.1 |
| ash | 279,395 | <0.1 | <0.1 | 94.6 | 5.2 |
| both | 124,622 | <0.1 | 4.1 | 46.8 | 49.2 |

**Table 2.** Results of the classification ANN with respect to the simulated test data in percent; only samples with volcanic ash and meteorological clouds are considered; *above* denotes that no meteorological clouds are below the volcanic ash cloud bottom and *below* that no meteorological cloud is above the ash cloud top; the retrieval categories are the same as in Table 1.

| | | Retrieval/% | | | |
|---|---|---|---|---|---|
| **Cloud Location** | **Samples** | **Clear** | **Clouds** | **Ash** | **Both** |
| above | 21,833 | <0.1 | 15.1 | 48.8 | 36.1 |
| below | 81,630 | <0.1 | 0.3 | 48.0 | 51.6 |

### *2.2. Dependence on Volcanic Ash Cloud Properties, Meteorological Clouds and Geographic Coordinates*

Next we analyze the binary ash flag and the regression retrievals in detail. As metrics we calculate the accuracy for the binary ash flag, and MAPE and MPE for the retrievals of $\tau_{10.8}$, $z_{\mathrm{top}}$ and $r_{\mathrm{eff}}$ for simulated samples within certain intervals of the true values $\tau'_{10.8}$, $z'_{\mathrm{top}}$ or $r'_{\mathrm{eff}}$ (in the rest of this work, primed quantities will always denote the reference data, which might be the truth when using simulated data, or in situ measurement/retrieval/model results in the other cases). As discussed in Piontek et al. [2], $\tau'_{10.8}$ can be converted to a mass column concentration $m'_{\mathrm{col}}$ using the mass extinction coefficient at 10.8 µm, with a mean value of ~200 $\mathrm{m^2\,kg^{-1}}$. Thus, the investigated range $\tau'_{10.8} \in [0.01, 10]$ corresponds approximately to $m'_{\mathrm{col}} \in [0.05, 50]\,\mathrm{g\,m^{-2}}$. $m'_{\mathrm{col}} = 0.05\,\mathrm{g\,m^{-2}}$ is quite low; typical mass loads are about one order of magnitude larger (Section 4). Figure 1 shows subsets with land and sea surfaces, and with and without meteorological clouds. Figure 2 shows results for ash-containing samples with meteorological clouds above and below the ash layer (as defined before). Test data set A is considered for the binary ash flag when investigating the dependence on $\tau'_{10.8}$, otherwise only the ash-loaded samples are used. For the retrieval of $\tau_{10.8}$ only the ash-loaded samples of test data set A are used, and for the retrieval of $z_{\mathrm{top}}$ and $r_{\mathrm{eff}}$ the test data set B, which also contains only ash-loaded samples [2]. Note that no prior selection is made based on whether or not ash is detected in a sample using the binary ash flag or the retrieved $\tau_{10.8}$. The sample distribution for test data set B is given in Figures 1h and 2h; generally, the distribution is similar for test data set A with differences of <10%, except for the first bin which contains also the ash-free samples when considering the accuracy with respect to $\tau'_{10.8}$.

For the binary ash flag, high accuracies of 90–100% are found for usual ash clouds ($\tau'_{10.8} > 0.1$) and in absence of volcanic ash (left-most bin in Figure 1a1). The additional presence of meteorological clouds decreases the accuracy: if they are above the ash layer the difference is of the order of 20%, whereas the influence is much smaller when they are below. This demonstrates that ash layers might often be hidden by the meteorological clouds above. The accuracy is also close to 100% for $z'_{\mathrm{top}} > 5$ km, but decreases with decreasing $z'_{\mathrm{top}}$. The latter might be partly connected to the impact of water vapor above the ash cloud, as their column load above the ash layer increases with decreasing $z'_{\mathrm{top}}$. However, as the accuracy decreases only slightly for $z'_{\mathrm{top}} < 5$ km compared to higher $z'_{\mathrm{top}}$ in the absence of meteorological clouds, the impact of water vapor appears to be limited. The presence of meteorological clouds leads to a much worse performance, especially for $z'_{\mathrm{top}} < 5$ km and if the meteorological clouds are above the ash layer, where the accuracy drops well below 50%. The dependence on $r'_{\mathrm{eff}}$ is generally small, except when meteorological clouds are present above, leading to a decreasing accuracy with ~90% for $r'_{\mathrm{eff}} = 0.6$ µm, but less than 60% for $r'_{\mathrm{eff}} = 6$ µm. The dependence on the surface (land/sea) is small.

For the regression ANNs, the MAPE generally decreases from roughly 100% for $\tau'_{10.8} = 0.03$ / $z'_{\mathrm{top}} = 1$ km to less than 30% for $\tau'_{10.8} = 10$ / $z'_{\mathrm{top}} = 18$ km with increasing $\tau'_{10.8}$ and $z'_{\mathrm{top}}$, and is up to 35% with respect to $r'_{\mathrm{eff}}$. In all cases, the MAPE is smallest in the absence of meteorological clouds and largest in their presence, with significantly larger errors for meteorological clouds above with respect to $\tau'_{10.8} > 0.3$ and $r'_{\mathrm{eff}}$, and for meteorological clouds below with respect to $z'_{\mathrm{top}}$. The MAPEs for land and sea surfaces are again rather similar.

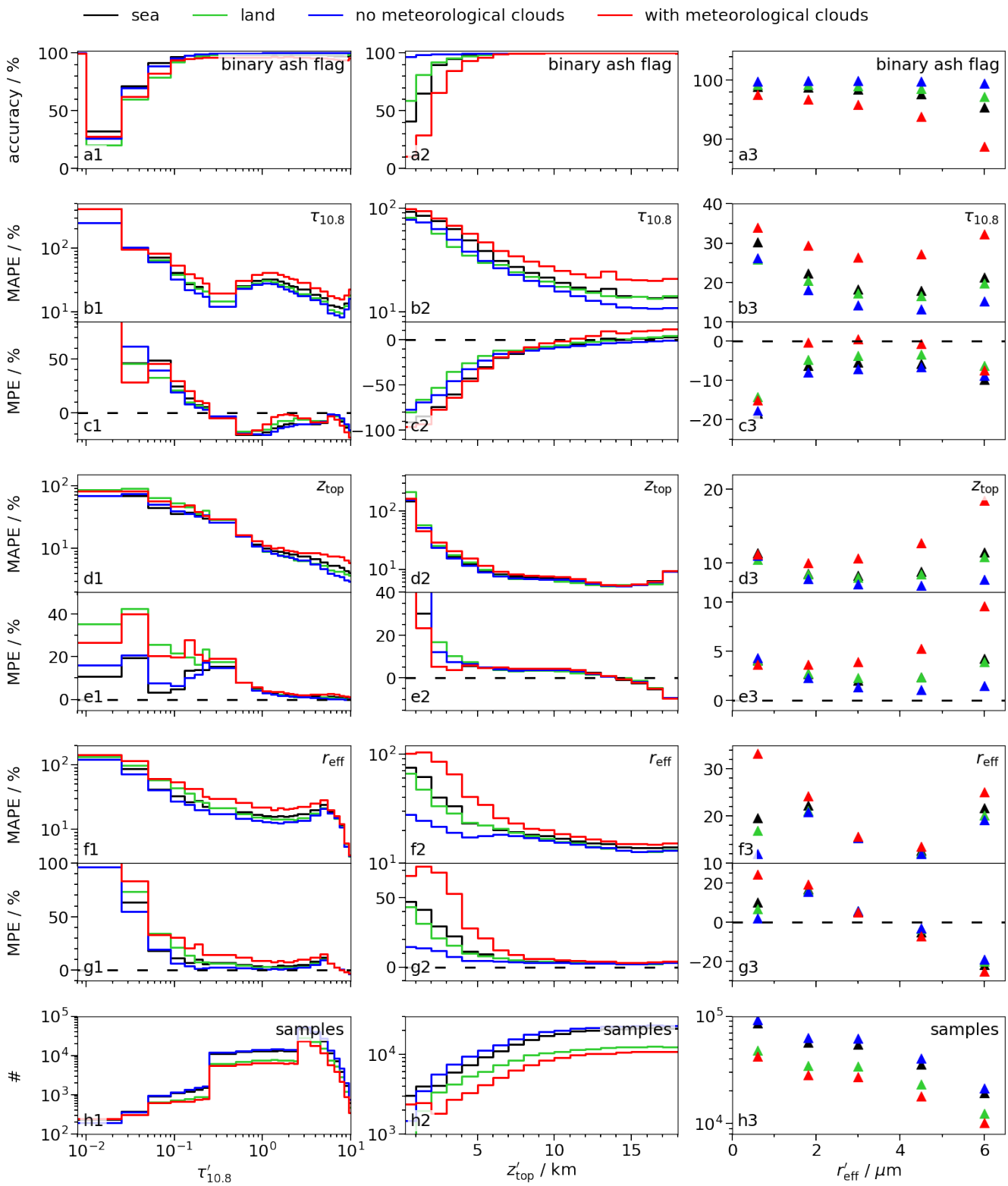


**Figure 1.** Estimations of the accuracy of the binary ash flag (**a**), and MAPE and MPE for the retrievals of $\tau_{10.8}$ (**b**,**c**), $z_{top}$ (**d**,**e**) and $r_{eff}$ (**f**,**g**) based on the simulated test data sets; the columns show the performance for different $\tau'_{10.8}$ (**1**), $z'_{top}$ (**2**) and $r'_{eff}$ (**3**); for (**a**–**c**) the test data set A is used, for (**d**–**g**) test data set B [2]; for (**b**,**c**) only ash-loaded samples are considered; the sample distribution of test data set B is shown in (**h**); different subsets are shown, i.e., only sea (black) or land (green) surfaces, only samples with meteorological clouds (red) or without meteorological clouds (blue).

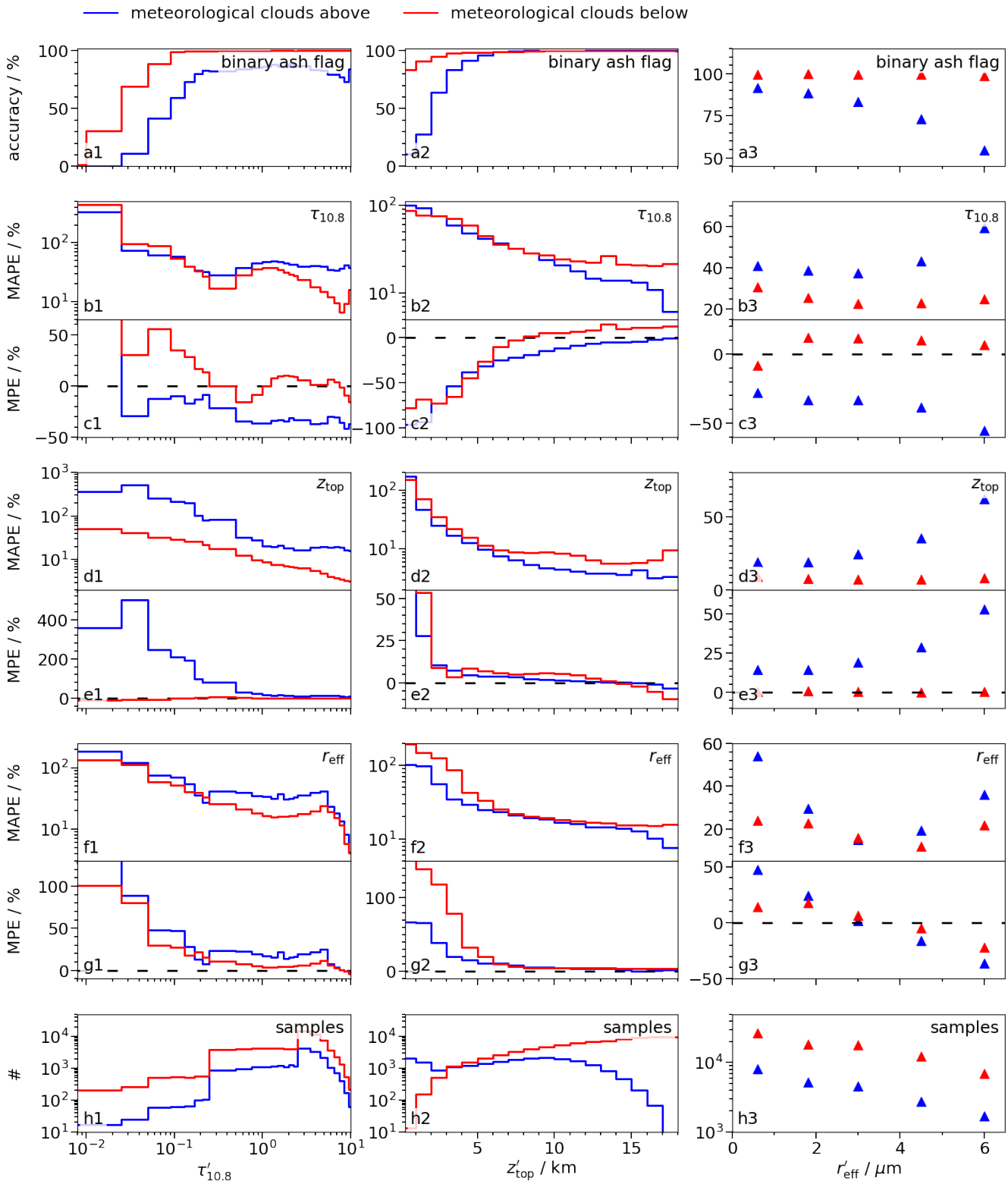


**Figure 2.** Similar as in Figure 1: Estimations of the accuracy of the binary ash flag (**a**), and MAPE and MPE for the retrievals of $\tau_{10.8}$ (**b**,**c**), $z_{top}$ (**d**,**e**) and $r_{eff}$ (**f**,**g**) based on the simulated test data sets; the columns show the performance for different $\tau'_{10.8}$ (**1**), $z'_{top}$ (**2**) and $r'_{eff}$ (**3**); for (**a**–**c**) the test data set A is used, for (**d**–**g**) test data set B [2]; for (**b**,**c**) only ash-loaded samples are considered; the sample distribution of test data set B is shown in (**h**); only samples with meteorological clouds above (blue) and below (red) the volcanic ash layer are considered.

On average, the retrieval of $\tau_{10.8}$ is biased towards high values for $\tau'_{10.8} < 0.25$ (i.e., MPE $> 0$) and towards low values otherwise (MPE $< 0$); the MPE has values of $-20$ to 60% for $\tau'_{10.8} > 0.025$. The MAPE has minima for $\tau'_{10.8}$ around 0.3 and 8; the first minimum might be explained by the increased sample weights applied during training for $\tau'_{10.8}$ at corresponding values [2]. For $z'_{\text{top}} < 10$ km, the retrieved $\tau_{10.8}$ is underestimated with the MPE being $-50$ to $-100$% for $z'_{\text{top}} < 4$ km and 0 to $-50$% for 4 km $< z'_{\text{top}} < 10$ km.

The retrieved $z_{\text{top}}$ is generally overestimated, with MPEs up to 50% but below 20% for $\tau'_{10.8} > 0.5$ and below 10% for $z'_{\text{top}} > 4$ km. The bias is larger for optically thin ash clouds (e.g., $\tau'_{10.8} < 0.17$) with meteorological clouds above, whereas nearly no bias is apparent in the presence of meteorological clouds below. For $z'_{\text{top}} > 15$ km, the retrieval error of $z_{\text{top}}$ slightly increases again; a physical reason might be that at high latitudes the tropopause is located at similar heights, such that the disappearance or inversion of the vertical temperature gradient makes the determination of $z_{\text{top}}$ more difficult.

The retrieved $r_{\text{eff}}$ is overestimated for all values of $\tau'_{10.8}$ and $z'_{\text{top}}$; the MPE becomes >50% for $\tau'_{10.8} < 0.05$ and between 10% and more than 140% for $z'_{\text{top}} < 3$ km, strongly depending on the presence of meteorological clouds. For $r'_{\text{eff}} < 4$ µm, the retrieved $r_{\text{eff}}$ is overestimated, and underestimated beyond; the MPE is generally between $-20$% and 20%.

Our simulated test data sets consist of samples which are calculated for specific geographical locations. The latitude/longitude coordinates are drawn randomly, but are equally distributed with respect to the SEVIRI disc [2]; thus, more samples are located around 0°N, 0°E than at larger viewing zenith angles. The georeferenced test data are used to investigate the dependence of the accuracy, POD and FAR of the binary ash flag on the geographical position in Figure 3, and the MAPE and MPE of the regression ANNs in Figure 4. In all cases, four different subsets are investigated: with meteorological clouds, without meteorological clouds, with meteorological clouds above and below (as defined before). The samples are arranged in boxes of 10° × 10°, except for the FAR in Figure 3c1,c2, which is given for 45° × 45° boxes to accumulate enough samples given its small numerical value. The decreasing sample density towards the edges of the plots can explain the worse retrieval performances at higher viewing zenith angles. Thus, we focus on the central regions of ±40° around 0°N, 0°E.

The binary ash flag has a high accuracy and POD (both close to 100%) in the absence of clouds except for the desert regions of Northern Africa and the Arabian peninsula, where both metrics decrease by 1–2%, whereas the FAR rises to about 0.008%. This might be connected to the surface emissivity of quartz-rich soils that can lead to a negative $BTD_{10.8\text{–}12}$ [7]. In the presence of clouds, the accuracy and POD remain close to 100% above Africa, especially above the tropical forest and in proximity of the equator; otherwise the metrics decrease by up to 3% and 10%, respectively. The decrease is even more pronounced if meteorological clouds are above, which might be connected to the fact that the simulated samples are mostly located above tropical Africa; thus, the ANNs are in this case mainly exposed to samples of a very specific type. Meteorological clouds below are predominantly above the south east Atlantic off the coast of Africa, where an extensive marine stratus deck at low altitudes is usual [8]. The non-uniform distribution of the different sample types resembles reality, as the occurrence of meteorological clouds in the radiative transfer simulation is based on their presence in the ECMWF model [2]. To try to improve the performance of the ANNs for the physically less common cases, one could increase their amount in the training data set in the future, by specifically selecting those samples during the data set creation, or by increasing their sample weight during the training. However, this would also distort the underlying probability distributions, e.g., by artificially increasing the number of samples with meteorological clouds above the ash layer above the Atlantic, the corresponding probability would be higher for the training data set than in reality. A priori it is not clear whether this would improve the overall performance of the algorithm. Note that other retrievals exhibited similar properties as the binary ash flag, e.g., the ice cloud retrieval CiPS had the highest POD above forest for cirrus clouds with an optical thickness up to 0.5, and at the same time a high FAR above equatorial Africa as cirrus clouds often occur in this region (i.e., above tropical

rainforests) and, thus, corresponding samples made up a significant part of the used training data set [9,10].

The retrieval of $\tau_{10.8}$ has a MAPE of mostly 20–30%, independently of meteorological cloud presence. Again there is a high MAPE of more than 60% above the Atlantic west of southern Africa if meteorological clouds are above the ash. $\tau_{10.8}$ is generally underestimated with MPEs of 0 to −20%, except if meteorological clouds are below the ash layer, which leads to MPEs of 0–15%.

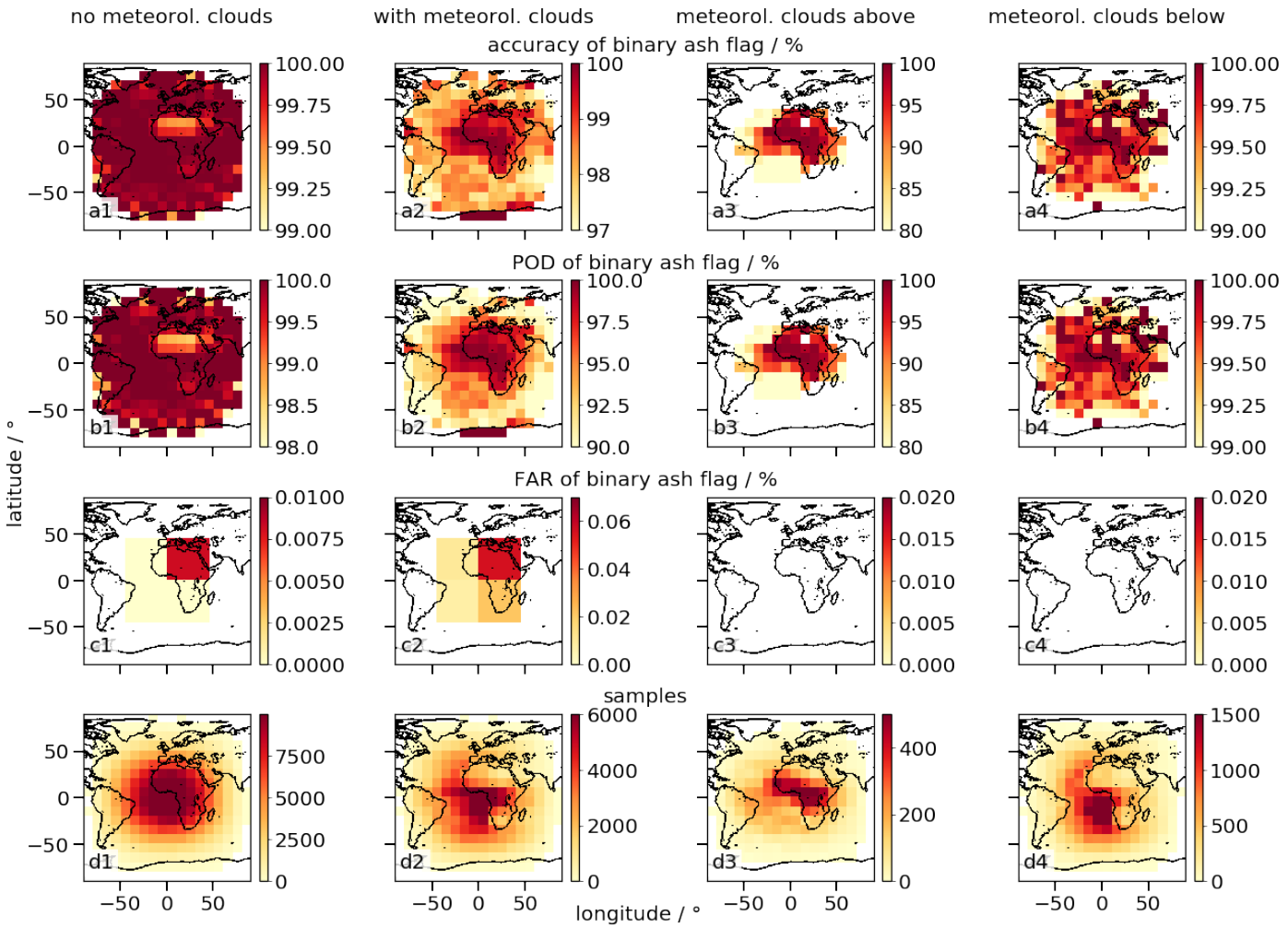


**Figure 3.** Estimations of the accuracy (**a**), the POD (**b**) and the FAR (**c**) for the binary ash flag for different geographical coordinates and subsets without meteorological clouds (**1**), with meteorological clouds (**2**), with meteorological clouds above (**3**) and below (**4**) a volcanic ash layer; the number of samples is given in (**d**); no metrics are shown if a grid cell contains <100 (<50,000 for FAR) samples; mind the different color scales.

The retrieval of $z_{top}$ shows a latitudinal dependence of the MAPE: it is 5–10% at the equator, but rises towards the poles up to 20% at ±50°N. Similarly, the MPE rises from ~0% around the equator to about 10%. A reason for the latitudinal dependence of MAPE and MPE could be that the ANN might learn mainly the vertical temperature profile at the tropics, as there the sample density in the training data is the highest. Since the temperatures are generally lower towards the poles [11], the retrieved $z_{top}$ from the measured brightness temperatures using the tropical temperature profile is systematically too high. Theoretically, this issue might be overcome by using a training data set of samples equally distributed over the complete latitudinal range, again either by accordingly increasing the amount of samples or the weight of the given samples. Then there should be comparable focus on all the different temperature profiles. The ANN's decision on which

temperature profile to use could be based on the latitude, but also on, for instance, the time of day and day of year, all of which are used as input data for VACOS. However, another problem might be the decreasing height of the tropopause and the corresponding vertical temperature inversion at higher latitudes, which makes it harder to deduce $z_{\mathrm{top}}$ from the measured brightness temperatures for ash clouds above the tropopause. Differences in the surface emissivity due to ice and snow surfaces [5] might also introduce errors in the most poleward regions. The last two issues would not be solved by using a training data set evenly distributed across latitudes.

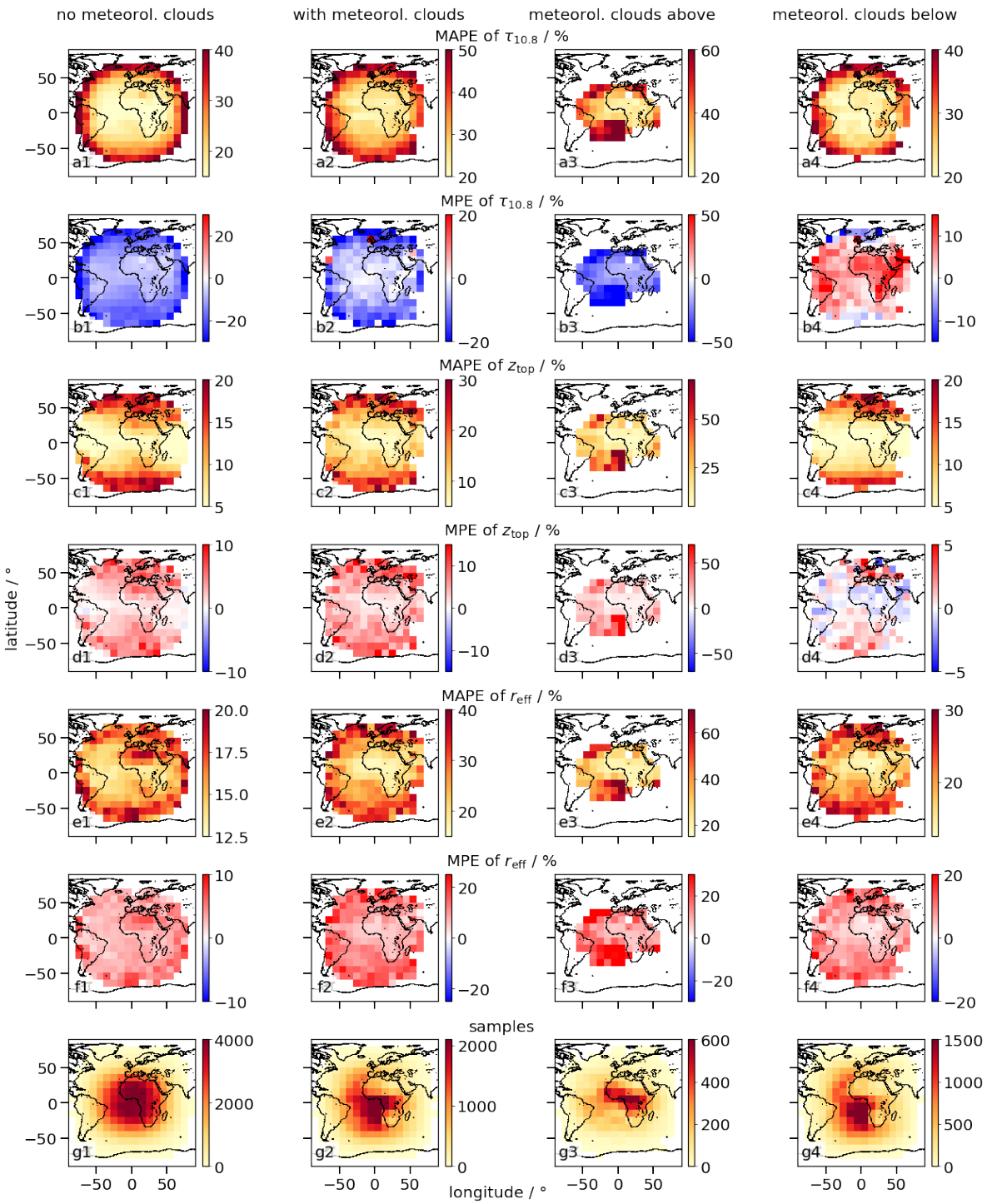


**Figure 4.** As in Figure 3, but given are MAPE and MPE for the retrieval for $\tau_{10.8}$ (**a**,**b**), $z_{\mathrm{top}}$ (**c**,**d**) and $r_{\mathrm{eff}}$ (**e**,**f**) and the number of samples (**g**) according to test data set B.

The retrieval of $r_{\text{eff}}$ is generally overestimated, with MAPEs at the equator around 15% if no meteorological clouds are present, and 20% on average in their presence. Again, the error is higher above the Sahara in the absence of meteorological clouds.

### 2.3. Detection of Volcanic Ash

Volcanic ash can be detected using the following threshold rules: a sample is classified as ash-containing if one of $BTD_{12\text{–}10.8}$, $\tau_{10.8}$ or the probability for ash due to the binary ash flag $P_{\text{ash}}$ is larger than a given threshold $BTD_{12\text{–}10.8,\text{thrs}}$, $\tau_{10.8,\,\text{thrs}}$ or $P_{\text{ash},\,\text{thrs}}$, respectively. Notice that the first possibility is independent of VACOS. Figure 5 shows POD and FAR for all three methods for different thresholds. Generally, by increasing the threshold the POD as well as the FAR decrease. Thus, it is necessary to find a trade-off between both properties. In case of doubt a higher POD is favored with regard to the relevance of ash detection in aviation-security. As thin ash layers are harder to detect (Section 2), two subsets are considered besides the full test data set: samples with $\tau'_{10.8} < 0.2$ and $\tau'_{10.8} < 0.5$. Using $BTD_{12\text{–}10.8}$ (e.g., [7,12,13]) with $BTD_{12\text{–}10.8,\text{thrs}} = 0\,\text{K}$ gives a POD of 100% and a FAR of about 10%. The former is due to the selection of ash samples in the simulated data sets, i.e., only ash-loaded samples with $BTD_{10.8\text{–}12} < 0$ have been considered [2]. For $BTD_{12\text{–}10.8,\text{thrs}} = 1.58$, the POD is ca. 70% and the FAR is about 0.25% for the full test data set. For the subsets of lower $\tau'_{10.8}$, the POD is much lower, whereas the FAR remains high. Using $\tau_{10.8,\,\text{thrs}}$ leads to higher PODs compared to $BTD_{12\text{–}10.8,\text{thrs}}$ for all three sets of test data, the curves move towards the upper left corner of Figure 5. Again the PODs are smaller for lower $\tau'_{10.8}$. For example, $\tau_{10.8,\,\text{thrs}} = 0.04$ leads to a FAR of 1% and a POD of 98.7% (95.4%, 86.8%) for the full test data set (only $\tau'_{10.8} < 0.5$, <0.2). Using $P_{\text{ash}}$ leads to an even better performance in all subsets: up to roughly $P_{\text{ash},\,\text{thrs}} = 0.8$, the POD decreases only slightly, whereas the FAR decreases by multiple orders of magnitude. Only for higher $P_{\text{ash},\,\text{thrs}}$, the POD drops as well. For $P_{\text{ash},\,\text{thrs}} = 0.8$, the FAR is 0.008% and the POD is 98.6% (95.5%, 88.2%) for the full test data set (only $\tau'_{10.8} < 0.5$, <0.2).

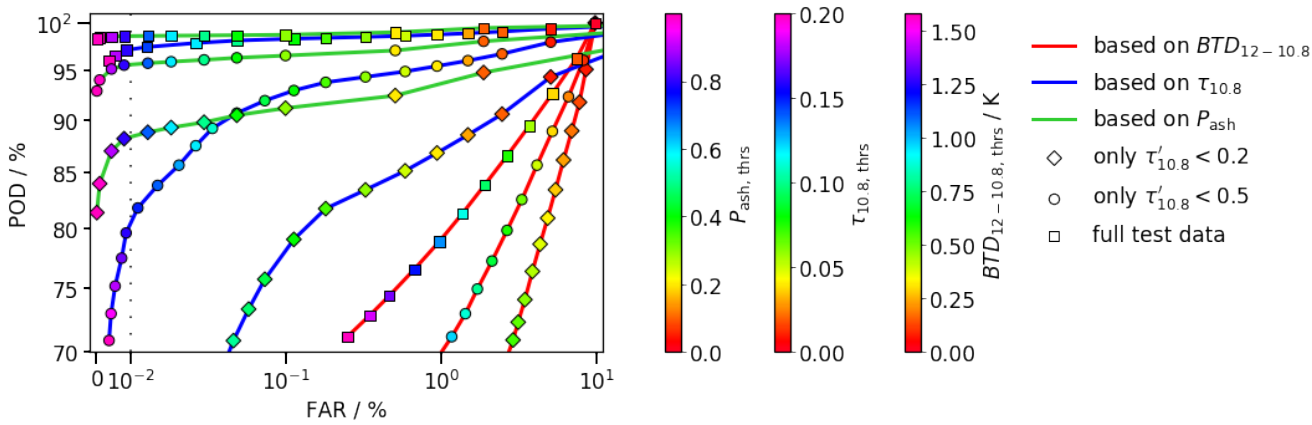


**Figure 5.** Estimations of the POD and the FAR for the detection of volcanic ash using $BTD_{12\text{–}10.8}$ (connected by a red line), $\tau_{10.8}$ (blue line) and the probability of the binary ash flag for ash $P_{\text{ash}}$ (green line), and a corresponding threshold (color of marker, see colorbars); different subsets of the test data set [2] are used and encoded in the marker type, i.e., the full data set (square), only samples with $\tau'_{10.8} < 0.5$ (circle) and <0.2 (diamond); the *x*-axis is linear left of the black, dotted, vertical line and logarithmic right of it.

Instead of subsets defined by the $\tau'_{10.8}$ as in Figure 5, one can also select sets according to $m'_{\text{col}}$: For $\tau_{10.8,\,\text{thrs}} = 0.04$, corresponding to $0.2\,\text{g}\,\text{m}^{-2}$ when considering a mean mass extinction coefficient at 10.8 µm of $200\,\text{m}^2\,\text{kg}^{-1}$[2], and $m'_{\text{col}} \in [0.2, 1]\,\text{g}\,\text{m}^{-2}$, a typical regime for distal volcanic ash clouds (Section 4), the POD is ca. 93% and the MAPE for $m_{\text{col}}$ roughly 40%, whereas $m'_{\text{col}} \in [1, 10]\,\text{g}\,\text{m}^{-2}$ leads to a POD of 99% and a MAPE of 26%. For the ash-free samples, the FAR is about 1%.

## 3. Sensitivity to Volcanic Ash Cloud Profiles

For the training data set, we made the ad hoc assumption of a single, homogeneous volcanic ash layer with $z_{top}$ up to 18 km, geometrical thicknesses up to 7.2 km and $m_{col}$ up to 30 g m$^{-2}$ [2]. Here we consider the sensitivity of the brightness temperatures and the ANNs on the ash cloud profile. In all cases we apply the refractive index of Eyjafjallajökull ash [14], a log-normal particle size distribution with $r_{eff} = 0.6$ µm, a geometric standard deviation $s = 1.5$ and a representative shape distribution of spheroids as considered in Piontek et al. [3]. A thick ash cloud is assumed with $m_{col} = 10$ g m$^{-2}$, corresponding to $\tau_{10.8} = 2$ for a mass extinction coefficient at 10.8 µm of 200 m$^2$ kg$^{-1}$. This order of magnitude of $m_{col}$ can be found in close proximity of a volcano (Section 5); for lower $m_{col}$, the absolute impact of the investigated macrophysical properties on the brightness temperatures is assumed to be smaller.

Using ECMWF ERA5 data for 2010 and the methods described in Piontek et al. [2], a random set of 500 atmospheric and geographical conditions is chosen and used for the calculation of the brightness temperatures for each cloud setting. Only cases without meteorological but with volcanic ash clouds are investigated as meteorological clouds were already shown to influence the retrievals significantly.

### *3.1. Multiple Ash Layers*

To quantify the variability in the brightness temperatures due to multiple layers, we compare a single layer with four different multi-layer structures, Figure 6a. All four setups keep $z_{top}$ and $m_{col}$ fixed (i.e., the parameters that are retrieved by the ANNs). Layers #1 and #2 also keep the mass concentration $c$ fixed and introduce a gap in the volcanic ash cloud. Layers #3 and #4 keep the cloud bottom height fixed but increase $c$. The brightness temperatures of the infrared channels of SEVIRI are simulated and the differences compared to the single layer are calculated, Figure 6b. Layers #1 and #2 show that the brightness temperature increases with a decreasing height for the lower ash layer; the differences are generally positive, as more of the mass is in warmer parts of the atmosphere. For a gap of 0.5 km the differences can be >0.5 K, but for a gap of 2 km the differences are even >2 K, with outliers even >3 K. For the more condensed structures #3 and #4, the differences are mostly between 0 K and −0.5 K and negative as more of the mass is in cooler parts of the atmosphere. Figure 6c shows the relative differences in the retrievals with respect to the true values. The median $z_{top}$ retrieval is overestimated by ca. 3%, the retrieved $r_{eff}$ is underestimated by about 7%. In both cases is the influence of multi-layer structures compared to single layers on the order of 1%. The median retrieved $\tau_{10.8}$ for a single layer is about 20% higher than the true value. Again structure #2 leads to the largest difference: here the median retrieved $\tau_{10.8}$ is about 10% lower than the true value. The structures #3 and #4 lead only to minor differences compared to the single layer.

### *3.2. Non-Homogeneous Ash Profiles*

The assumption of a uniform ash layer [2] is often not fulfilled in reality, where vertical ash mass profiles do not have discontinuities and might have a clear peak [15–17]; thus, a more realistic description would be a normal distribution or the Π-sigmoid distribution (Appendix B and [18]), which has the ability to approximate uniform and normal distributions as limiting cases, Figure 7a. To quantify the influence of the cloud profile, different assumptions are compared. A uniform cloud with a typical height of 8–9 km is assumed [2]; thus, the mean height is 8.5 km and the standard deviation 0.289 km. These values are assumed for the other distributions as well. For the Π-sigmoid distribution, the variables parameterizing the lower and upper end of the cloud are varied (Π-sigmoid #1: 8.01 km and 8.99 km, #2: 8.05 km and 8.95 km, #3: 8.1 km and 8.9 km). The continuous distributions are cut off at 7.5 km and 9.5 km; within this regime they are modeled by 100 sublayers of depth 0.02 km, each having a mass volume concentration corresponding to $m_{col}$ times the density of the normalized vertical mass distribution at the mean height of the sublayer. The brightness temperatures of the infrared channels of SEVIRI are simulated and the differences of the various profiles compared

to the uniform distribution are calculated, Figure 7b. The absolute differences are mostly <0.1 K and, therefore, smaller or of the same order as the instrumental noise [19]. Outliers are <−0.2 K. In some channels (e.g., $BT_{8.7}$ or $BT_{9.7}$) the differences for all profiles are mostly negative, indicating that a more realistic cloud profile might lead to slightly lower brightness temperatures. Applying the ANNs to the different profiles leads to negligible differences (not shown).

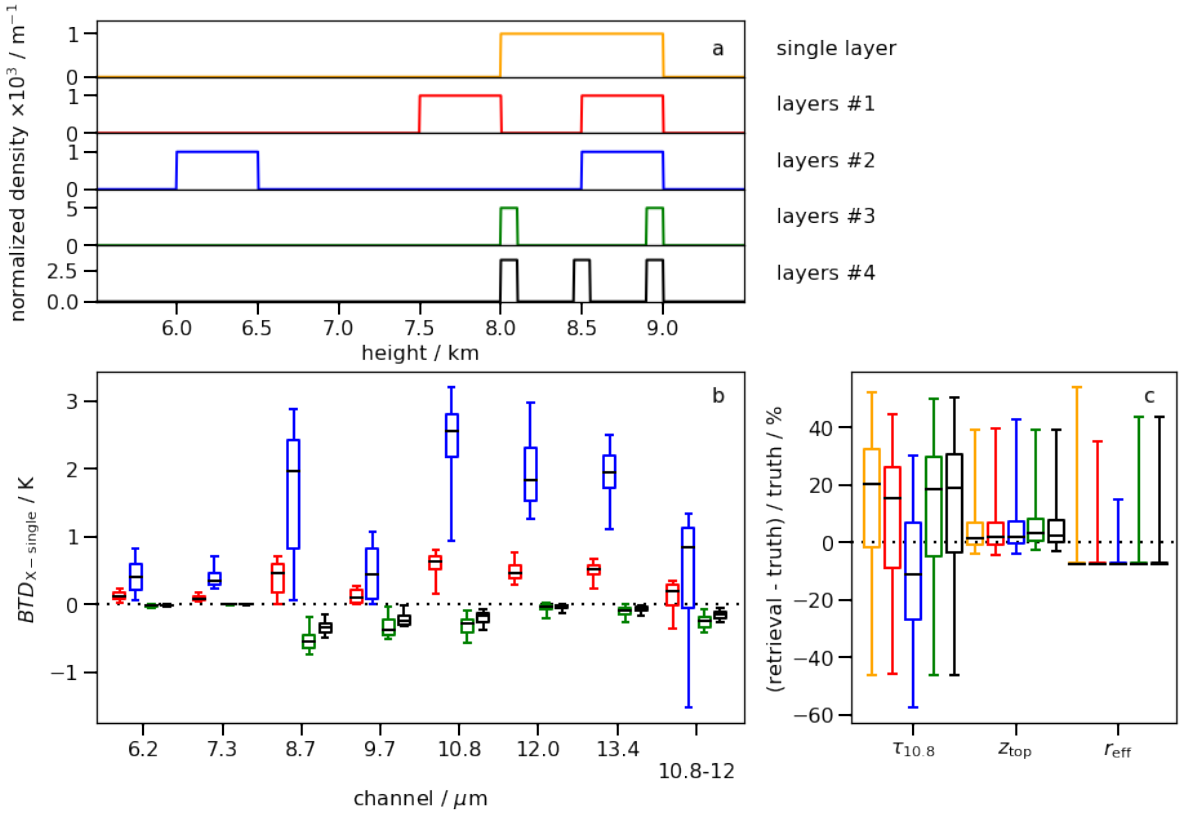


**Figure 6.** Analysis of the impact of different ash layerings with (**a**) the normalized vertical cloud profiles for multiple layers, (**b**) the *BTD* of different channels between a single mass layer and the layerings in (**a**), (**c**) the relative differences in the retrievals of $\tau_{10.8}$, $z_{\text{top}}$ and $r_{\text{eff}}$ compared to the true values for the different layerings in (**a**); for each setup 500 simulations are averaged (see text); the boxplot shows the median, first and third quartile (box) and the 5th and 95th percentile (whiskers).

### *3.3. Geometrical Ash Cloud Thickness*

Although the geometrical cloud thickness is varied within the training data set, it is not retrieved explicitly by the ANNs, and it is not clear whether they are able to derive this information internally as a side product. Here we quantify the impact of this property with respect to the brightness temperature and the retrieval results. Therefore, layers with thicknesses of 0.5 km, 1 km, 2 km and 3 km are considered, with $z_{\text{top}} = 9$ km and $m_{\text{col}} = 10\,\text{g}\,\text{m}^{-2}$ kept constant. The difference compared to the 1 km thick case are considered, Figure 8a. As expected, thicker clouds have higher brightness temperatures as more mass is in lower and warmer parts of the troposphere; the thinner layer leads to lower brightness temperatures. The geometrical cloud thickness introduces a variability of the brightness temperatures of −1 to 4 K. Figure 8b shows the results of the retrievals. Whereas the impact of the cloud thickness is generally negligible for $r_{\text{eff}}$, an increased thickness (and, therefore, decreased cloud base height) leads to smaller retrievals for $\tau_{10.8}$ and $z_{\text{top}}$. The influence on the latter is only small (between −4% and 8%), but the former can exhibit differences of more than 20% comparing cloud geometrical thicknesses of 0.5 km and 3 km.

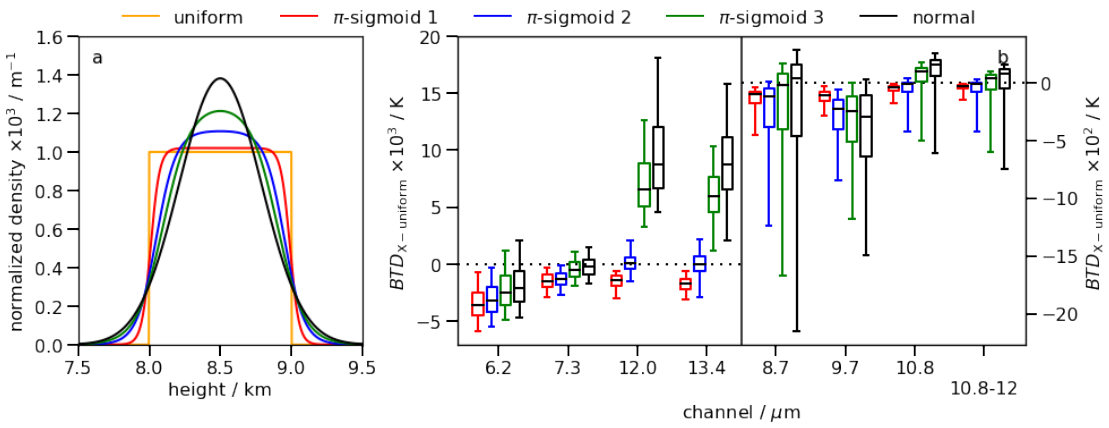


**Figure 7.** Analysis of the impact of different ash profiles with the same mean and standard deviation with respect to the height of the center of the cloud, with (**a**) the different profiles and (**b**) the *BTD* of different channels between a uniform vertical mass distribution and the other distributions in (**a**); for each setup 500 simulations are averaged (see text); the boxplot shows the median, first and third quartile (box) and the 5th and 95th percentile (whiskers).

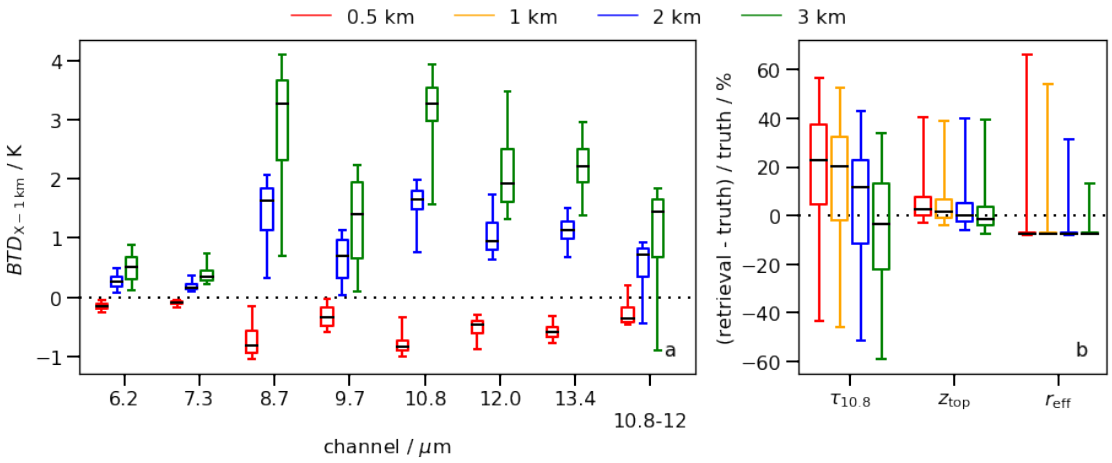


**Figure 8.** Analysis of the impact of different geometrical ash layer thicknesses, with (**a**) the *BTD* of different channels between a layer with a thickness of 1 km and the other thicknesses, (**b**) the relative differences in the retrievals of $\tau_{10.8}$, $z_{\text{top}}$ and $r_{\text{eff}}$ compared to the true values for the different layer thicknesses; for each setup 500 simulations are averaged (see text); the boxplot shows the median, first and third quartile (box) and the 5th and 95th percentile (whiskers).

Comparing different volcanic ash clouds, geometrical layer thickness and multi-layering represent the largest sources of error. The uncertainties introduced by those properties with respect to the brightness temperatures are larger than the instrumental noise [19] and are of the order of 30% for $\tau_{10.8}$, 5% for $z_{\text{top}}$ and negligible for $r_{\text{eff}}$. The shape of a single layer profile is negligible.

## 4. Comparisons with Independent Measurements

To prove the applicability of the retrievals to real data, we compare our results with other in situ and remote sensing measurements as well as the outcome of the predecessor VADUGS for selected scenes.

### *4.1. Puyehue-Cordón Caulle Eruption (2011)*

Lidar measurements represent an excellent source for comparison since they provide accurate estimates for $z_{\text{top}}$ and the vertical profile. Here we use data from the CALIPSO/CALIOP [20] version 4.10 level 2 aerosol products, which include information about volcanic ash layers in the stratosphere [21]. The extinction profiles of those

layers were used to calculate their optical depth at 532 nm, which was converted to $m_{col}$ using a mass extinction coefficient of 690 $m^2\,kg^{-1}$ [22,23]. $z_{top}$ corresponds to the top of the uppermost ash layer. Only ash samples with extinction quality control flag zero (initial lidar ratio resulted in stable extinction retrievals, i.e., "unconstrained" retrievals) or one (when the lidar ratio could be inferred directly from the data, i.e., "constrained" retrievals) were used. For the unconstrained retrievals, a lidar ratio of 58 sr (median of the directly retrieved lidar ratios) was used to update the ash optical depth to correct for the low bias resulting from the use of the default lidar ratio of 44 sr for ash in CALIPSO version 4.10. The final data set has a horizontal resolution of 5 km and a vertical resolution of 60 m.

The six scenes in consideration are listed in Table 3 and sketched in Figure 9; data are plotted in Figure 10 (blue line). They show volcanic ash clouds from the Puyehue-Cordón-Caulle eruption, starting at 4 June 2011. The flyovers took place above the southern Atlantic ocean between 15 June 2011 and 18 June 2011 during day and night. $z_{top}$ was 10–15 km and $m_{col}$ reached up to 1.5 $g\,m^{-2}$; note that the uncertainty of the latter is roughly a factor of 2, see Figure 10. $r_{eff}$ is not derived from CALIOP data, but Bignami et al. [24] used MODIS data to retrieve mean values of 4–6 µm within 300 km from the volcano. Due to sedimentation processes $r_{eff}$ should be smaller in the scenes considered here. Ishimoto et al. [25] retrieved from IASI spectra at distances of ~1000 km for most samples $r_{eff} < 0.5$ µm. The silica content was around 70 wt.% or slightly below [14,26,27].

**Table 3.** Investigated CALIPSO flyovers in June 2011 with timespan, coordinates of start and endpoint, number of samples and track number according to Figure 9.

| Day | Start Time/UTC | End Time/UTC | Start Coordinates | End Coordinates | Samples | Track Number |
|---|---|---|---|---|---|---|
| 15 June 2011 | 18:30 | 18:40 | −55.7°N, −59.8°E | −40.4°N, −66.0°E | 300 | 1 |
| 16 June 2011 | 15:51 | 16:05 | −48.8°N, −24.4°E | −39.3°N, −27.7°E | 162 | 2 |
| 16 June 2011 | 17:29 | 17:43 | −60.9°N, −42.7°E | −44.6°N, −50.7°E | 187 | 4 |
| 17 June 2011 | 03:00 | 03:13 | −40.6°N, −27.7°E | −62.0°N, −37.8°E | 251 | 5 |
| 17 June 2011 | 14:55 | 15:10 | −44.4°N, −12.1°E | −37.3°N, −14.4°E | 82 | 3 |
| 18 June 2011 | 02:04 | 02:18 | −35.4°N, −12.2°E | −64.4°N, −25.9°E | 199 | 6 |

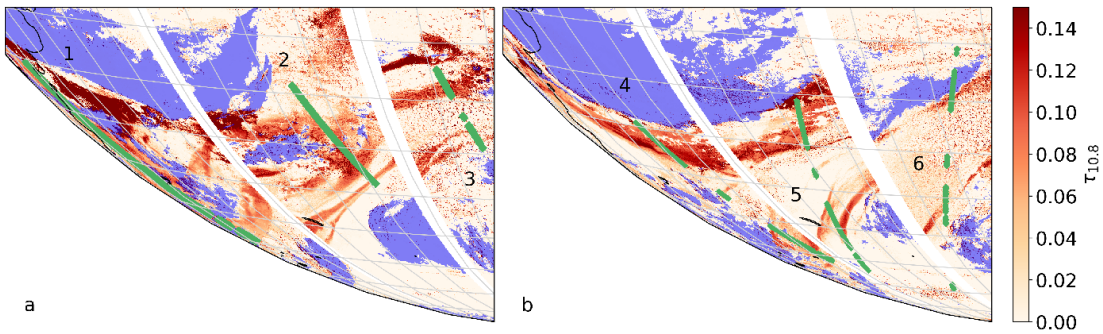


**Figure 9.** Overview of the CALIPSO transits (green) as described and numbered in Table 3 with the corresponding VACOS retrievals of $\tau_{10.8}$ (red colors) and the cirrus flag of CiPS (blue); Figure (**a**,**b**) are made up of three stripes each, showing the VACOS and CiPS retrievals at the times of the corresponding CALIPSO transits; thus, the retrievals of the three stripes in each plot correspond to three different times.

We compare the CALIOP measurements with the results of the ANNs applied to SEVIRI images at close times. The coordinates given by CALIPSO are corrected such that the light path of the SEVIRI measurements penetrates the top of the ash cloud (parallax correction). The regression retrievals are shown on a single pixel basis (faint red), and after a mean filter of 5 × 5 pixels was applied (red); the classification result is shown only on a single pixel basis. $\tau_{10.8}$ is converted to $m_{col}$ using a mean mass extinction coefficient at 10.8 µm of 152 $m^2\,kg^{-1}$, which holds for silica contents of 70 wt.% and $r_{eff} = 0.6$ µm [2].

Additionally, the retrievals of volcanic ash by VADUGS and of cirrus clouds by CiPS [9,10] are shown in Figure 10. The MAPE and MPE for the retrievals of $m_{col}$ and $z_{top}$ are given in Table 4, the PODs using $m_{col}$ and $P_{ash}$ and different thresholds are given in Figure 11.

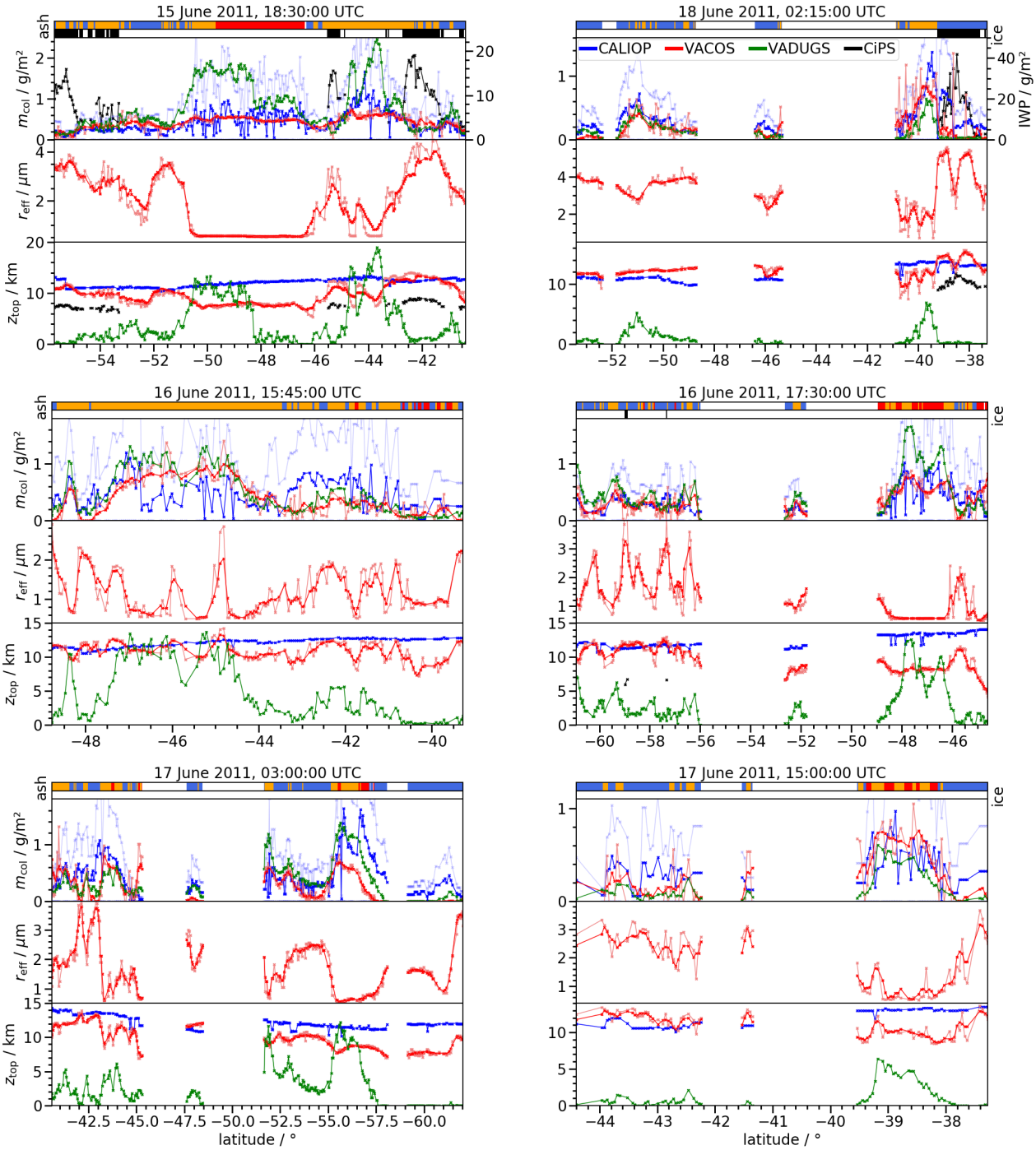


**Figure 10.** Pixel classification (*ash*) and retrievals of $m_{col}$ (derived from $\tau_{10.8}$), $r_{eff}$ and $z_{top}$ as determined using CALIOP (blue), VADUGS (green) and VACOS (red) for volcanic ash clouds of the Puyehue-Cordón Caulle eruption 2011 above the Atlantic on 15–18 June 2011, see Table 3; the times above the plots indicate the start of measurement of the SEVIRI image used; the VACOS regression results are averaged on 5 × 5 pixels with the 1 × 1 pixel result shown in faint red, whereas the for the classification the single pixel result is shown; the upper uncertainty of $m_{col}$ by CALIOP is indicated in faint blue; the ash classification shows: clear skies (green), meteorological clouds (blue), volcanic ash (red), ash and meteorological clouds (orange); a cirrus cloud flag (*ice*) and, if applicable, the ice water path (IWP) are derived using CiPS (black); the cirrus flag shows: cirrus (black), no cirrus (white); the latitude refers to the position of CALIPSO; note that vertical axes are scaled differently in the plots.

**Table 4.** Comparison of the retrievals VADUGS and VACOS against CALIOP data; different subsets depending on $m'_{col}$ from CALIOP are considered; the MAPE and MPE for the retrieval of $m_{col}$ and $z_{top}$ are calculated; the retrieval is analyzed after application of a $3 \times 3$ pixels (px) and $5 \times 5$ px uniform filter.

| | $m_{col}$ | | $z_{top}$ | |
|---|---|---|---|---|
| **Algorithm** | **MAPE** | **MPE** | **MAPE** | **MPE** |
| full data set (1181 samples) | | | | |
| VADUGS | 123% | 70% | 75% | −74% |
| VACOS (1 px) | 190% | 93% | 19% | −14% |
| VACOS (9 px) | 111% | 43% | 18% | −14% |
| VACOS (25 px) | 112% | 49% | 18% | −14% |
| only $m'_{col} \geq 0.2\,g\,m^{-2}$ (875 samples) | | | | |
| VADUGS | 62% | 12% | 71% | −70% |
| VACOS (1 px) | 56% | −24% | 18% | −14% |
| VACOS (9 px) | 47% | −20% | 18% | −14% |
| VACOS (25 px) | 45% | −20% | 18% | −14% |

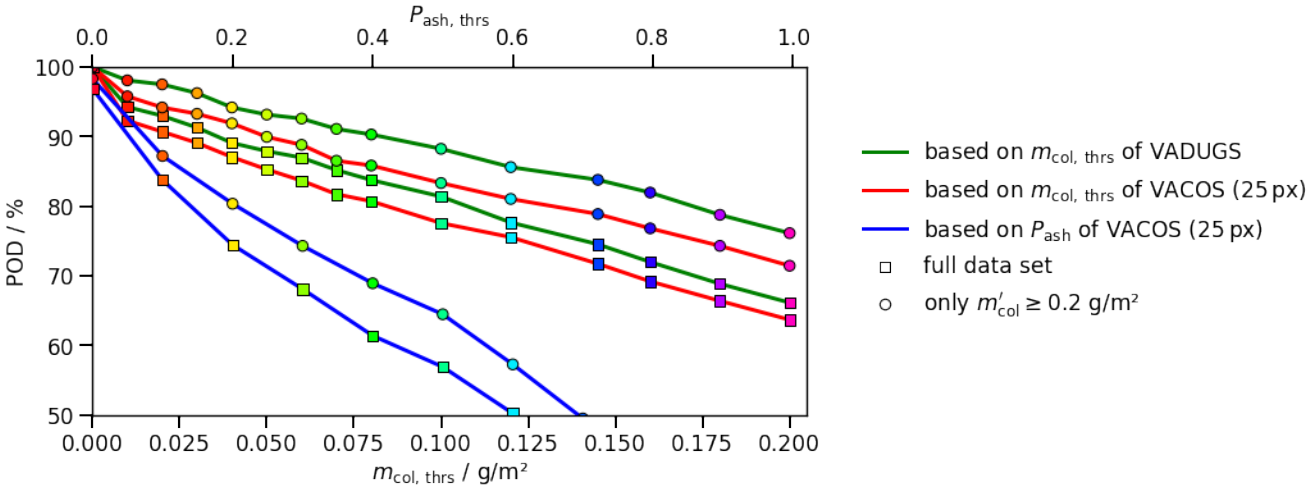


**Figure 11.** Estimations of the POD of volcanic ash using $m_{col}$ and $P_{ash}$ of VACOS (connected by red and blue lines, respectively) and $m_{col}$ of VADUGS (green line), and a corresponding threshold; different subsets of the test data (Table 3), are used and encoded in the marker type, i.e., the full data set (square), only samples with target $m'_{col} \geq 0.2\,g\,m^{-2}$ (circle).

Again the mass load due to CALIOP (i.e., the "true" value) is denoted $m'_{col}$. For $m'_{col} \geq 0.2\,g\,m^{-2}$, the retrieval of $m_{col}$ using VADUGS has a MAPE of 62% and a MPE of 12%, indicating a slight overestimation; this is visible in Figure 10 for 15 June 2011 at 18:30 UTC or 16 June 2011 at 17:30 UTC, although the VADUGS results are mostly within the uncertainty interval of the CALIOP data. VACOS has a smaller MAPE of 56%, but underestimates $m_{col}$ due to a MPE of −24%. Remember that VACOS is more complex than VADUGS, consisting of four instead of only one ANN, using more input features, with each ANN having three compared to just a single hidden layer (although with 100 instead of 600 neurons per hidden layer) [1,2]. As a consequence, VACOS has significantly more trainable parameters and has the potential to learn more complex functions, such that their pixelwise application can lead to rather abrupt jumps in the retrievals; this can be seen, for instance, at 18 June 2011, 02:15 UTC in Figure 10 and the corresponding track 6 in Figure 9b. Thus, the VACOS retrievals are also calculated after the application of a $3 \times 3$ and a $5 \times 5$ pixels uniform averaging, which leads to a further reduction of MAPE (47% and 45%, respectively) and MPE (−20% each). Note that this MAPE is similar to the values found for the simulated test data. Whereas the reduction in the errors is of the order of 10% when comparing the unfiltered results with the results after an averaging over $3 \times 3$ pixels, the further decrease is only on the order of a few percent when considering

$5 \times 5$ pixels. Note that averaging over even larger areas might worsen the retrieval of fine structured ash clouds, e.g., thin plumes close to the volcanic vent; therefore, this is not done here. Considering the full CALIOP data set leads to significantly higher errors than for the subset with $m'_{\mathrm{col}} \geq 0.2\,\mathrm{g\,m^{-2}}$, showing that the retrieval of thin ash layers is much harder. VADUGS has a MAPE of 123% and a MPE of 70%. VACOS has higher errors before averaging the results, but performs better after averaging over $3 \times 3$ pixels, with a MAPE of 111% and a MPE of 43%. Averaging over $5 \times 5$ pixels slightly increases the errors. The reason might be that small $m_{\mathrm{col}}$ are often located at the edges of ash clouds, where the averaging over larger areas includes ash-free pixels. The retrieval of $z_{\mathrm{top}}$ is mostly independent of the subset and the averaging for both VADUGS and VACOS. MAPE and absolute MPE of VADUGS are 70–75%. Although VADUGS is able to retrieve the correct heights in some cases (especially when $m_{\mathrm{col}} \geq 1\,\mathrm{g\,m^{-2}}$), it often strongly underestimates $z_{\mathrm{top}}$; compare, for instance, 16 June 2011 at 15:45 UTC in Figure 10. VACOS retrieves $z_{\mathrm{top}}$ with a MAPE $< 20\%$, but also slightly underestimates the true height as indicated by a MPE of $-14\%$. The retrieved $r_{\mathrm{eff}}$ exhibits large variations with values between 0.6 µm (the lower end of the training data regime [2]) and 4 µm; thus, they are smaller than the values retrieved by Bignami et al. [24] close to the volcano, but significantly larger than the results by Ishimoto et al. [25]. Note that the lowest $r_{\mathrm{eff}}$ are retrieved for the highest $m_{\mathrm{col}}$ (e.g., at 16 June 2011, 17:30 UTC). As the errors of $r_{\mathrm{eff}}$ decrease with increasing $\tau_{10.8}$ (as shown in Section 2), the retrieved $r_{\mathrm{eff}}$ is most reliable for thick clouds. The small $r_{\mathrm{eff}}$ also supports the choice of the mass extinction coefficient at 10.8 µm above.

The classification ANN indicates the presence of volcanic ash especially for thick ash layers, whereas thinner layers are often misclassified as meteorological clouds. The POD using $P_{\mathrm{ash}}$ of the resulting binary ash flag and using $m_{\mathrm{col}}$ of VADUGS and VACOS (compare Section 2.3) are given for different thresholds in Figure 11. For VACOS, the averages over $5 \times 5$ pixels are used for $m_{\mathrm{col}}$ and the single pixel result for $P_{\mathrm{ash}}$. VACOS performs slightly worse than VADUGS with respect to volcanic ash detection using $m_{\mathrm{col}}$. Setting $m_{\mathrm{col,\,thrs}} = 0.2\,\mathrm{g\,m^{-2}}$ leads to a POD of 65–75% for VACOS; for $m_{\mathrm{col,\,thrs}} = 0.1\,\mathrm{g\,m^{-2}}$, the POD is around 80%. Both values are significantly smaller than for the simulated test data set, which indicates that there are differences between the simulated data set and data collected in reality. However, note that the different performances of VADUGS and VACOS can be explained in part by the retrievals MPEs: VADUGS overestimates $m_{\mathrm{col}}$ whereas VACOS underestimates it. Correcting this would lead to a decrease of the POD of VADUGS and to an increase for VACOS. Furthermore, the assumed mass extinction coefficient at 10.8 µm for the transformation of $\tau_{10.8}$ to $m_{\mathrm{col}}$ has an impact for VACOS: using a smaller value increases $m_{\mathrm{col}}$ due to VACOS and consequently also the POD. The performance of the binary ash flag is significantly lower here as compared to the simulated test data and the results using the retrieved $m_{\mathrm{col}}$, independently of the threshold; $P_{\mathrm{ash,\,thrs}} = 0.5$ leads to a POD around 60%. This indicates that the use of $m_{\mathrm{col}}$ for detection is more reliable than the classification ANN in this situation. The FAR has not been quantified here, but Figure 9 shows mostly large-scale structures representing the ash clouds, and only in some scenes are tiny patches with significant $\tau_{10.8}$ which are not connected to the ash clouds and might be false detections. Thus, we assume the FAR to be reasonably low.

Two scenes, 15 June 2011 at 18:30 UTC and 18 June 2011 at 02:15 UTC, contained cirrus clouds underneath the ash layer, with ice water paths up to $20\,\mathrm{g\,m^{-2}}$ and $40\,\mathrm{g\,m^{-2}}$, respectively. In both cases the cirrus has a moderate impact on the retrieved $z_{\mathrm{top}}$, but the retrieved $r_{\mathrm{eff}}$ is significantly increased in the presence of the cirrus clouds; meanwhile, the retrieved $\tau_{10.8}$ drops to zero, especially at 18 June 2011, 02:15 UTC. This shows that it seems recommendable to always evaluate VACOS results alongside cirrus retrievals.

### *4.2. Eyjafjallajökull Ash Cloud (17 May 2010)*

Following the 2010 eruption of the Eyjafjallajökull, the Deutsches Zentrum für Luft- und Raumfahrt (DLR, the German aerospace center) and the Facility for Airborne Atmospheric Measurements, United Kingdom (FAAM) independently performed airborne

in situ and lidar measurements of the volcanic ash clouds [15,16,28]. Here we consider measurements from 17 May 2010, when both aircraft simultaneously investigated the same ash cloud above the North Sea [17]. The VACOS retrieval of $\tau_{10.8}$ and the cirrus mask of CiPS are given for an example scene, Figure 12b, showing that the ash and ice clouds are well separated. VACOS can be compared to volcanic ash detections by Schumann et al. [15] for a scene two hours later, using $BTD_{10.8\text{–}12}$ with a threshold of −1 K for detection and applying a low-pass filter (Figure 15 in [15]). Both methods exhibit similar distributions of the optically thickest ash clouds, e.g., patches above the North Sea, west of Norway and above Iceland. However, VACOS finds additional, extended ash clouds with $\tau_{10.8} \leq$ ~0.05 above Germany and Norway. The ash cloud investigated by DLR and FAAM as well as the flight trajectories of the two aircraft are sketched in Figure 12a.

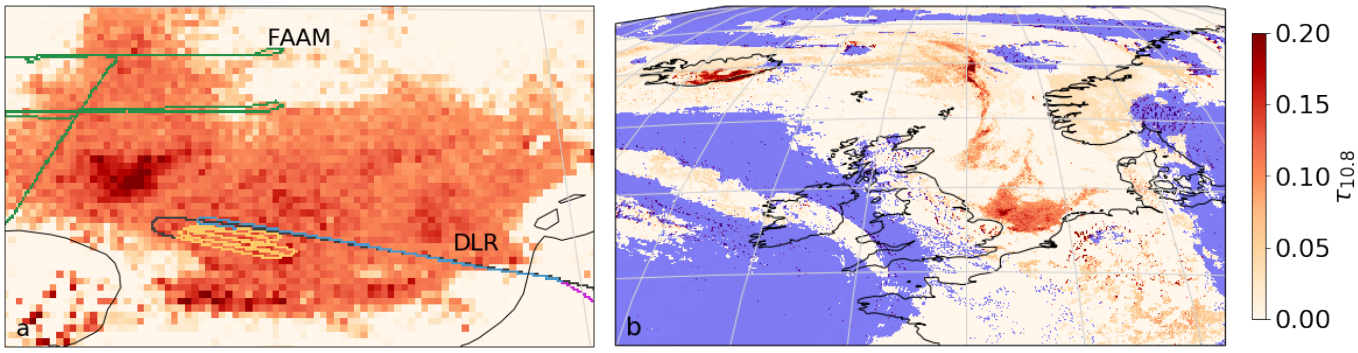


**Figure 12.** VACOS retrieval of $\tau_{10.8}$ at 17 May 2010, 16:00 UTC; shown is (**a**) the North Sea between the Netherlands and England, and (**b**) north-western Europe up to Iceland; blue areas are covered by cirrus clouds according to CiPS [9]; panel (**a**) also shows the flight tracks of the DLR Falcon aircraft (with different parts of the track in black, yellow, blue and violet) and the FAAM aircraft (green) [15,16].

Schumann et al. [15] provided in situ measurements with a time resolution of 1 s for the altitude and 10 s for the mass volume concentration. To derive the latter they made two different assumptions on the refractive index of the volcanic ash (case L: 1.59 + 0.0 i, case M: 1.59 + 0.004 i; at 630 nm), leading to an upper and a lower estimate of the mass concentration. A third case (H: 1.59 + 0.008 i) was evaluated by Schumann et al. [15], but based on their full analysis they expected the true value to be between case L and M. Ball et al. [29] measured for the refractive index of Eyjafjallajökull ash at a wavelength of 650 nm a real part of 1.554 ± 0.01 and an imaginary part of 0.00085 ± 0.00069, which would support case L. Schumann et al. [15] pointed out that the imaginary part of the refractive index was the major source of uncertainty. The effective radius was estimated to be 0.65–1.05 µm [15]. Considering altitude and mass concentration shows that the aircraft enters the ash cloud from above at 15:50 UTC, reaches a minimum altitude around 16:35 UTC (yellow in Figure 12), and rises afterwards until it leaves the ash cloud again at ca. 17:00 UTC (blue in Figure 12), see Figure 13. Data of the two transits (from above and from below) are treated separately; the corresponding measured vertical mass profiles as well as their linearly interpolated and over 200 m averaged profiles are shown in Figure 14. Although different parts of the ash cloud are probed during the two flight legs, the vertical mass profiles are relatively similar, indicating a horizontally homogeneous ash distribution (over distances in the order of ~50 km). However, vertically the ash cloud has a highly variable mass profile. Ash cloud top and bottom height are roughly at 6.3 km and 3.3 km, respectively. Integrating the vertical mass profiles of Figure 14 and averaging $m_{\mathrm{col}}$ of the two flight legs gives 0.52 g m$^{-2}$ and 2.13 g m$^{-2}$ for the lower (L) and upper (M) estimate, respectively. The DLR data are shown in the left panel of Figure 13.

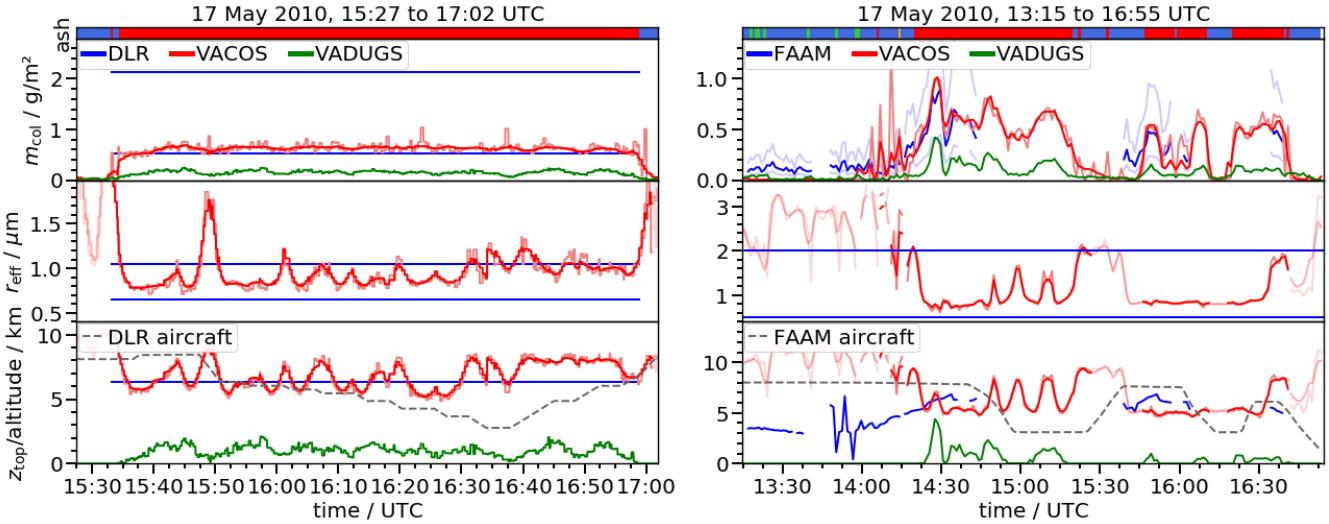


**Figure 13.** Pixel classification (*ash*) and retrievals of $m_{col}$ (derived from $\tau_{10.8}$), $r_{eff}$ and $z_{top}$ as measured in situ by DLR (blue, left panel [15]), derived using an airborne lidar by FAAM (blue, right panel [16]), VADUGS (green) and VACOS (red) for an Eyjafjallajökull ash cloud above the North Sea at 17 May 2010; the VACOS regression results are averaged on $5 \times 5$ pixels with the $1 \times 1$ pixel result plotted in faint red, whereas only the single pixel result is shown for the classification; also VACOS retrievals of $r_{eff}$ and $z_{top}$ for $m_{col} < 0.1\,\mathrm{g\,m^{-2}}$ are plotted in faint red; for the in situ data, only mean values or upper and lower estimates are given; for the lidar-derived data, the upper and lower uncertainty of $m_{col}$ is indicated in faint blue; the ash classification shows: clear skies (green), meteorological clouds (blue), volcanic ash (red), ash and meteorological clouds (orange); the altitudes of the aircrafts are given (grey dashed).

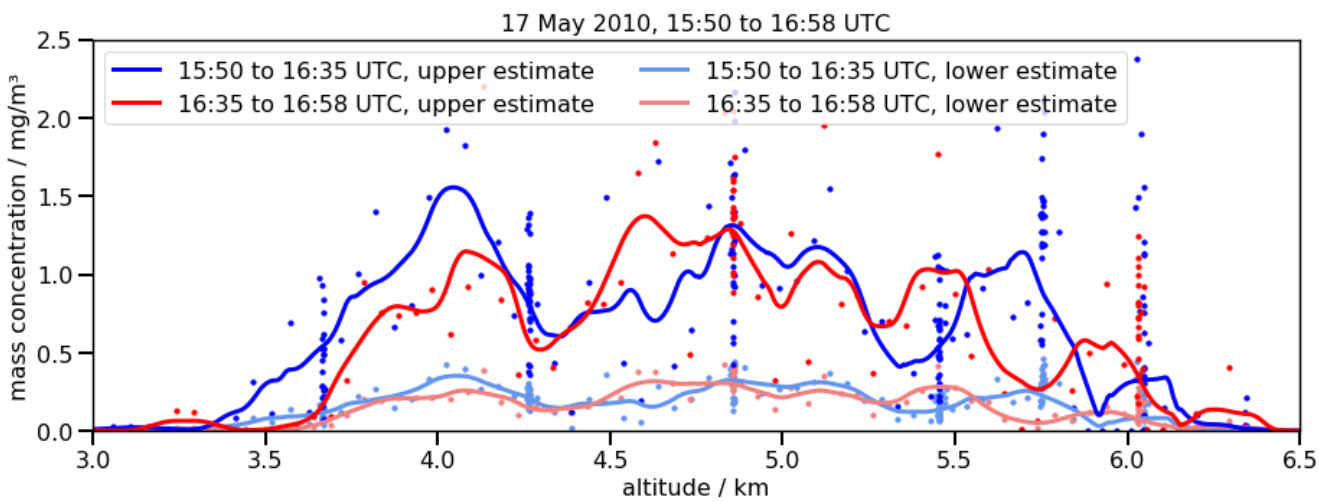


**Figure 14.** Vertical mass profiles of the volcanic ash cloud as measured by Schumann et al. [15] during two flight legs (see text) indicated by the color (blue, red); based on different assumptions, there is an upper estimate (M, bold colors) and a lower estimate (L, faint colors) of the in situ measurements; 10 s averages are given as dots, derived 200 m means are shown as lines.

From Marenco et al. [16] the lidar-derived mass profiles are used, which have a vertical resolution of 45 m and a temporal resolution of 60 s, corresponding to a horizontal resolution of $9 \pm 2$ km at typical aircraft speeds. The uncertainty of the masses is given by a factor of two [16]. We calculate $m_{col}$ by integrating the vertical mass profile, whereas we define $z_{top}$ as the height where the mass volume concentration (median over 315 m, i.e., 7 height levels) exceeds $50\,\mathrm{\mu g\,m^{-3}}$; averaging kernel and mass concentration threshold are based on visual inspection of the mass profiles. In situ measurements performed in April and May 2010 by the FAAM led to $r_{eff}$ of ca. 0.5–2 µm [28]. The FAAM data for

the flight at 17 May 2010 are shown in the right panel in Figure 13. Just as the DLR, the FAAM aircraft dipped into the ash cloud several times; to avoid incomplete mass profiles, measurements of $m_{col}$ and $z_{top}$ are discarded if the FAAM aircraft is <500 m above $z_{top}$ or if the aircraft is below 5 km.

Apart from different instrumentation and processing for the in situ measurements [17], the flights by DLR and FAAM followed fundamentally different strategies: the DLR aircraft remained in an self-contained area well within the ash cloud, hence the relatively constant $m_{col}$, whereas the FAAM entered and left the ash-containing area multiple times, see Figure 12a. Still, the data from both measurements shows some similarities, Figure 13. The lower estimate of $m_{col}$ from DLR is generally in good agreement with the maximum best estimate $m_{col}$ due to the FAAM, whereas the upper estimate from DLR and the maximum of the uncertainty of $m_{col}$ by the FAAM are both around 2 g m$^{-2}$. The lower estimate of $r_{eff}$ is similar for DLR and FAAM, but the upper estimate differs by roughly 1 µm; differences in the ash particle size distributions were also reported by Turnbull et al. [17]. $z_{top}$ from DLR agrees with the largest estimate derived from FAAM data, but the latter varies between roughly 4 km and 7 km, again indicating that a more diverse area of the ash cloud was sampled.

For the VACOS and VADUGS retrievals, a parallax correction is implemented, i.e., coordinates are considered such that the light path crosses the coordinates of the DLR and FAAM aircraft at a height of 6 km and 5 km, respectively, and penetrate the observed ash clouds. The heights correspond roughly to the measured $z_{top}$ of DLR/FAAM. The SEVIRI images with a time resolution of 15 min are processed and the temporally closest image is chosen for each measurement; the SEVIRI line acquisition time is considered. The FAAM's mean aircraft velocity of ~146 m s$^{-1}$ (on ground) and a SEVIRI pixel size of roughly 6.8 km times 3.2 km (at 54°N, 1.5°E) indicate that it takes the aircraft generally about 47 s to cross a pixel in north–south direction and 22 s in east–west direction. As the FAAM data has a time resolution of 60 s, a minimum averaging of $1 \times 3$ SEVIRI pixels is necessary to compare the satellite retrievals to the FAAM data, assuming the aircraft moves only in east–west direction. Based on the results of Section 4.1, an averaging over $5 \times 5$ pixels is considered here. As $r_{eff}$ due to DLR and FAAM data is around 1 µm, a mass extinction coefficient at 10.8 µm of 200 m$^2$ kg$^{-1}$ is assumed [2]; note that this conversion factor is applied in the rest of this work when dealing with Eyjafjallajökull ash clouds. VACOS retrievals of $r_{eff}$ and $z_{top}$ are shown in faint red if $m_{col} < 0.1$ g m$^{-2}$, as the former are ill-defined in the absence of ash clouds. The resulting retrieval data is given in Figure 13.

Considering the DLR case (left panel in Figure 13) we find that the VACOS $m_{col}$ lies at the lower end of the uncertainty interval of the DLR measurement with relatively low variability. $z_{top}$ varies between 5.5 km and 8.5 km, which includes the value found from the DLR data. For the most parts, $r_{eff}$ lies well between the estimates by Schumann et al. [15]. The classification ANN flags the whole ash cloud correctly.

The FAAM measurements (right panel in Figure 13) and the VACOS retrievals for $m_{col}$, $z_{top}$ and $r_{eff}$ are generally in agreement. VACOS slightly underestimates the mass load with $m_{col} \approx 0$ g m$^{-2}$ compared to the FAAM value of ~0.1 g m$^{-2}$ before 14:00 UTC (and consequently derives too high estimates for $r_{eff}$ and $z_{top}$), but retrieves similar $m_{col}$ around 0.6 g m$^{-2}$ as the FAAM later on. VACOS retrieved $r_{eff}$ and $z_{top}$ show plateaus around 0.9 µm and 5 km, respectively, at 14:30 to 14:45 UTC as well as 15:45 to 16:30 UTC. At other times, e.g., around 14:20 or 15:20 UTC, there are coincident increases of $r_{eff}$ and $z_{top}$, which can be attributed at least partially to thin ash clouds with $m_{col} < 0.3$ g m$^{-2}$ at the edges of the ash clouds; thus, these retrievals can be assumed to be unphysical. Other peaks in $r_{eff}$ and $z_{top}$, e.g., around 15:00 UTC, appear although there is a significant amount of volcanic ash (i.e., VACOS retrieves $m_{col} \geq 0.4$ g m$^{-2}$). The classification correctly classifies the major parts of the ash encounters.

Although the comparisons of VADUGS retrievals with the CALIOP results in the case of the Puyehue-Cordón Caulle ash cloud showed a good agreement, VADUGS seems

hardly applicable in the present case: $m_{col}$ and $z_{top}$ are strongly underestimated in both comparisons and at all times.

### 4.3. Eyjafjallajökull Ash Plume at Vent (11 May 2010)

The concentrations that have been compared up to now are rather low. Here the retrieval ability closer to the vent is investigated. Researchers from the University of Iceland used a piston-driven aircraft to probe the outer parts of the ash plume of Eyjafjallajökull in 2010 at distances of 45–60 km from the vent [30]. Plume heights of 3–4.3 km have been reported [30,31], and at 11 May 2010, mass volume concentrations of 0.5–2 mg m$^{-3}$ [30]. Assuming a geometrical thickness of 1–2 km, this corresponds to $m_{col}$ being 0.5–4 g m$^{-2}$ for the fringes of the ash plume; in the center of the plume the values should obviously be higher. Note that Weber et al. [30] reported the boundary of the ash plume to be inhomogeneous, with ash cloud puffs of diameter 0.5–2 km. These small scale structures are not resolvable by SEVIRI [2].

As an example we consider a scene at 11 May 2010, 14:00 UTC, Figure 15. The Eyjafjallajökull ash plume moves southwards from the vent and is surrounded by different cloud fields (a). The cirrus cloud retrieval CiPS [9,10] shows ice water clouds collocated with the ash plume up to some hundred kilometers from the vent. With roughly 1–6 g m$^{-2}$, the ice water path (b) is rather low (e.g., compared to the retrievals in Figure 10), and the cirrus clouds are located at 9–11 km height (c), i.e., above the heights given by Weber et al. [30]. Weber et al. [30] also report that the top of the ash plume above the sea appeared white, whereas it was darker below, and significant ice contents have been found in volcanic ash plumes before [32–34]. The additional ice content might spoil the volcanic ash retrieval in this scene (compare Section 4.1). Note that although it was shown that aerosol layers below cirrus clouds have only a small impact on CiPS [10], the volcanic ash plume in this scene is by no means negligible (f). Therefore, the CiPS retrievals have to be treated with caution as well. The ash plume is detected by VADUGS (d), but with $m_{col} \approx 0.03$ g m$^{-2}$ it underestimates the mass load by one to two orders of magnitude compared to Weber et al. [30]. The classification due to VACOS (e) shows the (mostly pure) ash plume moves southwards and then bends eastwards. A visual comparison of the classification results with (a) indicates that too few pixels might be classified as clear sky (green). The VACOS retrievals of $m_{col}$ (f), $z_{top}$ (g) and $r_{eff}$ (h) are shown for pixels with $\tau_{10.8} > 0.02$. $m_{col}$ (f) shows the plume with decreasing values downwind. The upper end and the center of the ash plume show values around 3 g m$^{-2}$ and larger, the edges values of the order 1 g m$^{-2}$; this is in agreement with the in situ measurements by Weber et al. [30]. Downwind the plume bends eastwards. The ash has dispersed and $m_{col}$ is ca. 0.5–1 g m$^{-2}$. The retrieved $z_{top}$ (g) has values of 10–12 km close to the vent, which is much larger than the literature values. When the plume bends eastward, $z_{top}$ retrievals drop to 5–6 km. Similarly, we find large $r_{eff}$ (h) around 3 µm close to the volcano and then a sudden drop to values around 1 µm. In all three cases the sudden change in the retrievals happens at the edge of the retrieved cirrus cloud, compare (b) and (f), indicating that the presence of the cirrus cloud might lead to the overestimation of $m_{col}$, $z_{top}$ and $r_{eff}$. Apart from the impact by the cirrus cloud, the retrievals also have some inherent limitations that might lead to inaccuracies close to the vent: the ash properties used in the training data correspond rather to those of aged ash clouds than to fresh ash (e.g., only small particles without porosity are considered) and typical gas emissions (e.g., water vapor, sulfur dioxide) have not been included [2].

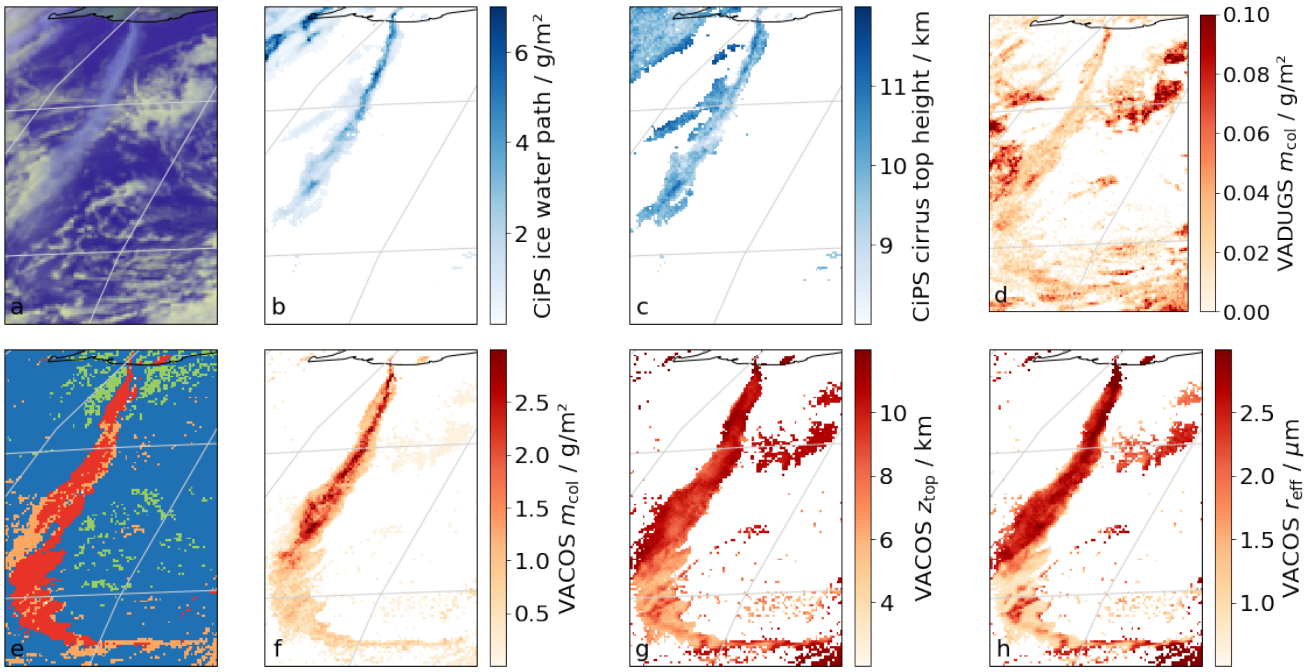


**Figure 15.** Retrieval results for the Eyjafjallajökull eruption at 11 May 2010, 14:00 UTC with Iceland outlined in the top of the plots; (**a**) false color overview composite from SEVIRI data, from CiPS (**b**) cirrus ice water path and (**c**) cloud top height, (**d**) $m_{col}$ from VADUGS, and from VACOS (**e**) the classification (color code as in Figure 10), (**f**) $m_{col}$, (**g**) $z_{top}$ and (**h**) $r_{eff}$.

## 5. Comparison with a Model Ensemble

To check the general performance of VACOS on large scales, the retrievals are compared with the results of a volcanic ash transport and dispersion model. Note that the model is an approximation of the reality as, for instance, inaccuracies in the volcanic ash source term or the meteorological conditions are transferred to the ash distribution. Thus, the scope of this section is to quantify the agreement of the spatial distribution of volcanic ash clouds and to compare the order of magnitude of $m_{col}$.

Here the multi model multi source term ensemble by Plu et al. [35] is used. They simulated the Eyjafjallajökull eruption at 13–19 May 2010 and the area from Iceland in the north-west to Italy in the south-east. We consider scenes every six hours. Four models were used: the atmospheric Lagrangian transport model FLEXPART, the Eulerian chemical transport model MATCH and the chemical transport models MOCAGE and WRF-Chem, considering in varying ways phenomena such as atmospheric transport and mixing, gravitational settling, wet and dry deposition, and chemical reactions. An a posteriori source term is used, determined using a FLEXPART-based optimal estimation model and estimates of $m_{col}$ from satellite data, as well as upper and lower bounds for the source term based on the uncertainties of the optimal estimation result. All models spin-up for at least 3 days, their results are vertically integrated and averaged on a $0.2° \times 0.2°$ grid, as only the large-scale distribution of ash is of interest here. The ensemble result $m'_{col}$ is the median of all simulations.

VACOS and VADUGS retrievals of $m_{col}$ are averaged on the same grid. Instead of the simple uniform averaging of the retrieval results performed in Section 4, the following accumulation rule is applied to alleviate the impact of (a) the different spatial resolutions, (b) possible temporal and spatial shifts between model and satellite retrieval and (c) false satellite detections: a grid cell at time $t$ is assumed to be ash-contaminated if at least a fraction $f_{thrs}$ of all pixels within the cell and within the time $[t - 15\,\text{min}, t + 15\,\text{min}]$ exceeds a threshold of $m_{col,\,thrs}$; then the estimate of $m_{col}$ is the mean of this fraction of the pixels. For VADUGS, $f_{thrs} = 0.5$ and $m_{col,\,thrs} = 0.1\,\text{g}\,\text{m}^{-2}$ is used. For VACOS, three different settings are applied: the same as for VADUGS; $f_{thrs} = 0.5$ and $m_{col,\,thrs} = 0.2\,\text{g}\,\text{m}^{-2}$;

$f_{\text{thrs}} = 0.9$ and $m_{\text{col, thrs}} = 0.2\,\text{g}\,\text{m}^{-2}$. Grid cells covered by cirrus clouds according to the retrieval COCS [36] are discarded.

Three example scenes are shown in Figure 16. The model ensemble shows thick volcanic ash plumes close to the Eyjafjallajökull with $m'_{\text{col}} \geq 10\,\text{g}\,\text{m}^{-2}$, and ash clouds with $m'_{\text{col}} < 1\,\text{g}\,\text{m}^{-2}$ extending over large parts of Europe. VADUGS detects only very limited ash clouds, which correspond spatially to the thickest parts of the simulated ash clouds but with a lower $m_{\text{col}}$. However, in some cases it does not detect ash directly at the volcano, although a prominent plume is simulated. VACOS detects more ash contamination, especially also the plumes in the direct surroundings of the vent, and retrieves higher $m_{\text{col}}$ for them compared to VADUGS. Still, the model ensemble often produces larger ash-loaded areas in the surroundings of the volcano than retrieved by VACOS. At greater distances VADUGS hardly retrieves any ash, whereas VACOS regularly finds ash clouds above central Europe. For instance, in Figure 16b3 volcanic ash is found above the Atlantic north of Scotland, south-east England and at the Atlantic coast of France; then, the ash cloud bends towards north-east and continues over central France and central Germany with concentrations around 0.2–0.3 $\text{g}\,\text{m}^{-2}$. The model ensemble produces a similar distribution, but the ash cloud heads further south after the bending, continuing above the Mediterranean sea (panel a3). Similar offsets between the model and the VACOS retrieval are also visible comparing the other two scenes; in both cases there are faint ash clouds that are detected further east by VACOS than they are simulated by the model ensemble. This indicates that the model is less reliable at large distances, e.g., above central Europe, which might also influence the following comparisons, but at the same time it confirms that the satellite retrievals over here are plausible and reliable.

Figure 17 shows the POD and the FAR for the different retrievals and accumulation rules with respect to different subsets of the model ensemble. Furthermore, offsets up to 100 km are taken into account, i.e., an ash-loaded grid cell of the simulation is considered detected if the retrievals find ash within the given radius, and a retrieved ash-loaded cell is considered a false alarm if no ash is modeled within the same radius. VADUGS is found to have the smallest POD and FAR, whereas both metrics are larger for VACOS but decrease for more conservative accumulation and threshold rules. Increasing the offset distance leads to significant increases in POD, whereas the decrease of FAR is mostly rather small. When increasing $m'_{\text{col, thrs}}$, the POD as well as the FAR increase. The latter is explained by samples with $m'_{\text{col}} < m'_{\text{col, thrs}}$ but $m_{\text{col}} > m_{\text{col, thrs}}$, existing either because of overestimation by the retrievals, or in the case of the subset with $m'_{\text{col, thrs}} = 0.2\,\text{g}\,\text{m}^{-2}$ due to $m_{\text{col, thrs}} = 0.1\,\text{g}\,\text{m}^{-2}$, such that samples with correctly retrieved mass loads in between those two values lead to false alarms. Considering $m'_{\text{col}} \geq 0.01\,\text{g}\,\text{m}^{-2}$ and an offset of 100 km leads for VADUGS to a POD of ~30% and a FAR of 0.02%, whereas VACOS (with $m_{\text{col, thrs}} = 0.2\,\text{g}\,\text{m}^{-2}$, $f_{\text{thrs}} = 0.5$) has a POD of close to 60% at a FAR of about 2%. The PODs increase by ~20% for $m'_{\text{col}} \geq 0.1\,\text{g}\,\text{m}^{-2}$ and by 25–30% for $m'_{\text{col}} \geq 0.2\,\text{g}\,\text{m}^{-2}$. In the latter case, the POD of VACOS is nearly 90% and the FAR is 2–3%.

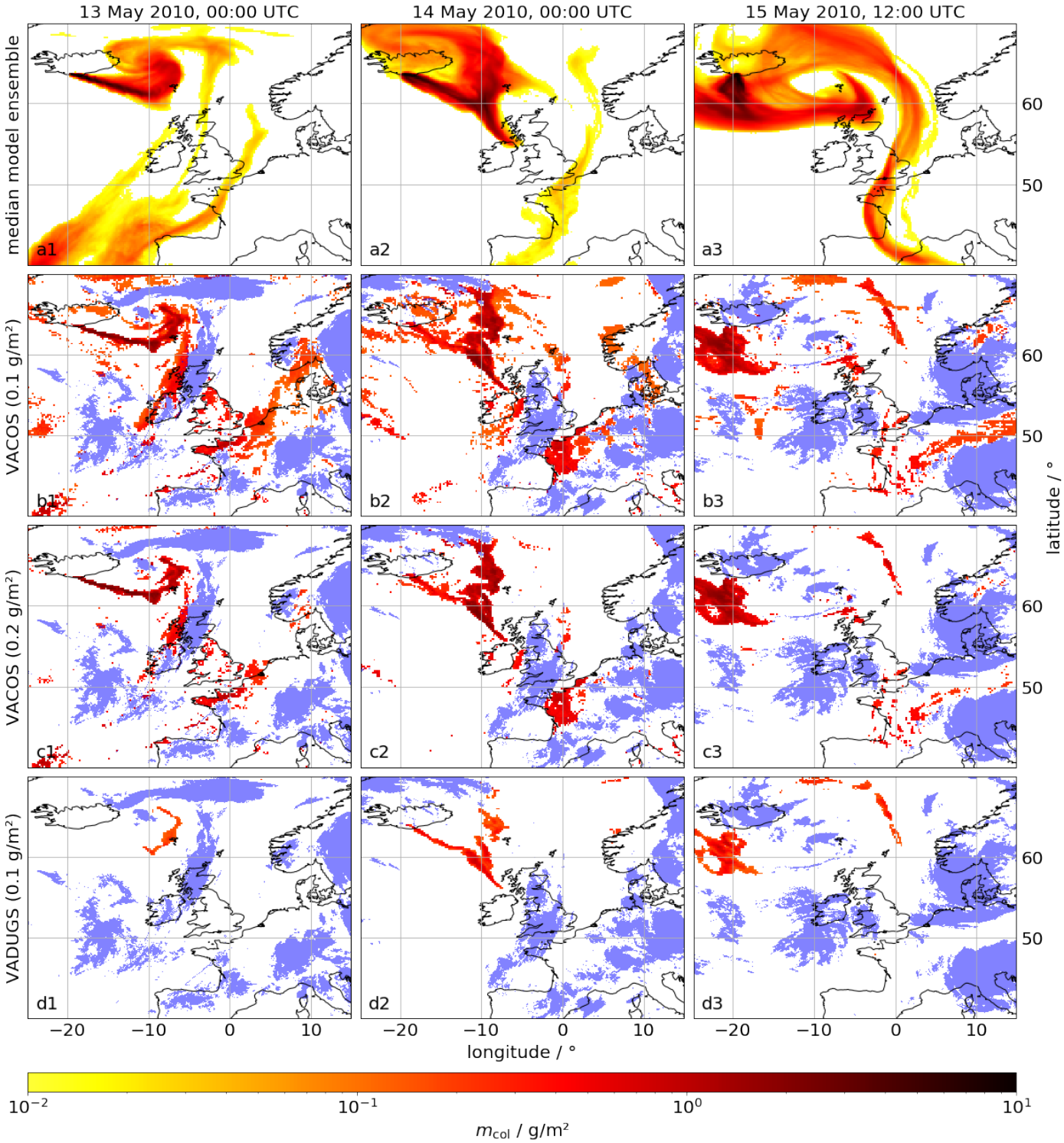


**Figure 16.** $m_{\mathrm{col}}$ (red) according to the median of a model ensemble (**a**), VACOS ($m_{\mathrm{col,thrs}} = 0.1\,\mathrm{g\,m^{-2}}$ and $0.2\,\mathrm{g\,m^{-2}}$, $f_{\mathrm{thrs}} = 0.5$; **b** and **c**) and VADUGS ($m_{\mathrm{col,thrs}} = 0.1\,\mathrm{g\,m^{-2}}$, $f_{\mathrm{thrs}} = 0.5$; **d**) for three scenes (1: 13 May 2010, 00:00 UTC; 2: 14 May 2010, 00:00 UTC; 3: 15 May 2010, 12:00 UTC); for the model $m_{\mathrm{col}} < 0.01\,\mathrm{g\,m^{-2}}$ is not shown; cirrus presence according to COCS is indicated (blue).

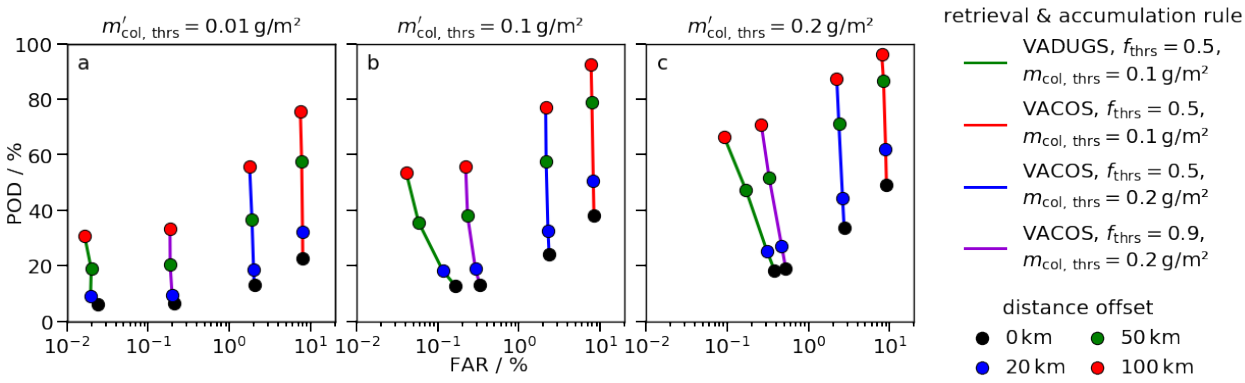


**Figure 17.** Estimations of the POD and the FAR for the detection of volcanic ash using $m_{col}$ of VACOS (connected by red, blue and violet lines) and of VADUGS (green line) applying different thresholds and accumulation rules (see text); different thresholds for the model data are used, e.g., only samples with $m'_{col} \geq 0.01\,g\,m^{-2}$ (**a**), $\geq 0.1\,g\,m^{-2}$ (**b**) or $\geq 0.2\,g\,m^{-2}$ (**c**) are classified as ash-containing; only pixels in absence of cirrus clouds are used, ca. 66,000 in total; different offset distances between the model and the satellite data are considered and indicated by the marker color (see text).

Table 5 gives the MAPE and MPE for the retrieval of $m_{col}$ for VADUGS and VACOS, different accumulation and threshold rules and different subsets of the modeled data, not considering any distance offsets. For $m'_{col} \geq 0.01\,g\,m^{-2}$ the MAPE is around 100% and the MPE is −96% for VADUGS, whereas for VACOS the MAPE is higher (106–138%) and the MPE is less negative (−26 to −83%), i.e., the underestimation is smaller compared to VADUGS. However, considering only grid cells that are classified as ash-contaminated by the model and the retrieval, i.e., $m'_{col}$ and $m_{col} \geq 0.2\,g\,m^{-2}$, the MAPE and MPE of VADUGS change to 65% and −60%, respectively. Using the same accumulation and threshold ($m_{col,\,thrs} = 0.1\,g\,m^{-2}$, $f_{thrs} = 0.5$) for VACOS leads to a MAPE of only 57% and a MPE of 0%; thus, the retrievals of VACOS are in better agreement with the model results than those of VADUGS, indicating that VACOS is more reliable for these mass concentrations.

**Table 5.** Comparison of the $m_{col}$ retrieval of VADUGS and VACOS against the model ensemble median; MAPE and MPE of different subsets depending on $m'_{col}$ from the model ensemble and $m_{col}$ from the satellite retrieval are considered; for VACOS a mass extinction coefficient at 10.8 µm of 200 $m^2\,kg^{-1}$ is considered for the conversion of $\tau_{10.8}$ to $m_{col}$; different accumulation rules and thresholds are used for the satellite retrievals; pixels with cirrus cloud presence are excluded.

| Algorithm | Accumulation Rule | $m'_{col} \geq 0.01\,g\,m^{-2}$ | | | $m'_{col} \geq 0.2\,g\,m^{-2}$ | | | $m'_{col}$ and $m_{col} \geq 0.2\,g\,m^{-2}$ | | |
|---|---|---|---|---|---|---|---|---|---|---|
| | ($m_{col,\,thrs}$; $f_{thrs}$) | Samples | MAPE | MPE | Samples | MAPE | MPE | samples | MAPE | MPE |
| VADUGS | $0.1\,g\,m^{-2}$; 0.5 | 222,932 | 99% | −96% | 63,595 | 94% | −94% | 6201 | 65% | −60% |
| VACOS | $0.1\,g\,m^{-2}$; 0.5 | 221,663 | 138% | −26% | 63,363 | 79% | −56% | 26,200 | 57% | 0% |
| VACOS | $0.2\,g\,m^{-2}$; 0.5 | 221,633 | 127% | −52% | 63,357 | 87% | −62% | 21,331 | 60% | 12% |
| VACOS | $0.2\,g\,m^{-2}$; 0.9 | 221,663 | 106% | −83% | 63,363 | 94% | −76% | 12,006 | 68% | 25% |

## 6. Unraveling the Black Box: How Do the ANNs Work?

In this section, we aim to shed light upon the working principles of our ANNs. Therefore, we first perform additional radiative transfer calculations for different ash cloud settings to investigate how the brightness temperatures (differences) depend on the ash cloud properties and show examples on how to deduce those properties from different combinations of channels. Second, we analyze the importance of the different input features of the ANNs with respect to their performance and connect these results with the conclusions drawn from the simulations.

A single, homogeneous ash layer of geometrical thickness 1 km without meteorological clouds is assumed; $m_{col}$ is varied to be 0.1–1000 $g\,m^{-2}$ and $z_{top}$ is 3–12 km above

ground. The volcanic ash has the refractive index of Eyjafjallajökull ash [14], a log-normal size distribution with $r_{\mathrm{eff}}$ =0.6 µm, 3 µm and 6 µm, $s = 1.5$ and a representative shape distribution of spheroids as considered by Piontek et al. [3]. The brightness temperatures of the infrared channels of SEVIRI are simulated for the different ash clouds 500 times for different atmospheric settings and geographical locations in 2010 with the methods outlined in Piontek et al. [2]; finally, the median is determined. Figure 18 shows the dependence of the brightness temperatures on $m_{\mathrm{col}}$. Panel (a) shows (for $z_{\mathrm{top}} = 9$ km and $r_{\mathrm{eff}} = 0.6$ µm) that the brightness temperature decreases with increasing $m_{\mathrm{col}}$. Clearly visible are the atmospheric window channels ($BT_{8.7}$, $BT_{10.8}$, $BT_{12}$), which exhibit a S-curve behavior with plateaus for $m_{\mathrm{col}} < 0.1\,\mathrm{g\,m^{-2}}$ and $m_{\mathrm{col}} > 100\,\mathrm{g\,m^{-2}}$. The water vapor channels ($BT_{6.2}$, $BT_{7.3}$) reach saturation at higher $m_{\mathrm{col}}$. The absolute changes in brightness temperature are largest for the atmospheric window channels, about half as large for $BT_{7.3}$, $BT_{9.7}$, $BT_{13.4}$ and smallest for $BT_{6.2}$. The reason is that all brightness temperatures are around 240 K for a thick ash layer (e.g., $m_{\mathrm{col}} = 100\,\mathrm{g\,m^{-2}}$) which dominates over all other atmospheric constituents, whereas in the absence of an ash layer the brightness temperature depends on the impact of the atmospheric gases on the different channels. Panel (b) shows the results for $BT_{10.8}$ for $r_{\mathrm{eff}} \in \{0.6, 3, 6\}$ µm and $z_{\mathrm{top}} \in \{3, 6, 9, 12\}$ km. It shows that with increasing $z_{\mathrm{top}}$ the asymptotic value of $BT_{10.8}$ at large $m_{\mathrm{col}}$ decreases (from roughly 280 K to 220 K), as the opaque ash layer completely hides the surface and the top of atmosphere brightness temperature is mostly determined by the atmospheric temperature at $z_{\mathrm{top}}$, which decreases with increasing $z_{\mathrm{top}}$ within the troposphere. The influence of $r_{\mathrm{eff}}$ is smaller and mainly visible in the intermediate regime (i.e., for $m_{\mathrm{col}} \in [1, 30]\,\mathrm{g\,m^{-2}}$), where $BT_{10.8}$ is smallest for $r_{\mathrm{eff}} = 3$ µm and largest for 6 µm. This can be understood from the size dependence of the mass extinction coefficient, which is largest for $r_{\mathrm{eff}} = 3$ µm and smallest for 6 µm with respect to the three considered $r_{\mathrm{eff}}$ [2]. Note that both an increase in $z_{\mathrm{top}}$ and in $m_{\mathrm{col}}$ leads to a lower $BT_{10.8}$.

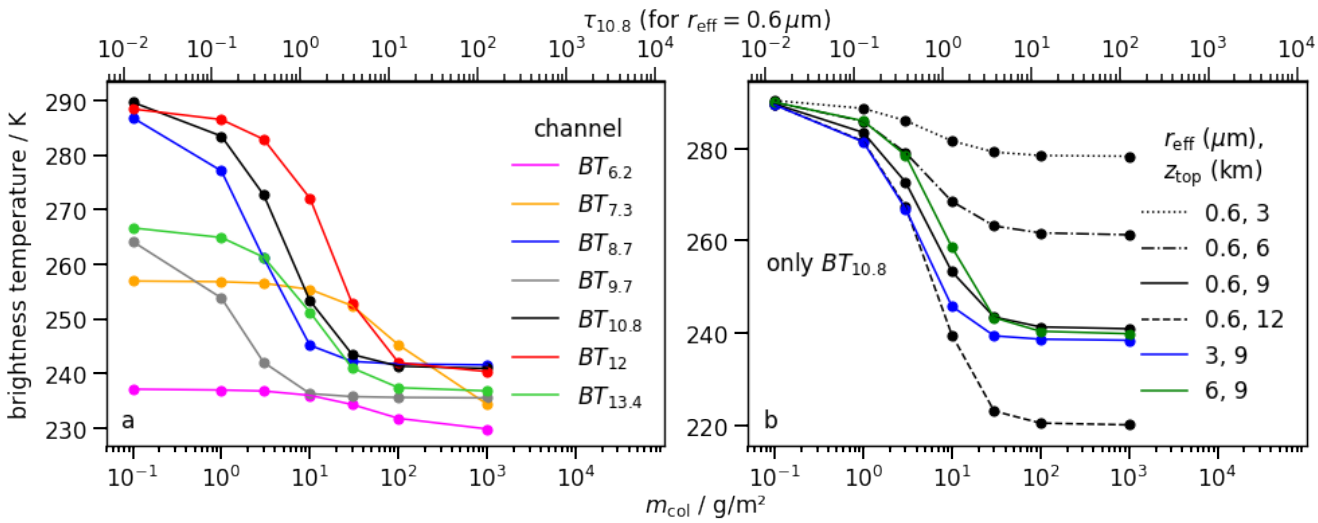


**Figure 18.** Median brightness temperature of different SEVIRI channels averaged for 500 simulations (see text); (**a**) brightness temperatures for an ash cloud with $z_{\mathrm{top}} = 9$ km and $r_{\mathrm{eff}} = 0.6$ µm for different $m_{\mathrm{col}}$, (**b**) $BT_{10.8}$ for different $z_{\mathrm{top}}$ and $r_{\mathrm{eff}}$.

Figure 19 shows combinations of different brightness temperatures and brightness temperature differences for the same simulations. The size of the markers encodes $m_{\mathrm{col}}$. Markers of constant $z_{\mathrm{top}}$ and $r_{\mathrm{eff}}$ but different $m_{\mathrm{col}}$ are connected by black, blue and violet lines for $r_{\mathrm{eff}}$ =0.6 µm, 3 µm and 6 µm, respectively, whereas the linestyle denotes $z_{\mathrm{top}}$. Additionally, points of constant $m_{\mathrm{col}}$, $r_{\mathrm{eff}}$ and variable $z_{\mathrm{top}}$ are connected by red lines, and points of constant $m_{\mathrm{col}}$, $z_{\mathrm{top}}$ and variable $r_{\mathrm{eff}}$ by green lines. Thus, Figure 19 shows whether the variation of different parameters leads to similar behaviors with respect to certain brightness temperatures (differences). Panel (a) shows $BT_{10.8}$ against $BTD_{10.8\text{–}12}$;

this combination has often been studied [37,38]. For $m_{col} < 3\,g\,m^{-2}$ an increase in $m_{col}$ (along the black lines) reduces $BT_{10.8–12}$ and $BTD_{10.8–12}$; the latter is related to the spectral dependence of the mass extinction coefficient of volcanic ash [3]. An increase in $z_{top}$ (along the red line) also reduces $BT_{10.8}$ and leads overall to a similar change in this two-dimensional phase space, i.e., the black and the red curves are parallel and lie on top of each other. However, for $m_{col} > 3\,g\,m^{-2}$ the directions of these curves deviate as $BTD_{10.8–12}$ vanishes if the ash cloud becomes opaque in the thermal infrared; thus, $m_{col}$ and $z_{top}$ can be distinguished. In (c), $BT_{13.4}$ and $BT_{12-13.4}$ are combined. Here the black and the red curve proceed in different directions already for $m_{col} < 1\,g\,m^{-2}$ and allow the separation of the influence of $m_{col}$ and $z_{top}$: Increasing either of the two quantities reduces $BT_{13.4}$, but increasing $z_{top}$ changes $BT_{12}$ and $BT_{13.4}$ similarly, thus $BTD_{12-13.4}$ shows only minor changes. Yet, increasing $m_{col}$ leads to a reduction of $BTD_{12-13.4}$, which is ~20 K in the absence of volcanic ash due to the impact of carbon dioxide (see Figure 18), but vanishes as the ash cloud becomes opaque. In principle, the same behavior is visible for $r_{eff} = 3\,\mu m$ in (b) and (d), but the curves corresponding to different $z_{top}$ are located closer together. Note that for $r_{eff} = 6\,\mu m$ (violet curve) $BTD_{10.8–12}$ is positive independent of $m_{col}$ for $z_{top} = 9\,km$ [3,38].

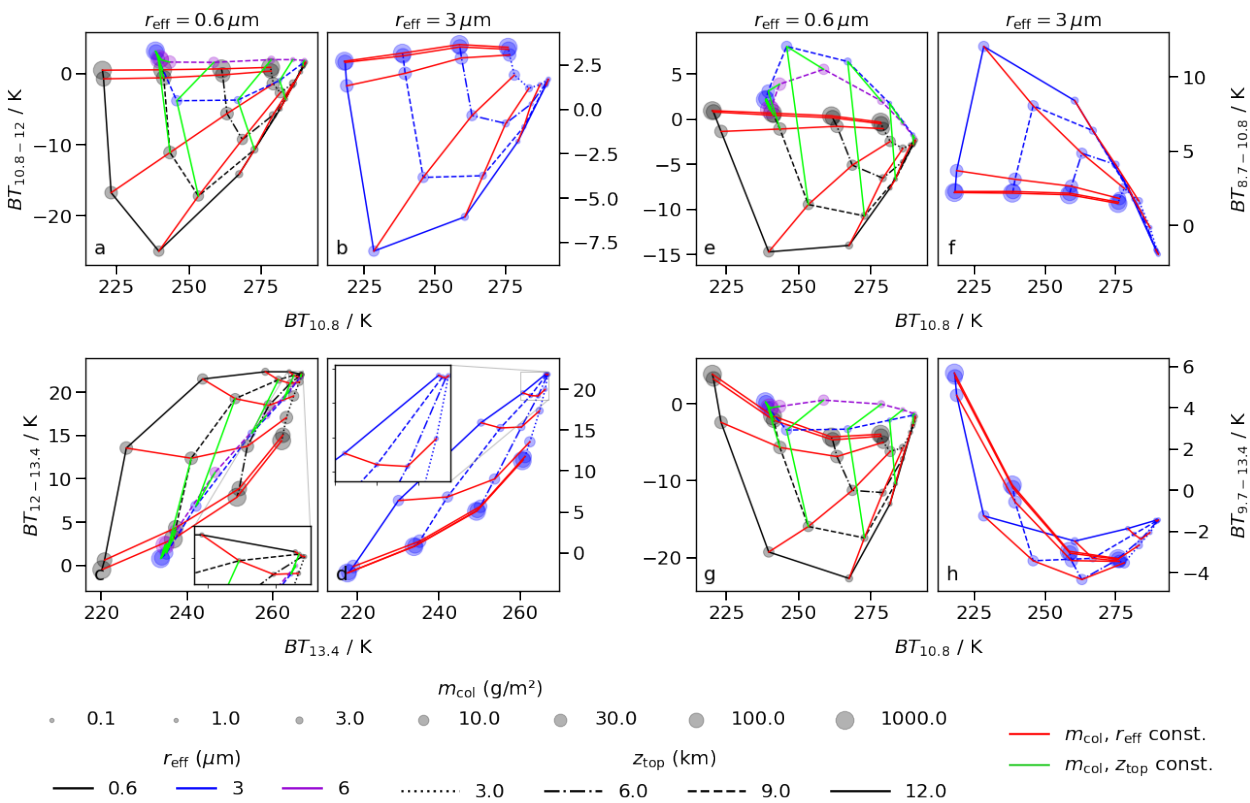


**Figure 19.** Combinations of the medians of different brightness temperatures and brightness temperature differences, calculated from 500 simulations for each volcanic ash cloud (see text); mainly two different $r_{eff}$ are used: 0.6 µm (**a**,**c**,**e**,**g**) and 3 µm (**b**,**d**,**f**,**h**); $m_{col}$ is given by the size of the markers; markers with constant $z_{top}$ and $r_{eff}$ but different $m_{col}$ are connected by black, blue and violet lines for $r_{eff}$ =0.6 µm, 3 µm and 6 µm, respectively; the linestyle encodes $z_{top}$; points of constant $m_{col}$, $r_{eff}$ and variable $z_{top}$ are connected by red lines, and points of constant $m_{col}$, $z_{top}$ and variable $r_{eff}$ by green lines.

The variation of brightness temperatures (differences) due to $r_{eff}$ is shown by the green lines as an example. In (a) and (c), $r_{eff}$ cannot be determined easily as it is entangled with $m_{col}$ and $z_{top}$. Therefore, we consider $BT_{8.7}$, $BT_{9.7}$ and $BT_{10.8}$, which are located at the typical absorption peak of volcanic ash and which are influenced differently depending on the particle size [3]. Panel (e) shows $BT_{10.8}$ against $BTD_{8.7-10.8}$. Here $r_{eff} = 0.6\,\mu m$ mostly leads to $BTD_{8.7-10.8} < 0$, in contrast to $r_{eff}$ =3 µm and 6 µm (except for $m_{col} < 1\,g\,m^{-2}$, but even

there the $r_{\text{eff}}$ can be separated). Panel (g) shows $BTD_{9.7-13.4}$ on the y-axis. The blue curve for $r_{\text{eff}} = 3\,\mu\text{m}$ is convex, whereas the violet curve for $r_{\text{eff}} = 6\,\mu\text{m}$ is concave. A threshold at roughly $-1.5\,\text{K}$ with respect to $BTD_{9.7-13.4}$ would allow to separate the different $r_{\text{eff}}$ except for $m_{\text{col}} > 30\,\text{g}\,\text{m}^{-2}$. To summarize, it is possible to disentangle the physical quantities $m_{\text{col}}$, $z_{\text{top}}$ and $r_{\text{eff}}$ using the MSG/SEVIRI channels in the thermal infrared and exploiting the dependence of the mass extinction coefficient of volcanic ash on the wavelength and the particle size as well as the relatively constant impact of other atmospheric gases (e.g., carbon dioxide).

The actual working principles of ANNs are hard to determine. However, one can try to quantify the importance of the individual input features for each ANN and thereby deduce which physical principles are exploited and which functions might be implemented internally. Neglecting those features and retraining the ANNs might also allow to simplify the algorithms [39,40]. We define two metrics: The first, $M_x$, is the relative contribution of the $x$th input neuron to the total weight between the input layer and the first hidden layer, defined as

$$M_x = \frac{\sqrt{\sum_{j=0}^{m} w_{x,j}^2}}{\sum_{i=0}^{n} \sqrt{\sum_{j=0}^{m} w_{i,j}^2}} \tag{1}$$

for an input layer of $n$ neurons, a first hidden layer of $m$ neurons and the connecting weights $w_{i,j}$ [10]. The expectation is that the weights of unimportant features will vanish during training such that they have no impact on the calculation of the ANNs. However, in case of multiple hidden layers it might be possible that the impact of a feature significantly changes in the subsequent layers. Therefore, we consider a second metric: the relative change in loss, $K_x$, when a feature is set to zero (simulating $w_{x,j} = 0$ for all $j \in [1, m]$) for the complete test data set, i.e.,

$$K_x = \frac{L_x - L_0}{L_0} \tag{2}$$

with $L_0$ being the loss (here the mean squared error for regressions and the categorical cross entropy for the classification) for the full test data set, whereas $L_x$ is the loss for the test data set when setting the $x$th input to zero. When dropping an unimportant feature $L_x$ should not change significantly, no matter whether it has vanishing weights already between the input and the first hidden layer or deeper in the network. However, dropping an important feature that is necessary for the calculation of the ANN will lead to a worse performance and, therefore, a larger loss $L_x$.

Figure 20 shows $M_x$ and $K_x$ for all four ANNs and their input features. The two metrics quantitatively lead to different results. Whereas $M_x$ shows for all features always at least a small value, $K_x$ produces relatively large contrasts; thus, using $K_x$ it becomes more obvious whether an input is important or not. However, qualitatively both methods lead to similar pictures: For example, for the classification both metrics (a, b) indicate $BT_{10.8}$ to be the most important of all brightness temperatures. Compared with the results of the other ANNs also the total column water and the total column water vapor appear to be important, and finally the viewing zenith angle.

For the $\tau_{10.8}$ retrieval (c, d) only ash-loaded samples are considered, with $BT_{12}$ being the most important channel. Furthermore, $BT_{8.7}$, $BT_{10.8}$ and $BT_{13.4}$ are prominent in both metrics. This is in agreement with the conclusions drawn from Figure 19. Compared to the retrievals of $z_{\text{top}}$ and $r_{\text{eff}}$ also the total column water and water vapor have significant impact on $K_x$ (d); they might be used to take the corresponding atmospheric constituents into account. For the $z_{\text{top}}$ retrieval, $M_x$ (e) implies $BT_{8.7}$, $BT_{9.7}$, $BT_{10.8}$ and $BT_{13.4}$ to be the most important brightness temperatures, and furthermore $\tau_{10.8}$ and surprisingly the day of year variables have large metrics. However, generally the contrast is not very large between the features. $K_x$ (f) however points out $BT_{9.7}$, $BT_{13.4}$ and $\tau_{10.8}$. The importance of $BT_{13.4}$ is again in agreement with the conclusions from Figure 19. The large values for $\tau_{10.8}$ show that the performance of the $z_{\text{top}}$ algorithm heavily depends on the accuracy of the $\tau_{10.8}$ retrieval. For the $r_{\text{eff}}$ retrieval, $M_x$ (g) slightly highlights $BT_{8.7}$, $BT_{12}$, $BT_{13.4}$.

From the auxiliary features the latitude, the cosine of the viewing zenith angle, $\tau_{10.8}$ and the ash-free temperatures $BT_{8.7,\mathrm{clr}}$, $BT_{10.8,\mathrm{clr}}$ and $BT_{12,\mathrm{clr}}$ stand out. Again, the contrast between features is overall small. Using $K_x$ (h) leads roughly to the same result but stresses the leading channels $BT_{8.7}$, $BT_{12}$, $BT_{13.4}$ even more. The importance of these channels for the derivation of $r_{\mathrm{eff}}$ was also visible in Figure 19.

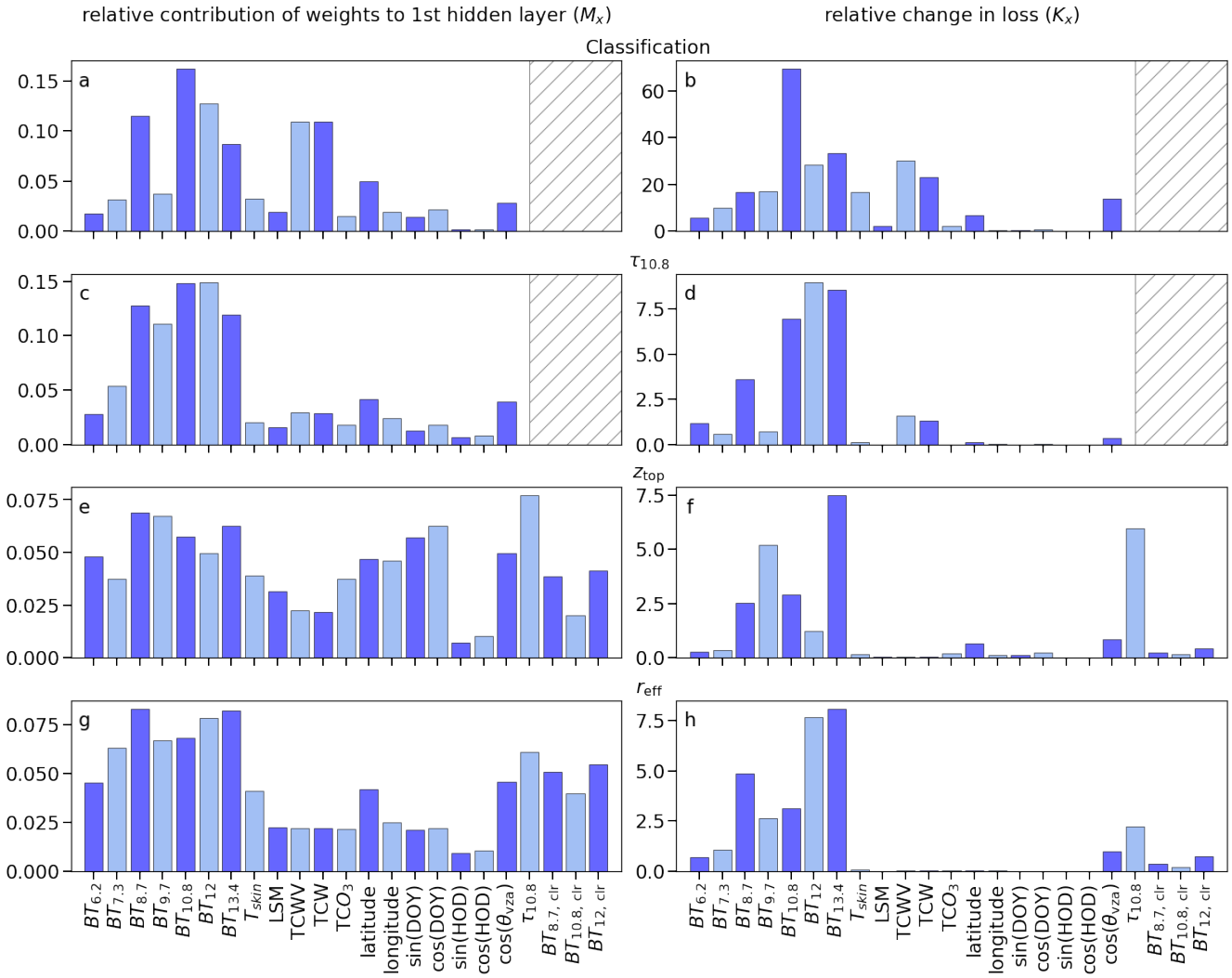


**Figure 20.** Two estimations of the feature importance: the relative contribution to the total weight at the 1st hidden layer ($M_x$; **a**,**c**,**e**,**g**) and the relative change in loss ($K_x$; **b**,**d**,**f**,**h**) (see text for definition) for all four ANNs and all input features, including the viewing zenith angle ($\theta_{\mathrm{vza}}$), the hour of day (HOD) and the day of year (DOY); the loss function used for $K_x$ is is the mean squared error for regressions and the categorical cross entropy for classification; bars are alternately colored blue and light blue for better readability.

Let us focus on $K_x$ (b, d, f, h) now: From the auxiliary input features the total column water vapor and the total column water play a minor role in the retrieval of $\tau_{10.8}$ and a larger one for the classification; for height and effective radius retrievals they are unimportant. The latitude appears to be important mostly for the $z_{\mathrm{top}}$ retrieval and the classification, and the skin temperature only for the classification. The land/sea mask, the total column ozone, the longitude, the day of year and the hour of day are rather negligible in all cases.

The metric $M_x$ was also derived for the input features of the cirrus cloud retrieval CiPS, which also consisted of several ANNs to derive, e.g., the cirrus optical depth or the cloud top height, trained using collocated SEVIRI and CALIOP measurements [10]. Comparing the results CiPS and VACOS shows similarities, e.g., in both cases the brightness temperatures play a dominant role, but the day of year and surface classifications are rather

negligible. A noteworthy difference is that whereas the $z_{top}$ retrieval of CiPS mainly depends on latitude (as maximum cirrus cloud top height strongly depends thereon; thus, a statistical effect), our results show only a smaller dependence on this quantity.

Generally, the metrics support the observations made before in Figure 19, with the brightness temperatures having the major impact, whereas the auxiliary data seem to be of minor importance (even the skin temperature). The low values for the geographical coordinates imply that the ANNs do not learn the geography of the Earth as visible from SEVIRI. Similarly, the low values for the land/sea mask show that even this rough classification of the Earth's surface remains unregarded. The low values for the times (day of year, hour of day) indicate that the ANNs do also not learn seasonal or diurnal variations. Reasons why the ANNs do not internalize those more evolved concepts might be a too small training data set, or they are just not helpful enough as the central physical quantities are rather obtained in the observations. For example, although the atmospheric state undergoes a seasonal variation, volcanic ash clouds are independent of them as volcanic eruptions can take place at any time of year. The hint that the ANNs do not learn the map indicates that the method might be applicable to other regions of the Earth (e.g., using GOES or Himawari satellites).

## 7. Conclusions

In a companion paper, we introduced a new algorithm to retrieve volcanic ash properties, i.e., a pixel classification, the cloud top height ($z_{top}$), the effective particle radius ($r_{eff}$) and (indirectly from the optical depth at 10.8 µm, $\tau_{10.8}$) the mass column concentration ($m_{col}$) from MSG/SEVIRI data using artificial neural networks; it is called VACOS (*Volcanic Ash Cloud properties Obtained from SEVIRI* [2]). The input data encompass the seven brightness temperatures of the imager's channels in the thermal infrared and additional data from ECMWF. VACOS allows spatially and temporally highly resolved retrievals of volcanic ash clouds independent of daylight.

For the validation, VACOS is compared to independent measurements. With respect to CALIOP retrievals of the Puyehue-Cordón Caulle ash clouds (2011), VACOS shows quite a large variability on a single pixel basis. A regional average over $5 \times 5$ pixels reduces this variability and leads to lower deviations between $m_{col}$ of VACOS and the lidar retrieval: the mean absolute percentage error (MAPE) of $m_{col}$ decreases to 45% and the MAPE of $z_{top}$ is 18% when considering only samples with a lidar retrieval of $m_{col} \geq 0.2\,\mathrm{g\,m^{-2}}$. Therefore, this averaging is recommended for future applications of the new algorithm. The VACOS-derived $m_{col}$ is in good agreement with the CALIOP measurements in most, but not all, cases. Deviations are generally within the uncertainties of the reference data. $z_{top}$ and $r_{eff}$ by VACOS have the correct order of magnitude but exhibit significant scattering, with $z_{top}$ being slightly underestimated (having a mean percentage error of −14%), whereas $r_{eff}$ lies within the regime constrained by literature values. The four category classification of VACOS detects the volcanic ash clouds with the highest mass loads, but ash layers with $m_{col}$ less than ~$0.4\,\mathrm{g\,m^{-2}}$ are often misclassified as meteorological clouds (which includes liquid and ice water clouds). Similarly, SEVIRI images indicate that clear sky might be too often misclassified as cloudy, but here dedicated retrievals of meteorological clouds should provide help. Additionally considering a cirrus retrieval also shows that thick ice clouds have the potential to completely hide the volcanic ash or distort their retrieval; thus, we also recommend to consider VACOS results always together with a cirrus cloud retrieval to avoid misinterpretations.

As another reference, airborne lidar and in situ data of an Eyjafjallajökull ash cloud (2010) are used as obtained during two different measurement campaigns by FAAM and DLR, respectively. The various measurement results for $m_{col}$, $z_{top}$ and $r_{eff}$ agree well, considering that different instrumentation was used and different parts of the ash cloud were probed. Main differences are a higher upper estimate of $m_{col}$ according to the DLR (roughly $2\,\mathrm{g\,m^{-2}}$ compared to mostly around $1\,\mathrm{g\,m^{-2}}$) and a higher upper limit for $r_{eff}$ in the FAAM data (2 µm compared to 1 µm); $z_{top}$ estimates are up to ~6 km in both cases.

For the most part, the VACOS retrievals of $m_{col}$ and $r_{eff}$ lie within the uncertainty intervals of the airborne measurements, whereas $z_{top}$ from the new retrieval scatters around the reference values with deviations in the order of 1–2 km. Concurrent overestimations of $z_{top}$ and $r_{eff}$ can be explained by low $m_{col}$ in some cases, but not generally. The classification algorithm correctly detects the ash cloud.

Results of a volcanic ash transport and dispersion multi model multi source term ensemble simulating the eruption of Eyjafjallajökull (2010) are used to analyze the performance of VACOS on large scales. Different accumulation rules are investigated when regridding the satellite retrievals. Example scenes indicate that the model results and the VACOS retrievals are in good agreement close to the volcano, but that there are displacements of the ash clouds at larger distances, e.g., for ash clouds above continental Europe; those might be caused by inaccuracies in the model calculations. As a consequence, distance offsets up to 100 km are considered. The model ensemble covers a larger interval of possible $m_{col}$ than VACOS: $m_{col}$ can be an order of magnitude larger in the model calculations than in the VACOS retrieval in a surrounding of some 100 km around the vent, whereas it can be more than one order of magnitude smaller at distances of >1000 km. Considering only samples with $m_{col} \geq 0.2\,\mathrm{g\,m^{-2}}$ according to both the model ensemble and VACOS results in a MAPE of ~60% for $m_{col}$ of VACOS.

To further quantify the performance of VACOS, a simulated test data set similar to its training data is used. The four category classification classifies correctly more than 94% of the simulated cases, except when both volcanic ash and meteorological clouds are present, which reduces the amount of correct classifications to ~50%. Simplifying classification results to a binary ash flag results in a probability of detection (POD) of close to 100%. The retrievals of $\tau_{10.8}$, $z_{top}$ and $r_{eff}$ have mostly MAPEs of 10–100%. For $\tau_{10.8}$, the MAPE is ~40% or less for ash layers with a true $\tau_{10.8}$ of 0.1 (corresponding to $m_{col}$ of 0.3–0.7 $\mathrm{g\,m^{-2}}$) or more; the retrieval error of $z_{top}$ is up to ~10% for ash layers above 5 km; and $r_{eff}$ has an error of up to 35% for true radii of 0.6–6 µm. The performance increases with increasing $\tau_{10.8}$ and $z_{top}$ of the ash layers. Thus, the greatest errors occur for the thinnest and lowest ash clouds, for which the MAPE can even exceed 100%. No significant differences exist between underlying land and sea surfaces, in contrast to the presence of meteorological clouds (particularly if they are located above the ash layer), which can increase the MAPE by up to one order of magnitude and decrease the POD by a factor of two. Analysis of the geographical dependence shows that deserts lead to a decreased performance for clear sky cases, e.g., the accuracy of the binary ash flag slightly decreases (ca. 1%), whereas the MAPE for $r_{eff}$ increases. An increased performance of the binary ash flag is observable in the presence of clouds above areas that are typically cloudy, i.e., where many cloudy samples are included in the simulated (training and test) data sets. The retrievals of $\tau_{10.8}$ and $r_{eff}$ show increased MAPEs with increasing viewing zenith angle, whereas the MAPE of $z_{top}$ increases with the absolute latitude. Using further simulated test data sets, the dependence of the retrievals with respect to the ash layer(s) is investigated. The (unretrieved) geometrical layer thickness and the presence of multiple layers might introduce errors of about 30% for $\tau_{10.8}$, 5% for $z_{top}$, but are negligible for $r_{eff}$.

Volcanic ash detection can be performed using the binary ash flag or $\tau_{10.8}/m_{col}$ and corresponding thresholds. Using the simulated data shows that the detection ability of the binary ash flag is better than the one using $\tau_{10.8}$, and both outperform the usage of the brightness temperature difference between the channels centered at 10.8 µm and 12 µm; using for $m_{col}$ a threshold of 0.2 $\mathrm{g\,m^{-2}}$ and considering only ash layers with 0.2–1 $\mathrm{g\,m^{-2}}$ leads to a POD of more than 90% and a false alarm rate (FAR) of ca. 1%. For the CALIOP data, higher PODs can be found when using $m_{col}$ compared to the binary ash flag; a similar threshold as before leads to a POD of ~70%. Using the model results as reference data, we find for similar thresholds PODs of 20–85% and FARs of 0.3–3%, which strongly depend on the accumulation rule and the allowed distance offsets. Note that the model result is not a perfect representation of reality; therefore, POD and FAR should be regarded as metrics

quantifying the agreement of model and retrieval results rather than performance metrics attributed exclusively to VACOS.

VACOS is also compared to its direct predecessor VADUGS. The latter exhibits a better detection performance on the CALIOP data and has a smaller FAR for the model data, but it also misses significantly more modeled ash clouds than VACOS, especially also ash plumes close to the vent. Whereas the $m_{\mathrm{col}}$ retrieval of VADUGS performs similar to VACOS for the CALIOP data, it underestimates $m_{\mathrm{col}}$ compared to the airborne lidar and in situ findings. The VADUGS retrieval of $z_{\mathrm{top}}$ is reliable only for ash clouds with $m_{\mathrm{col}}$ of the order $1\,\mathrm{g\,m^{-2}}$ or larger. Overall, VADUGS seems much more sensitive to specific cases than VACOS. In the end, we consider the importance of different input features of the VACOS retrievals, showing that they are mostly dependent on the SEVIRI brightness temperatures, and partly also on the viewing zenith angle as well as total column water and water vapor estimates from ECMWF. Longitude, land/sea-mask and times have negligible impact on the output.

In the future it would be desirable to further analyze the retrieval performance also with respect to mineral dust. As volcanic ash and mineral dust share similar optical properties due to the common high silica content, it is likely that VACOS might misclassify dust as volcanic ash [7,41,42]. In this case, it would be interesting to see if VACOS could be used to retrieve dust cloud properties as well. The aviation industry considers similar risks for volcanic ash and for dust, hence a combined retrieval seems advantageous. Furthermore, VACOS has been tailored for Meteosat-9/MSG2. The usage of the retrieval algorithm with the currently operational MSG satellite as well as the satellites in other operation modes (i.e., rapid scan mode, Indian Ocean data coverage) should be investigated. As other infrared imagers aboard geostationary weather satellites such as GOES-R [43], Himawari-8/9 [44] and Fengyun-4A [45] share similar channels with MSG/SEVIRI one could also investigate the transferability of VACOS to those instruments. The error of the VACOS retrievals decreases when a local average is calculated. To expand on this idea, further processing of the retrieval map seems desirable, e.g., to cluster ash-containing pixels and quantify the resulting ash patches, or even track them in time. Possible fields of application of VACOS include the Volcanic Ash Advisory Centers, the intercomparison with other volcanic ash retrievals (as in [46]), calibrating and validating volcanic ash transport and dispersion models [35,47–49] and flight planning for future in situ measurements [15]. Due to the high spatial and temporal resolution, it can be used to track individual ash clouds to investigate their lifecycle on timespans of days to weeks. In combination with information on liquid and ice water clouds, aerosol-cloud interaction could be analyzed.

In summary, VACOS is well characterized and shown to be reliably applicable under different atmospheric conditions and for various kinds of volcanic ash clouds. It can be utilized for atmospheric research as well as for air space monitoring with respect to volcanic ash. Operational use by the German weather service (DWD) as a follow-on of VADUGS is planned.

**Author Contributions:** Conceptualization, D.P. and L.B.; methodology, D.P.; software, D.P.; validation, D.P.; formal analysis, D.P.; investigation, D.P.; data sources, J.K., U.S., F.M., M.P. and L.B.; writing—original draft preparation, D.P.; writing—review and editing, L.B., C.V., J.K., U.S., F.M. and M.P.; visualization, D.P.; supervision, L.B. and C.V.; project administration, L.B.; funding acquisition, C.V. and L.B. All authors have read and agreed to the published version of the manuscript.

**Funding:** D. Piontek and L. Bugliaro were supported by the European Unions's Horizon 2020 research and innovation program under grant agreement No. 723986 (EUNADICS-AV). C. Voigt acknowledges funding by the Helmholtz Association under contract HGF W2/W3-60.

**Institutional Review Board Statement:** Not applicable.

**Informed Consent Statement:** Not applicable.

**Data Availability Statement:** Data presented in this study is available on request from the corresponding author.

**Acknowledgments:** The MSG/SEVIRI data were provided by EUMETSAT (European Organisation for the Exploitation of Meteorological Satellites) and the auxiliary data were obtained from ECMWF (European Center for Medium-Range Weather Forecasts). Radiative transfer calculations have been performed on DLR's CARA (Deutsches Zentrum für Luft- und Raumfahrt; Cluster for Advanced Research in Aerospace). Airborne data were obtained by DLR using the Falcon 20E, operated by DLR flight experiment facilities, and using the BAe-146-301 Atmospheric Research Aircraft which in 2010 was operated by Directflight Ltd. and managed by FAAM (Facility for Airborne Atmospheric Measurements), a joint entity of NERC (Natural Environment Research Council) and the Met Office. Furthermore, we like to thank M. Vázquez-Navarro, J. Strandgren, B. Mayer and M. Rapp for constructive discussions and valuable feedback, W. Beer for technical support, as well as J. Wilzewski and two reviewers for the helpful comments to improve the manuscript. J. Kar acknowledges useful discussions with M. Vaughan on correcting the low bias from the default ash lidar ratios used in CALIOP version 4.10.

**Conflicts of Interest:** The authors declare no conflict of interest.

## Appendix A. Metrics

Different error metrics are used in this work, derived from a set of $n$ pairs of retrieved values $r_i$ and corresponding true values $t_i$. The *mean squared error* MSE is defined as

$$\mathrm{MSE} = \frac{1}{n}\sum_{i=1}^{n}(r_i - t_i)^2. \tag{A1}$$

The *mean absolute percentage error* MAPE is calculated by

$$\mathrm{MAPE} = \frac{100}{n}\sum_{i=1}^{n}\left|\frac{r_i - t_i}{t_i}\right|. \tag{A2}$$

The *mean percentage error* MPE is

$$\mathrm{MPE} = \frac{100}{n}\sum_{i=1}^{n}\frac{r_i - t_i}{t_i}. \tag{A3}$$

To quantify the performance of a boolean retrieval we consider the *probability of detection* POD and the *false alarm rate* FAR (also *probability of false detection* [50])

$$\mathrm{POD} = \frac{N_{tp}}{N_{tp} + N_{fn}} \tag{A4}$$

$$\mathrm{FAR} = \frac{N_{fp}}{N_{fp} + N_{tn}} \tag{A5}$$

with $N_{tp}$ being the number of true positives (here meaning that the retrieval signals the presence of volcanic ash, which is really present), $N_{fp}$ the false positives (presence of ash is signaled although none is present), $N_{tn}$ the true negatives (absence of of ash is signaled and none is present) and $N_{fn}$ the false negatives (absence of ash is signaled although it is present). The performance of multi-category classifications is described by the *accuracy* given as the number of correctly classified samples divided by the total number of samples. For two categories, the *accuracy* simplifies to

$$accuracy = \frac{N_{tp} + N_{tn}}{N_{tp} + N_{fp} + N_{tn} + N_{fn}} \tag{A6}$$

and if no negative samples are present, i.e., $N_{tn} = N_{fp} = 0$, the *accuracy* equals the POD.

## Appendix B. Π-Sigmoid Distribution

The Π-sigmoid distribution was introduced by Alivanoglou and Likas [18] and is defined as the difference of two sigmoid functions, i.e.,

$$\Pi(x) = \frac{1}{b-a}\left(\frac{1}{1+e^{-\lambda(x-a)}} - \frac{1}{1+e^{-\lambda(x-b)}}\right) \tag{A7}$$

with $a$ and $b > a$ parameterizing the positions of the rise of the corresponding sigmoid, and $\lambda > 0$ describing their steepness. The expectation value is $(a+b)/2$ and for the the standard deviation $\sigma$ holds

$$\sigma^2 = \frac{b^3-a^3}{3(b-a)} - \frac{a^2+b^2}{4} - \frac{ab}{2} + \frac{\pi^2}{3\lambda^2}. \tag{A8}$$

## References


1. Bugliaro, L.; Piontek, D.; Kox, S.; Schmidl, M.; Mayer, B.; Müller, R.; Vázquez-Navarro, M.; Gasteiger, J.; Kar, J. Combining radiative transfer calculations and a neural network for the remote sensing of volcanic ash using MSG/SEVIRI. 2021, in preparation.
2. Piontek, D.; Bugliaro, L.; Schmidl, M.; Zhou, D.K.; Voigt, C. The New Volcanic Ash Retrieval VACOS Using MSG/SEVIRI and Artificial Neural Networks: 1. Development. *Remote Sens.* **2021**, *13*, 3112. [CrossRef]
3. Piontek, D.; Hornby, A.; Voigt, C.; Bugliaro, L.; Gasteiger, J. Determination of complex refractive indices and optical properties of volcanic ashes in the thermal infrared based on generic petrological compositions. *J. Volcanol. Geotherm. Res.* **2021**, *411*, 107174. [CrossRef]
4. Zhou, D.K.; Larar, A.M.; Liu, X.; Smith, W.L.; Strow, L.L.; Yang, P.; Schlüssel, P.; Calbet, X. Global Land Surface Emissivity Retrieved From Satellite Ultraspectral IR Measurements. *IEEE Trans. Geosci. Remote Sens.* **2011**, *49*, 1277–1290. [CrossRef]
5. Zhou, D.K.; Larar, A.M.; Liu, X. MetOp-A/IASI Observed Continental Thermal IR Emissivity Variations. *IEEE J. Sel. Top. Appl. Earth Obs. Remote Sens.* **2013**, *6*, 1156–1162. [CrossRef]
6. Zhou, D.K.; Larar, A.M.; Liu, X. On the relationship between land surface infrared emissivity and soil moisture. *J. Appl. Remote Sens.* **2018**, *12*, 1–14. [CrossRef]
7. Watkin, S.C. The application of AVHRR data for the detection of volcanic ash in a Volcanic Ash Advisory Centre. *Meteorol. Appl.* **2003**, *10*, 301–311. [CrossRef]
8. Kaufman, Y.J.; Koren, I.; Remer, L.A.; Rosenfeld, D.; Rudich, Y. The effect of smoke, dust, and pollution aerosol on shallow cloud development over the Atlantic Ocean. *Proc. Natl. Acad. Sci. USA* **2005**, *102*, 11207–11212. [CrossRef] [PubMed]
9. Strandgren, J.; Bugliaro, L.; Sehnke, F.; Schröder, L. Cirrus cloud retrieval with MSG/SEVIRI using artificial neural networks. *Atmos. Meas. Tech.* **2017**, *10*, 3547–3573. [CrossRef]
10. Strandgren, J.; Fricker, J.; Bugliaro, L. Characterisation of the artificial neural network CiPS for cirrus cloud remote sensing with MSG/SEVIRI. *Atmos. Meas. Tech.* **2017**, *10*, 4317–4339. [CrossRef]
11. Thomas, G.E.; Stamnes, K. *Radiative Transfer in the Atmosphere and Ocean*, 1st ed.; Cambridge University Press: New York, NY, USA, 2002.
12. de Laat, A.; Vazquez-Navarro, M.; Theys, N.; Stammes, P. Analysis of properties of the 19 February 2018 volcanic eruption of Mount Sinabung in S5P/TROPOMI and Himawari-8 satellite data. *Nat. Hazards Earth Syst. Sci.* **2020**, *20*, 1203–1217. [CrossRef]
13. Schneider, D.J.; Van Eaton, A.R.; Wallace, K.L. Satellite observations of the 2016–2017 eruption of Bogoslof volcano: Aviation and ash fallout hazard implications from a water-rich eruption. *Bull. Volcanol.* **2020**, *82*, 29. [CrossRef]
14. Deguine, A.; Petitprez, D.; Clarisse, L.; Guđmundsson, S.; Outes, V.; Villarosa, G.; Herbin, H. Complex refractive index of volcanic ash aerosol in the infrared, visible, and ultraviolet. *Appl. Opt.* **2020**, *59*, 884–895. [CrossRef]
15. Schumann, U.; Weinzierl, B.; Reitebuch, O.; Schlager, H.; Minikin, A.; Forster, C.; Baumann, R.; Sailer, T.; Graf, K.; Mannstein, H.; et al. Airborne observations of the Eyjafjalla volcano ash cloud over Europe during air space closure in April and May 2010. *Atmos. Chem. Phys.* **2011**, *11*, 2245–2279. [CrossRef]
16. Marenco, F.; Johnson, B.; Turnbull, K.; Newman, S.; Haywood, J.; Webster, H.; Ricketts, H. Airborne lidar observations of the 2010 Eyjafjallajökull volcanic ash plume. *J. Geophys. Res. Atmos.* **2011**, *116*. [CrossRef]
17. Turnbull, K.; Johnson, B.; Marenco, F.; Haywood, J.; Minikin, A.; Weinzierl, B.; Schlager, H.; Schumann, U.; Leadbetter, S.; Woolley, A. A case study of observations of volcanic ash from the Eyjafjallajökull eruption: 1. In situ airborne observations. *J. Geophys. Res. Atmos.* **2012**, *117*. [CrossRef]
18. Alivanoglou, A.; Likas, A. Probabilistic Models Based on the Π-Sigmoid Distribution. In *Artificial Neural Networks in Pattern Recognition*; Prevost, L., Marinai, S., Schwenker, F., Eds.; Springer: Berlin/Heidelberg, Germany, 2008; pp. 36–43.
19. Typical Radiometric Noise, Calibration Bias and Stability for Meteosat-8, -9, -10 and -11 SEVIRI. European Organisation for the Exploitation of Meteorological Satellites. 2019. Available online: https://www-cdn.eumetsat.int/files/2020-04/pdf_typ_radiomet_acc_msg-1-2.pdf (accessed on 5 August 2021).

20. Winker, D.M.; Vaughan, M.A.; Omar, A.; Hu, Y.; Powell, K.A.; Liu, Z.; Hunt, W.H.; Young, S.A. Overview of the CALIPSO Mission and CALIOP Data Processing Algorithms. *J. Atmos. Ocean. Technol.* **2009**, *26*, 2310–2323. [CrossRef]
21. Kim, M.H.; Omar, A.H.; Tackett, J.L.; Vaughan, M.A.; Winker, D.M.; Trepte, C.R.; Hu, Y.; Liu, Z.; Poole, L.R.; Pitts, M.C.; et al. The CALIPSO version 4 automated aerosol classification and lidar ratio selection algorithm. *Atmos. Meas. Tech.* **2018**, *11*, 6107–6135. [CrossRef] [PubMed]
22. Gasteiger, J.; Groß, S.; Freudenthaler, V.; Wiegner, M. Volcanic ash from Iceland over Munich: mass concentration retrieved from ground-based remote sensing measurements. *Atmos. Chem. Phys.* **2011**, *11*, 2209–2223. [CrossRef]
23. Winker, D.M.; Liu, Z.; Omar, A.; Tackett, J.; Fairlie, D. CALIOP observations of the transport of ash from the Eyjafjallajökull volcano in April 2010. *J. Geophys. Res. Atmos.* **2012**, *117*. [CrossRef]
24. Bignami, C.; Corradini, S.; Merucci, L.; de Michele, M.; Raucoules, D.; De Astis, G.; Stramondo, S.; Piedra, J. Multisensor Satellite Monitoring of the 2011 Puyehue-Cordon Caulle Eruption. *IEEE J. Sel. Top. Appl. Earth Obs. Remote Sens.* **2014**, *7*, 2786–2796. [CrossRef]
25. Ishimoto, H.; Hayashi, M.; Mano, Y. Optimal ash particle refractive index model for simulating the brightness temperature spectrum of volcanic ash clouds from satellite infrared sounder measurements. *Atmos. Meas. Tech. Discuss.* **2021**, *2021*, 1–28. [CrossRef]
26. Debling, F.; Schneider, J.F.; Rosi, M.; Leoz-Garziandia, E.; Rorije, E. Technical Cooperation Mission, Effects of the Puyehue-Cordón Caulle Eruption Argentina, 4–19 July 2011. Joint UNEP/OCHA Environment Unit, 2011. Available online: https://www.eecentre.org/wp-content/uploads/2019/06/Argentina-volcan-eruption-2011-report.pdf (accessed on 5 August 2021).
27. Botto, I.L.; Canafoglia, M.E.; Gazzoli, D.; González, M.J. Spectroscopic and Microscopic Characterization of Volcanic Ash from Puyehue-(Chile) Eruption: Preliminary Approach for the Application in the Arsenic Removal. *J. Spectrosc.* **2013**, *2013*, 254517. [CrossRef]
28. Johnson, B.; Turnbull, K.; Brown, P.; Burgess, R.; Dorsey, J.; Baran, A.J.; Webster, H.; Haywood, J.; Cotton, R.; Ulanowski, Z.; et al. In situ observations of volcanic ash clouds from the FAAM aircraft during the eruption of Eyjafjallajökull in 2010. *J. Geophys. Res. Atmos.* **2012**, *117*. [CrossRef]
29. Ball, J.G.C.; Reed, B.E.; Grainger, R.G.; Peters, D.M.; Mather, T.A.; Pyle, D.M. Measurements of the complex refractive index of volcanic ash at 450, 546.7, and 650 nm. *J. Geophys. Res. Atmos.* **2015**, *120*, 7747–7757. [CrossRef]
30. Weber, K.; Eliasson, J.; Vogel, A.; Fischer, C.; Pohl, T.; van Haren, G.; Meier, M.; Grobéty, B.; Dahmann, D. Airborne in situ investigations of the Eyjafjallajökull volcanic ash plume on Iceland and over north-western Germany with light aircrafts and optical particle counters. *Atmos. Environ.* **2012**, *48*, 9–21.10.1016/j.atmosenv.2011.10.030. [CrossRef]
31. Gudmundsson, M.T.; Thordarson, T.; Höskuldsson, A.; Larsen, G.; Björnsson, H.; Prata, F.J.; Oddsson, B.; Magnússon, E.; Högnadóttir, T.; Petersen, G.N.; et al. Ash generation and distribution from the April-May 2010 eruption of Eyjafjallajökull, Iceland. *Sci. Rep.* **2012**, *2*, 572. [CrossRef]
32. Rose, W.; Gu, Y.; Watson, I.; Yu, T.; Blut, G.; Prata, A.; Krueger, A.; Krotkov, N.; Carn, S.; Fromm, M.; et al. The February–March 2000 Eruption of Hekla, Iceland from a Satellite Perspective. In *Volcanism and the Earth's Atmosphere*; American Geophysical Union: Washington, DC, USA, 2004; pp. 107–132. [CrossRef]
33. Rose, W.I.; Bluth, G.J.S.; Watson, I.M. Ice in Volcanic Clouds: When and Where? In Proceedings of the 2nd International Conference on Volcanic Ash and Aviation Safety, Alexandria, VA, USA, 21–24 June 2004; Office of the Federal Coordinator for Meteorological Services and Supporting Research: Silver Spring, MD, USA, 2004; pp. 3.27–3.33.
34. Durant, A.J.; Shaw, R.A.; Rose, W.I.; Mi, Y.; Ernst, G.G.J. Ice nucleation and overseeding of ice in volcanic clouds. *J. Geophys. Res. Atmos.* **2008**, *113*. [CrossRef]
35. Plu, M.; Scherllin-Pirscher, B.; Arnold Arias, D.; Baro, R.; Bigeard, G.; Bugliaro, L.; Carvalho, A.; El Amraoui, L.; Eschbacher, K.; Hirtl, M.; et al. A tailored multi-model ensemble for air traffic management: Demonstration and evaluation for the Eyjafjallajökull eruption in May 2010. *Nat. Hazards Earth Syst. Sci. Discuss.* **2021**, *2021*, 1–32. [CrossRef]
36. Kox, S.; Bugliaro, L.; Ostler, A. Retrieval of cirrus cloud optical thickness and top altitude from geostationary remote sensing. *Atmos. Meas. Tech.* **2014**, *7*, 3233–3246. [CrossRef]
37. Prata, A.J. Infrared radiative transfer calculations for volcanic ash clouds. *Geophys. Res. Lett.* **1989**, *16*, 1293–1296. [CrossRef]
38. Wen, S.; Rose, W.I. Retrieval of sizes and total masses of particles in volcanic clouds using AVHRR bands 4 and 5. *J. Geophys. Res. Atmos.* **1994**, *99*, 5421–5431. [CrossRef]
39. LeCun, Y.; Denker, J.S.; Solla, S.A. Optimal Brain Damage. In *Advances in Neural Information Processing Systems 2*; Touretzky, D.S., Ed.; Morgan-Kaufmann: San Francisco, CA, USA, 1990; pp. 598–605.
40. Piscini, A.; Carboni, E.; Del Frate, F.; Grainger, R.G. Simultaneous retrieval of volcanic sulphur dioxide and plume height from hyperspectral data using artificial neural networks. *Geophys. J. Int.* **2014**, *198*, 697–709. [CrossRef]
41. Ackerman, S.A. Remote sensing aerosols using satellite infrared observations. *J. Geophys. Res. Atmos.* **1997**, *102*, 17069–17079. [CrossRef]
42. Gray, T.M.; Bennartz, R. Automatic volcanic ash detection from MODIS observations using a back-propagation neural network. *Atmos. Meas. Tech.* **2015**, *8*, 5089–5097. [CrossRef]
43. Schmit, T.J.; Gunshor, M.M.; Menzel, W.P.; Gurka, J.J.; Li, J.; Bachmeier, A.S. Introducing the Next-Generation Advanced Baseline Imager on GOES-R. *Bull. Am. Meteorol. Soc.* **2005**, *86*, 1079–1096. [CrossRef]

44. Bessho, K.; Date, K.; Hayashi, M.; Ikeda, A.; Imai, T.; Inoue, H.; Kumagai, Y.; Miyakawa, T.; Murata, H.; Ohno, T.; et al. An Introduction to Himawari-8/9 - Japan's New-Generation Geostationary Meteorological Satellites. *J. Meteorol. Soc. Jpn. Ser. II* **2016**, *94*, 151–183. [CrossRef]
45. Yang, J.; Zhang, Z.; Wei, C.; Lu, F.; Guo, Q. Introducing the New Generation of Chinese Geostationary Weather Satellites, Fengyun-4. *Bull. Am. Meteorol. Soc.* **2017**, *98*, 1637–1658. [CrossRef]
46. Meeting on the Intercomparison of Satellite-Based Volcanic Ash Retrieval Algorithms, Madison WI, USA, 29 June–2 July 2015, Final Report. World Meteorological Organization, 2015. Available online: https://web.archive.org/web/20171113102551/http://www.wmo.int/pages/prog/sat/documents/SCOPE-NWC-PP2_VAIntercompWSReport2015.pdf (accessed on 5 August 2021).
47. Stohl, A.; Prata, A.J.; Eckhardt, S.; Clarisse, L.; Durant, A.; Henne, S.; Kristiansen, N.I.; Minikin, A.; Schumann, U.; Seibert, P.; et al. Determination of time- and height-resolved volcanic ash emissions and their use for quantitative ash dispersion modeling: The 2010 Eyjafjallajökull eruption. *Atmos. Chem. Phys.* **2011**, *11*, 4333–4351. [CrossRef]
48. Dacre, H.F.; Harvey, N.J.; Webley, P.W.; Morton, D. How accurate are volcanic ash simulations of the 2010 Eyjafjallajökull eruption? *J. Geophys. Res. Atmos.* **2016**, *121*, 3534–3547. [CrossRef]
49. Plu, M.; Bigeard, G.; Sič, B.; Emili, E.; Bugliaro, L.; El Amraoui, L.; Guth, J.; Josse, B.; Mona, L.; Piontek, D. Modelling the volcanic ash plume from Eyjafjallajökull eruption (May 2010) over Europe: Evaluation of the benefit of source term improvements and of the assimilation of aerosol measurements. *Nat. Hazards Earth Syst. Sci. Discuss.* **2021**, *2021*, 1–24. [CrossRef]
50. Barnes, L.R.; Schultz, D.M.; Gruntfest, E.C.; Hayden, M.H.; Benight, C.C. CORRIGENDUM: False Alarm Rate or False Alarm Ratio? *Weather Forecast.* **2009**, *24*, 1452–1454. [CrossRef]

# Chapter 4

# Conclusions and outlook

The focus of this cumulative dissertation is the development of a new method for the detection of volcanic ash and the retrieval of the corresponding ash cloud properties using satellite remote sensing with the aim to be applicable to any volcanic eruption and volcanic ash type as far as possible. This retrieval is called VACOS; it uses brightness temperature measurements from MSG/SEVIRI and is based on artificial neural networks. VACOS provides information on no-fly zones for aviation in the event of a future eruption and reference data for numerical ash transport and dispersion models.

In **P1** the microphysical and petrological properties of volcanic ash were considered and especially their impact on the complex refractive index and the resulting scattering and absorption optical properties. Building upon these results, **P2** described the creation of an extensive training data set and the development of VACOS. Finally, **P3** includes the validation and characterization of the method as well as further comparisons with numerical model calculations (which are extended in **P5** and **P6**). In the following, the main results are summarized in light of the three scientific questions/hypotheses formulated in Section 1.2 and corresponding outlooks are given. The abbreviations from **P3** are used, with the mass column concentration $m_{\mathrm{col}}$, the ash optical thickness at 10.8 µm $\tau_{10.8}$ (or any other wavelength for that matter), the ash cloud top height $z_{\mathrm{top}}$, the effective ash particle radius $r_{\mathrm{eff}}$, the brightness temperature of the MSG/SEVIRI channel centered at the wavelength $\lambda$ being $BT_{\lambda}$, and the brightness temperature difference between the channels centered at the wavelengths $\alpha$ and $\beta$ denoted as $BTD_{\alpha-\beta}$. Primed quantities always denote the reference data. The retrieval performance is described by the mean absolute percentage error MAPE, the probability of detection POD, the false alarm rate FAR, and the accuracy denoting the fraction of correctly classified samples.

**1.** *For volcanic ash, the petrological composition and the effective particle radius have a similarly strong impact on its optical properties in the thermal infrared spectrum, such that both need to be accounted for in radiative transfer.*

To confirm this hypothesis, a new method for calculating the complex refractive index of volcanic ash in the thermal infrared based on its petrological composition was outlined in **P1**. It assumes a volume-weighted averaging approach of the refractive indices of the

individual components (including the crystalline minerals, the volcanic glasses and the voids from exsolved gases) to derive an effective refractive index. The refractive indices of the minerals as derived from laboratory measurements were collected from the literature. The mineral phase distribution was related to the bulk silica content. Using the effective refractive indices of volcanic ash from Deguine et al. (2020), the new method was used to obtain the refractive indices of different volcanic glasses. Finally, a wavelength-dependent linear regression of both parts of the refractive index of volcanic glass with respect to the bulk silica content was performed; the resulting functions were used to derive volcanic glass refractive indices for various bulk silica contents.

Combining the refractive indices of the minerals with the ones derived for volcanic glass, the new method allowed to investigate the impact of different petrological compositions on the effective refractive index (see Figure 8 in **P1**). Varying the silica content, the glass-to-crystal ratio and the porosity within typical ranges, it was found that the porosity can have the largest impact; as the porosity can be in excess of 80 % with respect to the ash particle volume, the peak in the imaginary part of the refractive index could be reduced by up to ~80 %. Generally, an increased porosity led to a flattened real and a reduced imaginary part of the refractive index and, thus, reduced its spectral signature in the thermal infrared. Increasing the silica content from 45 wt.% to 75 wt.% increased the spectral variability; the peak in the imaginary part of the refractive index rose correspondingly by ~50 %. The glass-to-crystal ratio had the smallest impact on the refractive index; increasing the glass fraction with respect to the solid part of the ash particle from 45 % to 100 %, the variations remained mostly within the uncertainty of the volcanic glass refractive index.

The glass fraction also influenced the bulk density of the volcanic ash, and both the bulk density and the refractive index impacted the optical properties; only the compositions without porosity but a non-zero glass fraction were considered in the rest of the study. Still, the single scattering albedo and the asymmetry parameter were mainly affected by the particle size (for $r_{\mathrm{eff}}$ being 0.6–6 µm, Figure 9 in **P1**) and experienced only minor contributions from the composition (Figure 12 in **P1**) and the shape (different spherical and spheroidal shape distributions, Figure 10 in **P1**). Of course, as pointed out in Section 2.1.3, ash particles are generally neither spherical nor spheroidal and the corresponding approximation loses validity for larger particles (Kylling et al., 2014). Considering the mass extinction coefficient (Figure 12 in **P1**), one could see that the glass-to-crystal ratio had a notable impact and even more so the silica content; the latter could induce a variability of a factor of 1.5–3 when comparing silica contents of 45 wt.% and 75 wt.%, especially for small particles ($r_{\mathrm{eff}} = 0.6$ µm). Different particle sizes (e.g., $r_{\mathrm{eff}} = 0.6$ µm and 6 µm) led to a variability of a factor of ~4 (Figure 9 in **P1**). Thus, the influences of composition and particle size on the mass extinction coefficient are indeed comparable, whereas the investigated shapes are of subordinate importance (Figure 10 in **P1**).

The results stress that the volcanic ash composition is of significant importance and cannot be neglected with respect to the particle sizes. Similar conclusions were also drawn by Prata et al. (2019) when investigating the dependence of the volcanic ash refractive index on the chemical composition. The new extensive data set of refractive indices and optical properties established in **P1** can be used to develop new volcanic ash retrievals (as

was done in this work) or to estimate uncertainties of existing methods.

Future work to better validate the proposed method would be beneficial. The few laboratory measurements of volcanic ash refractive indices provide analyses of the chemical composition for the used samples, but petrological compositions are missing in all cases (Deguine et al., 2020, Pollack et al., 1973, Reed et al., 2018); corresponding studies are necessary. Generally, the impact of the petrological composition on the refractive index compared to the impact of the chemical composition needs further attention. Comparing measurements of the refractive index of real ash samples (i.e., including minerals) with remelted and then quenched glass samples (i.e., with the same chemical composition but without crystalline structures) would allow to do so; such approaches have been used before to investigate the impact of crystallinity in other respects (e.g., Maters et al., 2019). The same attention must be paid to the effects of microphysical properties on the refractive index, e.g., the internal porosity or thin layers of water/ice/$H_2SO_4$ covering the ash surface. In this context it might also be worth quantifying the uncertainty due to different effective medium theories to calculate the effective refractive index (Kolokolova and Gustafson, 2001). A notable problem (discussed also by Deguine et al., 2020) for the experimentally-determined volcanic ash refractive indices is the assumption of the particle shape: Reed et al. (2018) assumed the Rayleigh continuous distribution of ellipsoids whereas Deguine et al. (2020) assumed Mie theory, leading in parts to large differences. Clearly, potential inaccuracies directly carry over to subsequent studies such as the one presented here or by Prata et al. (2019).

**2.** *What is the information content of typical spaceborne geostationary infrared observations by passive imagers like MSG/SEVIRI with respect to volcanic ash cloud properties?*

To answer this question, the refractive indices and the optical properties of volcanic ash from **P1** were used to perform various radiative transfer calculations in **P3**. As pointed out in the previous answer, the particle shape had only minor impact on the optical properties (mass extinction coefficient, single scattering albedo, asymmetry parameter) for small particles ($r_{\mathrm{eff}} = 0.6\,\mu\mathrm{m}$) with relative differences of 5–10 % for different shape distributions (Figure 10 in **P1**). In the considered particle size range, particle shape was of least importance compared to composition and size (Table 4 in **P1**) and, thus, is rather not retrievable using MSG/SEVIRI. Instead, a representative shape distribution was chosen for all subsequent calculations.

In the previous answer it was mentioned that the composition had a significant impact on the optical properties (Figure 12 in **P1**) which is carried over to the top-of-atmosphere brightness temperatures. A simple model of a thin ash layer ($m_{\mathrm{col}} = 0.5\,\mathrm{g\,m^{-2}}$, $z_{\mathrm{top}} \approx 10\,\mathrm{km}$, $r_{\mathrm{eff}} = 0.6\,\mu\mathrm{m}$) as typically observed at distances in the order of 1000 km was considered (Figure 13 in **P1**). Decreasing the silica content from 75 wt.% to 45 wt.% decreased $BT_{11}$ by ~2.5 K and $BTD_{11-12}$ by ~2 K. The impact of the glass-to-crystal ratio on the same brightness temperatures was about one order of magnitude smaller, with variations of 0.2–0.3 K; this is comparable to typical instrumental noise of MSG/SEVIRI

(EUMETSAT/3, Schmetz et al., 2002b). Thus, the glass-to-crystal ratio might not be retrievable from MSG/SEVIRI measurements, but it might be possible to estimate the silica content from satellite. In fact, Ishimoto et al. (2016) used high-resolution spectra from the *Atmospheric Infrared Sounder* (AIRS) to derive the imaginary part of the volcanic ash refractive index from various ash clouds, and Ishimoto et al. (2021) used IASI spectra to determine the refractive index of different ash clouds based on a set of 21 different ash refractive indices.

The effective radius $r_{\text{eff}}$ was retrieved from moderate resolution radiometers (e.g., Prata, 1989, Wen and Rose, 1994). Calculating corresponding optical properties (for $r_{\text{eff}}$ of 0.6–6 µm) confirmed that this is possible (Figure 9 in **P1**): in the case of Eyjafjallajökull ash (from Deguine et al., 2020), the peak of the mass extinction coefficient at 9–12 µm shifted and increased with decreasing $r_{\text{eff}}$, whereas the asymmetry parameter decreased by a factor of ~4. Also the single scattering albedo decreased significantly for the smallest particles. Consequently, $r_{\text{eff}}$ had also a notable impact on the brightness temperatures. E.g., considering an Eyjafjallajökull ash layer with $m_{\text{col}}$ between 1–30 g m$^{-2}$ and $z_{\text{top}} = 9$ km led to variations in $BT_{10.8}$ of 5–10 K due to $r_{\text{eff}}$ (Figure 18 in **P3**). Note that in this case, there was not a strictly monotonic relation between $BT_{10.8}$ and $r_{\text{eff}}$, i.e., $BT_{10.8}$ for $r_{\text{eff}} = 0.6$ µm lays between the corresponding values for 3 µm and 6 µm.

The retrieval of mass load $m_{\text{col}}$ or the optical depth $\tau_{10.8}$ (they are equivalent as they can be converted into each other using the mass extinction coefficient if the ash layer has constant optical properties) was also performed regularly (e.g., Wen and Rose, 1994, Yu et al., 2002). For an Eyjafjallajökull ash layer with $z_{\text{top}} = 9$ km and $r_{\text{eff}} = 0.6$ µm, brightness temperature measurements in the atmospheric window were found to be sensitive to $m_{\text{col}}$ between ~0.1 g m$^{-2}$ and 100 g m$^{-2}$ (Figure 18 in **P3**), which covers typical $m_{\text{col}}$ of ash layers even at distances of few kilometers from the vent (see Section 2.1.2). The atmospheric window brightness temperatures decreased from ~290 K to ~240 K with increasing $m_{\text{col}}$. Beyond the $m_{\text{col}}$ thresholds, brightness temperatures remained relatively constant. Note that some channels (e.g., the water vapor channels) showed variability even in excess of 100 g m$^{-2}$. Increasing the $z_{\text{top}}$ from 3 to 12 km lowered $BT_{10.8}$ at the high-$m_{\text{col}}$ plateau from ~280 K to ~220 K (Figure 18 in **P3**). This indicates the sensitivity to $z_{\text{top}}$, and that also the sensitivity to $m_{\text{col}}$ increases with increasing $z_{\text{top}}$ (this was rediscovered at the characterization of VACOS with its retrieval errors decreasing with increasing $z_{\text{top}}$).

Sounding of volcanic ash clouds is usually not performed with radiometers such as MSG/SEVIRI. The impact of varying geometrical thicknesses (0.5–3 km) on MSG/SEVIRI brightness temperatures for an Eyjafjallajökull ash layer with $m_{\text{col}} = 10$ g m$^{-2}$, $z_{\text{top}} = 9$ km and $r_{\text{eff}} = 0.6$ µm was simulated (Figure 8 in **P3**). Comparing with a geometrical thickness of 1 km, a thinner layer of 0.5 km lowered the brightness temperatures by up to 1 K (as relatively more ash mass was in higher/colder parts of the atmosphere), whereas thicker layers of 2 km and 3 km increased the brightness temperatures by up to 2 K and 4 K, respectively (relatively more ash in lower/warmer parts of the atmosphere). The impact was smallest in the water vapor channels. More generally, the sensitivity to the vertical mass profile was investigated by splitting the 1 km thick ash layer into multiple layers with overall constant $m_{\text{col}}$ and $z_{\text{top}}$ as before (Figure 6 in **P3**). Lowering the bottom half of the

layer by 0.5 km or dividing the single layer into two or three layers of higher mass volume concentrations but with fixed cloud bottom height led to absolute changes in the brightness temperatures of $< 1$ K with respect to the single layer configuration. However, lowering the bottom half by 2 km increased the deviations in the brightness temperatures up to 3 K. Again, the water vapor channels were affected the least. Finally, comparing different vertical mass profiles for the single layer (i.e., uniform, $\pi$-sigmoid and normal distributions) showed that the resulting impacts on the brightness temperatures are negligible (Figure 7 in **P3**). Thus, MSG/SEVIRI is sensitive to typical variations in the geometrical thickness and multi-layer structures, but much less to more realistic (i.e., continuous) vertical profiles of single layers. The impact on the MSG/SEVIRI brightness temperatures seems to be caused by the relocation of ash mass to higher/colder or lower/warmer parts of the atmosphere and the corresponding changes in the ash layer temperature and emitted radiation.

Overall, the sensitivity of MSG/SEVIRI brightness temperatures to $m_{\mathrm{col}}$, $z_{\mathrm{top}}$ and $r_{\mathrm{eff}}$ was found to be largest; thus, these quantities are retrieved by the new algorithm VACOS. The vertical mass profile (i.e., geometrical thickness and multiple layers) and the composition (specifically, the silica content) had comparable, smaller impact on the satellite signal; their estimation might be possible under certain, favorable conditions (e.g., homogeneous Earth surface; absence of meteorological clouds; perhaps holding some macrophysical parameters fixed). The exact vertical profile (i.e., with a continuous mass distribution for layers of fixed vertical extent), the particle shape and the glass-to-crystal ratio had the smallest impact in the considered cases. An important issue to be tackled in more detail in future studies involves the particle size. As confirmed in **P1** (e.g., Figure 9), $BTD_{10.8-12}$ might be non-negative for $r_{\mathrm{eff}} \geq 6\,\mu\mathrm{m}$ (also Prata, 1989, Wen and Rose, 1994) which can lead to an underestimation of retrieved $r_{\mathrm{eff}}$ and $m_{\mathrm{col}}$ (Stevenson et al., 2015). Furthermore, Mackie et al. (2016) point out that the particle size distribution generally needs more attention, as it is a central input data for remote sensing algorithms and transport and dispersion models. However, currently available estimations of it (by remote sensing methods, in situ or in the field) were done with different measurement techniques which exhibit significant differences in their particle size sensitivity and the resulting particle size distributions.

**3.** *How accurate is the general-purpose volcanic ash satellite retrieval VACOS for MSG/SEVIRI using artificial neural networks with respect to the detection of volcanic ash clouds and the derivation of their mass column concentration, cloud top height and effective particle radius?*

VACOS was developed in **P2** with the aim to build a general-purpose volcanic ash retrieval for MSG/SEVIRI using artificial neural networks. This included mainly three key points: background atmospheric data were collected from several years and checked to cover daily, annual and inter-annual variabilities; macrophysical ash layer properties covered the full range of typical values; and an extensive set of volcanic ash optical properties was utilized to cover various types of ashes, including variations in the silica content, the crystallinity and the particle size. Including such a wide range of possible cases constitutes the main difference to the predecessor VADUGS and other existing ANN-based volcanic ash satel-

lite retrievals. VACOS retrieves $\tau_{10.8}$ (convertable to $m_{\mathrm{col}}$), $z_{\mathrm{top}}$, $r_{\mathrm{eff}}$ and a four-category classification (clear sky, only liquid and ice water clouds, only volcanic ash clouds, both volcanic ash and liquid/ice water clouds); based on the latter, a binary ash flag was derived. To answer the question on the performance of VACOS, a comprehensive validation was performed in **P3** with respect to different eruptions; different ash clouds; different geographical locations; and ash in the presence of ice water clouds.

VACOS was applied to ash clouds of the Eyjafjallajökull eruption in 2010 and the Puyehue-Cordón Caulle eruption in 2011. The former was investigated in situ and using an airborne lidar by the Deutsches Zentrum für Luft- und Raumfahrt (DLR) and the Facility for Airborne Atmospheric Measurements (FAAM), whereas the latter was observed by the spaceborne lidar CALIOP. The two cases were quite different: the Icelandic Eyjafjallajökull, located in the northern Hemisphere, emitted ash with a silica content of ~59 wt.% and the considered ash cloud was located in the mid-troposphere with a $z_{\mathrm{top}} \approx 6\,\mathrm{km}$. The Chilean Puyehue-Cordón Caulle emitted ash with a silica content of ~70 wt.% up to $z_{\mathrm{top}}$ of 10–15 km, i.e., up to the tropopause/lower stratosphere. However, $m_{\mathrm{col}} \lesssim 1.5\,\mathrm{g\,m^{-2}}$ was similar. In both cases, VACOS retrievals of $m_{\mathrm{col}}$ were in good agreement with the reference data (Figure 10 and 13 in **P3**). With respect to the CALIOP retrieval, $m_{\mathrm{col}}$ of VACOS had a MAPE of ~50 % for $m'_{\mathrm{col}} \geq 0.2\,\mathrm{g\,m^{-2}}$ (Table 4 in **P3**). VACOS retrievals for $z_{\mathrm{top}}$ were of the same order of magnitude as the reference values, although underestimations of few kilometers appeared sporadically; compared to the CALIOP results, the MAPE of $z_{\mathrm{top}}$ was 18 % for $m'_{\mathrm{col}} \geq 0.2\,\mathrm{g\,m^{-2}}$ (Table 4 in **P3**). In the Eyjafjallajökull case, retrieved $r_{\mathrm{eff}}$ were generally within the uncertainty range of the in situ measurements (Figure 13 in **P3**). The classification algorithm correctly classified the thickest ash clouds, but tended to fail for thinner layers. Notably, the predecessor VADUGS performed rather bad: $m_{\mathrm{col}}$ was in reasonable agreement with the CALIOP data for the Puyehue-Cordón Caulle, but was strongly underestimated in the Eyjafjallajökull case; $z_{\mathrm{top}}$ was too low in all scenes except for a few situations related to rather thick ash clouds.

The performance of VACOS with respect to different ash clouds was investigated by performing systematic tests of the retrievals with respect to $\tau'_{10.8}$, $z'_{\mathrm{top}}$ and $r'_{\mathrm{eff}}$ using a data set of synthetic observations which was created similarly as the original training data (Figure 1 in **P3**). In general, MAPEs of $\tau_{10.8}$, $z_{\mathrm{top}}$ and $r_{\mathrm{eff}}$ decreased with increasing $\tau'_{10.8}$ and $z'_{\mathrm{top}}$ from ~100 % for $\tau'_{10.8} \approx 0.03$ / $z_{\mathrm{top}} \approx 1\,\mathrm{km}$ to $\lesssim 30\,\%$ for $\tau'_{10.8} \approx 10$ / $z_{\mathrm{top}} \approx 18\,\mathrm{km}$. Selecting $\tau'_{10.8} \geq 0.1$ (to consider typical values for an ash cloud) led to a MAPE of $\lesssim 40\,\%$ for the retrieval of $\tau_{10.8}$; $z'_{\mathrm{top}} \geq 5\,\mathrm{km}$ resulted in a MAPE of $\lesssim 10\,\%$ for $z_{\mathrm{top}}$; and for $r'_{\mathrm{eff}}$ of 0.6–6 µm one ended up with a MAPE of $\lesssim 35\,\%$ for $r_{\mathrm{eff}}$. The accuracy of the binary ash flag increased from 20–30 % for $\tau'_{10.8} \approx 0.02$ to >90 % for $\tau'_{10.8} > 0.1$, and from ~50 % for $z'_{\mathrm{top}} < 1\,\mathrm{km}$ to >90 % for $z'_{\mathrm{top}} > 3\,\mathrm{km}$. The dependence on $r'_{\mathrm{eff}}$ was much smaller. As described in the answer to the previous scientific questions, radiative transfer simulations were performed to investigate the impact of the vertical profile, specifically the presence of multiple layers and variations in the geometrical thickness under the assumption of constant $m_{\mathrm{col}}$ and $z_{\mathrm{top}}$ (Figure 6 and 8 in **P3**). On average, minor sensitivity was found for the retrieval for $r_{\mathrm{eff}}$, but an impact of the order of ~5 % for $z_{\mathrm{top}}$ and ~30 % for $\tau_{10.8}/m_{\mathrm{col}}$.

Generally, the sensitivity of the retrievals to the underlying surface type (i.e., land or

sea) was insignificant (Figure 1 in **P3**), but the geographical location had some impact (Figure 4 in **P3**): Considering only scenes free of meteorological clouds, the MAPE of $\tau_{10.8}$ increased from ~20 % at the sub-satellite point to ~40 % at viewing zenith angles >60°, presumably due to the increased optical path. The MAPE of $z_{\mathrm{top}}$ increased with the absolute value of the latitude, i.e., from 5–10 % at the equator to 15–20 % at latitudes of ~50° N/S; here, one reason could have been differences in the atmospheric temperature profile between the equatorial and the polar regions (i.e., overall lower temperatures and tropopause at higher latitudes) together with a training data set whose sample density had a maximum at the sub-satellite point. The MAPE of $r_{\mathrm{eff}}$—being generally ~15 % at the center of the MSG/SEVIRI disc—increased to 17.5–20 % above the Sahara, probably due to similar optical signatures caused by mineral dust surfaces and volcanic ash aerosol (Watkin, 2003). Similarly, the binary ash flag's accuracy/POD exhibited a decrease (from ~100 % to 98.5–99.5 %) with a simultaneous increase in FAR (from close to 0 % to ~0.008 %) above the Sahara (Figure 3 in **P3**).

As explained in the introduction, volcanic ash is commonly detected by $BTD_{11-12} < 0\,\mathrm{K}$ (Prata, 1989); this spectral signature might also be used internally by VACOS. As ice clouds produce a positive brightness temperature difference for the same channels (Gangale et al., 2010, Inoue, 1985), they have the ability to effectively hide volcanic ash layers (Watkin, 2003). An example test case is the Eyjafjallajökull ash plume on 11 May 2010, 14:00 UTC, for which ice was indicated by Weber et al. (2012) and the algorithm *Cirrus Properties from SEVIRI* (CiPS, Strandgren et al., 2017a) with an ice water path of 1–5 $\mathrm{g\,m^{-2}}$ (Figure 15 in **P3**). Still, VACOS was able to detect the ash plume (with $m_{\mathrm{col}}$ up to ~3 $\mathrm{g\,m^{-2}}$) and the retrieved $m_{\mathrm{col}} \approx 1\,\mathrm{g\,m^{-2}}$ at the fringes was in good agreement with in situ measurements by Weber et al. (2012), whereas $z_{\mathrm{top}}$ appeared to be overestimated where ice is present. Cirrus clouds with ice water paths of roughly 10–30 $\mathrm{g\,m^{-2}}$ were also detected underneath the ash layers of the Puyehue-Cordón Caulle eruption in 2011 by combining VACOS and CiPS (Figure 10 in **P3**). In the two considered cases, increases in the retrieved $z_{\mathrm{top}}$ and $r_{\mathrm{eff}}$ were found. In one case with an ice water path >20 $\mathrm{g\,m^{-2}}$, the ash cloud was not observed at all, neither by the classification nor by the $m_{\mathrm{col}}$ retrieval. The situation was investigated more systematically by using the simulated test data set. It was found that the increases of the MAPEs of the retrievals in the presence of meteorological clouds (here defined to include liquid and ice water clouds) were often only in the order of 10–20 % (Figure 1 in **P3**). However, the MAPE of the retrievals increased significantly if the meteorological clouds were above the ash layer, sometimes by roughly one order of magnitude compared to the situation with the meteorological cloud below the ash (Figure 2 in **P3**). An exception were the MAPEs of the retrievals of $\tau_{10.8}$, $z_{\mathrm{top}}$ and $r_{\mathrm{eff}}$ with respect to $z'_{\mathrm{top}}$, which were lower for meteorological clouds above than below for $z'_{\mathrm{top}} \gtrsim 10\,\mathrm{km}$. Overall, even if meteorological clouds were above, MAPEs were <100 % if $\tau'_{10.8} > 0.2$ or $z'_{\mathrm{top}} > 1\,\mathrm{km}$ and for all considered $r'_{\mathrm{eff}}$, and <50 % if $\tau'_{10.8} > 0.5$ or $z'_{\mathrm{top}} > 4\,\mathrm{km}$. The accuracy of the binary ash flag fell below 50 % for $\tau'_{10.8} < 0.1$ or $z'_{\mathrm{top}} < 2\,\mathrm{km}$.

Ash detection can be performed using either the binary ash flag or the retrieved $m_{\mathrm{col}}$ together with corresponding thresholds. Considering the POD and the FAR for different thresholds for the simulated test data (Figure 5 in **P3**), the binary ash flag performed

better than the $m_{\mathrm{col}}$-based detection scheme (i.e., higher PODs at lower FARs), and both outperformed a procedure based on $BTD_{10.8-12}$. Considering only test samples with $m'_{\mathrm{col}} \in [0.2, 1]\,\mathrm{g\,m^{-2}}$ and for $m_{\mathrm{col}}$ a threshold value of 0.04 (which roughly equals $0.2\,\mathrm{g\,m^{-2}}$), the POD was ~93 % and the FAR was ~1 %. However, the POD was only ~70 % for a comparable calculation based on the Puyehue-Cordón Caulle reference data from CALIOP (Figure 11 in **P3**).

To conclude, the validation showed that VACOS is able to perform with reasonable accuracy over a wide range of atmospheric and geographic conditions as well as macro- and microphysical volcanic ash properties. In particular, VACOS is preferred over its predecessor VADUGS with respect to retrievals and a conventional threshold-based scheme using $BTD_{10.8-12}$ with respect to detections. Especially the satisfying results for two different eruptions indicate that VACOS can be applied to arbitrary volcanic ash clouds. Remaining uncertainties of a factor of ~2 are not untypical for volcanic ash-related measurements (e.g., Marenco et al., 2011, Schumann et al., 2011). As indicated in the introduction, one important field of application of volcanic ash retrievals is the comparison with ash transport and dispersion models for configuration and validation. Here, satellite retrievals of the Eyjafjallajökull eruption in 2010 were compared to the median of a model ensemble (Figure 16 in **P3**). In contrast to VADUGS, the new algorithm VACOS was able to detect ash plumes not only within the surrounding of the vent, but even at large distances, e.g., above continental Europe. An important outcome of the direct comparison was that the simulated ash clouds might be mislocated at distances >1000 km with displacements of few 100 km. This also stresses the importance of satellite retrievals of distal ash clouds for air traffic control, as model simulations alone are not reliable enough in these cases; as far as VACOS is concerned, an operational application at the German weather service is planned. Further model comparisons were performed in **P5** and **P6**.

Concerning further developments of volcanic ash retrieval capacities building upon VACOS, three pathways are available. First, the training data set could be expanded and the ANNs retrained. An obvious choice would be the inclusion of $SO_2$ which is often (but not always) emitted together and collocated with volcanic ash (Carn et al., 2009, Thomas and Prata, 2011) and influences the MSG/SEVIRI channels at 7.3 µm and 8.7 µm (Gray and Bennartz, 2015). Scenarios with ice covering or being collocated with volcanic ash (Section 2.1.3) could be improved: although the training data set might have included samples with ash and ice at the same altitude by chance, the frequency of their occurrence might have been underestimated with respect to reality, or the amounts of ash mass/particle number relative to the ice water path might not have resembled real cases as no physical relation was implemented. Also samples with layers of mineral dust could be included, as dust shares similar refractive indices with volcanic ash due to their silica contents (Watkin, 2003); this might allow to train an additional ANN which differentiates between volcanic ash and dust.

Second, one could leave the training data as is but modify the ANNs. **P3** showed that local averaging of the VACOS retrievals led to an overall better performance. Instead of this averaging one could try to make the ANNs more robust in the first place, e.g., by applying further regularization such as Gaussian noise to all inputs. Also further input

data could be used to constrain the phase space, e.g., vertical temperature profiles from models (Zhu et al., 2020). Using the training data set in its current form, strategies such as bootstrap aggregating (Section 2.4) might improve the overall retrieval: one could train multiple ANNs for each task using only a subset of the complete training data; the retrievals of the resulting ANNs could then be combined to derive a final result. Another possibility would be to use either temporally consecutive or spatially linked observations: "close" measurements should share properties, and discontinuities in the retrieval results should be suppressed. When considering extended areas, the volcanic ash retrieval might also profit from distinct features such as sharp edges at the rim of the ash cloud or straight plumes close to the vent. To do so, the radiative transfer model needs to be coupled to a transport and dispersion model; then convolutional neural networks could be applied to the resulting images (Drönner et al., 2018).

Third, one could leave VACOS as is but focus on further processing the retrieval outputs. It might be promising to further evaluate the pixel-based retrievals altogether to detect clusters of ash-contaminated pixels (i.e., ash clouds), evaluate their mean properties (Pavolonis et al., 2015) and track them in time, potentially connecting them to their volcanic source. Note that such a post-processing would exploit the strengths of a geostationary instrument such as MSG/SEVIRI, i.e., the high temporal and spatial resolution compared to polar-orbiting instruments such as MODIS.

The composition-dependence of volcanic ash refractive indices was shown to notably influence brightness temperatures in the atmospheric window. Thus, it might be promising to develop a retrieval for the volcanic ash composition, e.g., for the bulk silica content. However, to exploit the full potential of this data set, one might make use of hyperspectral instruments (e.g., AIRS or IASI), which already proved sensibility to volcanic ash composition (Clarisse et al., 2010, Gangale et al., 2010, Ishimoto et al., 2016, 2021, Klüser et al., 2013). This points also to one shortcoming of MSG/SEVIRI (and all moderate resolution radiometers for that matter): the limited number of spectral channels. However, large areas of the Earth are covered by multiple geostationary imagers (Figure 2.12) with slightly different channels (Figure 2.10), such that in principle one might profit from simultaneous observations of different instruments. As explained in Section 2.3, various other passive imagers carried by geostationary spacecraft have similar spectral channels as MSG/SEVIRI. Using adequate spectral band adjustment factors (Chander et al., 2013, Scarino et al., 2016), VACOS could be applied to their observations, thereby potentially covering nearly the full globe. This would also be the preferred path to apply VACOS to the upcoming Flexible Combined Imager (FCI) on board of the Meteosat Third Generation (MTG) satellites.

### A scientific outlook: Combining VACOS with COCS/CiPS to study ash-induced ice formation

Aerosol–cloud interactions introduce one of the largest uncertainties in current climate simulations using general circulation models. This is especially due to the differences in the scales of the individual cloud processes and the comparably coarse resolutions of

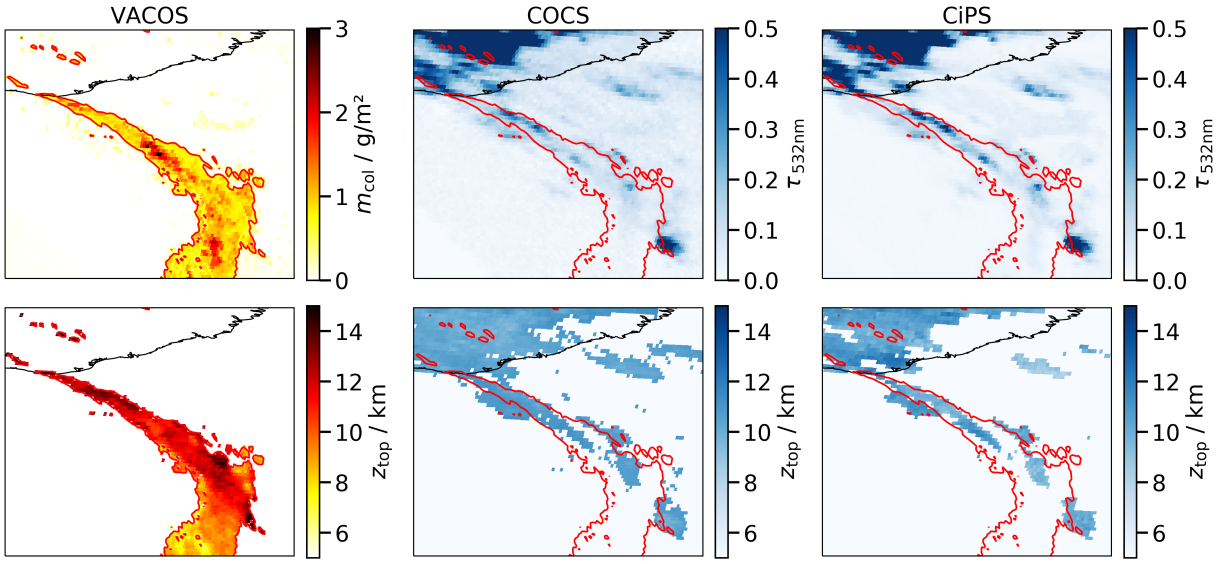


Figure 4.1: Simultaneous retrieval of $m_{col}$ and $z_{top}$ due to Eyjafjallajökull volcanic ash using VACOS (left column), and $\tau_{532\,nm}$ and $z_{top}$ of cirrus clouds using COCS (middle column) and CiPS (right column) on 7 May 2010, 12:45 UTC; the ash plume is given in all plots as red contour ($m_{col} > 0.5\,g\,m^{-2}$); $z_{top}$ is given for ash and ice if $m_{col} > 0.5\,g\,m^{-2}$ and $\tau_{532\,nm} > 0.1$, respectively; the coast of Iceland is given in the top left (black).

the model grids. To better constrain existing model parameterizations of aerosol–cloud interactions, further global measurements of these processes are necessary (Seinfeld et al., 2016). The effects of aerosols on clouds might even depend on the region, the cloud type or the atmospheric state, such that it might be necessary to investigate the different possibilities individually (Stevens and Feingold, 2009). One example might be volcanic ash particles that induce ice formation by acting as ice nuclei, potentially affecting cirrus coverage, ice water path, ice crystal size and precipitation (Durant et al., 2008). The ice nucleation ability of volcanic ash was studied extensively in the laboratory (e.g., Hoyle et al., 2011, Steinke et al., 2011) and in nature (e.g., Belosi et al., 2011, Rolf et al., 2012, Seifert et al., 2011). Still, there is a need for corresponding large-scale satellite-based studies (see Section 2.1.3 for details). Combining VACOS with existing cirrus retrievals, e.g., *Cirrus Optical Properties derived from CALIOP and SEVIRI Algorithm during Day and Night* (COCS, Kox et al., 2014) or CiPS (Strandgren et al., 2017a), might allow to fill this gap by exploiting the high spatial coverage and temporal resolution of MSG/SEVIRI.

In a first test, VACOS is applied alongside both ice cloud retrievals COCS and CiPS to the eruption of Eyjafjallajökull on 7 May 2010, 12:45 UTC to check whether or not the two cirrus retrievals produce different results in the presence of ash. A mass extinction coefficient of $200\,m^2\,kg^{-1}$ is assumed (as in **P3**) to convert the retrieved $\tau_{10.8}$ of ash into $m_{col}$. Figure 4.1 shows a comparison of the retrievals of $z_{top}$ and $m_{col}$ / $\tau_{532\,nm}$ of volcanic ash and ice. A few minutes earlier, the Terra satellite crossed the same area, carrying the MISR instrument. The MISR data were investigated by Kahn and Limbacher (2012),

indicating the presence of patches of ice clouds within the ash plume (see Figure 3 in their paper). The retrievals of COCS and CiPS give a similar picture: they show small areas where $\tau_{532\,\mathrm{nm}}$ has values of 0.2–0.5 at $z_{\mathrm{top}} \approx 10\,\mathrm{km}$. In particular, the retrievals of COCS and CiPS are very similar in this scene; thus, both retrievals seem to be similarly suited to consider ash–ice interactions. VACOS retrieves for $m_{\mathrm{col}}$ mass loads of 0.5–3 $\mathrm{g\,m^{-2}}$ at $z_{\mathrm{top}} \approx 11\,\mathrm{km}$, i.e., a similar height as given by the cirrus retrievals. Note that $z_{\mathrm{top}}$ is again increased where COCS and CiPS indicate the presence of ice.

Next, the retrieval results of VACOS and COCS of the May 2010 period are scanned manually for scenes which show ice detection in spatial congruence with a simultaneous ash detection. The temporal evolution of six events is given in the examples in Figure 4.2 to 4.4. Figure 4.2 contains two events similar to the one in Figure 4.1, i.e., with ice detections in the ash plume close to the vent. The event on 16 May 2010, 08–12 UTC shows how multiple patches of ice are transported downwind with the ash plume, whereas the event on 17 May 2010, 01–09 UTC demonstrates how a previously ice-free ash plume turns into an ice-contaminated ash plume within a few hours. Figure 4.3 displays two ash clouds which are already slightly aged. The event on 14 May 2010, 08–11 UTC includes an ash cloud moving westwards over the eastern coast of Iceland and subsequently forming ice according to COCS. The second event on 14 May 2010, 16–19:30 UTC shows how an arc-shaped ash cloud moves towards the north-east over the Faroe Islands. Afterwards, VACOS does not detect the ash anymore, but COCS detects an extended cirrus cloud with exactly the same shape as the ash cloud before. Figure 4.4 shows two events south-east of Greenland. In both cases, COCS detects small elongated patches of ice in spatial agreement with the ash detections. The event on 15 May 2010, 20–23:45 UTC is related to a relatively thick ash cloud with $m_{\mathrm{col}}$ being 0.5–1 $\mathrm{g\,m^{-2}}$, whereas much less ash is detected for the event on 16 May 2010, 13–17 UTC, but the alignment of ash clouds in the area indicates that the ice-formation could be connected to volcanic ash.

Different mechanisms could explain the described scenarios. Ice close to the vent (Figure 4.2) might be caused by an increased emission of water vapor, e.g., due to contact of lava with external water or the glacier on the volcano's surface. The apparent ice formation when the ash cloud crosses the coasts of Iceland and the Faroe Islands (Figure 4.3) might be explained by orographic lift resulting in lower temperatures. The ice creation off the coast of Greenland (Figure 4.4) might be triggered by cool or moist air from Greenland as it seems as if the cirrus cloud above Greenland slowly extends towards the south-east along the ash cloud.

Although these examples are intriguing, they can only be considered a first step; further investigation is necessary. First, the applied methods need further checking. VACOS was also trained on ash clouds in the presence of cirrus, but not specifically for (partly) ice-covered ash (i.e., in many training cases, the ash and the cirrus layer were well separated). Similarly, COCS as well as CiPS were not trained specifically for the combination of ice and thick aerosol layers; thus, it is not clear how reliable these retrievals perform in the considered cases. The typical spectral signature of ash and ice in the thermal infrared leads to $BTD_{11-12}$ being negative (Prata, 1989) or positive (Inoue, 1985), respectively. If both ash and ice are present, $BTD_{11-12}$ is influenced by both. As a consequence, ash might be

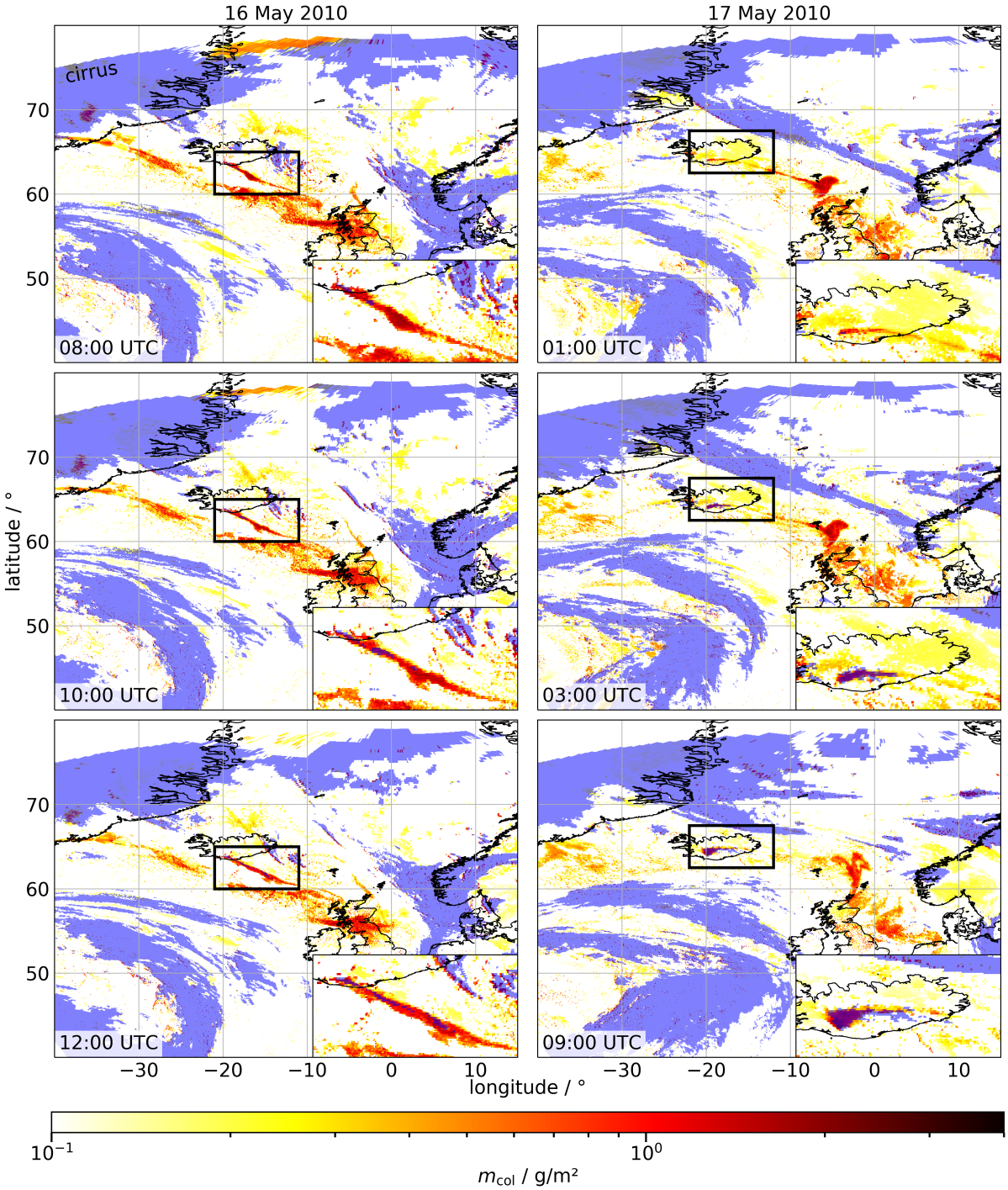


Figure 4.2: Simultaneous retrieval of $m_{col}$ due to Eyjafjallajökull volcanic ash using VACOS (in yellow and red) and detection of cirrus clouds using COCS (blue) on 16 and 17 May 2010; the plots of ash and ice are semi-opaque such that collocated retrievals are visible; two events (left and right column, respectively) show ice detections collocated with the ash plume close to the vent; both events are marked by black boxes, with zoomed plots given as insets on the lower right corner.

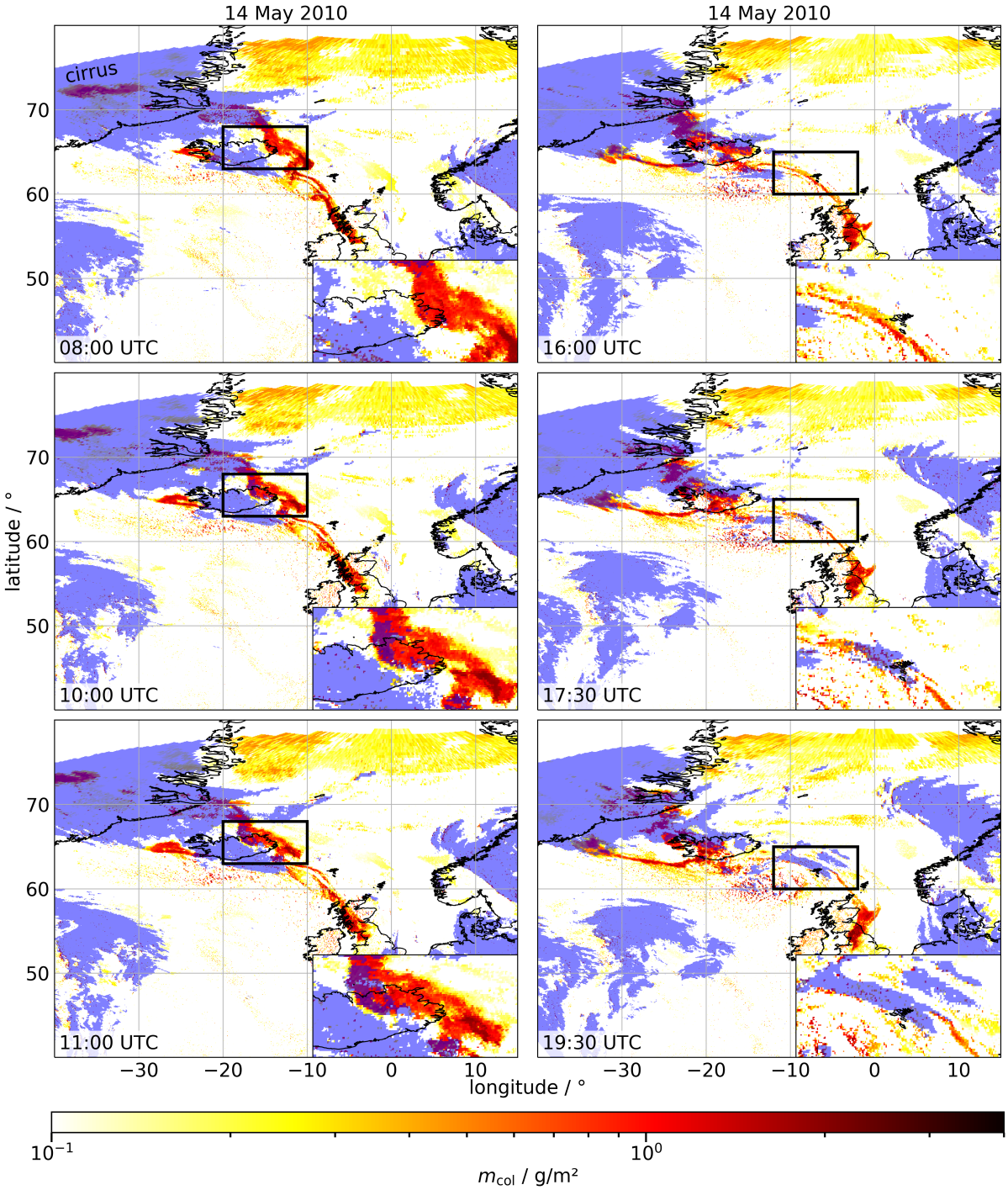


Figure 4.3: As in Figure 4.2: Simultaneous retrieval of $m_{col}$ due to Eyjafjallajökull volcanic ash using VACOS (in yellow and red) and detection of cirrus clouds using COCS (blue) on 14 May 2010; the plots of ash and ice are semi-opaque such that collocated retrievals are visible; two events north-east of Iceland (left column) and around the Faroe Islands (right column) are marked by black boxes, with zoomed plots given as insets on the lower right corner.

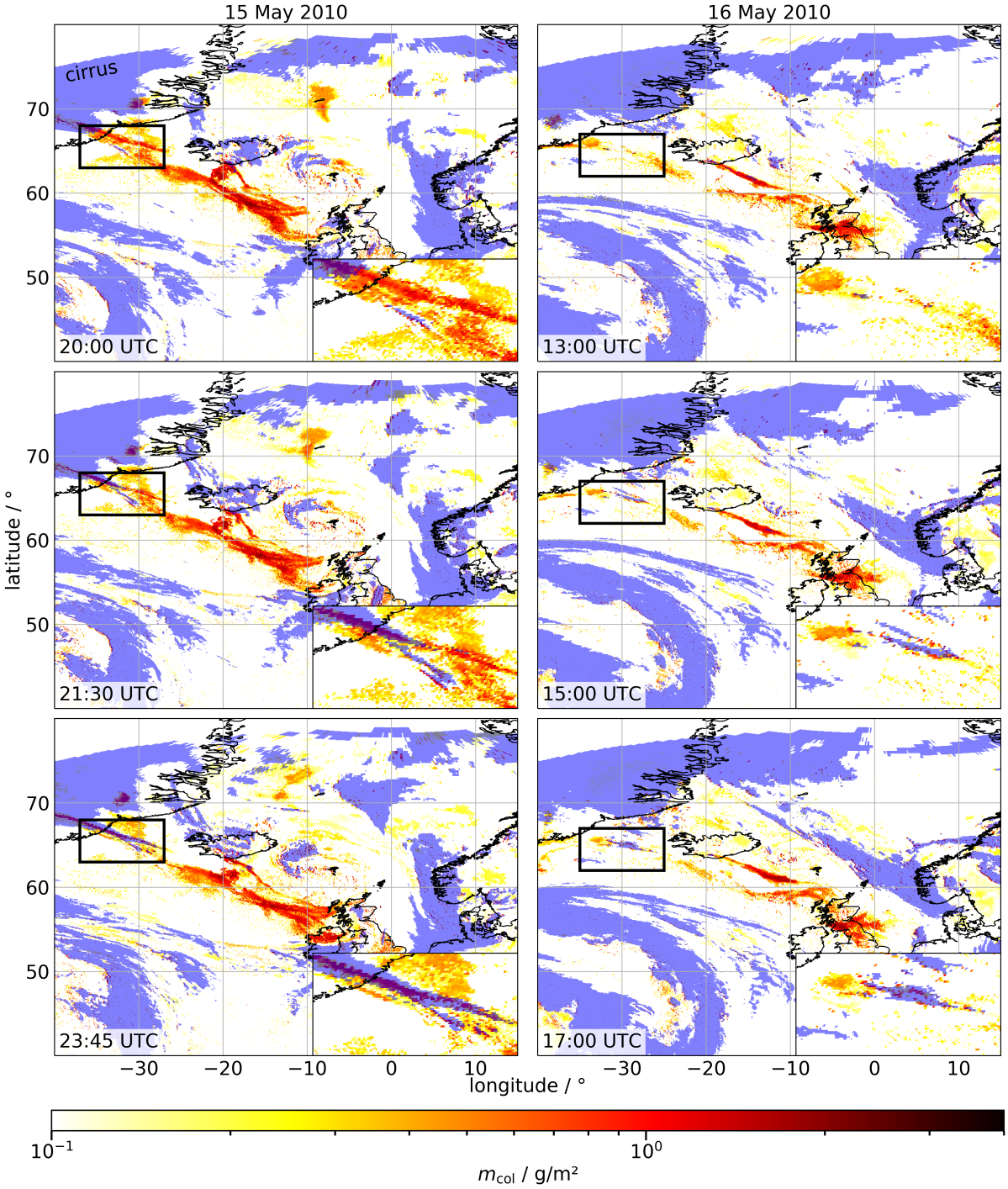


Figure 4.4: As in Figure 4.2: Simultaneous retrieval of $m_{col}$ due to Eyjafjallajökull volcanic ash using VACOS (in yellow and red) and detection of cirrus clouds using COCS (blue) on 15 and 16 May 2010; the plots of ash and ice are semi-opaque such that collocated retrievals are visible; two events south-east of Greenland (left and right column, respectively) are marked by black boxes, with zoomed plots given as insets on the lower right corner.

hidden by the cirrus clouds or the other way around. Second, the vertical collocation of ash and ice needs to be checked to make sure that potential ice formation is related to volcanic ash particles acting as ice nuclei. To this end, cloud top retrievals of VACOS and COCS can be considered, as well as CALIPSO/CALIOP soundings for selected cases. Third, other possible explanations/aerosols for ice formation need to be ruled out. Specifically, sulfates are a common by-product of volcanic eruptions. Considering scenes which are dominated by volcanic ash (e.g., as $SO_2$/sulfates are spatially separated due to vertical wind shear) might allow to do so. Fourth, the overall meteorology needs to be analyzed. Is the onset of ice formation related to sudden temperature decreases, e.g., by orographic lifting? Is supersaturation with respect to liquid water/ice given? In addition, as the formation and the transport of cirrus clouds is driven by the given meteorology, which also determines the ash transport, one needs to consider the possibility that potential collocations are just by chance (Boucher et al., 2013).

If this is done and the given observations are confirmed, one may investigate how the ice formation events unfold with time; under which atmospheric conditions they take place; how ash-contaminated areas differ from ash-free regions statistically with respect to ice formation; whether the results of ash transport and dispersion models including a description for ice formation resemble the satellite observations, thereby testing the applied parameterizations.

# Appendix A

# List of abbreviations

| | |
|---|---|
| **1D** | One-Dimensional |
| **ABI** | Advanced Baseline Imager |
| **AGRI** | Advanced Geostationary Radiation Imager |
| **AHI** | Advanced Himawari Imager |
| **AIRS** | Atmospheric Infrared Sounder |
| **AMI** | Advanced Meteorological Imager |
| **ANN** | Artificial Neural Network |
| **BT** | Brightness Temperature |
| **BTD** | Brightness Temperature Difference |
| **CALIOP** | Cloud Aerosol Lidar with Orthogonal Polarization |
| **CALIPSO** | Cloud-Aerosol Lidar and Infrared Pathfinder Satellite Observation |
| **CARA** | Cluster for Advanced Research in Aerospace |
| **CCN** | Cloud Condensation Nucleus |
| **CiPS** | Cirrus Properties from SEVIRI |
| **COCS** | Cirrus Optical Properties from CALIOP and SEVIRI |
| **DISORT** | Discrete Ordinate Radiative Transfer Solver |
| **DLR** | Deutsches Zentrum für Luft- und Raumfahrt |
| **DOY** | Day of Year |
| **DWD** | Deutscher Wetterdienst |
| **ECMWF** | European Centre for Medium-Range Weather Forecasts |
| **ERA** | ECMWF Reanalysis |
| **EUMETSAT** | European Organisation for the Exploitation of Meteorological Satellites |
| **FAAM** | Facility for Airborne Atmospheric Measurements |
| **FAR** | False Alarm Rate |
| **FCI** | Flexible Combined Imager |
| **FLEXPART** | Flexible Particle Dispersion Model |
| **FY** | Feng-Yun |
| **GOES** | Geostationary Operational Environmental Satellite |
| **HOD** | Hour of Day |

| | |
|---|---|
| **HRV** | High Resolution Visible |
| **HYSPLIT** | Hybrid Single Particle Lagrangian Integrated Trajectory |
| **IASI** | Infrared Atmospheric Sounding Interferometer |
| **ICAO** | International Civil Aviation Organization |
| **IN** | Ice Nucleus |
| **IR** | Infrared |
| **IWP** | Ice Water Path |
| **LIDAR** | Light Detection and Ranging |
| **LSM** | Land/Sea Mask |
| **MAPE** | Mean Absolute Percentage Error |
| **MATCH** | Multi-scale Atmospheric Transport and Chemistry |
| $m_{\mathrm{col}}$ | Mass Column Concentration |
| **MISR** | Multi-angle Imaging SpectroRadiometer |
| **MOCAGE** | Modèle de Chimie Atmosphérique à Grande Echelle |
| **MODIS** | Moderate Resolution Imaging Spectroradiometer |
| **MOPSMAP** | Modeled Optical Properties of Ensembles of Aerosol Particles |
| **MPE** | Mean Percentage Error |
| **MSE** | Mean Squared Error |
| **MSG** | Meteosat Second Generation |
| **MTG** | Meteosat Third Generation |
| **NADAM** | Nesterov-accelerated Adaptive Moment Estimation |
| **PMA** | Particle Mineralogical Analysis |
| **POD** | Probability of Detection |
| **POLDER** | Polarization and Directionality of Earth Reflectance |
| **QEMSCAN** | Quantitative Evaluation of Minerals by Scanning Electron Microscopy |
| $r_{\mathrm{eff}}$ | Effective Radius |
| **RH** | Relative Humidity |
| **SEM** | Scanning Electron Microscopy |
| **SEVIRI** | Spinning Enhanced Visible and Infrared Imager |
| $\tau_{10.8}$ | Optical Depth due to Volcanic Ash at 10.8 µm |
| **$TCO_3$** | Total Column Ozone |
| **TCW** | Total Column Water |
| **TCWV** | Total Column Water Vapor |
| **UTC** | Coordinated Universal Time |
| **VAAC** | Volcanic Ash Advisory Center |
| **VADUGS** | Volcanic Ash Detection Utilizing Geostationary Satellites |
| **VACOS** | Volcanic Ash Cloud Properties Obtained from SEVIRI |
| **VZA** | Viewing Zenith Angle |
| **WMO** | World Meteorological Organization |
| **WRF-Chem** | Weather Research and Forecasting Model Coupled with Chemistry |
| $x_s$ | Silica Content |
| $z_{\mathrm{top}}$ | Cloud Top Height |

# Bibliography


S. A. Ackerman. Remote sensing aerosols using satellite infrared observations. *Journal of Geophysical Research: Atmospheres*, 102(D14):17069–17079, 1997. doi: 10.1029/96JD03066.

S. A. Ackerman, W. L. Smith, H. E. Revercomb, and J. D. Spinhirne. The 27–28 October 1986 FIRE IFO Cirrus Case Study: Spectral Properties of Cirrus Clouds in the 8–12 $\mu$m Window. *Monthly Weather Review*, 118(11):2377–2388, 1990. doi: 10.1175/1520-0493(1990)118<2377:TOFICC>2.0.CO;2.

B. A. Albrecht. Aerosols, Cloud Microphysics, and Fractional Cloudiness. *Science*, 245(4923):1227–1230, 1989. doi: 10.1126/science.245.4923.1227.

D. Alexander. Volcanic ash in the atmosphere and risks for civil aviation: A study in European crisis management. *International Journal of Disaster Risk Science*, 4(1):9–19, 2013. doi: 10.1007/s13753-013-0003-0.

F. Belosi, G. Santachiara, and F. Prodi. Eyjafjallajökull Volcanic Eruption: Ice Nuclei and Particle Characterization. *Atmospheric and Climate Sciences*, 1(2):48–54, 2011. doi: 10.4236/acs.2011.12005.

Y. Bengio. Practical Recommendations for Gradient-Based Training of Deep Architectures. In G. Montavon, G. B. Orr, and K. R. Müller, editors, *Neural Networks: Tricks of the Trade*. Springer, Berlin and Heidelberg, Germany, 2nd edition, 2012. doi: 10.1007/978-3-642-35289-8_26.

K. Bessho, K. Date, M. Hayashi, A. Ikeda, T. Imai, H. Inoue, Y. Kumagai, T. Miyakawa, H. Murata, T. Ohno, A. Okuyama, R. Oyama, Y. Sasaki, Y. Shimazu, K. Shimoji, Y. Sumida, M. Suzuki, H. Taniguchi, H. Tsuchiyama, D. Uesawa, H. Yokota, and R. Yoshida. An Introduction to Himawari-8/9 - Japan's New-Generation Geostationary Meteorological Satellites. *Journal of the Meteorological Society of Japan*, 94(2):151–183, 2016. doi: 10.2151/jmsj.2016-009.

M. G. Best. *Igneous and Metamorphic Petrology*. Blackwell, Malden, MA, USA and Oxford, United Kingdom and Melbourne, Australia and Berlin, Germany, 2nd edition, 2003.

P. Bird. An updated digital model of plate boundaries. *Geochemistry, Geophysics, Geosystems*, 4(3), 2003. doi: 10.1029/2001GC000252.

C. M. Bishop. *Neural Networks for Pattern Recognition*. Clarendon Press, Oxford, United Kingdom, 1995. ISBN 9780198538646.

T. Bolić and Z. Sivčev. Eruption of Eyjafjallajökull in Iceland: Experience of European Air Traffic Management. *Transportation Research Record*, 2214(1):136–143, 2011. doi: 10.3141/2214-17.

O. Boucher, D. Randall, P. Artaxo, C. Bretherton, G. Feingold, P. Forster, V.-M. Kerminen, Y. Kondo, H. Liao, U. Lohmann, P. Rasch, S. Satheesh, S. Sherwood, B. Stevens, and X. Zhang. *Climate Change 2013: The Physical Science Basis. Contribution of Working Group I to the Fifth Assessment Report of the Intergovernmental Panel on Climate Change*, chapter Clouds and Aerosols. Cambridge University Press, Cambridge, United Kingdom and New York, NY, USA, 2013.

R. Brown, C. Bonadonna, and A. Durant. A review of volcanic ash aggregation. *Physics and Chemistry of the Earth*, 45-46:65–78, 2012. doi: 10.1016/j.pce.2011.11.001.

L. Budd, S. Griggs, D. Howarth, and S. Ison. A Fiasco of Volcanic Proportions? Eyjafjallajökull and the Closure of European Airspace. *Mobilities*, 6(1):31–40, 2011. doi: 10.1080/17450101.2011.532650.

S. A. Carn, A. J. Krueger, N. A. Krotkov, K. Yang, and K. Evans. Tracking volcanic sulfur dioxide clouds for aviation hazard mitigation. *Natural Hazards*, 51:325–343, 2009. doi: 10.1007/s11069-008-9228-4.

T. J. Casadevall. The 1989–1990 eruption of Redoubt Volcano, Alaska: impacts on aircraft operations. *Journal of Volcanology and Geothermal Research*, 62(1):301–316, 1994. doi: 10.1016/0377-0273(94)90038-8.

CGMS. Status of current and future Russian satellite systems by Roscosmos/Roshydromet. `https://www.cgms-info.org/Agendas/GetWpFile.ashx?wid=42833d40-cbef-4e4e-91cf-aace91183d90&aid=e656c459-2da5-498b-8010-af1c6dbf30e0`. Last accessed: 16 Nov. 2021.

G. Chander, N. Mishra, D. L. Helder, D. B. Aaron, A. Angal, T. Choi, X. Xiong, and D. R. Doelling. Applications of Spectral Band Adjustment Factors (SBAF) for Cross-Calibration. *IEEE Transactions on Geoscience and Remote Sensing*, 51(3):1267–1281, 2013. doi: 10.1109/TGRS.2012.2228007.

R. Cioni, M. Pistolesi, A. Bertagnini, C. Bonadonna, A. Hoskuldsson, and B. Scateni. Insights into the dynamics and evolution of the 2010 Eyjafjallajökull summit eruption (Iceland) provided by volcanic ash textures. *Earth and Planetary Science Letters*, 394: 111–123, 2014. doi: 10.1016/j.epsl.2014.02.051.

L. Clarisse, F. Prata, J.-L. Lacour, D. Hurtmans, C. Clerbaux, and P.-F. Coheur. A correlation method for volcanic ash detection using hyperspectral infrared measurements. *Geophysical Research Letters*, 37(19), 2010. doi: 10.1029/2010GL044828.

S. Colucci, D. M. Palladino, G. K. Mulukutla, and A. A. Proussevitch. 3-D reconstruction of ash vesicularity: Insights into the origin of ash-rich explosive eruptions. *Journal of Volcanology and Geothermal Research*, 255:98–107, 2013. doi: 10.1016/j.jvolgeores.2013.02.002.

S. Corradini, S. Pugnaghi, A. Piscini, L. Guerrieri, L. Merucci, M. Picchiani, and M. Chini. Volcanic Ash and $SO_2$ retrievals using synthetic MODIS TIR data: comparison between inversion procedures and sensitivity analysis. *Annals of Geophysics*, 57(0), 2014. doi: 10.4401/ag-6616.

S. Corradini, M. Montopoli, L. Guerrieri, M. Ricci, S. Scollo, L. Merucci, F. S. Marzano, S. Pugnaghi, M. Prestifilippo, L. J. Ventress, R. G. Grainger, E. Carboni, G. Vulpiani, and M. Coltelli. A Multi-Sensor Approach for Volcanic Ash Cloud Retrieval and Eruption Characterization: The 23 November 2013 Etna Lava Fountain. *Remote Sensing*, 8(1), 2016. doi: 10.3390/rs8010058.

H. F. Dacre, N. J. Harvey, P. W. Webley, and D. Morton. How accurate are volcanic ash simulations of the 2010 Eyjafjallajökull eruption? *Journal of Geophysical Research: Atmospheres*, 121(7):3534–3547, 2016. doi: 10.1002/2015JD024265.

F. Debling, J. F. Schneider, M. Rosi, E. Leoz-Garziandia, and E. Rorije. Technical Cooperation Mission, Effects of the Puyehue-Cordón Caulle Eruption Argentina, 4–19 July 2011. Joint UNEP/OCHA Environment Unit, 2011. `https://www.eecentre.org/wp-content/uploads/2019/06/Argentina-volcan-eruption-2011-report.pdf`. Last accessed: 17 Nov. 2021.

A. Deguine, D. Petitprez, L. Clarisse, S. Guđmundsson, V. Outes, G. Villarosa, and H. Herbin. Complex refractive index of volcanic ash aerosol in the infrared, visible, and ultraviolet. *Applied Optics*, 59(4):884–895, Feb 2020. doi: 10.1364/AO.59.000884.

T. Dozat. Incorporating Nesterov Momentum into Adam, 2016. `https://openreview.net/pdf?id=OM0jvwB8jIp57ZJjtNEZ`. Last accessed: 17 Nov. 2021.

J. Drönner, N. Korfhage, S. Egli, M. Mühling, B. Thies, J. Bendix, B. Freisleben, and B. Seeger. Fast Cloud Segmentation Using Convolutional Neural Networks. *Remote Sensing*, 10(11), 2018. doi: 10.3390/rs10111782.

Y. Durand, P. Hallibert, M. Wilson, M. Lekouara, S. Grabarnik, D. Aminou, P. Blythe, B. Napierala, J.-L. Canaud, O. Pigouche, J. Ouaknine, and B. Verez. The flexible combined imager onboard MTG: from design to calibration. In R. Meynart, S. P. Neeck, and H. Shimoda, editors, *Sensors, Systems, and Next-Generation Satellites XIX*, volume 9639, pages 1–14. International Society for Optics and Photonics, SPIE, 2015. doi: 10.1117/12.2196644.

A. J. Durant and R. A. Shaw. Evaporation freezing by contact nucleation inside-out. *Geophysical Research Letters*, 32(20), 2005. doi: 10.1029/2005GL024175.

A. J. Durant, R. A. Shaw, W. I. Rose, Y. Mi, and G. G. J. Ernst. Ice nucleation and overseeding of ice in volcanic clouds. *Journal of Geophysical Research: Atmospheres*, 113(D9), 2008. doi: 10.1029/2007JD009064.

DWD. Jahresbericht 2015: Flugwetterdienst. Deutscher Wetterdienst, 2015. `https://www.dwd.de/DE/fachnutzer/luftfahrt/download/jahresberichte_flugwetterdienst/2015.pdf?__blob=publicationFile&v=3`. Last accessed: 17 Nov. 2021.

S. K. Ebmeier, A. M. Sayer, R. G. Grainger, T. A. Mather, and E. Carboni. Systematic satellite observations of the impact of aerosols from passive volcanic degassing on local cloud properties. *Atmospheric Chemistry and Physics*, 14(19):10601–10618, 2014. doi: 10.5194/acp-14-10601-2014.

J. Eliasson and J. Yoshitani. Airborne Measurements of Volcanic Ash and Current State of Ash Cloud Prediction. *Disaster Prevention Research Institute Annuals*, 58(B):35–41, 2015. `http://hdl.handle.net/2433/210094`. Last accessed: 17 Nov. 2021.

J. Eliasson, N. Yasuda, K. Weber, A. Vogel, and T. Palsson. The role of in-situ measurements of volcanic ash concentrations in preventing economic disasters due to volcanic ash clouds. *Journal of Integrated Disaster Risk Management*, 4(1):48–60, 2014. doi: 10.5595/idrim.2014.0092.

C. Emde, R. Buras-Schnell, A. Kylling, B. Mayer, J. Gasteiger, U. Hamann, J. Kylling, B. Richter, C. Pause, T. Dowling, and L. Bugliaro. The libRadtran software package for radiative transfer calculations (version 2.0.1). *Geoscientific Model Development*, 9 (5):1647–1672, 2016. doi: 10.5194/gmd-9-1647-2016.

EUMETSAT/1. `https://nwp-saf.eumetsat.int/site/software/rttov/download/coefficients/spectral-response-functions`. Last accessed: 17 Nov. 2021.

EUMETSAT/2. The Conversion from Effective Radiances to Equivalent Brightness Temperatures. European Organisation for the Exploitation of Meteorological Satellites, 2012. `https://www-cdn.eumetsat.int/files/2020-04/pdf_effect_rad_to_brightness.pdf`. Last accessed: 17 Nov. 2021.

EUMETSAT/3. Typical Radiometric Noise, Calibration Bias and Stability for Meteosat-8, -9, -10 and -11 SEVIRI. European Organisation for the Exploitation of Meteorological Satellites, 2019. `https://www-cdn.eumetsat.int/files/2020-04/pdf_typ_radiomet_acc_msg-1-2.pdf`. Last accessed: 17 Nov. 2021.

J. Fan, Y. Wang, D. Rosenfeld, and X. Liu. Review of Aerosol–Cloud Interactions: Mechanisms, Significance, and Challenges. *Journal of the Atmospheric Sciences*, 73(11):4221–4252, 2016. doi: 10.1175/JAS-D-16-0037.1.

N. H. Farlow, V. R. Orberbeck, K. G. Snetsinger, G. V. Ferry, G. Polkowski, and D. M. Hayes. Size Distributions and Mineralogy of Ash Particles in the Stratosphere from

Eruptions of Mount St. Helens. *Science*, 211(4484):832–834, 1981. doi: 10.1126/science.211.4484.832.

M. G. Flanner, A. S. Gardner, S. Eckhardt, A. Stohl, and J. Perket. Aerosol radiative forcing from the 2010 Eyjafjallajökull volcanic eruptions. *Journal of Geophysical Research: Atmospheres*, 119(15):9481–9491, 2014. doi: 10.1002/2014JD021977.

A. P. Fornea, S. D. Brooks, J. B. Dooley, and A. Saha. Heterogeneous freezing of ice on atmospheric aerosols containing ash, soot, and soil. *Journal of Geophysical Research: Atmospheres*, 114(D13), 2009. doi: 10.1029/2009JD011958.

G. Gangale, A. Prata, and L. Clarisse. The infrared spectral signature of volcanic ash determined from high-spectral resolution satellite measurements. *Remote Sensing of Environment*, 114(2):414–425, 2010. doi: https://doi.org/10.1016/j.rse.2009.09.007.

M. Gardner and S. Dorling. Artificial neural networks (the multilayer perceptron)—a review of applications in the atmospheric sciences. *Atmospheric Environment*, 32(14): 2627–2636, 1998. doi: 10.1016/S1352-2310(97)00447-0.

S. Gassó. Satellite observations of the impact of weak volcanic activity on marine clouds. *Journal of Geophysical Research: Atmospheres*, 113(D14S19), 2008. doi: 10.1029/2007JD009106.

K. Genareau, A. A. Proussevitch, A. J. Durant, G. Mulukutla, and D. L. Sahagian. Sizing up the bubbles that produce very fine ash during explosive volcanic eruptions. *Geophysical Research Letters*, 39(15), 2012. doi: 10.1029/2012GL052471.

K. Genareau, G. K. Mulukutla, A. A. Proussevitch, A. J. Durant, W. I. Rose, and D. L. Sahagian. The size range of bubbles that produce ash during explosive volcanic eruptions. *Journal of Applied Volcanology*, 2(1):4, 2013. doi: 10.1186/2191-5040-2-4.

K. Genareau, S. M. Cloer, K. Primm, M. A. Tolbert, and T. W. Woods. Compositional and Mineralogical Effects on Ice Nucleation Activity of Volcanic Ash. *Atmosphere*, 9(7), 2018. doi: 10.3390/atmos9070238.

I. Goodfellow, Y. Bengio, and A. Courville. *Deep Learning: Das umfassende Handbuch*. mitp, Frechen, Germany, 1st edition, 2018. ISBN 9783958457003.

K. Graf, S. Kox, M. Schmidl, J. Gasteiger, and R. Buras. VADUGS algorithm: Volcanic Ash Detection using Geostationary Satellites. Presentation at the Meeting on the Intercomparison of Satellite-based Volcanic Ash Retrieval Algorithms, Madison, WI, USA, 29 June–2 July 2015, 2015. `http://cimss.ssec.wisc.edu/meetings/vol_ash15/PDFs/20150630/Item2.10_20150630_WMO_Madison_Graf.pdf`. Last accessed: 26 Nov. 2021.

R. G. Grainger, D. M. Peters, G. E. Thomas, A. J. A. Smith, R. Siddans, E. Carboni, and A. Dudhia. Measuring volcanic plume and ash properties from space. *Geological Society, London, Special Publications*, 380:293–320, 2013. doi: 10.1144/SP380.7.

T. M. Gray and R. Bennartz. Automatic volcanic ash detection from MODIS observations using a back-propagation neural network. *Atmospheric Measurement Techniques*, 8(12): 5089–5097, 2015. doi: 10.5194/amt-8-5089-2015.

M. T. Gudmundsson, R. Pedersen, K. Vogfjörd, B. Thorbjarnardóttir, S. Jakobsdóttir, and M. J. Roberts. Eruptions of Eyjafjallajökull Volcano, Iceland. *Eos, Transactions American Geophysical Union*, 91(21):190–191, 2010. doi: 10.1029/2010EO210002.

M. T. Gudmundsson, T. Thordarson, r. Höskuldsson, G. Larsen, H. Björnsson, F. J. Prata, B. Oddsson, E. Magnússon, T. Högnadóttir, G. N. Petersen, C. L. Hayward, J. A. Stevenson, and I. Jónsdóttir. Ash generation and distribution from the April-May 2010 eruption of Eyjafjallajökull, Iceland. *Scientific Reports*, 2:572, 2012. doi: 10.1038/srep 00572.

M. Guffanti, G. C. Mayberry, T. J. Casadevall, and R. Wunderman. Volcanic hazards to airports. *Natural Hazards*, 51(2):287–302, 2009. doi: 10.1007/s11069-008-9254-2.

M. Guffanti, T. J. Casadevall, and K. Budding. Encounters of aircraft with volcanic ash clouds; A compilation of known incidents, 1953–2009. U.S. Geological Survey Data Series 545, ver. 1.0, 12 p., plus 4 appendixes including the compilation database, 2010. `https://pubs.usgs.gov/ds/545/DS545.pdf`. Last accessed: 17 Nov. 2021.

Hecht-Nielsen. Theory of the backpropagation neural network. In *International 1989 Joint Conference on Neural Networks*, pages 593–605 vol.1, 1989. doi: 10.1109/IJCNN.1989.1 18638.

F. Hilton, R. Armante, T. August, C. Barnet, A. Bouchard, C. Camy-Peyret, V. Capelle, L. Clarisse, C. Clerbaux, P.-F. Coheur, A. Collard, C. Crevoisier, G. Dufour, D. Edwards, F. Faijan, N. Fourrié, A. Gambacorta, M. Goldberg, V. Guidard, D. Hurtmans, S. Illingworth, N. Jacquinet-Husson, T. Kerzenmacher, D. Klaes, L. Lavanant, G. Masiello, M. Matricardi, A. McNally, S. Newman, E. Pavelin, S. Payan, E. Péquignot, S. Peyridieu, T. Phulpin, J. Remedios, P. Schlüssel, C. Serio, L. Strow, C. Stubenrauch, J. Taylor, D. Tobin, W. Wolf, and D. Zhou. Hyperspectral Earth Observation from IASI: Five Years of Accomplishments. *Bulletin of the American Meteorological Society*, 93(3): 347–370, 2012. doi: 10.1175/BAMS-D-11-00027.1.

A. J. Hornby, Y. Lavallée, J. E. Kendrick, G. Rollinson, A. R. Butcher, S. Clesham, U. Kueppers, C. Cimarelli, and G. Chigna. Phase partitioning during fragmentation revealed by QEMSCAN Particle Mineralogical Analysis of volcanic ash. *Scientific Reports*, 9(1):126, 2019. doi: 10.1038/s41598-018-36857-4.

K. Hornik. Approximation capabilities of multilayer feedforward networks. *Neural Networks*, 4(2):251–257, 1991. doi: 10.1016/0893-6080(91)90009-T.

K. Hornik, M. Stinchcombe, and H. White. Multilayer feedforward networks are universal approximators. *Neural Networks*, 2(5):359–366, 1989. doi: 10.1016/0893-6080(89)90020-8.

C. J. Horwell and P. J. Baxter. The respiratory health hazards of volcanic ash: a review for volcanic risk mitigation. *Bulletin of Volcanology*, 69(1):1–24, 2006. doi: 10.1007/s00445-006-0052-y.

C. R. Hoyle, V. Pinti, A. Welti, B. Zobrist, C. Marcolli, B. Luo, A. Höskuldsson, H. B. Mattsson, O. Stetzer, T. Thorsteinsson, G. Larsen, and T. Peter. Ice nucleation properties of volcanic ash from Eyjafjallajökull. *Atmospheric Chemistry and Physics*, 11(18): 9911–9926, 2011. doi: 10.5194/acp-11-9911-2011.

W. W. Hsieh and B. Tang. Applying Neural Network Models to Prediction and Data Analysis in Meteorology and Oceanography. *Bulletin of the American Meteorological Society*, 79(9):1855–1870, 09 1998. doi: 10.1175/1520-0477(1998)079<1855:ANNMTP>2.0.CO;2.

ICAO. Volcanic Ash Contingency Plan: European and North Atlantic Regions, Edition 2.0.0. International Civil Aviation Organization, European and North Atlantic Office, 2016. `https://web.archive.org/web/20200827203551/https://www.icao.int/EURNAT/EUR%20and%20NAT%20Documents/EUR+NAT%20VACP.pdf`. Last accessed: 17 Nov. 2021.

T. Inoue. On the Temperature and Effective Emissivity Determination of Semi-Transparent Cirrus Clouds by Bi-Spectral Measurements in the 10 $\mu$m Window Region. *Journal of the Meteorological Society of Japan*, 63(1):88–99, 1985. doi: 10.2151/jmsj1965.63.1_88.

H. Ishimoto, K. Masuda, K. Fukui, T. Shimbori, T. Inazawa, H. Tuchiyama, K. Ishii, and T. Sakurai. Estimation of the refractive index of volcanic ash from satellite infrared sounder data. *Remote Sensing of Environment*, 174:165–180, 2016. doi: 10.1016/j.rse.2015.12.009.

H. Ishimoto, M. Hayashi, and Y. Mano. Optimal ash particle refractive index model for simulating the brightness temperature spectrum of volcanic ash clouds from satellite infrared sounder measurements. *Atmospheric Measurement Techniques Discussions*, 2021: 1–28, 2021. doi: 10.5194/amt-2021-103.

L. G. Jahn, W. D. Fahy, D. B. Williams, and R. C. Sullivan. Role of Feldspar and Pyroxene Minerals in the Ice Nucleating Ability of Three Volcanic Ashes. *ACS Earth and Space Chemistry*, 3(4):626–636, 2019. doi: 10.1021/acsearthspacechem.9b00004.

D. Jerram and N. Petford. *The Field Description of Igneous Rocks*. Wiley and Blackwell, Chichester, United Kingdom, 2nd edition, 2011. ISBN 978-0-470-02236-8.

JMA. AHI-8 Performance Test Results. `https://www.data.jma.go.jp/mscweb/en/himawari89/space_segment/fig/AHI8_performance_test_en.pdf`. Last accessed: 16 Nov. 2021.

B. Johnson, K. Turnbull, P. Brown, R. Burgess, J. Dorsey, A. J. Baran, H. Webster, J. Haywood, R. Cotton, Z. Ulanowski, E. Hesse, A. Woolley, and P. Rosenberg. In situ observations of volcanic ash clouds from the FAAM aircraft during the eruption of Eyjafjallajökull in 2010. *Journal of Geophysical Research: Atmospheres*, 117(D20), 2012. doi: 10.1029/2011JD016760.

R. A. Kahn and J. Limbacher. Eyjafjallajökull volcano plume particle-type characterization from space-based multi-angle imaging. *Atmospheric Chemistry and Physics*, 12(20): 9459–9477, 2012. doi: 10.5194/acp-12-9459-2012.

F. Kahnert. Numerical methods in electromagnetic scattering theory. *Journal of Quantitative Spectroscopy and Radiative Transfer*, 79-80:775–824, 2003. doi: 10.1016/S0022-4073(02)00321-7.

C. Klug and K. V. Cashman. Vesiculation of May 18, 1980, Mount St. Helens magma. *Geology*, 22(5):468–472, 05 1994. doi: 10.1130/0091-7613(1994)022<0468:VOMMSH>2.3.CO;2.

L. Klüser, T. Erbertseder, and J. Meyer-Arnek. Observation of volcanic ash from Puyehue–Cordón Caulle with IASI. *Atmospheric Measurement Techniques*, 6(1):35–46, 2013. doi: 10.5194/amt-6-35-2013.

KMA. `https://nmsc.kma.go.kr/enhome/html/base/cmm/selectPage.do?page=satellite.gk2a.userReadinessInformation`. Last accessed: 16 Nov. 2021.

L. Kolokolova and B. S. Gustafson. Scattering by inhomogeneous particles: microwave analog experiments and comparison to effective medium theories. *Journal of Quantitative Spectroscopy and Radiative Transfer*, 70(4):611–625, 2001. doi: 10.1016/S0022-4073(01)00033-4.

S. Kox, M. Schmidl, K. Graf, H. Mannstein, R. Buras, and J. Gasteiger. A new approach on the detection of volcanic ash clouds. In *Proceedings of the 2013 EUMETSAT Meteorological Satellite Conference*, 2013. `https://www-cdn.eumetsat.int/files/2020-04/pdf_conf_p_s11_06_kox_v.pdf`. Last accessed: 17 Nov. 2021.

S. Kox, L. Bugliaro, and A. Ostler. Retrieval of cirrus cloud optical thickness and top altitude from geostationary remote sensing. *Atmospheric Measurement Techniques*, 7(10):3233–3246, 2014. doi: 10.5194/amt-7-3233-2014.

G. Kulkarni, M. Nandasiri, A. Zelenyuk, J. Beranek, N. Madaan, A. Devaraj, V. Shutthanandan, S. Thevuthasan, and T. Varga. Effects of crystallographic properties on the ice nucleation properties of volcanic ash particles. *Geophysical Research Letters*, 42(8): 3048–3055, 2015. doi: 10.1002/2015GL063270.

A. Kylling, M. Kahnert, H. Lindqvist, and T. Nousiainen. Volcanic ash infrared signature: porous non-spherical ash particle shapes compared to homogeneous spherical ash particles. *Atmospheric Measurement Techniques*, 7(4):919–929, 2014. doi: 10.5194/amt-7-919-2014.

L3Harris. `https://www.l3harris.com/all-capabilities/advanced-baseline-imager-solutions`. Last accessed: 17 Nov. 2021.

B. Langmann. Volcanic Ash versus Mineral Dust: Atmospheric Processing and Environmental and Climate Impacts. *ISRN Atmospheric Sciences*, 2013, 2013. doi: 10.1155/2013/245076.

B. Langmann. On the Role of Climate Forcing by Volcanic Sulphate and Volcanic Ash. *Advances in Meteorology*, 2014(340123), 2014. doi: 10.1155/2014/340123.

B. Langmann, A. Folch, M. Hensch, and V. Matthias. Volcanic ash over Europe during the eruption of Eyjafjallajökull on Iceland, April–May 2010. *Atmospheric Environment*, 48:1–8, 2012. doi: 10.1016/j.atmosenv.2011.03.054.

Y. A. LeCun, L. Bottou, G. B. Orr, and K. R. Müller. Efficient BackProp. In G. Montavon, G. B. Orr, and K. R. Müller, editors, *Neural Networks: Tricks of the Trade*. Springer, Berlin and Heidelberg, Germany, 2nd edition, 2012. doi: 10.1007/978-3-642-35289-8_3.

K.-M. Lee and J.-H. Park. Optical constants for Asian dust in midinfrared region. *Journal of Geophysical Research: Atmospheres*, 119(2):927–942, 2014. doi: 10.1002/2013JD020207.

E. Limpert, W. A. Stahel, and M. Abbt. Log-normal Distributions across the Sciences: Keys and Clues. *BioScience*, 51(5):341–352, 05 2001. doi: 10.1641/0006-3568(2001)051[0341:LNDATS]2.0.CO;2.

K. N. Liou. *An Introduction to Atmospheric Radiation*. Academic Press, San Diego, CA, USA and London, United Kingdom, 2nd edition, 2002. ISBN 9780124514515.

Z. Liu, C. Peng, W. Xiang, D. Tian, X. Deng, and M. Zhao. Application of artificial neural networks in global climate change and ecological research: An overview. *Chinese Science Bulletin*, 55(34):3853–3863, 2010. doi: 10.1007/s11434-010-4183-3.

J. P. Lockwood and R. W. Hazlett. *Volcanoes: Global Perspectives*. Wiley-Blackwell, Oxford and Chichester, United Kingdom and Hoboken, NJ, USA, 1st edition, 2010. ISBN 978-1-4051-6249-4.

S. Mackie, K. Cashman, H. Ricketts, A. Rust, and M. Watson, editors. *Volcanic Ash: Hazard Observation*. Elsevier, Amsterdam, Netherlands, 1st edition, 2016. ISBN 978-0-08-100405-0.

F. F. Malavelle, J. M. Haywood, A. Jones, A. Gettelman, L. Clarisse, S. Bauduin, R. P. Allan, I. H. H. Karset, J. E. Kristjánsson, L. Oreopoulos, N. Cho, D. Lee, N. Bellouin, O. Boucher, D. P. Grosvenor, K. S. Carslaw, S. Dhomse, G. W. Mann, A. Schmidt, H. Coe, M. E. Hartley, M. Dalvi, A. A. Hill, B. T. Johnson, C. E. Johnson, J. R. Knight, F. M. O'Connor, D. G. Partridge, P. Stier, G. Myhre, S. Platnick, G. L. Stephens, H. Takahashi, and T. Thordarson. Strong constraints on aerosol–cloud interactions from volcanic eruptions. *Nature*, 546(7659):485–491, 2017. doi: 10.1038/nature22974.

F. Marenco, B. Johnson, K. Turnbull, S. Newman, J. Haywood, H. Webster, and H. Ricketts. Airborne lidar observations of the 2010 Eyjafjallajökull volcanic ash plume. *Journal of Geophysical Research: Atmospheres*, 116(D20), 2011. doi: 10.1029/2011JD016396.

J. F. Mas and J. J. Flores. The application of artificial neural networks to the analysis of remotely sensed data. *International Journal of Remote Sensing*, 29(3):617–663, 2008. doi: 10.1080/01431160701352154.

E. C. Maters, D. B. Dingwell, C. Cimarelli, D. Müller, T. F. Whale, and B. J. Murray. The importance of crystalline phases in ice nucleation by volcanic ash. *Atmospheric Chemistry and Physics*, 19(8):5451–5465, 2019. doi: 10.5194/acp-19-5451-2019.

E. C. Maters, C. Cimarelli, A. S. Casas, D. B. Dingwell, and B. J. Murray. Volcanic ash ice-nucleating activity can be enhanced or depressed by ash-gas interaction in the eruption plume. *Earth and Planetary Science Letters*, 551:116587, 2020. doi: 10.1016/j.epsl.2020.116587.

B. Mayer and A. Kylling. Technical note: The libRadtran software package for radiative transfer calculations - description and examples of use. *Atmospheric Chemistry and Physics*, 5(7):1855–1877, 2005. doi: 10.5194/acp-5-1855-2005.

B. Mayer, A. Kylling, C. Emde, R. Buras, U. Hamann, J. Gasteiger, and B. Richter. libRadtrans users's guide, 2019. `https://web.archive.org/web/20200822040829/http://www.libradtran.org/doc/libRadtran.pdf`. Last accessed: 17 Nov. 2021.

L. O. Muser, G. A. Hoshyaripour, J. Bruckert, A. Horváth, E. Malinina, S. Wallis, F. J. Prata, A. Rozanov, C. von Savigny, H. Vogel, and B. Vogel. Particle aging and aerosol–radiation interaction affect volcanic plume dispersion: evidence from the Raikoke 2019 eruption. *Atmospheric Chemistry and Physics*, 20(23):15015–15036, 2020. doi: 10.5194/acp-20-15015-2020.

M. Nakagawa and T. Ohba. Minerals in Volcanic Ash 1: Primary Minerals and Volcanic Glass. *Global Environmental Research*, 6:41–51, 2002.

M. J. Pavolonis, J. Sieglaff, and J. Cintineo. Spectrally Enhanced Cloud Objects—A generalized framework for automated detection of volcanic ash and dust clouds using passive satellite measurements: 2. Cloud object analysis and global application. *Journal of Geophysical Research: Atmospheres*, 120(15):7842–7870, 2015. doi: 10.1002/2014JD022969.

G. N. Petersen. A short meteorological overview of the Eyjafjallajökull eruption 14 April–23 May 2010. *Weather*, 65(8):203–207, 2010. doi: 10.1002/wea.634.

M. Picchiani, M. Chini, S. Corradini, L. Merucci, P. Sellitto, F. Del Frate, and S. Stramondo. Volcanic ash detection and retrievals using MODIS data by means of neural networks. *Atmospheric Measurement Techniques*, 4(12):2619–2631, 2011. doi: 10.5194/amt-4-2619-2011.

M. Picchiani, M. Chini, S. Corradini, L. Merucci, A. Piscini, and F. D. Frate. Neural network multispectral satellite images classification of volcanic ash plumes in a cloudy scenario. *Annals of Geophysics*, 57(0), 2014. doi: 10.4401/ag-6638.

A. Piscini, M. Picchiani, M. Chini, S. Corradini, L. Merucci, F. Del Frate, and S. Stramondo. A neural network approach for the simultaneous retrieval of volcanic ash parameters and $SO_2$ using MODIS data. *Atmospheric Measurement Techniques*, 7(12): 4023–4047, 2014. doi: 10.5194/amt-7-4023-2014.

J. B. Pollack, O. B. Toon, and B. N. Khare. Optical properties of some terrestrial rocks and glasses. *Icarus*, 19(3):372–389, 1973. doi: 10.1016/0019-1035(73)90115-2.

A. J. Prata. Infrared radiative transfer calculations for volcanic ash clouds. *Geophysical Research Letters*, 16(11):1293–1296, 1989. doi: 10.1029/GL016i011p01293.

A. J. Prata and I. F. Grant. Retrieval of microphysical and morphological properties of volcanic ash plumes from satellite data: Application to Mt Ruapehu, New Zealand. *Quarterly Journal of the Royal Meteorological Society*, 127(576):2153–2179, 2001. doi: 10.1002/qj.49712757615.

A. J. Prata and A. T. Prata. Eyjafjallajökull volcanic ash concentrations determined using Spin Enhanced Visible and Infrared Imager measurements. *Journal of Geophysical Research: Atmospheres*, 117(D20), 2012. doi: 10.1029/2011JD016800.

A. T. Prata, A. Folch, A. J. Prata, R. Biondi, H. Brenot, C. Cimarelli, S. Corradini, J. Lapierre, and A. Costa. Anak Krakatau triggers volcanic freezer in the upper troposphere. *Scientific Reports*, 10(1):3584, 2020. doi: 10.1038/s41598-020-60465-w.

G. S. Prata, L. J. Ventress, E. Carboni, T. A. Mather, R. G. Grainger, and D. M. Pyle. A New Parameterization of Volcanic Ash Complex Refractive Index Based on NBO/T and $SiO_2$ Content. *Journal of Geophysical Research: Atmospheres*, 124(3):1779–1797, 2019. doi: 10.1029/2018JD028679.

L. Prechelt. Early Stopping – But When? In G. Montavon, G. B. Orr, and K. R. Müller, editors, *Neural Networks: Tricks of the Trade*. Springer, Berlin and Heidelberg, Germany, 2nd edition, 2012. doi: 10.1007/978-3-642-35289-8_5.

Z. J. Przedpelski and T. J. Casadevall. Impact of Volcanic Ash from 15 December 1989 Redoubt Volcano Eruption on GE CF6-80C2 Turbofan Engines. In *Volcanic Ash and Aviation Safety: Proceedings of the First International Symposium on Volcanic Ash and Aviation Safety, U.S. Geological Survey Bulletin 2047*, pages 129–135, 1994.

S. Pugnaghi, L. Guerrieri, S. Corradini, L. Merucci, and B. Arvani. A new simplified approach for simultaneous retrieval of $SO_2$ and ash content of tropospheric volcanic clouds: an application to the Mt Etna volcano. *Atmospheric Measurement Techniques*, 6(5):1315–1327, 2013. doi: 10.5194/amt-6-1315-2013.

B. E. Reed, D. M. Peters, R. McPheat, and R. G. Grainger. The Complex Refractive Index of Volcanic Ash Aerosol Retrieved From Spectral Mass Extinction. *Journal of Geophysical Research: Atmospheres*, 123(2):1339–1350, 2018. doi: 10.1002/2017JD027362.

M. Reichstein, G. Camps-Valls, B. Stevens, M. Jung, J. Denzler, N. Carvalhais, and Prabhat. Deep learning and process understanding for data-driven Earth system science. *Nature*, 566(7743):195–204, 2019. doi: 10.1038/s41586-019-0912-1.

A. Robock. Volcanic eruptions and climate. *Reviews of Geophysics*, 38(2):191–219, 2000. doi: 10.1029/1998RG000054.

C. D. Rodgers. *Inverse Methods for Atmospheric Sounding*. World Scientific, Singapore, 2000. doi: 10.1142/3171.

N. Rogers. The composition and origin of magmas. In H. Sigurdssonn, B. Houghton, S. R. McNutt, H. Rymer, and J. Stix, editors, *The Encyclopedia of Volcanoes*, pages 93–112. Academic Press, London, 2nd edition, 2015. ISBN 978-0-12-385938-9.

C. Rolf, M. Krämer, C. Schiller, M. Hildebrandt, and M. Riese. Lidar observation and model simulation of a volcanic-ash-induced cirrus cloud during the Eyjafjallajökull eruption. *Atmospheric Chemistry and Physics*, 12(21):10281–10294, 2012. doi: 10.5194/acp-12-10281-2012.

J. Rose, William I. Scavenging of volcanic aerosol by ash: Atmospheric and volcanologic implications. *Geology*, 5(10):621–624, 10 1977. doi: 10.1130/0091-7613(1977)5<621:SOVABA>2.0.CO;2.

W. I. Rose, G. J. S. Bluth, and I. M. Watson. Ice in Volcanic Clouds: When and Where? In *Proceedings of the 2nd International Conference on Volcanic Ash and Aviation Safety, 21–24 June 2004, Alexandria, VA, USA*, pages 3.27–3.33. Office of the Federal Coordinator for Meteorological Services and Supporting Research, 2004.

D. Rosenfeld, Y. Rudich, and R. Lahav. Desert dust suppressing precipitation: A possible desertification feedback loop. *Proceedings of the National Academy of Sciences*, 98(11): 5975–5980, 2001. doi: 10.1073/pnas.101122798.

D. Rosenfeld, U. Lohmann, G. B. Raga, C. D. O'Dowd, M. Kulmala, S. Fuzzi, A. Reissell, and M. O. Andreae. Flood or Drought: How Do Aerosols Affect Precipitation? *Science*, 321(5894):1309–1313, 2008. doi: 10.1126/science.1160606.

A. N. Rublev, E. V. Gorbarenko, V. V. Golomolzin, E. Y. Borisov, J. V. Kiseleva, Y. M. Gektin, and A. A. Zaitsev. Inter-calibration of Infrared Channels of Geostationary Meteorological Satellite Imagers. *Frontiers in Environmental Science*, 6:142, 2018. doi: 10.3389/fenvs.2018.00142.

S. Ruder. An overview of gradient descent optimization algorithms, 2016. `https://arxiv.org/pdf/1609.04747.pdf`. Last accessed: 17 Nov. 2021.

D. E. Rumelhart, G. E. Hinton, and R. J. Williams. Learning Internal Representations by Error Propagation. In D. E. Rumelhart and J. L. McClelland, editors, *Parallel Distributed Processing: Explorations in the Microstructure of Cognition, Vol. 1: Foundations*, pages 318–362. MIT Press, Cambridge, MA, USA, 1986a.

D. E. Rumelhart, G. E. Hinton, and R. J. Williams. Learning representations by back-propagating errors. *Nature*, 323:533–536, 1986b. doi: 10.1038/323533a0.

B. R. Scarino, D. R. Doelling, P. Minnis, A. Gopalan, T. Chee, R. Bhatt, C. Lukashin, and C. Haney. A Web-Based Tool for Calculating Spectral Band Difference Adjustment Factors Derived From SCIAMACHY Hyperspectral Data. *IEEE Transactions on Geoscience and Remote Sensing*, 54(5):2529–2542, 2016. doi: 10.1109/TGRS.2015.2502904.

G. P. Schill, K. Genareau, and M. A. Tolbert. Deposition and immersion-mode nucleation of ice by three distinct samples of volcanic ash. *Atmospheric Chemistry and Physics*, 15 (13):7523–7536, 2015. doi: 10.5194/acp-15-7523-2015.

J. Schmetz, P. Pili, S. Tjemkes, D. Just, J. Kerkmann, S. Rota, and A. Ratier. An Introduction to Meteosat Second Generation (MSG). *Bulletin of the American Meteorological Society*, 83(7):977–992, 07 2002a. doi: 10.1175/1520-0477(2002)083<0977:AITMSG>2.3.CO;2.

J. Schmetz, P. Pili, S. Tjemkes, D. Just, J. Kerkmann, S. Rota, and A. Ratier. Radiometric Performance fo SEVIRI. *Bulletin of the American Meteorological Society*, 83(7):ES50–ES51, 2002b.

T. J. Schmit, M. M. Gunshor, W. P. Menzel, J. J. Gurka, J. Li, and A. S. Bachmeier. Introducing the Next-Generation Advanced Baseline Imager on GOES-R. *Bulletin of the American Meteorological Society*, 86(8):1079–1096, 08 2005. doi: 10.1175/BAMS-86-8-1079.

T. J. Schmit, P. Griffith, M. M. Gunshor, J. M. Daniels, S. J. Goodman, and W. J. Lebair. A Closer Look at the ABI on the GOES-R Series. *Bulletin of the American Meteorological Society*, 98(4):681–698, 2017. doi: 10.1175/BAMS-D-15-00230.1.

U. Schumann, B. Weinzierl, O. Reitebuch, H. Schlager, A. Minikin, C. Forster, R. Baumann, T. Sailer, K. Graf, H. Mannstein, C. Voigt, S. Rahm, R. Simmet, M. Scheibe, M. Lichtenstern, P. Stock, H. Rüba, D. Schäuble, A. Tafferner, M. Rautenhaus, T. Gerz, H. Ziereis, M. Krautstrunk, C. Mallaun, J.-F. Gayet, K. Lieke, K. Kandler, M. Ebert, S. Weinbruch, A. Stohl, J. Gasteiger, S. Groß, V. Freudenthaler, M. Wiegner, A. Ansmann, M. Tesche, H. Olafsson, and K. Sturm. Airborne observations of the Eyjafjalla volcano ash cloud over Europe during air space closure in Apri and May 2010. *Atmospheric Chemistry and Physics*, 11(5):2245–2279, 2011. doi: 10.5194/acp-11-2245-2011.

P. Seifert, A. Ansmann, S. Groß, V. Freudenthaler, B. Heinold, A. Hiebsch, I. Mattis, J. Schmidt, F. Schnell, M. Tesche, U. Wandinger, and M. Wiegner. Ice formation in ash-influenced clouds after the eruption of the Eyjafjallajökull volcano in April 2010. *Journal of Geophysical Research: Atmospheres*, 116(D20), 2011. doi: 10.1029/2011JD015702.

J. H. Seinfeld, C. Bretherton, K. S. Carslaw, H. Coe, P. J. DeMott, E. J. Dunlea, G. Feingold, S. Ghan, A. B. Guenther, R. Kahn, I. Kraucunas, S. M. Kreidenweis, M. J. Molina, A. Nenes, J. E. Penner, K. A. Prather, V. Ramanathan, V. Ramaswamy, P. J. Rasch, A. R. Ravishankara, D. Rosenfeld, G. Stephens, and R. Wood. Improving our fundamental understanding of the role of aerosol-cloud interactions in the climate system. *Proceedings of the National Academy of Sciences*, 113(21):5781–5790, 2016. doi: 10.1073/pnas.1514043113.

S. Self and G. P. L. Walker. Ash Clouds: Characteristics of Eruption Columns. In T. J. Casadevall, editor, *Volcanic Ash and Aviation Safety: Proceedings of the First International Symposium on Volcanic Ash and Aviation Safety in Seattle, WA, USA in July 1991, U.S. Geological Survey Bulletin 2047*, pages 65–74, Washington, DC, USA, 1991. United States Government Printing Office. doi: 10.3133/b2047.

R. A. Shaw, A. J. Durant, and Y. Mi. Heterogeneous Surface Crystallization Observed in Undercooled Water. *The Journal of Physical Chemistry B*, 109(20):9865–9868, 2005. doi: 10.1021/jp0506336.

V. Shcherbakov, O. Jourdan, C. Voigt, J.-F. Gayet, A. Chauvigne, A. Schwarzenboeck, A. Minikin, M. Klingebiel, R. Weigel, S. Borrmann, T. Jurkat, S. Kaufmann, R. Schlage, C. Gourbeyre, G. Febvre, T. Lapyonok, W. Frey, S. Molleker, and B. Weinzierl. Porous aerosol in degassing plumes of Mt. Etna and Mt. Stromboli. *Atmospheric Chemistry and Physics*, 16(18):11883–11897, 2016. doi: 10.5194/acp-16-11883-2016.

S. Shipley and A. M. Sarna-Wojcicki. Distribution, Thickness, and Mass of Late Pleistocene and Holocene Tephra from Major Volcanoes in the Northwestern United States: a Preliminary Assessment of Hazards from Volcanic Ejecta to Nuclear Reactors in the

Pacific Northwest. U.S. Geological Survey Miscellaneous Field Studies Map 1435, 1982. https://doi.org/10.3133/mf1435. Last accessed: 17 Nov. 2021.

L. Siebert, T. Simkin, and P. Kimberly. *Volcanoes of the World*. University of California Press, Berkely and Los Angeles, CA, USA and London, United Kingdom, 3rd edition, 2011. ISBN 9780520268777.

F. Sigmundsson, S. Hreinsdóttir, A. Hooper, T. Árnadóttir, R. Pedersen, M. J. Roberts, N. Óskarsson, A. Auriac, J. Decriem, P. Einarsson, H. Geirsson, M. Hensch, B. G. Ófeigsson, E. Sturkell, H. Sveinbjörnsson, and K. L. Feigl. Intrusion triggering of the 2010 Eyjafjallajökull explosive eruption. *Nature*, 468(7322):426–432, 2010. doi: 10.1038/nature09558.

H. Sigurdsson, B. Houghton, H. Rymer, J. Stix, and S. McNutt, editors. *Encyclopedia of Volcanoes*. Academic Press, San Diego, CA, USA, 1st edition, 1999.

W. L. Smith, S. Ackerman, H. Revercomb, H. Huang, D. H. DeSlover, W. Feltz, L. Gumley, and A. Collard. Infrared spectral absorption of nearly invisible cirrus clouds. *Geophysical Research Letters*, 25(8):1137–1140, 1998. doi: 10.1029/97GL03491.

I. N. Sokolik and O. B. Toon. Incorporation of mineralogical composition into models of the radiative properties of mineral aerosol from UV to IR wavelengths. *Journal of Geophysical Research: Atmospheres*, 104(D8):9423–9444, 1999. doi: 10.1029/1998JD200048.

R. Sparks. The dynamics of bubble formation and growth in magmas: A review and analysis. *Journal of Volcanology and Geothermal Research*, 3(1):1–37, 1978. doi: 10.1016/0377-0273(78)90002-1.

R. J. Sparks, J. G. Moore, and C. J. Rice. The initial giant umbrella cloud of the May 18th, 1980, explosive eruption of Mount St. Helens. *Journal of Volcanology and Geothermal Research*, 28(3):257–274, 1986. doi: 10.1016/0377-0273(86)90026-0.

R. S. J. Sparks. The dimensions and dynamics of volcanic eruption columns. *Bulletin of Volcanology*, 48:3–15, 1986. doi: 10.1007/BF01073509.

R. J. S. Spence, I. Kelman, P. J. Baxter, G. Zuccaro, and S. Petrazzuoli. Residential building and occupant vulnerability to tephra fall. *Natural Hazards and Earth System Sciences*, 5(4):477–494, 2005. doi: 10.5194/nhess-5-477-2005.

I. Steinke, O. Möhler, A. Kiselev, M. Niemand, H. Saathoff, M. Schnaiter, J. Skrotzki, C. Hoose, and T. Leisner. Ice nucleation properties of fine ash particles from the Eyjafjallajökull eruption in April 2010. *Atmospheric Chemistry and Physics*, 11(24):12945–12958, 2011. doi: 10.5194/acp-11-12945-2011.

B. Stevens and G. Feingold. Untangling aerosol effects on clouds and precipitation in a buffered system. *Nature*, 461(7264):607–613, 2009. doi: 10.1038/nature08281.

J. A. Stevenson, S. C. Millington, F. M. Beckett, G. T. Swindles, and T. Thordarson. Big grains go far: understanding the discrepancy between tephrochronology and satellite infrared measurements of volcanic ash. *Atmospheric Measurement Techniques*, 8(5): 2069–2091, 2015. doi: 10.5194/amt-8-2069-2015.

A. Stohl, A. J. Prata, S. Eckhardt, L. Clarisse, A. Durant, S. Henne, N. I. Kristiansen, A. Minikin, U. Schumann, P. Seibert, K. Stebel, H. E. Thomas, T. Thorsteinsson, K. Tørseth, and B. Weinzierl. Determination of time- and height-resolved volcanic ash emissions and their use for quantitative ash dispersion modeling: the 2010 Eyjafjallajökull eruption. *Atmospheric Chemistry and Physics*, 11(9):4333–4351, 2011. doi: 10.5194/acp-11-4333-2011.

T. Storelvmo and I. Tan. The Wegener-Bergeron-Findeisen process – Its discovery and vital importance for weather and climate. *Meteorologische Zeitschrift*, 24(4):455–461, 07 2015. doi: 10.1127/metz/2015/0626.

J. Strandgren, L. Bugliaro, F. Sehnke, and L. Schröder. Cirrus cloud retrieval with MSG/SEVIRI using artificial neural networks. *Atmospheric Measurement Techniques*, 10(9):3547–3573, 2017a. doi: 10.5194/amt-10-3547-2017.

J. Strandgren, J. Fricker, and L. Bugliaro. Characterisation of the artificial neural network CiPS for cirrus cloud remote sensing with MSG/SEVIRI. *Atmospheric Measurement Techniques*, 10(11):4317–4339, 2017b. doi: 10.5194/amt-10-4317-2017.

G. E. Thomas and K. Stamnes. *Radiative Transfer in the Atmosphere and Ocean*. Cambridge University Press, Cambridge, United Kingdom, 1st edition, 1999.

H. E. Thomas and A. J. Prata. Sulphur dioxide as a volcanic ash proxy during the April-May 2010 eruption of Eyjafjallajökull Volcano, Iceland. *Atmospheric Chemistry and Physics*, 11:6871–6880, 2011. doi: 10.5194/acp-11-6871-2011.

C. Timmreck. Modeling the climatic effects of large explosive volcanic eruptions. *Wiley Interdisciplinary Reviews: Climate Change*, 3(6):545–564, 2012. doi: 10.1002/wcc.192.

S. Twomey. The Influence of Pollution on the Shortwave Albedo of Clouds. *Journal of Atmospheric Sciences*, 34(7):1149–1152, 1977. doi: 10.1175/1520-0469(1977)034<1149: TIOPOT>2.0.CO;2.

E. Venzke, editor. *Global Volcanism Program, 2013. Volcanoes of the World, v. 4.10.2 (24 Aug 2021)*. Smithsonian Institution, 2021. doi: 10.5479/si.GVP.VOTW4-2013. Last accessed: 7 Septemer 2021.

A. Vogel, S. Diplas, A. J. Durant, A. S. Azar, M. F. Sunding, W. I. Rose, A. Sytchkova, C. Bonadonna, K. Krüger, and A. Stohl. Reference data set of volcanic ash physicochemical and optical properties. *Journal of Geophysical Research: Atmospheres*, 122 (17):9485–9514, 2017. doi: 10.1002/2016JD026328.

F. E. Volz. Infrared Optical Constants of Ammonium Sulfate, Sahara Dust, Volcanic Pumice, and Flyash. *Applied Optics*, 12(3):564–568, 1973. doi: 10.1364/AO.12.000564.

J. M. Wallace and P. V. Hobbs. *Atmospheric Science: An Introductory Survey*. Academic Press, Burlington, MA, USA and San Diego, CA, USA and London, United Kingdom, 2nd edition, 2006. ISBN 9780127329512.

F. Waquet, F. Peers, P. Goloub, F. Ducos, F. Thieuleux, Y. Derimian, J. Riedi, M. Chami, and D. Tanré. Retrieval of the Eyjafjallajökull volcanic aerosol optical and microphysical properties from POLDER/PARASOL measurements. *Atmospheric Chemistry and Physics*, 14(4):1755–1768, 2014. doi: 10.5194/acp-14-1755-2014.

S. C. Watkin. The application of AVHRR data for the detection of volcanic ash in a Volcanic Ash Advisory Centre. *Meteorological Applications*, 10(4):301–311, 2003. doi: 10.1017/S1350482703001063.

I. Watson, V. Realmuto, W. Rose, A. Prata, G. Bluth, Y. Gu, C. Bader, and T. Yu. Thermal infrared remote sensing of volcanic emissions using the moderate resolution imaging spectroradiometer. *Journal of Volcanology and Geothermal Research*, 135(1): 75–89, 2004. ISSN 0377-0273. doi: 10.1016/j.jvolgeores.2003.12.017.

M. Watson. Test the effects of ash on jet engines. *Nature*, 520(7546):133–133, 2015. doi: 10.1038/520133a.

K. Weber, J. Eliasson, A. Vogel, C. Fischer, T. Pohl, G. van Haren, M. Meier, B. Grobéty, and D. Dahmann. Airborne in-situ investigations of the Eyjafjallajökull volcanic ash plume on Iceland and over north-western Germany with light aircrafts and optical particle counters. *Atmospheric Environment*, 48:9–21, 2012. doi: 10.1016/j.atmosenv.2011.10.030.

B. Weinzierl, D. Sauer, A. Minikin, O. Reitebuch, F. Dahlkötter, B. Mayer, C. Emde, I. Tegen, J. Gasteiger, A. Petzold, A. Veira, U. Kueppers, and U. Schumann. On the visibility of airborne volcanic ash and mineral dust from the pilot's perspective in flight. *Physics and Chemistry of the Earth*, 45-46:87–102, 2012. doi: 10.1016/j.pce.2012.04.003.

S. Wen and W. I. Rose. Retrieval of sizes and total masses of particles in volcanic clouds using AVHRR bands 4 and 5. *Journal of Geophysical Research: Atmospheres*, 99(D3): 5421–5431, 1994. doi: 10.1029/93JD03340.

L. M. Western, M. I. Watson, and P. N. Francis. Uncertainty in two-channel infrared remote sensing retrievals of a well-characterised volcanic ash cloud. *Bulletin of Volcanology*, 77 (8):67, 2015. doi: 10.1007/s00445-015-0950-y.

T. M. Wilson, C. Stewart, V. Sword-Daniels, G. S. Leonard, D. M. Johnston, J. W. Cole, J. Wardman, G. Wilson, and S. T. Barnard. Volcanic ash impacts on critical infrastructure. *Physics and Chemistry of the Earth*, 45-46:5–23, 2012. doi: 10.1016/j.pce.2011.06.006.

D. M. Winker, M. A. Vaughan, A. Omar, Y. Hu, K. A. Powell, Z. Liu, W. H. Hunt, and S. A. Young. Overview of the CALIPSO Mission and CALIOP Data Processing Algorithms. *Journal of Atmospheric and Oceanic Technology*, 26(11):2310–2323, 11 2009. ISSN 0739-0572. doi: 10.1175/2009JTECHA1281.1.

WMO, 2015. Meeting on the Intercomparison of Satellite-based Volcanic Ash Retrieval Algorithms, Madison WI, USA, 29 June–2 July 2015, Final Report. World Meteorological Organization, 2015. `https://web.archive.org/web/20171113102551/http://www.wmo.int/pages/prog/sat/documents/SCOPE-NWC-PP2_VAIntercompWSReport2015.pdf`. Last accessed: 17 Nov. 2021.

WMO/GHI. `https://space.oscar.wmo.int/instruments/view/ghi`. Last accessed: 16 Nov. 2021.

WMO/IMAGER-INSAT. `https://space.oscar.wmo.int/instruments/view/imager_insat`. Last accessed: 16 Nov. 2021.

WMO/MSG1. `https://space.oscar.wmo.int/satellites/view/meteosat_8_iodc`. Last accessed: 17 Nov. 2021.

WMO/MSU-GS. `https://space.oscar.wmo.int/instruments/view/msu_gs`. Last accessed: 16 Nov. 2021.

WMO/MX-LWIR. `https://www.wmo-sat.info/oscar/instruments/view/mx_lwir`. Last accessed: 16 Nov. 2021.

WMO/OSCAR. `https://www.wmo-sat.info/oscar/satellites/`. Last accessed: 16 Nov. 2021.

WMO/S-VISSR. `https://space.oscar.wmo.int/instruments/view/s_vissr_fy_2f_g_h`. Last accessed: 16 Nov. 2021.

T. Wriedt. Light scattering theories and computer codes. *Journal of Quantitative Spectroscopy and Radiative Transfer*, 110(11):833–843, 2009. doi: 10.1016/j.jqsrt.2009.02.023.

J. Yang, Z. Zhang, C. Wei, F. Lu, and Q. Guo. Introducing the New Generation of Chinese Geostationary Weather Satellites, Fengyun-4. *Bulletin of the American Meteorological Society*, 98(8):1637–1658, 2017. doi: 10.1175/BAMS-D-16-0065.1.

P. Yang, K.-N. Liou, L. Bi, C. Liu, B. Yi, and B. A. Baum. On the radiative properties of ice clouds: Light scattering, remote sensing, and radiation parameterization. *Advances in Atmospheric Sciences*, 32:32–63, 2015. doi: 10.1007/s00376-014-0011-z.

T. Yu, W. I. Rose, and A. J. Prata. Atmospheric correction for satellite-based volcanic ash mapping and retrievals using "split window" IR data from GOES and AVHRR. *Journal of Geophysical Research: Atmospheres*, 107(D16):AAC 10–1–AAC 10–19, 2002. doi: 10.1029/2001JD000706.

T. Yuan, L. A. Remer, and H. Yu. Microphysical, macrophysical and radiative signatures of volcanic aerosols in trade wind cumulus observed by the A-Train. *Atmospheric Chemistry and Physics*, 11(14):7119–7132, 2011. doi: 10.5194/acp-11-7119-2011.

W. Zhu, L. Zhu, J. Li, and H. Sun. Retrieving volcanic ash top height through combined polar orbit active and geostationary passive remote sensing data. *Remote Sensing*, 12: 953, 2020. doi: 10.3390/rs12060953.

# Acknowledgements

Carrying out this thesis would not have been possible without the guidance and support of many people. To begin, I want to thank Dr. Margarita Vázquez-Navarro who trusted me first and gave me the opportunity to write my thesis at the Institute of Atmospheric Physics of the German Aerospace Center. Next, I am very grateful to Prof. Dr. Bernhard Mayer, Prof. Dr. Christiane Voigt and Prof. Dr. Markus Rapp for their supervision of my work, their guidance and valuable feedback and comments. In particular, I want to express my deepest appreciation to Dr. Luca Bugliaro, who shared his time and knowledge with me. Who introduced me to passive remote sensing of clouds and aerosols, had always an open door for me to brainstorm and discuss scientific problems, and who reviewed all my papers, posters and presentations. It was a pleasure working with you and I owe you a lot!

Furthermore, I am thankful to numerous other people who contributed to this work in one way or another. To Prof. Dr. Donald Dingwell for sharing his expertise on volcanic processes and volcanic ash in particular. To Dr. Adrian J. Hornby for sharing his knowledge on volcanic ash properties and discussing the corresponding refractive indices. To Dr. Josef Gasteiger for introducing me to the MOPSMAP package. To Dr. Marius Schmidl for advising me in using RTSIM. To Dr. Daniel K. Zhou for providing a climatology of IASI-based surface emissivities. To Dr. Ka Lok Chan for providing modeled data of nitrogen dioxide mixing ratios. To Prof. Dr. Ulrich Schumann for providing the in situ measurements of the Eyjafjallajökull ash clouds in 2010 using the Falcon 20E aircraft operated by the flight experiment facilities of the German Aerospace Center. To Dr. Franco Marenco for providing the lidar measurements of the Eyjafjallajökull ash clouds in 2010 using the BAe-146-301 Atmospheric Research Aircraft operated by Directflight Ltd. and managed by the Facility for Airborne Atmospheric Measurements of the Natural Environment Research Council and the Met Office. To Dr. Jayanta Kar for providing CALIOP retrievals of the Puyehue-Cordón Caulle ash clouds in 2011. To Dr. Matthieu Plu for providing the volcanic ash transport and dispersion multi model multi source term ensemble of the Eyjafjallajökull eruption in 2010. To Dr. Winfried Beer and Susanne Flierl for helping me with all kinds of technical and administrative issues, respectively. To Dr. Jonas Wilzewski, Dr. Johan Strandgren, Georgios Dekoutsidis, Dr. Ralf Meerkötter and Christoph Linse for helpful comments on parts of this manuscript. To my office colleagues Dr. Eleni Marinou, Johannes Lucke, Markus Laufmann and Manuel Moser, as well as Dr. Andreas Luther, Eleni Tetoni and all members of the cloud physics department and the former passive remote sensing group for a productive and always enjoyable working environment, occasional dart matches

and extended breaks at the lake. I would like to stress again my gratitude to all the co-authors of the presented papers for discussing the results and reviewing the paper drafts.

Parts of this work were financially supported by and linked to the "European Natural Airborne Disaster Information and Coordination System for Aviation" (EUNADICS-AV) project funded by the European Union's Horizon 2020 research and innovation program under grant agreement No. 723986; the German weather service; the "Terrestrial Magmatic Systems Research Platform" (TeMaS) associated to the University Mainz; and the project "Der individuelle und automatisierte Luftverkehr" (DIAL) by the German Aerospace Center. I am also grateful to EUMETSAT and ECMWF for providing the satellite and model data, respectively. In addition, I am thankful to the German Aerospace Center for letting me participate at the "DLR Graduate Program" and supporting various conference and workshop visits.

A heartfelt thank you to Ineke Zimmermann for being by my side during these last years, for always encouraging me and—at the end of the day—reminding me not to forget to live! And last but not least to my parents Helmut and Monika Piontek and my sister Jennifer Piontek for believing in me even when I had doubts, and supporting me ever since the very beginning. Thank you so much!